Coupled thermo-geophysical inversion for permafrost monitoring

Soňa Tomaškovičová

PhD Thesis

Department of Civil Engineering
2017

DTU Civil Engineering Report R-387

DTU Civil Engineering
Department of Civil Engineering

Ph.D. Thesis
Doctor of Philosophy

DTU Civil Engineering
Department of Civil Engineering

Coupled thermo-geophysical inversion for permafrost monitoring

Soňa Tomaškovičová

Kongens Lyngby 2018

DTU

DTU Byg
Department of Civil Engineering
Technical University of Denmark

Brovej
Building 118
2800 Kongens Lyngby, Denmark
Phone +45 4525 1700
byg@byg.dtu.dk
www.byg.dtu.dk

Preface

This doctoral thesis was prepared at The Arctic Technology Centre, Department of Civil Engineering, Technical University of Denmark, in partial fulfillment of the requirements for acquiring a degree *Philosophiæ Doctor* (Ph.D.). The Ph.D. project has been carried out between January 2012 and April 2017, with Associate Professor Thomas Ingeman-Nielsen as supervisor. An external stay of two months took place in Spring 2014 at the Department of Geosciences, Université de Fribourg, Switzerland, under supervision of Professor Christian Hauck.

The work presented in this dissertation deals with development and testing of a coupled modeling framework for calibrating thermal properties of ground undergoing cycles of freezing and thawing with time lapse geoelectrical data. The dissertation summarizes field, laboratory and modeling studies. Parts of this work have been presented at 6 international conferences, in 2 articles published during the Ph.D. studies, and in one article currently submitted to a scientific journal.

Kongens Lyngby, 31. August 2017

Soňa Tomaškovičová

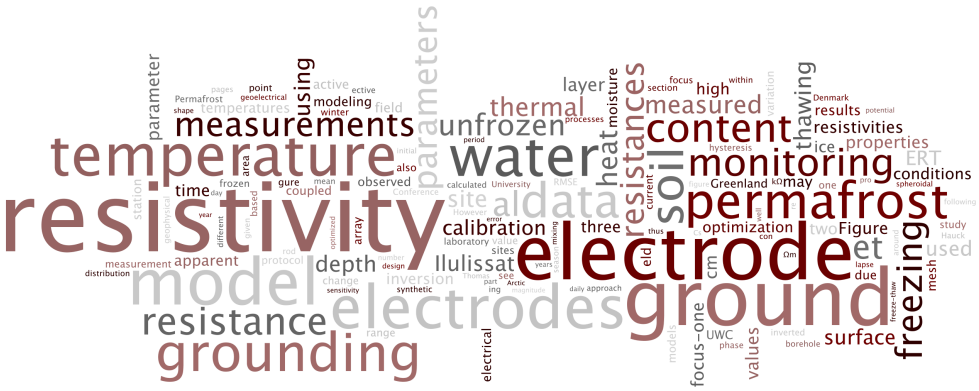
resistivity
temperature
model
electrodes
ground
electrode
grounding
resistance
measurements
water
permafrost
content
monitoring
soil
data
freezing
parameters
unfrozen
thawing
measured
resistances
thermal
heat
moisture
layer
parameter
using
depth
apparent
inversion
calibration
site
Ilulissat
focus-one
surface
values
properties
ice
ERT
conditions
Figure
used
time
coupled
observed
frozen
three
optimization
results
resistivities
Greenland
Denmark
UWC
borehole
electrical

Summary

This dissertation summarizes results of 5 years of field, laboratory and modeling studies of permafrost properties in Ilulissat, West Greenland. Ilulissat town and airport are located in an area of frost-susceptible, ice-rich marine sediments with residual salinity content in pore water, which effectively lowers the freezing point of the soil. Consequently, these sediments have strength properties similar to thawed ground in spite of ground temperatures well below 0 °C. In the view of increasing pressure on infrastructure development, better knowledge of such permafrost types, distribution, thermal and geotechnical properties is needed for informing sound and sustainable design choices.

Monitoring approaches using geophysical methods have become more widespread in permafrost studies, as they are indicative of spatial variation and in-situ processes rather than isolated properties in time and space. However, they only provide indirect information about the properties in question. To enable quantitative interpretation of in terms of thermal properties and ground ice changes, there is a need for extensive calibration and validation data.

In this project, we experimented with use of time lapse geoelectrical data for calibration of thermal model simulating heat transfer in active layer and permafrost. To acquire necessary calibration/validation data, we built a station for monitoring of ground temperature, electrical resistivity and soil moisture regimes. Automated resistivity measuring system was optimized for time lapse acquisitions in this environment characterized by extremely variable electrode grounding conditions between thawed *vs.* frozen season. Dense data series collected over three years provided insight into relationships between soil petro-physical parameters. We observed that temperature-dependent ground physical properties depend strongly on history of freeze-thaw cycles. Magnitudes of observed water content and resistivity hysteresis respectively have implications for thermal modeling and interpretation of resistivity changes in terms of temperature and ground ice content changes.

Thermal regime of the ground at the site can be simulated by one-dimensional model of conductive heat transfer in saturated porous medium. Sensitive thermal parameters were calibrated in an automated optimization scheme using gradient-search algorithm. When calibrated on borehole temperature data, the model reproduced training ground temperature dataset within ±0.55 °C, provided that the freeze-thaw water content hysteresis was accounted for. The calibrated model predicted the temperature variation in two testing datasets within ±0.32 to ±0.62 °C, depending on length of the testing timeseries.

The coupled inversion approach showed that the time lapse resistivity data contain information that constrains the optimization of thermal parameters of the heat model. In spite of not fully appropriate resistivity model, the thermal calibration was useful and reproduced the training dataset within $\pm 0.65\,^{\circ}\mathrm{C}$, which is comparable to calibration on borehole temperatures. Thermal parameters optimized in coupled inversion predicted the temperature variation in the two testing datasets within $\pm 0\,^{\circ}\mathrm{C}$ to $0\,^{\circ}\mathrm{C}$.

A number of possibilities and paths for improvement of both coupled and uncoupled optimization approaches has been identified and identification of these bottlenecks is considered one of the contributions of this thesis.

Sammenfatning

Denne afhandling opsummerer resultaterne af 5 års felt-, laboratorie- og modelleringsundersøgelser af egenskaber i permafrost i Ilulissat, Vestgrønland. Ilulissat by og lufthavnen er beliggende i et område med frost-modtagelige, marine sedimenter med masser af is med restindhold af salt i porevandet, hvilket effektivt sænker jordens frysepunkt. Disse sedimenter har således styrkeegenskaber svarende til optøet jord på trods af, at jordtemperaturerne ligger langt under 0 °C. I lyset af et stigende pres for en infrastrukturudvikling, er der behov for bedre kendskab til sådanne permafrosttyper, distribution, termiske og geotekniske egenskaber for at træffe sunde og bæredygtige designvalg.

Overvågning ved hjælp af geofysiske metoder er blevet mere udbredt i permafroststudier, da de er en indikator for rumlig variation og in situ-processer snarere end isolerede egenskaber i tid og rum. De giver dog kun indirekte oplysninger om de pågældende egenskaber. For at muliggøre en kvantitativ fortolkning af de termiske egenskaber og ændringer i grundisen, er der behov for omfattende kalibrerings- og valideringsdata.

I dette projekt eksperimenterede vi med tidsforskydning af geoelektriske data til kalibrering af en termisk model simulering af varmeoverførsel i aktive lag og permafrost. For at opnå de nødvendige kalibrerings- / valideringsdata byggede vi en station til overvågning af jordtemperatur, elektrisk resistivitet og jordfugtighedsregimer. Et Automatiseret resistivitetsmålesystem blev optimeret til tidsforskydning målinger i dette miljø præget af ekstremt variable elektrodejordningsforhold mellem den optøede contra frossen sæson. En massiv dataserie samlet over tre år gav indblik i forholdet mellem jordens petro-fysiske parametre. Vi observerede, at temperaturafhængige jordfysiske egenskaber afhænger stærkt fryse-optøningscykler. Størrelser af observeret vandindhold og resistivitets hysterese har hhv. Implikationer for termisk modellering og fortolkning af resistivitetsændringer med hensyn til ændringer i temperatur og jordis indhold.

Termisk regulering af jorden på stedet kan simuleres ved endimensionel model af ledende varmeoverførsel i mættet porøst medium. Følsomme termiske parametre blev kalibreret i et automatiseret optimeringsskema ved brug af gradientsøgningsalgoritme. Når data om borehulstemperaturen kalibreres, reproducerede modellen træning grund temperatur dataset indenfor 0.55 °C, forudsat at hysteresen af fryse-tø vand blev taget i betragtning.. Den kalibrerede model forudsagde temperaturvariationen i to testdata set inden for 0.32 °C - 00.63 °C afhængigt af længden af testtiderne.

Den koblede inversion tilgang viste, at tidsforløbets resistivitetsdata indeholder oplysninger, som begrænser optimeringen af termiske parametre i varmemodellen. På trods af en ikke fuldt passende resistivitetsmodel var den termiske kalibrering nyttig og reproducerede trænings dataset inden for 0.65 °C, hvilket kan sammenlignes med kalibrering ved borehulstemperaturer. Termiske parametre optimeret i koblet inversion forudsagde temperaturvariationen i de to testdata set inden for 0.30 °C - 00.55 °C.

En række muligheder og metoder til forbedring af både koblede og ukoblede optimeringsmetoder er blevet identificeret, og identifikationen af disse flaskehalse betragtes som et af bidragene fra denne afhandling.

To my mother and my grandmother.

Acknowledgements

"*The greatest challenge to any thinker is stating the problem in a way that will allow a solution.*" – Bertrand Russell

Six years ago, I was fortunate to be given a chance to work on a unique and exciting Ph.D. project. I traveled to some unexpected parts of the world and made many valuable acquaintances. I am grateful for being given this opportunity.

I wish to thank my colleagues at the Arctic Technology Centre and at KTI Sisimiut for creating a family-like working environment and for many enjoyable experiences during my stays in Greenland.

I am thankful to Prof. Christian Hauck, and colleagues and friends at the University of Fribourg for warm welcome during my external stay.

I wish to thank Prof. Bernd Etzelmüller for taking me along on a number of permafrost-related excursions and for always making me feel like part of his group.

I have been lucky to enjoy great company and refreshing humor of Prof. Emeritus Niels Nielsen Foged whom I also wish to thank for encouragement in the crucial moments of thesis writing.

Without the unconditional love and support from my friends and family, some of the hurdles of Ph.D. studies would be hard to overcome.

This thesis could be completed thanks to selfless help, encouragement and patience of my best friend and my sweetheart Linh. It is not a coincidence that I could significantly advance in my work after we've teamed up; you have contributed to this time being among the happiest, most fulfilling and formative years, and I am yet to thank you enough for that.

My warmest thanks go to my Ph.D. supervisor, Assoc. Prof. Thomas Ingeman-Nielsen. His unwavering support, kind understanding and exceptional work ethics have been my inspiration throughout this Ph.D. project and beyond.

List of publications

The dissertation is based on the following articles prepared during the course of the studies between 2012 - 2017.

Published articles:

- Ingeman-Nielsen, T, Tomaškovičová, S & Dahlin, T, 2016: Effect of electrode shape on grounding resistances - Part 1: The focus-one protocol. Geophysics, vol 81, no. 1, pp. WA159-WA167. DOI: 10.1190/geo2015-0484.1

- Tomaškovičová, S, Ingeman-Nielsen, T, Christiansen, AV, Brandt, I, Dahlin, T & Elberling, B, 2016: Effect of electrode shape on grounding resistances - Part 2: Experimental results and cryospheric monitoring. Geophysics, vol 81, no. 1, pp. WA159-WA172. DOI: 10.1190/GEO2015-0148.1

Submitted article:

- Tomaškovičová, S & Ingeman-Nielsen, T: Automated monitoring of resistivity, moisture and temperature regimes in fine-grained permafrost soils in Ilulissat, West Greenland. *Submitted to Permafrost and Periglacial Processes.*

8 conference abstracts were presented at international conferences during the course of the Ph.D. studies:

- Tomaškovičová, S, Paamand, E, Ingeman-Nielsen, T & Bauer-Gottwein, P 2012: Coupled Thermo-Geophysical Inversion for Permafrost Monitoring. Oral presentation. 10^{th} International Conference on Permafrost, Salekhard, Russian Federation.

- Tomaškovičová, S, Paamand, E, Ingeman-Nielsen, T & Bauer-Gottwein, P, 2013: Coupled thermo-geophysical inversion for high-latitude permafrost monitoring: assessment of the method and practical considerations. Oral presentation. Geophysical Research Abstracts, vol 15, EGU2013-764.

- Tomaškovičová, S & Ingeman-Nielsen, T, 2013: Comparison of alternative electrode types for improvement of electrodeground coupling in highly-resistive environment. Experience from the time lapse geoelectrical station for high-latitude permafrost monitoring, Ilulissat, West Greenland. Oral presentation. 2nd International Workshop on Geoelectrical Monitoring GELMON, Vienna, Austria.

- Tomaškovičová, S, Ingeman-Nielsen, T & Bauer-Gottwein, P, 2014: Optimization of thermal parameters of frozen ground using surface geoelectrical data from permafrost monitoring and surface temperature measurements. Oral presentation. in Book of Abstracts of EUCOP4 – 4th European Conference on Permafrost, pp. 458-458.

- Tomaškovičová, S, Ingeman-Nielsen, T, Christiansen, AV, Brandt, I, Dahlin, T & Elberling, B, 2016: Optimizing electrode shapes for ERT monitoring in permafrost areas. Oral presentation. in Proceedings of the XI. International Conference on Permafrost, pp. 988-989.

- Tomaškovičová, S & Ingeman-Nielsen, T, 2016: Automated long-term time lapse ERT monitoring of high-latitude permafrost – results of 3 years of monitoring and modeling study. Poster presentation. in Proceedings of the XI. International Conference on Permafrost, pp. 990-991.

- Tomaškovičová, S & Ingeman-Nielsen, T, 2017: Modeling in-situ hysteretic variation of unfrozen water content in high-latitude fine-grained permafrost. Poster presentation. Proceedings of the 2nd Asian Conference on Permafrost, Sapporo, Japan.

- Tomaškovičová, S & Ingeman-Nielsen, T, 2017: Modeling the ground resistivity from unfrozen water content in fine-grained high-latitude permafrost. Oral presentation. Proceedings of the 2nd Asian Conference on Permafrost, Sapporo, Japan.

1 invited plenary talk was given at the 2nd Asian Conference on Permafrost (5th July 2017, Sapporo, Japan)

- Tomaškovičová, S, 2017: Integrated site investigations for infrastructure planning in Greenland. Proceedings of the 2nd Asian Conference on Permafrost, Sapporo, Japan.

Contents

CHAPTER 1

Introduction

1.1 Problem statement

Permafrost underlies vast areas of sparsely inhabited land, predominantly in the Arctic. For scattered human communities living in the regions, building and maintaining infrastructure is costly and often inefficient due to lack of deeper knowledge about permafrost conditions. In the view of current industry and tourism expansion, there is a need for more reliable permafrost projections that will support more sustainable infrastructure design choices.

The Arctic regions are the most severely affected by climate warming (Smith et al., 2010; Romanovsky et al., 2015), with average air temperature increase for the ice-free portion of Greenland predicted at 1.3 °C (Daanen et al., 2011). Presence of thaw-sensitive marine sediments along the west coast of Greenland contributes to conditions favorable for permafrost retreat (Stendel et al., 2008). Prediction of permafrost degradation, risk evaluation and choice of adequate adaptation measures depends on knowledge of permafrost distribution, thermal state and properties. Acquisition of permafrost data with better temporal and spatial resolution is a precondition for this knowledge (Ingeman-Nielsen et al., 2017in press).

Traditional methods of assessing permafrost thermal state are based on ground temperature measurements in boreholes. However in particular geological settings (fine-grained sediments, sediments with residual salinity in pore water), ground temperature observations may fail to document anomalies such as lowered freezing point. Drilling and geotechnical testing remain the most reliable methods for evaluating ground conditions, though they only provide spatially discrete information without indication of variability of ground properties. Additionally, high costs and logistical constraints may be prohibitive of comprehensive site investigation campaigns in remote regions. Alternative observation techniques have been therefore steadily gaining popularity in permafrost studies.

In ice-rich and ice-bonded permafrost, changing thermal state of the ground is reflected in changing ground ice content. Due to the contrasting physical properties

of ice and water, *geophysical methods* such as electrical resistivity tomography, ground-penetrating radar, and seismic surveys have been increasingly used to delineate frozen ground and areas of high ground-ice content (Jørgensen and Andreasen, 2007; Fortier et al., 2008), and to map changes in ground ice content (Hilbich et al., 2011). When operated in monitoring mode, and with acquisition of sufficiently long and complete timeseries, the geophysical data provide insight into the in-situ processes rather than discrete (in time and space) ground properties.

Electrical resistivity tomography (ERT) has proved to be particularly suitable for monitoring applications, due to its repeatability, relative speed of data acquisition and comparatively easy data processing. Its high sensitivity to phase change between water and ice makes it capable of distinguishing unfrozen water content changes at subzero temperatures (Kneisel, 2006; Hilbich et al., 2011). The ERT has been successfully applied to monitor short-term changes in unfrozen water content during active layer freezing in arctic permafrost (Doetsch et al., 2015), and to monitor long-term resistivity changes and ground ice degradation in mountain permafrost (Hilbich et al., 2008; Mewes et al., 2016). Studies by Krautblatter and Hauck, 2007 and Hauck et al., 2008 demonstrate that there is a quantitative link between electrical and thermal properties of geological materials, pawing the way for quantitative temperature-geophysical interpretations. A *thermal model informed by surface geophysical measurements* would allow assessment of frozen ground conditions and prediction of ground stability changes under various climate scenarios reducing the need for invasive, costly and logistically demanding drilling investigations.

In spite of important advantages, numerous challenges continue to hamper wider deployment of ERT in permafrost monitoring:

- **Petro-physical relationship** The main challenge when using geoelectrical (and generally, geophysical) methods is that they provide *indirect* indication about ground properties. Understanding synergy of processes conditioning ground thermal regime is a prerequisite for correct setup of conceptual and mathematical models. Site-specific calibration is then required for quantitative interpretation of the geoelectrical data in terms of ground temperature and ice content changes.

- **Logistics** While permafrost covers approximately 26% of the dry land, these are at the same time some of the most remote areas where infrastructure is lacking and human communities are sparse. Limited access to the field installations puts more emphasis on software stability, energy self-sufficiency and reliable data backup and transmission.

- **Extremely high grounding resistances** Quality - and even feasibility - of ERT measurements depend on good contact between electrodes and their embedding medium. During frozen season, extremely high grounding resistances compromise data quality (Doetsch et al., 2015; Hilbich et al., 2011) or make the measurements impossible to carry out altogether (Tomaskovicova et al., 2016).

It is therefore crucial to optimize the electrodes of the array so that it can perform reasonably well in both winter and summer seasons.

- **Data quality and processing** Large amounts of monitoring data can only be efficiently handled if an automated framework for sorting, filtering and processing is in place.

Solutions to these challenges typically need to be tailored to the specific site's conditions, instrumentation used, and specific goals of the monitoring/modeling. Nonetheless, experience with ERT monitoring from diverse periglacial settings expands the knowledge base for future applications and comparisons.

1.2 Goals and scope of the thesis

Goals As exemplified by the arguments in the previous section, availability of ground heat transport model calibrated with surface geophysical data would hold important advantages for permafrost mapping and modeling. Our hypothesis, based on existing research, is that time lapse ground resistivity data contain information that can be used to calibrate a model of heat transfer. Consequently, the main goal of this project was to investigate feasibility of using time lapse geoelectrical data for modeling the thermal regime of active layer and permafrost.

To achieve this goal, we aimed to:

- Design and set up a monitoring station in high-latitude permafrost collecting complete, daily timeseries of environmental parameters needed for model development, calibration and validation. This required us to tackle numerous logistical challenges associated with long-term geoelectrical monitoring in remote, harsh environment, as discussed in section 1.1.
- Describe the petro-physical relationships between environmental parameters related to the ground thermal regime and coupling to resistivity, namely the ground temperature, soil moisture content and ground resistivity.
- Describe and evaluate modeling framework for simulating ground thermal regime using the time lapse geophysical data.
- Evaluate performance of heat model calibration on geophysical data in comparison to the traditional calibration on borehole temperature data.
- Provide an indication of length of datasets and sampling frequencies needed for successful model calibration.

Scope The coupled modeling framework is designed and tested with time lapse ground resistivity data. While the idea behind the coupled inversion approach is that,

in principle, any kind of geophysical data can be used (as long as the petro-physical relationship exists and can be calibrated), testing the method with other type of geophysical data is outside of the scope of this thesis.

In agreement with principle of parsimony, we develop and test the method with one-dimensional homogeneous model. Possibility of extending the model into two- or three dimensions is one of the expected benefits of the method and would be interesting part of future developments.

Focus of this thesis is acquisition, processing, interpretation and exploitation of acquired data in modeling. Consequently, extensive background knowledge associated with theory of conductive heat transport and electrical resistivity method is not detailed in this dissertation. Sizeable literature is available that discusses these topics; some of the textbooks used or cited throughout this thesis are the following: Telford et al. (1990), Reynolds (2011), and Parasnis (2012) for the theory of geoelectrical methods, and Carslaw and Jaeger (1959), Farouki (1981), and Lunardini (1981) for the theory of heat transfer.

1.3 Structure of the thesis

The thesis is structured around 2 published articles, 1 article to be submitted shortly and 2 chapters that collectively contain bulk of the findings of the Ph.D. project. The articles are briefly summarized in dedicated chapters, while full-texts are included in the Appendices A - C. In addition, 9 conference abstracts are included in Appendices D - L. The abstracts contain partial results of the studies which were eventually finalized in the journal articles and in this thesis.

The remaining of this thesis is structured as follows:

- Chapter 2 – **Ilulissat site** – explains the geological history of Ilulissat, and environmental conditions at the field site. In addition, results of field geophysical and drilling campaigns carried out within the scope of this Ph.D. project are referred to in this chapter. These include laboratory electrical and seismic measurements and geotechnical characterization of core samples.

- Chapter 3 – **Automated ERT monitoring in cryosphere – how to make it work?** – focuses on optimizing the electrodes of the ERT array for long-term monitoring in harsh periglacial environment. The chapter is a summary of two published journal articles A and B.

- Chapter 4 – **In-situ temperature, soil moisture and resistivity regimes in active layer and permafrost** – describes the petro-physical relationships between ground temperature, soil unfrozen water content and ground resistivity based on three years of monitoring data. Technical details of the ERT monitoring system and automated data transmission are discussed in this chapter. The chapter is summary of the submitted article C.

- Chapter 5 – **1D model for heat transfer in permafrost** – details setup of the 1D model for conductive heat transfer in active layer and permafrost. We describe the approach to identification of target optimization parameters, optimization algorithm and procedure and results of synthetic modeling tests. We then calibrate the model on borehole temperature data and assess the predictive value of the model.
- Chapter 6 – **The coupled thermo-geophysical inversion** – uses time lapse geoelectrical data for constraining calibration of the heat model parameters. Two commonly used resistivity mixing rules are evaluated with respect to actual field resistivity measurements. The final coupled inversion approach is compared with traditional calibration on borehole temperature records.
- Chapter 7 – **Conclusions** – summarizes and evaluates the presented research. Novelties and contributions of this Ph.D. project are discussed, along with suggestions for future work.

Appendices A to L contain articles and conference abstracts prepared in connection with this Ph.D. project.

CHAPTER 2

Ilulissat site

This chapter introduces the location and climate characteristics (section 2.1), geological history and present-day conditions at the Ilulissat monitoring site (section 2.2).

The site was extensively investigated in late 1970' when Ilulissat airport was built. Number of boreholes were drilled, both for retrieving core samples and for installation of thermistors; data from this period are briefly summarized in section 2.3.

In August 2012 and 2013, two field campaigns were carried out at the site within the scope of this Ph.D. project. The main purpose was to install the permanent monitoring station, and to gain further knowledge about the area by means of geoelectrical mapping and extraction of permafrost core samples for laboratory analysis. These data are briefly summarized in section 2.4 to complete the current knowledge about the area.

2.1 Location and climate

The Ilulissat monitoring site (69° 14' N, 51° 3' W, 33 m above sea level) is situated ca. 200 meters east of the airport in Ilulissat, on the mainland in the inner part of the Disko Bay (figure 2.1). The mean annual air temperature (MAAT) between 2003-2012 was −5.1 °C (data from Cappelen 2013). According to Brown et al. (1998), the site is located in the continuous permafrost zone.

2.2 Geological history and setting

At the time of the last glacial maximum (approximately 25 000 years before present (BP), Weichsel/Wisconsin glaciation), Greenland was covered by the Greenland Ice Sheet. According to Bennike and Björck (2002), the innermost part of the bay near Ilulissat was not deglaciated before 9600 years BP. Following the retreat of the ice

Figure 2.1: Map of Greenland with location of the town Ilulissat. Ortophoto of the location of the monitoring station (marked with red dot) near the airport, 4 km north of the town.

sheets, marine transgression resulted in the deposition of fine-grained marine sediments at relatively high sea levels of > 50 m above present. Most soil formations thus relate to the last Weichselian/Wisconsin glaciation and to the Holocene deglaciation. Onshore, the most important deposits are local side moraines and glacio-marine clay and silt sediments overlain by Holocene solifluction deposits and topsoil in form of only slightly decomposed peat (Ingeman-Nielsen et al., 2008).

Interaction between eustatic changes and isostatic uplift raised the area above sea level about 5000 years ago (Rasch, 2000), exposing the sediments to percolation of precipitation, and possibly groundwater flow. This resulted in depletion of salts in the upper part of the soil profile. At the end of the Holocene optimum (after 5000 years BP), climate allowed permafrost to develop as seen today (Dahl-Jensen et al., 1998; Hammer et al., 2001), effectively stopping the depletion process. The sediments have been exposed to the consolidation and fracturing phenomena caused by ice lens formation in fine-grained sediments (Foged, 1979). In Ilulissat, this history resulted in a complex profile consisting of an upper leached, ice-rich part of the permafrost and a lower (partly) unleached zone with high unfrozen water content and low or no ice content (Ingeman-Nielsen et al., 2008; Ingeman-Nielsen et al., 2010). Differences in residual salinity strongly affect the freezing temperature of the sediments and, in combination with the local ground thermal regime, affect the presence and distribution of ice features in the soil profile.

The active layer thickness at the site is approximately 0.9 m, below which ca. 2-3 meters of ice-rich permafrost are found. Deeper parts of the soil profile are, however, technically unfrozen, in spite of measured ground temperatures around −3.1 °C. The cause is the pore water, which gradually changes from freshwater to seawater, with concentration of Cl^- ions up to 19‰at the depths below 4 m (Foged and Ingeman-Nielsen, 2008)). Theoretical freezing point depression of the clay formations was calculated based on pure NaCl solution of the same chloride concentration; it ranges from −1 °C to −3.5 °C depending on the depth – and salinity concentration – in the profile. The gneiss bedrock is encountered at the site at 7 m depth (2.2) and it consists of Nagsugtoquidian gneisses with amphibolitic bands. It is affected by a series of fault and fracture systems, most importantly a northwest-southeast situated system (Ingeman-Nielsen et al., 2008).

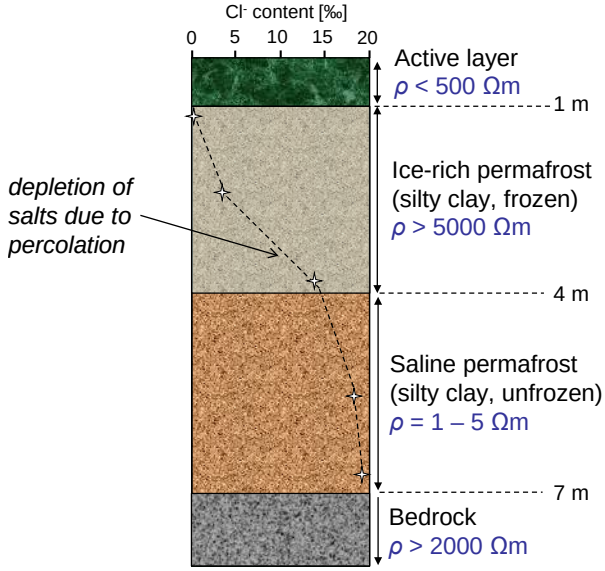

Figure 2.2: Schematic representation of sediment profile in Ilulissat (adapted from Foged and Ingeman-Nielsen (2008)). Active layer thickness reaches 0.9 – 1 m, below which 2-3 m of ice-rich permafrost are found. The deeper sediments are technically unfrozen in spite of ground temperatures below 0 °C, as salinity content in pore water gradually increases and causes freezing point depression. Alternating layers of low and high resistivities (active layer – ice-rich permafrost – saline permafrost – bedrock) result in a complicated geophysical model.

2.3 Ground temperature records

Number of boreholes was drilled in the vicinity of the Ilulissat airport as part of the airport site investigations in 1970'; temperature loggers installed in some of the boreholes were downloaded manually at irregular intervals. Borehole ILU2007-01, 4 m deep, is typical for the area and provided information about ground geological structure and temperature regime since summer 2007. Temperature variation at the bottom of the borehole averages −3.38 °C. More recent ground temperature records from borehole ILU2013-01 (drilled ca. 5 m SW from the ILU2007-01, 6 m deep) confirm that temperature near the point of zero annual amplitude is −3.1 °C at 6 m depth (figure 2.3).

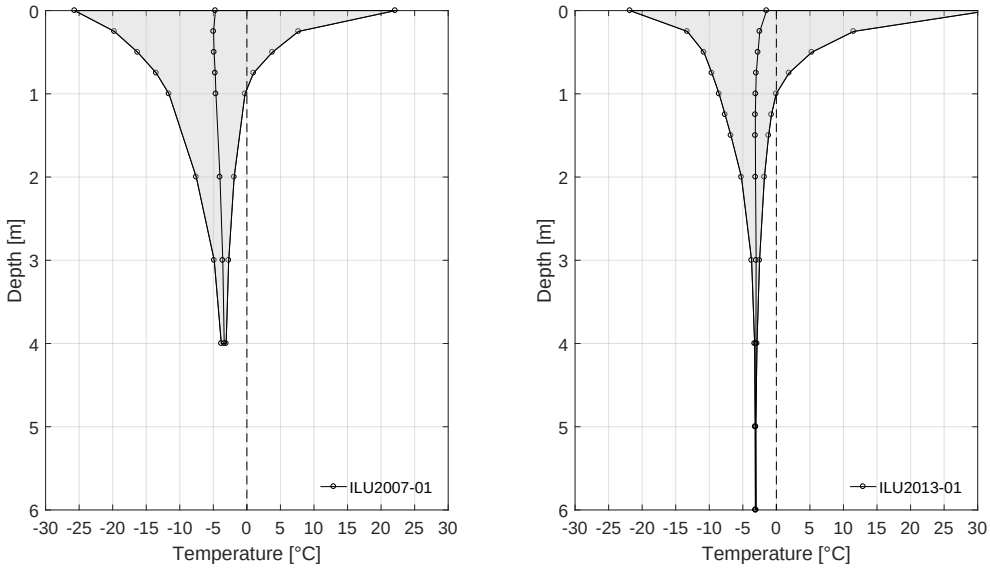

Figure 2.3: Temperature envelopes from historical and recent borehole data. (a) Borehole ILU2007-01, records between 2. September 2007 and 22. July 2008. The MAGT at 4 m depth is −3.38 °C ±0.25. (b) Borehole ILU2013-01, records between 11. August 2013 and 1. September 2014. The MAGT at 4 m depth is −3.05 °C; the MAGT at the deepest sensor at 6 m depth is −3.07 °C, with amplitude of annual temperature variation <0.09ř

.

2.4 Field and laboratory investigations in 2012-2013

In August 2012, automated permafrost monitoring station was established near the Ilulissat airport (detailed description of the station can be found in appendices C and E). As part of the field campaign, we carried out a series of geoelectrical surveys that

mapped the sedimentary basin east of the Ilulissat airport in a grid-like pattern. The result was a quasi-3D picture of the subsurface (figure 2.4).

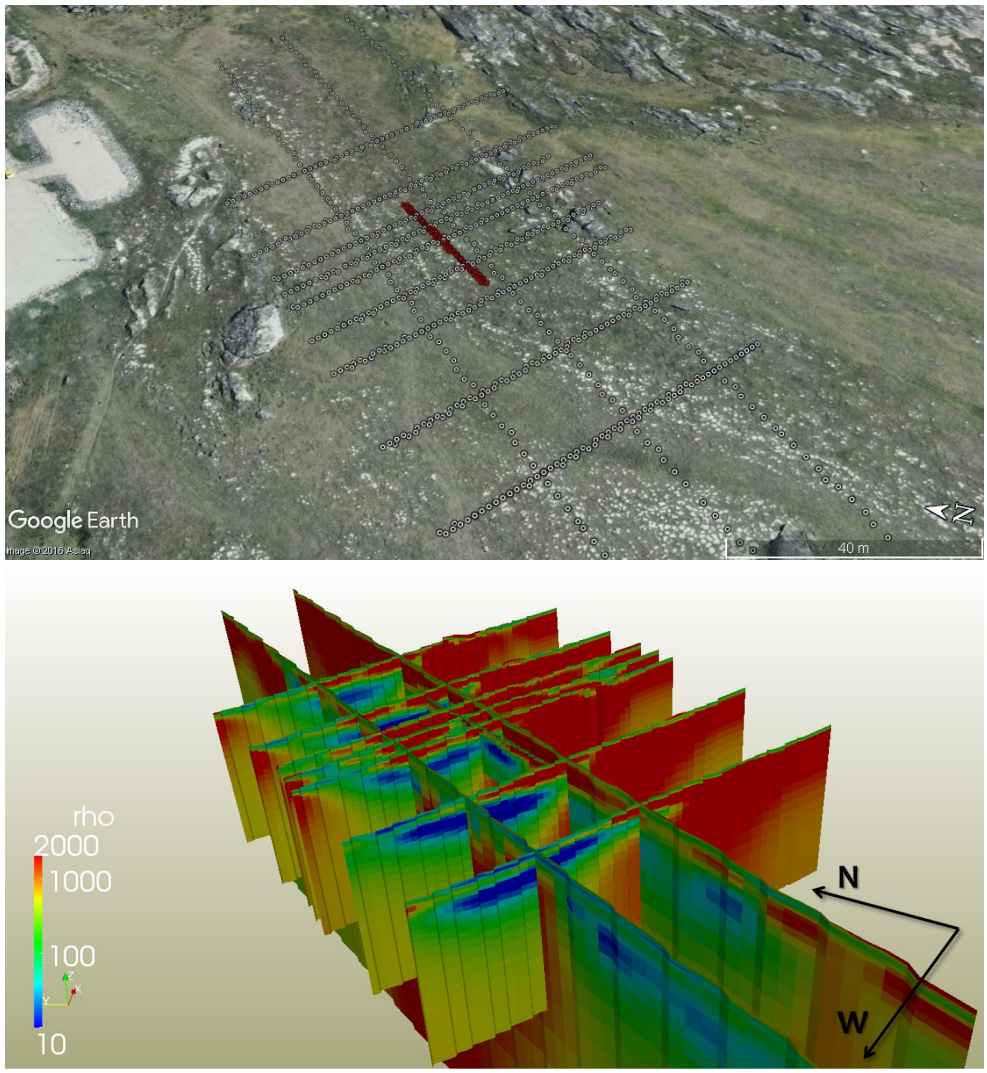

Figure 2.4: Geoelectrical mapping in the area east of the Ilulissat airport carried out in August 2012. The three NS-oriented profiles were 400 m long with 5 m electrode spacing. Nine EW-oriented profiles were 80 m long with 2 m electrode spacing. Short NS-oriented profile plotted in red marks the location of the time lapse ERT array. Grid-like pattern of the survey lines results in a pseudo-3D model of the subsurface. All the ERT profiles pictured were collected in Gradient configuration.

The main structures identified in the inverted models agree with borehole information. High-resistivity layer below active layer corresponds to the ice-rich permafrost. The ice-rich layer is thinning out in the EW-direction, and is not observed in ERT models in the SW-corner of the mapped area. Below the ice-rich permafrost, we observe a very low resistivity layer (resistivity in the order of 10 Ωm), which we interpret as the saline permafrost – sediments at temperatures below 0 °C, yet technically unfrozen due to high salinity content. Bedrock – outcropping in the NE-part of the mapped area – is dipping in SW-direction towards the sea. Depth to bedrock could not be properly resolved in the areas with presence of the ice-rich permafrost. We note that thicknesses and resistivities are not reliably resolved in the inverted models due to equivalency issues affecting the inversions, and different resolution of the profiles measured with 2 m electrode spacing (E-W profiles) *vs.* 5 m electrode spacing (N-S profiles).

In 2013, a series of boreholes were drilled across the area that was mapped with ERT one year earlier; core samples were extracted from active layer and ice-rich permafrost down to the depth of 3.1 m. According to grain size distribution analysis, soils are classified as silty clays, with 55% of grains below $< 2\mu$m and 25% between $2 - 6\mu$m. Porosity values fell in the range of 0.5 – 0.6 and samples were found to be near full saturation (degree of saturation 87.1 – 100 %). Visual inspection confirmed presence of ca. 0.5 m thick layer of almost pure ice in the top of permafrost (figure 2.5). Detailed description of the drilling locations, catalog of core samples and results of geotechnical tests carried out on these samples can be consulted in Pedersen (2013).

Figure 2.5: Large ice content is revealed in this back-lit photo of a 26 cm-long permafrost core from depth between 1.19 - 1.45 m. The core sample comes from a borehole drilled just 5 meters east of the automated ERT profile. *(photo: L. Pedersen)*

CHAPTER 3

Automated ERT monitoring in cryosphere - how to make it work?

In this chapter, we tackle the **grounding resistance challenge** (1.1); in other words, how do we assure a good performance of an ERT array, permanently installed in a remote area, throughout the entire year? This is particularly important for interpretation of the monitoring results - as pointed out by Hilbich et al., 2011, comparison of temporally sparse ERT data with continuous, long-term climate records is otherwise a challenging task.

The main contribution of this study is improvement of understanding of processes and properties affecting performance of real electrodes. In our experiment design, the focus was on electrodes as the primary source of errors in resistivity measuring systems (LaBrecque and Daily, 2008). We studied the improvements that can be achieved by optimizing electrode designs under various lithological conditions.

First, we describe a new measurement protocol for efficient measurement of single-electrode grounding resistance in field conditions - the focus-one protocol (section 3.2). Grounding resistance of three electrode designs is then evaluated at various ground temperatures in laboratory, three field tests sites and three authentic monitoring applications (section 3.3). We also provide quantitative information on the range of grounding resistances from three active or past monitoring stations in Greenland. An attempt is made to separate the contributions of different processes to the observed grounding resistance. Our findings serve as a reference and recommendations (3.4) for

practicing geophysicists planning for setup of automated long-term ERT monitoring installations, not only in the Arctic.

This chapter is a summary of the published journal articles found in appendices A and B. Partial results had been previously discussed in two conference contributions (appendices F and H).

3.1 Grounding resistances and ERT monitoring on permafrost

The grounding resistance is defined as the potential at the electrode surface divided by the current injected to the embedding medium by the electrode (e.g. Sunde, 1949; Wait, 2012; Hördt et al., 2013). Theoretical grounding resistance of an electrode can be estimated as a sum of the effect of the ground resistivity and additional resistance (Ingeman-Nielsen et al., 2016). The additional resistance combines an interfacial resistance between electrode and soil, and a resistivity contribution of anomalous zone near the electrode (zone of preferential drying/wetting, ice build-up around the electrode). In permafrost areas, the combined effect of high resistivity of frozen ground and anomalous zone means that the electrodes commonly suffer from poor grounding, to the point where measurements become impossible in the coldest periods of the year.

Number of techniques is known to improve the electrode grounding, both in loose soil and rock; these typically require human intervention before every measurement launch, and therefore are not suitable for automated monitoring in remote areas. Yet reducing the grounding resistance is crucial for the feasibility and quality of measurements. Changes of ground resistivity should primarily reflect environmental processes of interest, rather than noise resulting from, among other factors, changing grounding resistance. As the electrodes were identified as the primary source of errors in resistivity measurement systems, optimization of electrode design should be an essential part of designing a well-performing ERT monitoring system.

3.2 The focus-one protocol

Little information is available in geophysical literature on grounding resistances, mainly because they are difficult to measure. In practical field applications, electrode grounding is typically tested in a pairwise electrode test and single-electrode grounding resistance is not measured.

In Ingeman-Nielsen et al., 2016 (Appendix B), we describe a measurement protocol which may be used in field applications to provide an estimate of the single-electrode grounding resistance for individual electrodes of multi-electrode ERT arrays. During the focus-one measurement, resistance is measured between one single electrode - *the*

focus electrode - and all the remaining electrodes connected in parallel. This way, the measured resistance is dominated by, and thus provides estimate of the grounding resistance of the focus electrode.

Through a modeling study, we demonstrated that the protocol provides accurate estimate of single-electrode grounding resistance within ±7 % for arrays of 30 electrodes or more, provided that the ratio of instrument input impedance to half-space resistivity is $\geq$ 1000 m^{-1}. The focus-one protocol has been of great practical importance for optimizing array installation and electrode design throughout the field and laboratory measurements described in this thesis.

3.3 Experiments and results

Three electrode designs were tested in our study: rod electrodes, plate electrodes and mesh electrodes. All electrode types were made of stainless steel and the main difference, besides their shape, was their effective surface area (figure 3.1).

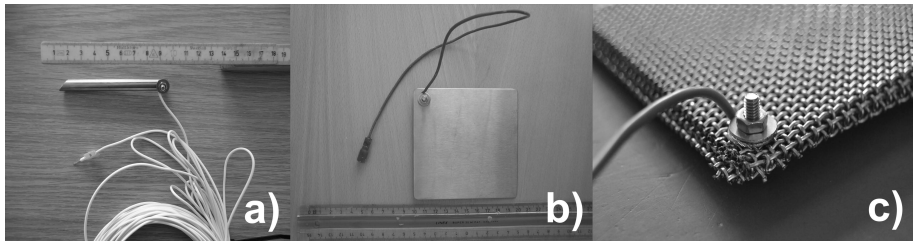

Figure 3.1: Electrode designs tested in this study, with their estimated effective surface area: (a) rod electrode with attached coated copper cable (27 cm^2), (b) plate electrode (204 cm^2), (c) mesh electrode (985 cm^2)

All three electrode types were tested in (1) temperature-controlled laboratory experiment, (2) field experimental setups, and in (3) authentic monitoring field applications.

3.3.1 Laboratory experiment

The idea with the laboratory experiment was to separate effects of soil properties and temperature on electrode performance. All three types of electrodes were placed in buckets of soil of same composition (silty clay from Kangerlussuaq, West Greenland) and gravimetric moisture content (40.1 ±1.5 %). The total circuit resistance of each bucket was then measured at three temperature steps: (a) at −1.4 °C ±0.3°, (b) at −14.3 °C ±0.6°, and (c) at 19.9 °C ±0.8°.

We found that increase of total circuit resistance of approximately two orders of magnitude accompanies the soil freezing. The choice of electrodes affected the total circuit resistance, with the rod electrodes performing the worst (largest resistance

and variance of measurements), followed by the plate electrodes. The mesh electrodes exhibited the lowest variation and the lowest measured circuit resistance, at all temperature steps. While the quantitative results of the laboratory tests are not comparable to field situation, they do qualitatively confirm the intuitive assumption about electrode surface area and ground temperature affecting the electrode performance. Statistical treatment of the data from the laboratory experiment confirmed that the effects of electrode type and temperature are statistically significant and that there is significant interaction between electrode type and temperature.

3.3.2 Field test sites

The three test sites for field experiments were all located in central West Greenland, however lithological and permafrost conditions at the sites were very different. In Sisimiut, an area affected by discontinuous permafrost, lithology is made of coarse-grained sandy sediment. Ilulissat lies in continuous permafrost zone in an area dominated by fine-grained silty clay marine deposits. Qeqertarsuaq lies in transitional area between Low and High Arctic. However, due to geothermal activity, permafrost at the site is discontinuous and no permafrost was observed from ground temperature measurements to the depth of 3.5 m at the actual test site. The Qeqertarsuaq site is located in bedrock valley filled with Holocene sands and gravels with topsoil thickness of 5-10 cm.

Experimental test sites consisted of 10 electrodes of each design. Grounding resistances of the electrodes at each of the three test sites were measured in summer, fall and winter 2013/2014. The findings qualitatively agreed with laboratory experiments. Rod electrodes generally showed higher focus-one resistances than plates, which in turn had higher focus-one resistances than mesh electrodes. Effect of ground freezing was manifested in two to three orders of magnitude increase of grounding resistance between unfrozen and frozen ground conditions (figure 3.2).

Statistical analysis of the data from the field experiments confirmed that mesh electrodes constitute a significant improvement over other electrode types at Ilulissat and Qeqertarsuaq sites. In Sisimiut, mesh electrodes performed comparatively to plates. Well-drained coarse-grained soil likely prevented fully benefiting from increased surface area of the mesh electrodes.

3.3.3 Example of ERT array optimization in Ilulissat

Experience with severe grounding resistance preventing any winter ERT measurements on monitoring station in Ilulissat initially inspired this entire grounding resistance study. Success of laboratory testing prompted us to replace original rod electrodes (installed in August 2012) by meshes after one year of station operation (in August 2013). After the electrode replacement, we observed immediate reduction of average single-electrode grounding resistance from 1.5 $\pm$0.9 kΩ for rods to 0.4 $\pm$0.1 kΩ for meshes. Completeness of ERT acquisition protocol was used as another in-

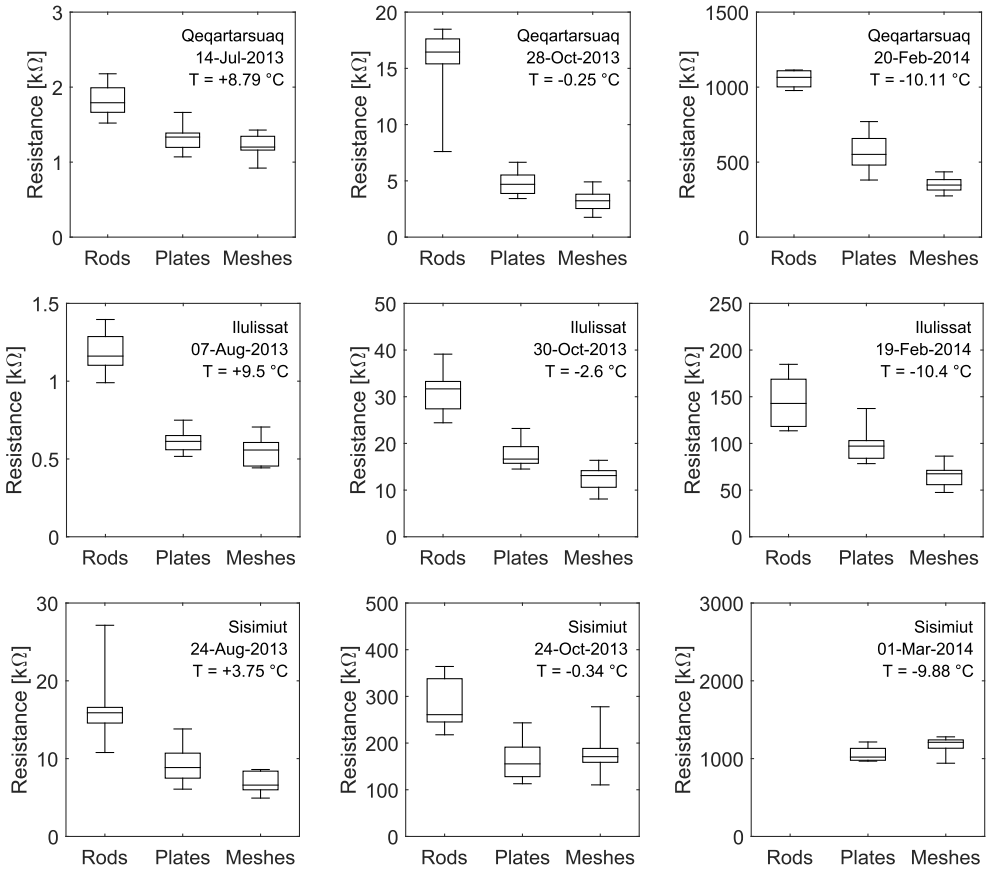

Figure 3.2: Variation in measured focus-one resistance for the three electrode types at the three field test sites. The height of the box corresponds to inter-quartile range, with the horizontal bar representing the median value. Whiskers indicate the maximum and minimum values recorded for the given electrode type. T is the temperature at 20 cm depth in the ground.

dicator of quality of electrode grounding. After electrode replacement, we observed dramatic improvement in performance of the array, with nearly complete data sets measured throughout the winter season. Gaps in data acquisition in the seasons following the electrode replacement are due to instrument software malfunction rather than extreme grounding resistance (figure 3.3).

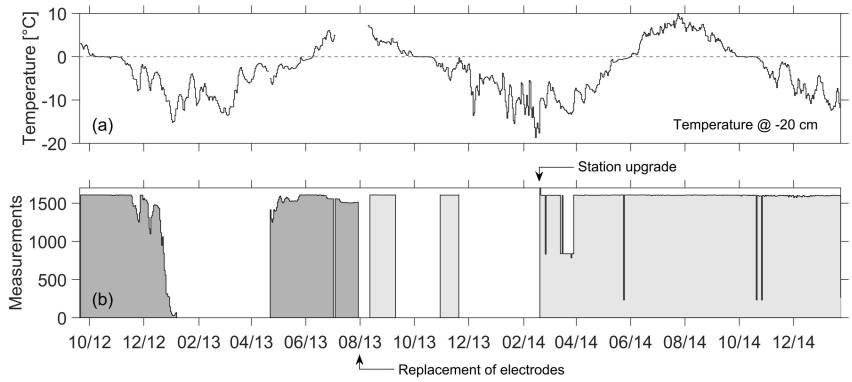

Figure 3.3: Effect of electrode replacement on completeness of acquisitions at permanent monitoring site in Ilulissat. Date ticks indicate the first day of every month. (a) Average daily ground temperature at 20 cm depth in the ground at the site. (b) Number of collected quadrupole resistivity measurements every day (complete protocol consists of 1625 measurements). Decrease of number of collected daily measurements correlates well with ground freezing (November-December 2012). Periods with zero records (such as 7 January 2013 to 22 April 2013) are due to the resistivity meter's software malfunction. Station upgrade marks the day (19 February 2014) when the station was upgraded with remote control and automated data transmission, after which we have not experienced a complete software failure.

3.3.4 Grounding resistance timeseries

Timeseries of electrode grounding resistance available from three (semi-)permanent permafrost monitoring stations showed that the real-world electrodes are rarely perfectly grounded. Estimated additional grounding resistance in summer ranges from 0 to 1.2 kΩ and 6.5 kΩ at Ilulissat and Qeqertarsuaq sites, respectively. In winter, the estimated additional grounding resistance is up to three orders of magnitude larger, ranging from 0 to 170 kΩ in Ilulissat, to more than >1 MΩ in Qeqertarsuaq and Sisimiut (figure 3.4).

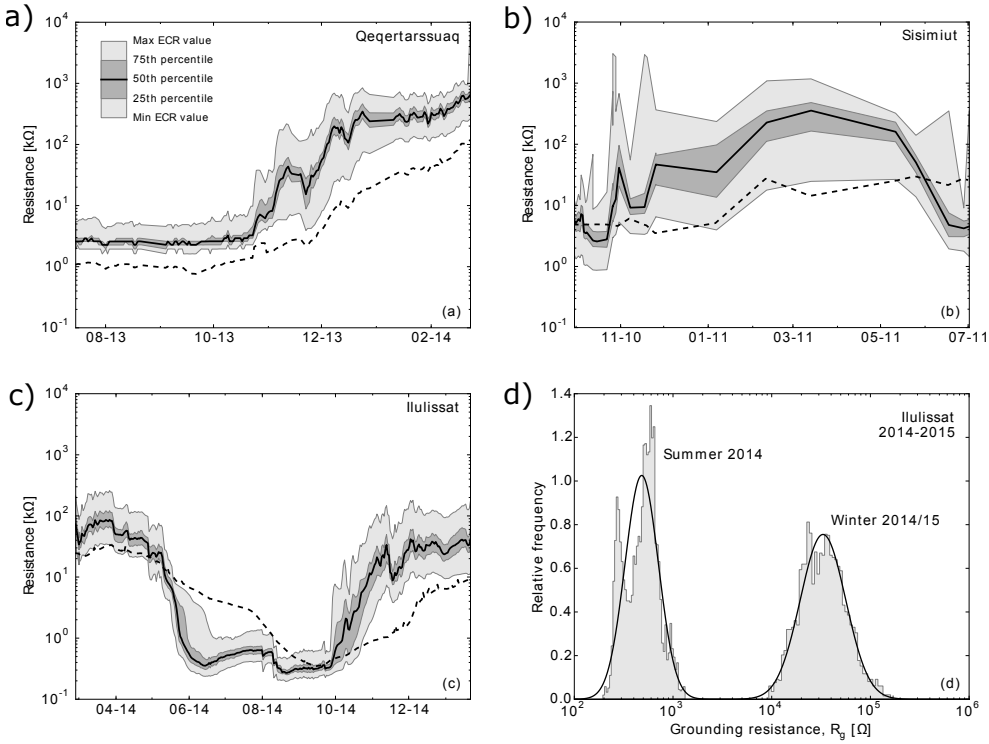

Figure 3.4: Timeseries of focus-one grounding resistances for monitoring stations in (a) Qeqertarsuaq, (b) Sisimiut and (c) Ilulissat. Plots show average array grounding resistance (solid black line), 25th and 75th percentiles (dark-grey shading) and maximum and minimum measured values (light-grey shading). The plots also show the theoretical grounding resistance of a perfectly grounded electrode using estimated half-space resistivities based on the measured average daily apparent resistivities for each profile (dashed black line). Histograms in (d) shows the log-normal distribution of grounding resistances in Ilulissat in summer (1 July to 1 September 2014) and winter (1 December 2014 to 31 January 2015).

3.4 Conclusions and recommendations

Addressing the issue of grounding resistance is of great practical importance for improved electrical resistivity imaging of ground. Particularly in cryospheric applications, ERT faces some of the most extreme conditions. High grounding resistances not only affect the ability of the instruments to carry out measurements; they also negatively impact the signal-to-noise ratio, resulting in noisy measurements. Errors in resistivity measurements can amount to >10% at receiver input impedances of 10 MΩ (Ingeman-Nielsen and Tomaskovicova, personal communication, 2015).

We found that the benefit of a particular electrode design depends on site conditions, namely litholigy. Even though the mesh electrodes outperformed other electrode types in almost all experiments of our study, they did not markedly improved array performance at Sisimiut site. Consequently we suggest that testing appropriate electrode design should be high on the list of priorities when preparing a monitoring campaign. An optimized electrode design for particular application not only prolongs the acquisition period, but also improves quality of measurements.

Considering the magnitude of errors the grounding resistances introduce to the measured resistivity datasets, we foresee the potential of incorporating the grounding resistance information into data processing and inversion algorithms for improved accuracy of interpretations.

CHAPTER 4

In-situ temperature, soil moisture and resistivity regimes in active layer and permafrost

The permafrost monitoring station in Ilulissat was designed with the primary aim to provide calibration data for a coupled thermo-geophysical model of heat transfer in permafrost (chapter 6, appendix D). Additional environmental parameters were monitored to enable validation of the model, including ground temperatures, soil moisture, snow depth and soil specific heat. Article in appendix C provides details about station components, measured parameters, data processing and results from the site. Special attention is paid to technical challenges linked to long-term electrical resistivity monitoring on permafrost. Conference abstracts in appendices E, G, I, J and K discuss partial results from the site.

Results and experiences from the monitoring study are summarized in this chapter. Section 4.1 presents the main station components and measured parameters. Section 4.2 describes the particularities of in-situ soil moisture regime and section 4.3 is dedicated to results of time-lapse resistivity measurements. In section 4.4, we discuss relationships between the in-situ parameters. Conclusions and recommendations regarding the long-term monitoring are given in section 4.5.

4.1 Station components and measured parameters

Details about measured parameters, sensors types and their logging frequencies are available in appendix C and only briefly recalled here. The monitoring station in Ilulissat (overview on figure 4.1) measures following environmental parameters:

- **Air temperature** Measured in a radiation shield placed on a 1.1 m-tall mast. On the same mast, five thermistors placed at increasing heights from the ground surface (C) provide indirect information about snow depth. A sonic ranging snow depth sensor was installed in February 2014, however, results of these measurements are not discussed in this study.

- **Ground temperature** Measured at three spots at the station (figure 4.1): borehole ILU2007-01, 4 m deep, borehole ILU2013-01, 6 m deep. Boreholes are instrumented with HOBO U12-008 loggers and TMC-HD sensors (*temperature sensors*). Detailed temperature in active layer and top of the ice-rich permafrost is measured by an MRC temperature probe, which is 1.5 m long with 16 thermistors spaced 10 cm.

- **Soil moisture** Dielectric permittivity of the soil is measured by frequency-domain reflectometry (FDR) method using two Stevens HydraProbe II sensors (*soil moisture probes*). The two probes are installed at depths 0.30 m and 0.55 m respectively. Two Specific Heat East 30 sensors are installed right next to the two soil moisture probes; results from these sensors are not included in discussions of this study.

- **Ground resistivity** Measured at a 31.5 m-long profile consisting of 64 electrodes, spaced by 0.5 m. The ERT instrumentation consists of ABEM Terrameter SAS1000 (*resistivity meter*) and electrode selector ES10-64. The ERT system collects measurements every 24 hours, in 1625 quadrupole configurations. The combined acquisition protocol consists of 233 measurements in Wenner-Schlumberger configuration and 1392 measurements in Gradient configuration. The Gradient data are used for visualizing the subsurface structure and progression of freezing/thawing front. Pseudo-1D Wenner-Schlumberger data are used for quantitative comparison of ground resistivity changes with borehole temperature measurements.

In the following text, we focus on analysis of data acquired in three-year period between 21st September 2012 and 15th October 2015. Discussion is centered around results of ground resistivity, soil moisture and ground temperature monitoring. Due to relatively short time scale of the project, we focus on analysis of relationship between ground parameters rather than long-term tendencies and predictions.

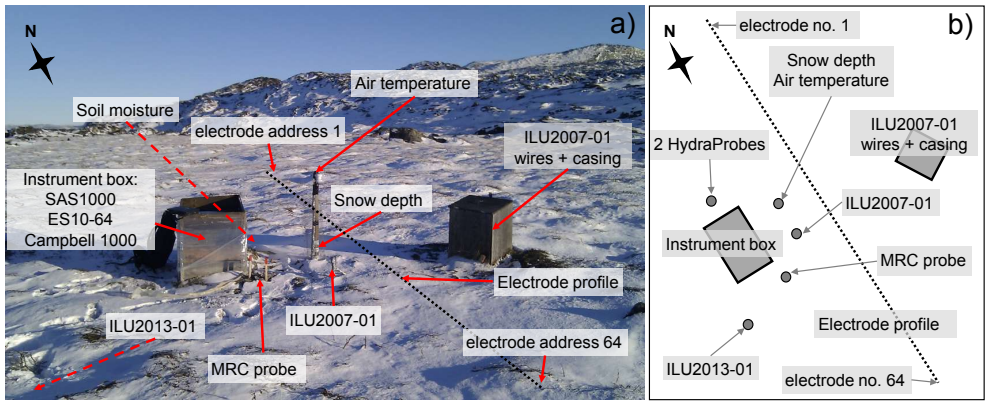

Figure 4.1: (a) Overview of the monitoring station in Ilulissat, view towards the north, with Ilulissat airport on the left (photo: T. Ingeman-Nielsen, February 2014); (b) Top-view drawing of positioning of station components (dimensions are not to scale).

4.2 Soil moisture regime

Soil moisture regime exhibits seasonal pattern. Maximum water content (at the depth of 0.3 m) is measured in the middle of June and again at the beginning of September. Very high water content (> porosity, chapter 2) right after the ground temperature rises above freezing point is likely due to thawing of ice lenses and limited drainage while ground immediately below the thaw front is still frozen. Fissures that occur (particularly) in fine-grained soil following repeated cycles of freezing and thawing cause higher water permeability and facilitate more rapid moisture redistribution in thawing soil by gravitational forces. The drainage will progress as more and more of the active layer thaws and the soil structure rearranges itself as the water drains away.

Zero-curtain during freezing lasts for approximately three weeks in October, during which unfrozen water content decreases steadily. Unfrozen water content reacts readily to ground temperature variations below freezing point and noticeable phase change occurs even at temperatures as low as −5 °C.

Contrary to slow and steady freezing, thawing occurs rather abruptly, according to the in-situ measurements. Frequency of eight FDR measurements per day is necessary to capture the fast increase of water content upon thawing.

Measurements from soil moisture sensors at both 0.30 m and 0.55 m depths agree that dependence of the unfrozen water content on ground temperature at the site is distinctly different during periods of soil freezing and thawing respectively (figure 4.2). Water content during freezing is consistently higher than during thawing at the same ground temperature in the temperature range from approximately −7 °C to 0 °C. Different freeze-thaw patterns can be observed even during events of partial thawing when ground temperature is below 0 °C. Nevertheless, the freezing and

thawing patterns respectively remain the same every year. The **freeze-thaw hysteresis** thus marks two distinct seasons at the site. Freezing season starts around the time when maximum depth of active layer is reached (1st September) and lasts until 28th February, when the lowest ground temperatures and water content are recorded. Thawing season is identified as the remainder of the year. Between ca. 15th June – 31st August (at the 0.30 m depth), the ground temperature is above the freezing point and the soil moisture regime is dominated by water circulation and drying, rather than temperature variation.

The hysteresis effect is well-known in soil science, where it is commonly explained by effects associated with capillary theory. Soil freezing is a dehydration process analogous to the drying of soils above 0 °C (Koopmans and Miller 1966; Krzewinski and Tart Jr 1985). Freeze-thaw hysteresis can thus partially be explained by the bottleneck effect (e.g. Lal and Shukla 2004): ice growing within the pores reduces their size and thus increases the soil's propensity to retain water through capillary forces.

A power function $\theta_w = \alpha|T|^\beta$, where θ_w is the volumetric unfrozen water content, T is a temperature below freezing point of the sample and α and β are empirical coefficients (Lovell Jr, 1957) has been successfully used to estimate soil unfrozen water content from ground temperature below freezing point (e.g. Anderson et al., 1973; Romanovsky and Osterkamp, 2000; Nicolsky et al., 2007). We fitted the empirical model to the freezing and thawing curves from 2012/2013 and found two sets of the α and β coefficients. The model fitted on freezing (figure 4.2b) and thawing (figure 4.2c) seasons 2012/2013 predicts the unfrozen water content measurements in the following two years 2013/2014 and 2014/2015 within 5% (appendix J and C).

Due to pronounced hysteresis of unfrozen water content, difference between parameterization of freezing and thawing curves should be accounted for in thermal modeling of permafrost, as the amount of unfrozen water is a key factor influencing bulk thermal properties of a soil (e.g. (Anderson et al., 1973; Nakano and Brown, 1972; Osterkamp and Romanovsky, 1997; Romanovsky and Osterkamp, 2000)).

4.3 Ground resistivity variation

Data measured in two (Gradient and Wenner-Schlumberger) configurations were both filtered for skipped measurements, negative resistivities and high-value outliers (see appendix C for details).

The **Gradient datasets** inverted with RES2DINV software reflect changing ground resistivity as a result of soil freezing and thawing (figure 4.3). However the resistivity variation - which is expected to mirror ground temperature variation and correspondingly attenuate with depth - remained far too large across the entire model depth. Meanwhile, the active layer depth was not properly resolved. The likely cause are serious *equivalency issues* caused by sharp transitions between highly-resistive ice-rich permafrost and low-resistivity saline permafrost (recall figure 2.2 of the geo-

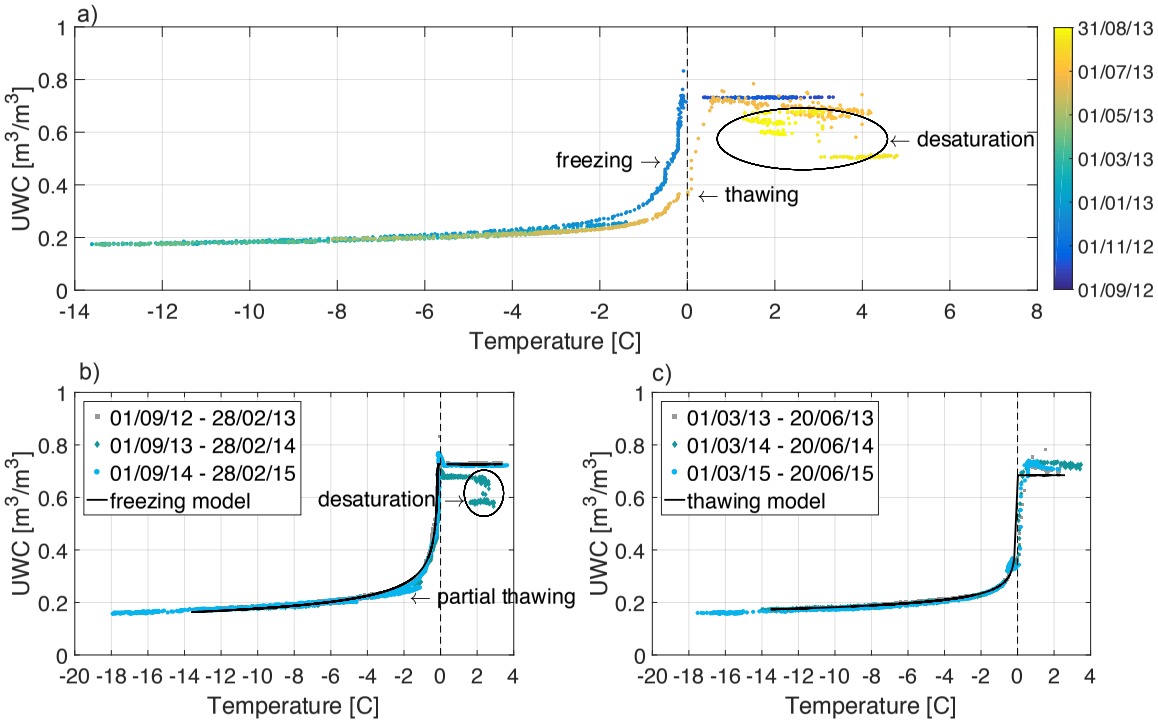

Figure 4.2: a) Field measurements (8 records/day, at 0.3 m depth) between 1st September 2012 and 31st August 2013 show the in-situ hysteretic variation of UWC during a course of one year. Desaturation due to water runoff and drying is observed after complete ground thawing at the given depth (after ca 25th June). b) The UWC follows the same freezing pattern year after year, as concluded from three consecutive freezing periods (1st September - 28th February, years 2012/2013 - 2014/2015). The freezing curve can be modeled with a set of soil-specific parameters $[a_f, b_f]$. Partial thawing is observed when the ground temperature fluctuates below 0°C. The slope of this partial thawing curve is the same as slope of the full thawing curve. c) UWC during thawing (1st March - 25th June, years 2013-2015) during the three consecutive thawing periods can be modeled with a set of soil-specific thawing parameters $[a_t, b_t]$.

logical model of the site). In spite of these challenges, the 2D inversions confirmed horizontally-layered ground structure and uniform top-down freezing pattern.

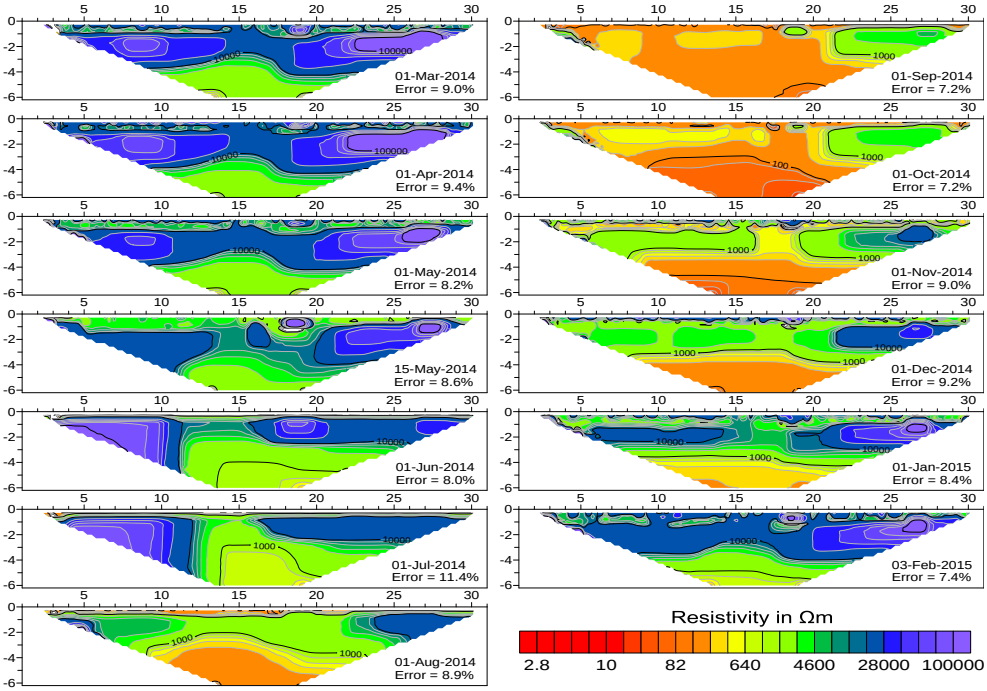

Figure 4.3: 2D inversions of Gradient data, showing the first day of every month

For better control over the inversion process, we focused on 1D-inversions of **Wenner-Schlumberger** soundings using *AarhusInv* inversion code (Auken et al., 2014). Details about the inversion and model settings are given in appendix C.

Timeseries of inverted 1D-resistivity soundings (figure 4.4c) clearly reflect processes of ground freezing and thawing. The resistivities in the active layer range from ≈20 Ωm to 100 Ωm in summer, and reach the order of 10^4 Ωm in winter. Water infiltration and percolation during thawing and summer months do not noticeably influence the inverted resistivity models. This is likely due to high level of saturation (2.4) and low hydraulic conductivity of the clayey soil. The zero-curtain period during freezing typically lasts for approximately 30 days during the month of October. Decrease of unfrozen water content from 70% to 25% is accompanied by the initial ground resistivity increase by ca. two orders of magnitude, from ≈20 Ωm to 2000 Ωm. In winter, high grounding resistances do not allow to collect measurements in the coldest periods of the year; however the highest resistivities of up to 30 kΩm are recorded at ground temperatures of −17 °C. Detailed discussion of resistivity timeseries and resistivity-water content relationship is given in appendix C.

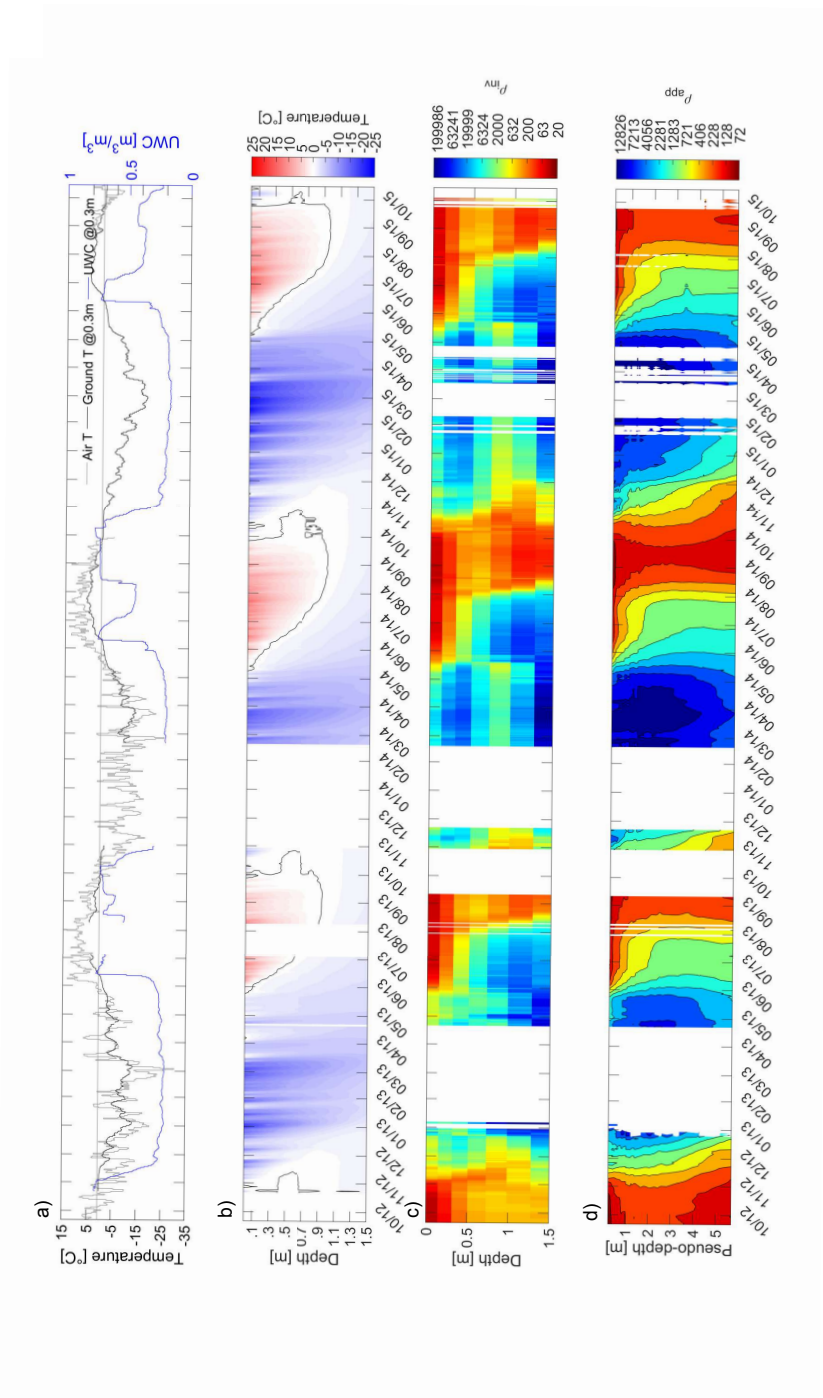

Figure 4.4: (a) Timeseries of air temperature, ground temperature (from HydraProbe) with unfrozen water content at 0.3 m depth. (b) Timeseries of ground temperature profiles down to 1.5 meters depth, data from MRC probe. (c) Timeseries of inverted 1D resistivity soundings measured by the Wenner-Schlumberger protocol. The plot is zoomed to the upper 1.5 meters of the profile to highlight the resistivity changes in the active layer. (d) Timeseries of apparent resistivity soundings. The apparent resistivity value for each day for every vertical focus pseudo-depth is averaged from up to nine acquisitions at that depth level. Date ticks indicate the first day of every month.

The resistivity soundings successfully register several warmer events during the freezing period when the ground temperature is overall below 0 °C. An example is a warmer period lasting for approximately 10 days in November 2014 (figure 4.4a, b, c). Ground temperature increase from −4.3 °C to −1.2 °C at 0.3 m depth causes partial thawing and unfrozen water content increase from 22% to 26%. This is reflected in inverted resistivities drop from 5500 Ωm down to 1300 Ωm in the top 30 cm of the inverted model. These observations evidence that the resistivity soundings are very sensitive to sub-zero water content variations and can therefore be successfully used to identify ongoing phase change in warm (close to thawing point) permafrost.

4.4 Resistivity, soil moisture and ground temperature relationships

Electrical resistivity is often used as a proxy for estimating unfrozen water and ice content (and their changes) in the ground. Comparison of indirect measurements from ground surface (resistivity) with point observations at a certain depth (temperature, soil moisture) inherently faces scale and resolution issues. Nevertheless, an attempt at this comparison reveals clear relationship between ground temperature, soil moisture and resistivity (figure 4.5). The ground resistivity exhibits expected hysteresis in relation to the ground temperature (figure 4.5b, e, h). However, the resistivity dependence on unfrozen water content also shows hysteretic pattern, with resistivities during freezing consistently higher than during thawing at the same water content.

Because of hysteresis, soils have been shown to exhibit markedly different properties at the same water content depending on whether this content was reached by wetting vs. drying or thawing vs. freezing (Williams, 1963; Farouki, 1965; Knight, 1991; Overduin et al., 2006). Based on our in-situ measurements, resistivities differing by as much as one order of magnitude can be observed at the same volumetric unfrozen water content, depending on the freeze-thaw history of the soil. This makes the resistivity hysteresis a considerable factor in quantitative estimation of unfrozen water content changes in a ground undergoing cycles of freezing and thawing.

4.5 Conclusions and recommendations

This study presented the longest-reported monitoring study of site dynamics in high-latitude permafrost to date. We addressed some of the technical challenges affecting reliability of long-term installation, namely performance of electrodes of resistivity array, data transmission and backup and powering solution.

Detailed timeseries of ground resistivity, temperature and moisture content over three years provided insight into the nature of petro-physical relationships between these parameters. We observed that thawing of a certain volume of soil is relatively

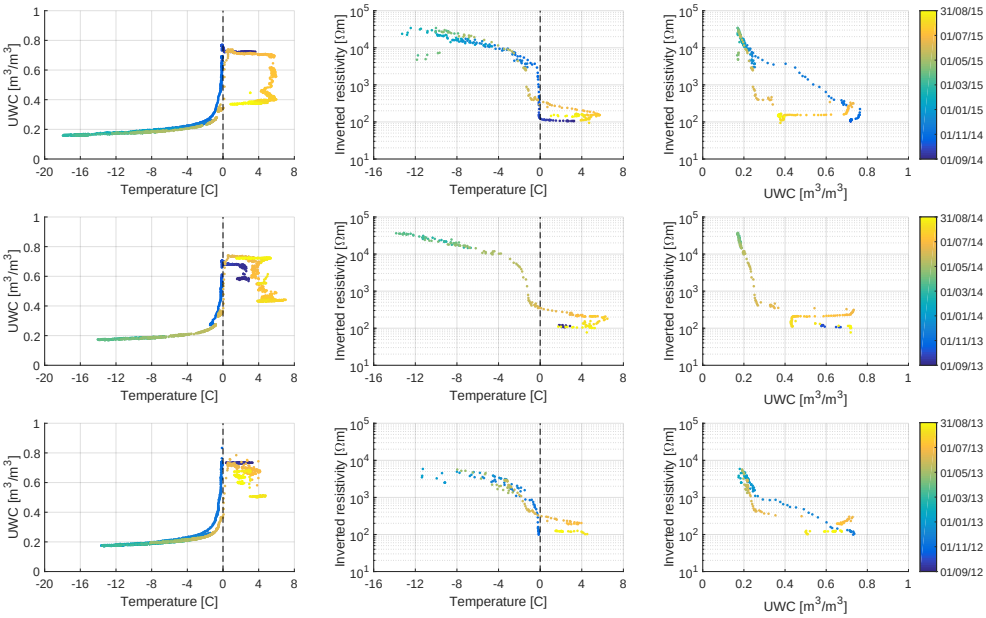

Figure 4.5: Scatter plots of ground temperature (from HydraProbe), inverted resistivity (Wenner-Schlumberger) and unfrozen water content (from HydraProbe), comparison at 0.3 m depth

fast process compared to freezing. This has implications on the nature of changes that can be expected in warming permafrost in Ilulissat area.

We confirmed that water content hysteresis, as well as resistivity hysteresis occur in soils undergoing cycles of freezing and thawing. Water content hysteresis has consequences for modeling of heat transport in active layer and permafrost as amount of liquid water is a key factor influencing soil's bulk thermal properties. Resistivity hysteresis complicates interpretation of time lapse resistivity changes in terms of ground ice/liquid water content changes.

CHAPTER 5

1D model for heat transfer in permafrost

Numerical modeling is considered a powerful - and often the only available - tool for assessing the current and forecasting the future thermal state of permafrost (Riseborough et al. 2008; Harris et al. 2009). Models rely on quality data for forcing, calibration and, ideally, validation. In thermal modeling of permafrost, calibration data are ideally borehole temperature measurements.

In this chapter, we use ground temperature records from Ilulissat monitoring station to set up and calibrate one-dimensional model of heat transfer in active layer and permafrost. Upon identifying a feasible calibration approach in a synthetic study, we recover a set of thermal parameters that satisfactorily predict available ground temperature records. A relatively simple, homogeneous three-phase model of conductive heat transfer is shown to reproduce the borehole data within $\pm$ 0.5°, given that freeze-thaw water content hysteresis (chapter 4.2) is taken into account.

5.1 1D model of conductive heat transfer

To describe the temporal evolution of the subsurface temperatures, we set up a model based on the one-dimensional heat conduction equation with phase change (Lunardini, 1981):

$$\left(C_e + L\frac{\partial}{\partial T}\theta_w(T,x)\right)\frac{\partial}{\partial t}T(x,t) = \frac{\partial}{\partial x}\lambda_e\frac{\partial}{\partial x}T(x,t) \tag{5.1}$$

In this formulation T [°C] is temperature, L [J/m^3] is the volumetric latent heat of phase change between water and ice, θ_w is the volumetric unfrozen water content of the bulk soil [m$^3_{\text{water}}$/m$^3_{\text{bulk}}$], C_e [J/m^3/K] and λ_e [W/m/K] are effective heat capacity and effective thermal conductivity, respectively, of the multi-phase media under consideration (section 5.1.2); x [m] is the depth below ground surface and t [s] is the time. Equation 5.1 applies under the assumptions that there are no additional internal sources or sinks of heat, that no volume change is associated with the phase changes, that migration of water is negligible, and that there are no lateral variation in topography and soil properties (standard 1D assumption).

Dirichlet boundary conditions are applied at the top and bottom of the model (at depths $x = 0$ and $x = l$ respectively), such that $T(0,t) = T_u(t)$ and $T(l,t) = T_l(t)$, where subscripts u and l denote the upper and lower boundaries. To calculate the temperature distribution $T(x,t)$ at any point in time, the initial temperature distribution is specified throughout the model domain, such that $T(x,0) = T_0(x)$, where $T_0(x)$ is the temperature at depth x and time $t = 0$ s.

5.1.1 Handling of the unfrozen water content

Following Lovell Jr (1957) and Anderson and Tice (1972), we use a power function to describe the soil unfrozen water content variation at temperatures below freezing point:

$$\theta_w = \eta\phi, \quad \phi = \begin{cases} S & T \geq T^* \\ \alpha|T_f - T|^{-\beta} & T < T^* \end{cases} \tag{5.2}$$

where θ_w is the volumetric unfrozen water content of the bulk soil [m$^3_{\text{water}}$/m$^3_{\text{bulk}}$], η is the porosity [m$^3_{\text{voids}}$/m$^3_{\text{bulk}}$], ϕ is the volumetric unfrozen pore water fraction [m$^3_{\text{water}}$/m$^3_{\text{voids}}$], S is the water saturation [m$^3_{\text{water}}$/m$^3_{\text{voids}}$] (assumed unity in this study) and a and b are empirical positive valued constants describing the intrinsic freezing characteristics of the given soil. T^* [°C] is the effective freezing point of the bulk soil – the lowest temperature at which all the water in the soil is unfrozen ($\phi = S$) – and is given by:

$$T^* = T_f - \left(\frac{S}{\alpha}\right)^{-\frac{1}{\beta}} \tag{5.3}$$

where T_f [°C] is the freezing point of the pore water as a free substance.

Given a certain value of unfrozen water content, and under the assumption that the soil is fully saturated at all times, the volumetric fractions of soil particles θ_s and ice θ_i are derived as:

$$\theta_s = 1 - \eta, \quad \theta_i = \begin{cases} 0 & T \geq T^* \\ \eta\,(S - \phi) & T < T^* \end{cases} \tag{5.4}$$

Pronounced hysteresis in unfrozen water content variation (section 4.2) means that two separate parameterizations are needed to realistically describe the freezing and thawing processes respectively.

5.1.2 Effective thermal parameters

The effective parameters of a bulk multi-phase soil are derived as a function of their respective volumetric fractions, which are essentially function of the temperature.

The *effective heat capacity* – C_e – may be expressed as the sum of the specific heat capacities of the soil phases weighted by their volumetric fractions (e.g. Anderson et al., 1973):

$$C_e = C_s\theta_s + C_w\theta_w + C_i\theta_i \tag{5.5}$$

Common Johansen's thermal parameterization is used for modeling the *effective thermal conductivity* – λ_e – of a n-phase soil (Johansen, 1977; Zhang et al., 2008):

$$\lambda_e = \prod_{i=1}^{N} {\lambda_i}^{\theta_i} \tag{5.6}$$

5.1.3 Implementation

For solving the heat equation, we use an in-house code (Thomas Ingeman-Nielsen, pers. comm., 2016) which implements a finite-difference scheme on a fixed grid with equidistant nodes. The code uses the unconditionally stable Crank-Nicholson algorithm with adaptive time-stepping to minimize the errors in the solution.

For sufficiently small time-steps, the analytical derivative of equation 5.2 may be used to estimate the change in unfrozen water content. However, to allow manageable step-sizes, we have implemented an iterative scheme for the change in water content. The first iteration for each time-step uses the analytical derivative, while subsequent iterations use a finite difference, based on the temperature estimate resulting from the previous iteration. Iterations proceed until the maximum change in estimated temperature is less than a specified threshold, or until a specified number of iterations have completed, in which case the time-step is reduced.

The solver is implemented in *Python* using the *numpy* module for optimized array and matrix computations.

5.1.4 Discretization in time and space

Heat model domain is set to be 6 m deep. This is sufficient for the relatively short temperature timeseries that we modeled (up to 180 days). Relatively shallow model is also computationally more efficient and allows for computation of more model realizations. Based on convergence testing, we specify equidistant mesh for the heat model solution with nodes every 0.05 m and we limit the maximum step size of any step taken by the differential equation solver to 1 h.

5.1.5 Modeling assumptions

In our modeling approach, certain simplifying assumptions were made:

1. Calibration data were collected on a site with soils made of very fine-grained, silty-clay sediments (section 2.4). Considering low hydraulic conductivity of clays, we assume that water movement in the soil is minimal and thus we neglect any heat transfer by advection.

2. Using the reasoning from the point above, and following successful application by Romanovsky and Osterkamp (2000) and Nicolsky et al. (2007), we consider the modeled ground to be fully-saturated porous media consisting of soil particles, water and ice.

3. For the sake of model parsimony, we choose to model ground as homogeneous, thus neglecting potential layers with varying thermal properties. This choice is justified by knowledge of lithology of the site, which is fairly uniform (section 2.2), and by results of experiments with heterogeneous model setup which did not substantially improve model performance and fit. We note, however, that heterogeneities are present, namely in form of ice lenses (mainly in depth between 0.9 m to 1.5 m) and increasing pore water salinity (in depth below 4 m) which ultimately affect bulk thermal properties of the ground at given depth.

4. Specific heat capacity and specific thermal conductivity of respective soil phases are functions of temperature. However, we choose not to correct the specific thermal parameters for the changes in temperature as using constant parameters results in errors of less than 10% in temperature range between −20 °C to 0 °C (Osterkamp, 1987).

5. Latent heat is function of temperature and of pore water salinity. It may, however, be assumed constant if the pore water contains only dilute solutions of salts and if the temperatures are above −20 °C (Anderson et al., 1973).

6. Fixed temperature is used as bottom model boundary. This is an acceptable simplification, considering that measured yearly temperature amplitude at the bottom of 6 m deep borehole is < 0.09 °(section 2.3), and when modeling relatively short temperature timeseries. Our modeled timeseries are limited to

180 days, given the need for separate parameterization of freezing and thawing seasons respectively (section 4.2, appendices C and J).

5.2 Optimization problem, choice of fitted parameters and convergence criteria

In inverse modeling, it is important to begin calibration by estimating a few, most descriptive parameters, as optimization with respect to many parameters at once is practically not feasible. *Sensitivity analysis* helps to identify the most influential parameters for calibration, or alternatively, to identify observations in a dataset that provide the most information for calibration of a given parameter. Because the calibration problem is nonlinear with respect to many parameters of interest, the sensitivity of the evaluated parameter will change for different values of parameters in the parameters vector, as well as for different model discretizations in time or space. An exhaustive analysis of parameter combinations would be, however, computationally inefficient. Assuming some degree of linearity in the model response to each input, these inputs can be regarded independently, thus simplifying the sensitivity analysis significantly. Carefully chosen starting point will in this case be descriptive for sensitivity of each of the fitted parameters.

We calculate the *composite scaled sensitivity* (CSS) (Hill, 1998) for each parameter of the heat model separately (figure 5.1). Parameters with comparatively less influence on model predictions, as well as parameters with well-known values that do not vary significantly are *fixed* according to well-established table values. We then investigate convergence properties of the optimization problem focusing on the remaining – *fitted* – parameters, with the aim of finding the parameter combinations that can be calibrated jointly. Overview of the fixed and fitted parameters, together with their fixed values or permitted calibration range (*bounds*), is in table 5.1. Specifying bounds for the fitted parameters prevents the solver from examining physically implausible parameter combinations.

Parameter optimization is based on iterative, nonlinear least-squares formulation using *trust-region reflective* algorithm based on the interior-reflective Newton method (Coleman and Li, 1996), as implemented in MATLAB solver *lsqnonlin*. The trust-region reflective algorithm is local search method; the solver identifies a local minimum which can correspond to global minimum if the optimization was started in the basin of attraction of global minimum. Choice of initial parameterization estimates is therefore important. Alternatively, starting the optimization from a range of initial values, or adding random perturbations to parameters starting from the same initial values, improves the chances of the solver returning the global minimum.

Cost function is the root mean square of deviations between field-measured and forward-calculated ground temperatures (root mean square error, RMSE). It is minimized by adjusting thermal parameters of the heat model. The RMSE is used to

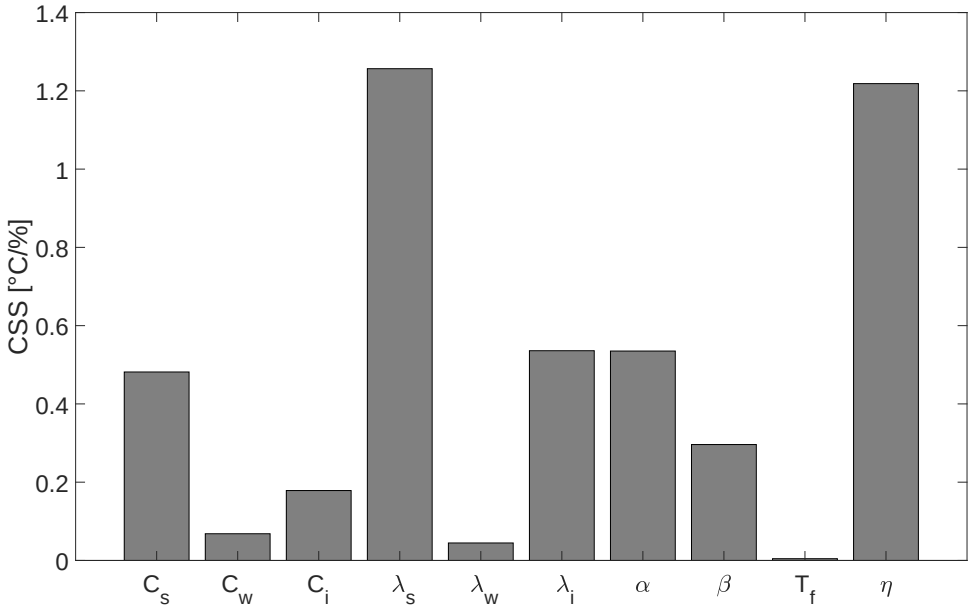

Figure 5.1: Composite scaled sensitivities of 10 parameters of the heat model. Measure of sensitivity corresponds to the change in simulated temperature field caused by 10% increase in the evaluated parameter. Parameters C_w (heat capacity of water), C_i (heat capacity of ice), k_w (thermal conductivity of water), k_i (ice) and T_f have relatively less influence on the heat model calculations in this particular model setting. Values of these parameters are also well known and can therefore be fixed based on average table values from literature. Parameters C_s and k_s (heat capacity and thermal conductivity of mineral grains), α and β (freezing/thawing parameters), and porosity (η) are soil-specific properties with substantial influence on model predictions. Therefore we target the synthetic optimization tests towards finding an approach that allows for joined calibration of these parameters.

Table 5.1: Parameterization of the heat model. For the *fixed parameters*, we show their fixed values in the optimization. For the *fitted parameters*, we list their bounds – maximum and minimum values that the optimization algorithm is permitted to investigate when searching for the optimal parameter value. The freezing point depression – T_f – is fixed on an empirical value, as it has shown to have relatively less influence on the model predictions (figure 5.1).

Fixed parameters	Value	Fitted parameters	Bounds
C_w	4.19e6 J/m^3/K	C_s	0.6e6 – 4.1e6 J/m^3/K
C_i	1.9228e6 J/m^3/K	λ_s	0.5 – 8 W/m/K
λ_w	0.56 W/m/K	η	0.1 – 0.9
λ_i	2.18 W/m/K	α	0.1 – 5
T_f	$-0.0001\,^\circ$C	β	0.01 – 5

evaluate the misfit between calculated *vs.* measured values of temperature field, and to evaluate deviations between model runs.

Convergence of the optimization is identified by meeting at least one of two criteria:

1. lower bound on *the size of a step*: if change of parameter value between iterations is smaller than the lower bound, the iterations end; or
2. lower bound on *the change in the value of the objective function*: if change in the RMSE value between previous and current iteration is smaller than the lower bound, the iterations end.

Strict tolerances lead to more precise solution, at higher computational cost. This makes sense when testing validity of the optimization approach in synthetic, noise-free scenario. When working with the real-world data, the tolerances should be proportional to the estimated error in the data. Given the uncertainty associated with the real-world data, attempting a very precise parameter estimation would only lead to over-fitting of the model.

We calculate the 95% confidence intervals for each parameter in the optimization. The 95% confidence intervals mean that there is 95% probability that the calculated confidence interval from a future parameter optimization contains the true value of the parameter.

5.3 Homogeneous heat model optimization

If the assumption of homogeneous ground properties (section 5.1.5) is correct, we expect to come up with a set of thermal parameters that reproduce the field-measured temperature field *reasonably well*.

First, we test the calibration approach in a synthetic scenario, where values of fitted parameters are known (section 5.3.1 for tests without noise, and 5.3.2 for tests with noise). Upon identifying a viable optimization approach, we apply it to the field data (section 5.3.3).

5.3.1 Calibration on synthetic data without noise

In synthetic tests, we first calculate *reference temperature field* in a forward problem (equation 5.1) and use it as experimental data against which we validate our optimization approach.

Heat model parameters are set to arbitrary – though realistic – values. These parameters are considered to be the *true parameter values* and the reference temperature field is considered the *synthetic data*. The values of the fixed parameters are set as in table 5.1. True values of the fitted parameters are specified as follows: $\alpha = 0.21$, $\beta = 0.6$, $\eta = 0.3$, $\lambda_s = 2$ W/m/K and $C_s = 2\text{e}^6$ J/m^3/K. One or more of these fitted parameters are then perturbed with an error coefficient ranging from 50 to 100%. New forward temperature field is calculated and RMSE between calculated

vs. reference temperature field is minimized by updating the value of the fitted parameter(s) with every iteration. The synthetic tests are conducted both for cases with and without noise added to the synthetic reference temperature field; this examines the model's ability to fit real-world data which inevitably contain some level of noise.

All the fitted parameters of the heat model converge towards their true values in single-parameter optimization on synthetic data without noise.

Porosity (η) is one of the most sensitive parameters in thermal calculations (see results of sensitivity analysis, figure 5.1). Starting the single-parameter calibration of porosity from anywhere within the parameter bounds (0.1 - 0.9), the optimization converges to the true value (0.3) within 7 iterations, with RMSE in the order of 10^{-4}.

β is the least sensitive of the fitted parameters; nevertheless, the optimization converges to its true value within 4 iterations, with RMSE in the order of 10^{-4} to 10^{-3} depending on the initial guess. All the parameters are well-determined with narrow 95%-confidence intervals.

We simulated a case of having *reduced amount of calibration data* by using only every second 'sensor' in the objective function (value of the reference temperature field every 0.2 m between 0 and 1.5 m, instead of every 0.1 m). Reduced number of experimental data did not influence convergence performance of the model (number of iterations and RMSE after inversion).

In practical applications, *daily averages* are sometimes used for model forcing and calibration. Our simulations show that in such a case, the optimization algorithm needs one more iteration to converge, however, accuracy of solution is not affected and true parameter values are accurately recovered.

Up to four parameters can be estimated at once in joined calibration. Joint optimization for parameters λ_s, α, β and η converges within 26 iterations, though the recovered parameters lay within 15 % from their true values.

Attempting joint calibration of five parameters causes the optimization to converge towards a solution far from the true parameter values. A way to get around fitting the fifth parameter (C_s) is to define an acceptable range for it and run a sequence of optimizations with C_s fixed at every step of the predefined range, while fitting the remaining four parameters at once. In result, we obtain a number of RMSE values for four-parameter optimizations with C_s fixed at respective values of the predefined range (such as figure 5.2a). Considering the improvement of RMSE with change of C_s, we may then choose to repeat the optimization with values of C_s refined around the found optimum. We call this the *4+1* optimization approach and we use it in the calibration of ground thermal parameters in Ilulissat on the field borehole temperature measurements (section 5.3.3).

Essential setting during optimization is control over finite difference steps the solver takes to estimate derivatives; in MATLAB, this is the so-called *DiffMinChange*

option for *lsqnonlin* optimization function. The optimization tends to get trapped in local minima around initial guess if solver steps are too small. Forcing larger steps encourages the solver to explore wider range of solutions and speeds up convergence. *DiffMinChange* value should be proportional to the magnitude and sensitivity of the fitted parameter; e.g. for porosity (range 0.1 - 0.9), the *DiffMinChange* is set to 0.1. During joint calibration of several parameters of very different magnitude, parameters should be scaled so that the effect of *DiffMinChange* is proportional on every one of them.

5.3.2 Influence of noised measurements

We added random noise with amplitude ±0.03°to each of the 'measurements' of the synthetic (reference) temperature field. The amplitude of noise was chosen based on precision of HOBO thermistors that were used to instrument deeper boreholes (4 m and 6 m deep). The perturbed parameters were then recovered by optimizing on this 'noisy' reference temperature field.

True values of all the fitted parameters were recovered in single-parameter calibration starting from an initial guess 50% higher than the true parameter value. Performance of the four-parameter calibration with noise was comparable to the case without noise – recovered parameters lay within 15% from the true value.

The calibration tests with synthetic datasets confirmed that the trust-region reflective algorithm is well-suited for handling our optimization problem, provided that right optimization settings are used. The essential optimization settings are convergence tolerances, size of finite-difference steps, and upper and lower bounds on the permitted parameter value range.

5.3.3 Calibration with field data

Next step following the synthetic tests was to attempt recovering the thermal parameters of the real ground. This meant to optimize the thermal parameters on real borehole temperature timeseries instead of synthetic reference temperature field.

Initial and boundary conditions were identical as in the synthetic tests (section 5.3.1. The difference is that the reference temperature field in this case are the actual in-situ ground temperature timeseries measured by the MRC probe in depth between 0 m to 1.5 m during freezing season 1st September 2014 – 28th February 2015. The reason to choose the shallow MRC probe records for calibration is mainly that they provided the longest uninterrupted set of boundary conditions for forcing the model (see figure 4.4b for overview of available forcing/calibration data from the MRC probe).

We used the *4+1* optimization approach developed in the synthetic tests (section 5.3.1). Maximum of four parameters can be calibrated at once. Thus we began by defining a plausible range for the fifth parameter, C_s, as 0.6e^6 – 4.1e^6 J/m^3/K.

We then ran the 4-parameter joint optimization of the remaining fitted parameters $[\alpha, \beta, \eta, \lambda s]$, with C_s fixed respectivelly at 0.1e^6-increments of the pre-defined range.

The smallest average error (RMSE = 0.5517) between field *vs.* simulated temperature fields was found for the following parameter combination: C_s = 3e6 J/m^3/K, $\alpha = 0.75$, $\beta = 0.10$, $\eta = 0.53$ and $\lambda_s = 1.71$ W/m/K. Very narrow 95%-confidence intervals (CI) suggest that the optimized parameter estimates are well-defined (table 5.2, RMSE1).

In spite of large range of C_s evaluated, change in RMSE between respective model runs is very small (on the third decimal, see figure 5.2a), which is below precision of our temperature sensors. This suggests that the model in its current setup is not sensitive to parameter C_s enough to enable its calibration. Consequently, refining the calibration with smaller increments between the values of C_s would not substantially improve the model fit.

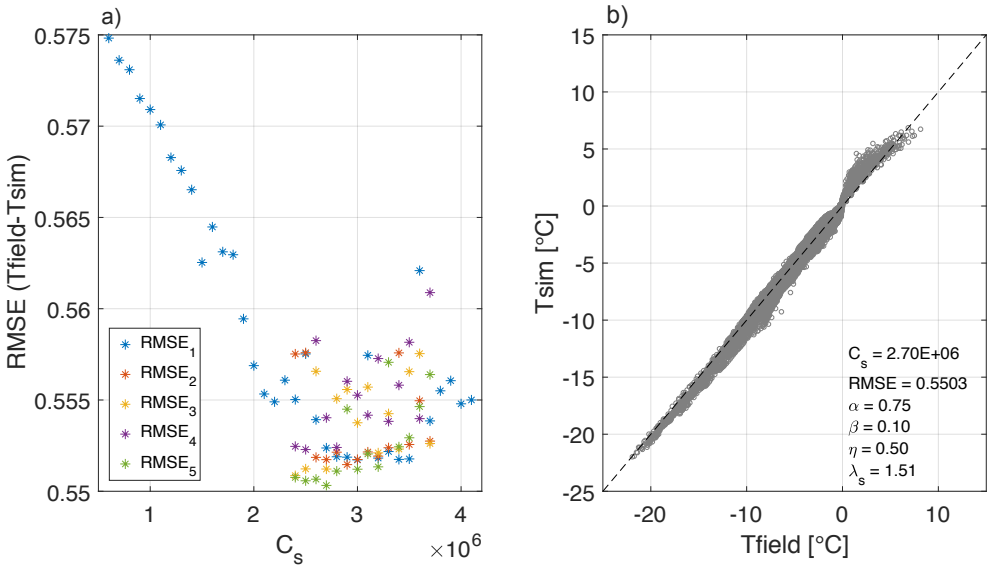

Figure 5.2: (a) RMSE after optimization for 92 model realizations starting from different initial parameter estimates. The same-color markers indicate the calibrations starting from the same initial values for parameters $[\alpha, \beta, \eta, \lambda s]$ and changing initial value for C_s. For each group of optimization runs RMSE1 through RMSE5, the initial values for parameters $[\alpha, \beta, \eta, \lambda s]$ were specified as in table 5.2, while the initial value for C_s was fixed on a 0.1e6-increments in the specified range (0.6e^6 – 4.1e^6 J/m^3/K for the group of runs RMSE1, and 2.4e^6 – 3.7e^6 J/m^3/K for RMSE2 –RMSE5). (b) Crossplot of field-measured temperature field *vs.* temperature field simulated with optimized parameters. *Tsim* is calculated with optimized parameter values resulting from RMSE5 calibration run – which is the run producing the lowest RMSE out of all the 92 calibration runs; optimized parameter estimates are indicated in the annotation. The average misfit between simulated and field temperatures is 0.55°.

Table 5.2: Summary of the 92 calibration runs. For each optimization sequence RMSE1 through RMSE5, the value of heat capacity of mineral phase (C_s) is fixed on a $0.1e^6$-increments in the specified *Initial* range. E.g. RMSE1 shows the minimum RMSE from 36 optimizations runs, each starting with C_s fixed at $0.1e^6$-increments between $0.6e^6$ – $4.1e^6$ J/m^3/K and remaining parameters $[\alpha, \beta, \eta, \lambda s]$ starting from the *Initial* values as specified. Similarly, the RMSE2 through RMSE5 shows minimum RMSE from 14 calibration runs each, starting with C_s fixed at $0.1e^6$-increments between $2.4e^6$ – $3.7e^6$ J/m^3/K and the remaining four fitted parameters starting from the *Initial* values as specified. RMSE for each of the 92 runs is plotted in figure 5.2a, where the respective combinations of initial parameterizations RMSE1 – RMSE5 are distinguished by color. The 95% confidence intervals (CI) indicate the range of values that one can be 95% certain contains the true mean value of the parameter.

Run	Parameter	Initial	Optimized	95% CI	Minimum RMSE
RMSE1	C_s	$0.6e^6$ – $4.1e^6$	$3e^6$	–	0.5517
	α	0.21	0.7468	± 0.0064	
	β	0.60	0.1006	± 0.0089	
	η	0.30	0.5258	± 0.0198	
	λ_s	2.00	1.7136	± 0.0955	
RMSE2	C_s	$2.4e^6$ – $3.7e^6$	$2.9e^6$	–	0.5515
	α	0.10	0.7738	± 0.0053	
	β	0.20	0.0839	± 0.0070	
	η	0.40	0.5935	± 0.0172	
	λ_s	3.00	2.0573	± 0.1328	
RMSE3	C_s	$2.4e^6$ – $3.7e^6$	$2.4e^6$	–	0.5509
	α	0.40	0.7916	± 0.0040	
	β	0.55	0.0792	± 0.0059	
	η	0.35	0.6308	± 0.0145	
	λ_s	1.80	2.2407	± 0.1413	
RMSE4	C_s	$2.4e^6$ – $3.7e^6$	$2.5e^6$	–	0.5523
	α	0.32	0.8129	± 0.0033	
	β	0.70	0.0719	± 0.0049	
	η	0.60	0.7276	± 0.0113	
	λ_s	2.20	4.1891	± 0.3923	
RMSE5	C_s	$2.4e^6$ – $3.7e^6$	$2.7e^6$	–	0.5503
	α	0.50	0.7482	± 0.0061	
	β	0.58	0.1045	± 0.0090	
	η	0.20	0.5012	± 0.0188	
	λ_s	1.90	1.5080	± 0.0713	

Initial parameter estimates influence the final, optimized parameter values. A large number of parameter combinations fit the data equally well, both because the inverse problem is under-determined, and due to noise in calibration data. To test the uniqueness of the model calibration, we re-ran the optimization on the range of C_s-values between 2.4e^6 and 3.7e^6 56 more times (5.2, RMSE2 – RMSE5). In total, we performed 92 optimizations starting from different initial parameter estimates. Overview of the respective initial and optimized parameterization estimates together with the RMSE of the runs is provided in table 5.2 and figure 5.2a. This work lead us to a range of optimized values for each parameter, depending on starting guess and value of C_s. The spread of the optimized parameter estimates can be appreciated on figure 5.3.

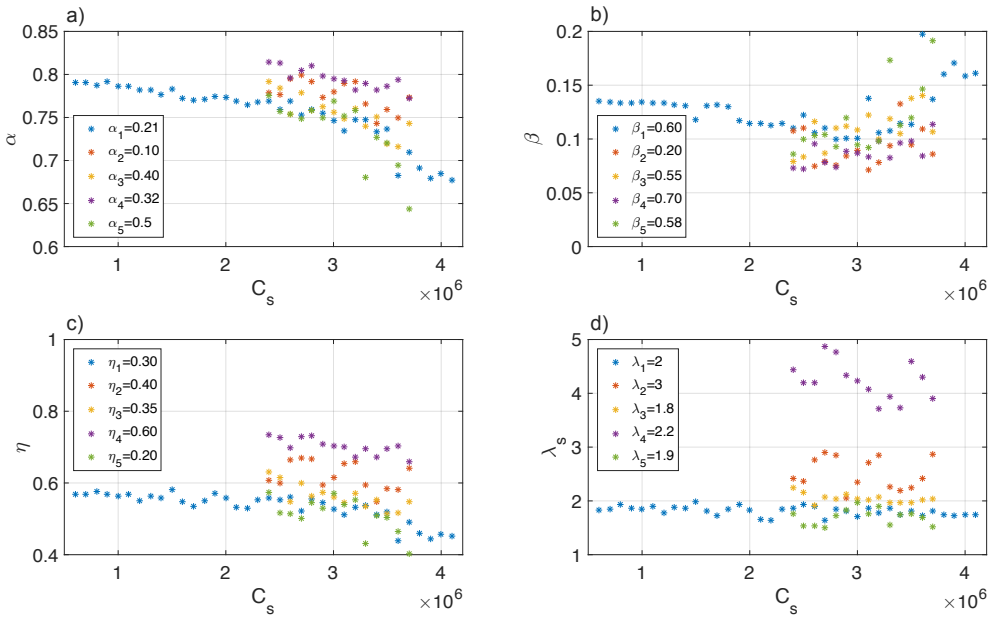

Figure 5.3: Spread of the optimized parameterization estimates depending on initial guess throughout the plausible range of C_s values. The same-color markers indicate the calibration runs starting from the same initial values for parameters $[\alpha, \beta, \eta, \lambda s]$ as specified in the legend of the plots, and on a range of initial value for C_s.

The lowest RMSE (=0.5503) among all the runs was found for parameter combination C_s = 3e^6 J/m^3/K, α = 0.75, β = 0.10, η = 0.50 and λ_s = 1.51 W/m/K (rounded to the second decimal), starting from initial estimates specified in table 5.2, RMSE5. The $Tsim$ calculated with such parameters is compared to $Tfield$ in a crossplot on figure 5.2b. Since sensitivity of model to input parameters depends on values of parameters themselves (section 5.2), we repeated the sensitivity analysis with calibrated parameter values. This analysis confirmed importance of the fitted

parameters for model prediction and did not reveal new optimization targets (figure 5.4). Thus we consider this calibration our best approximation of the actual ground thermal properties in Ilulissat and we refer to these values when evaluating other inversion approaches.

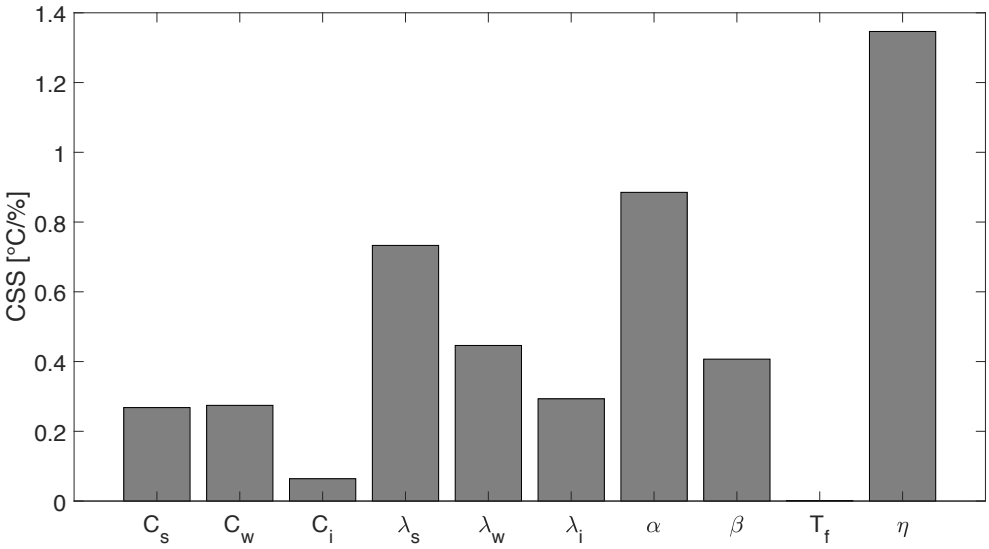

Figure 5.4: Sensitivity analysis of *optimized* heat model parameters. The graph shows average change in simulated temperature field caused by 10% increase in each evaluated parameter. Porosity remains the key parameter for model prediction, while influence of heat capacity and thermal conductivity of mineral phase has relatively decreased.

Figure 5.5 shows analysis of the misfits between simulated and field-measured temperatures at different depths throughout the modeled domain. As expected, the model struggles the most to reproduce rapid temperature fluctuations in the shallow subsurface (figure 5.5a). However, in general, the model simulates the temperature regime reasonably well, especially following the onset of ground freezing at the end of September, when the heat transfer is controlled by changing volumetric fractions of liquid water and ice in the pore space.

We conclude that fixing the value of C_s at any point around 2.7e6 J/m^3/K provides equally satisfying reproduction of field borehole temperatures within $\pm 0.55°$. The optimized values of the remaining fitted parameters $[\alpha, \beta, \eta, \lambda s]$ depend on their initial estimates and the value of C_s; however it is important to point out that all the parameter combinations resulting from 92 calibration runs come up with physically plausible values.

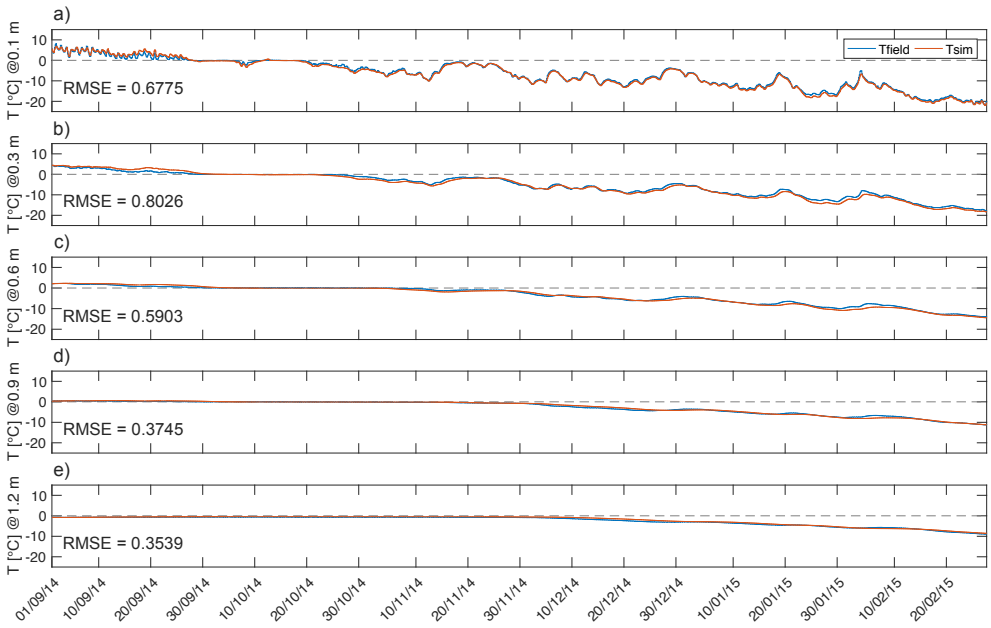

Figure 5.5: Difference between measured and simulated ground temperature timeseries at various depths in the active layer and top of permafrost throughout the calibration freezing season 2014/2015.

5.3.4 Validation of parameterization estimates

Direct measurements of the thermal properties are not available for validation of final parameter calibration from section 5.3.3. Thus we choose to validate the model by data-splitting (Power, 1993): using the parameter values optimized on the freezing season 2014/2015 to predict temperature regimes in previous freezing seasons 2012/2013 and 2013/2014.

The model calibrated on freezing season 2014/2015 predicts ground temperatures variation measured in freezing seasons 2012/2013 within ± 0.63°(figure 5.6a). Measurements from freezing season 2013/2014 (only two months between September and October 2013 were available) are reproduced within ± 0.32°(figure 5.6b).

5.4 Discussion and conclusions

Conclusion about whether a certain model fulfills its purpose (i.e. whether it is a *good model*) depends on an outcome of validation. While the validation is not necessarily a required part of model development (Mankin et al., 1975), it helps in determining the domain over which the model is applicable and increases model's credibility. According to Rykiel (1996), validation means that a model is acceptable

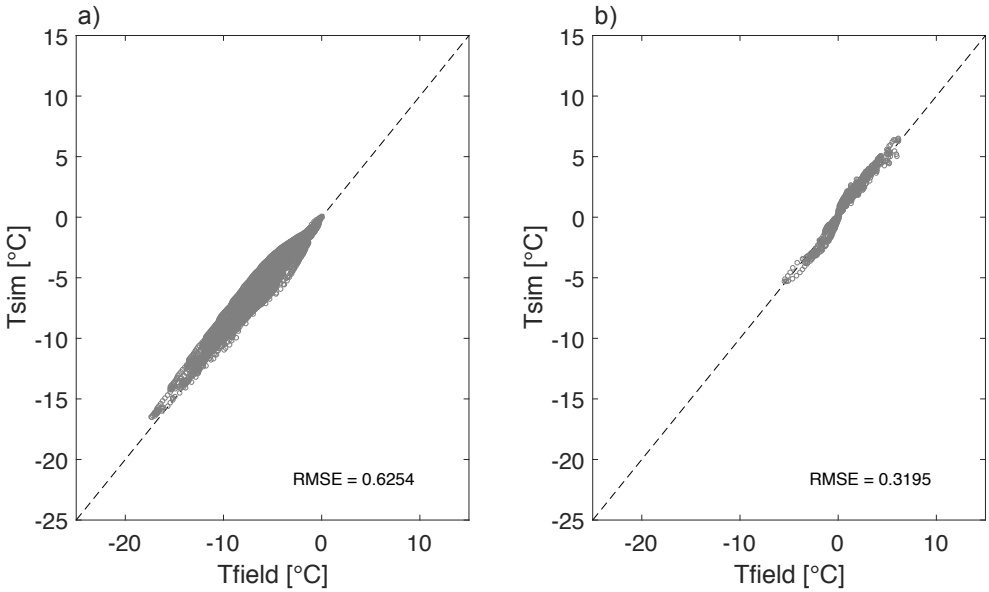

Figure 5.6: (a) Validation of heat model calibration on freezing season 2012/2013. Due to gaps in forcing temperature timeseries, we only use days between 1st November 2012 – 28th February 2013 for validation. (b) Validation on freezing season 2013/2014. Again, due to gaps in MRC probe dataset, only days between 1st September 2013 – 29th October 2013 are used for comparison between field-measured and simulated temperature fields.

for its intended use because it meets specified performance requirements. Thus before validation is undertaken, (1) the purpose of the model, (2) the performance criteria, and (3) the model context must be clarified.

In permafrost studies, the purpose of a model typically is long-term permafrost response to change in climate forcing. In such a case, the primary goal is to come up with a model and a set of parameter values that reproduce a training dataset within certain error bounds accepted by the modeler. The underlying assumption is that such model has succeeded in capturing the main structural and conceptual features of the modeled object; if the climate forcing is the only changing variable, the model should be able to predict system's response under changing boundary conditions with known uncertainty.

However, purely the fact that a model can match a set of calibration data does not guarantee its predictive value. In fact, due to the under-determined nature of the inverse problem, relatively large number of fitted parameters, uncertainty and noise in calibration data and assumptions and simplifications in conceptual model, it is *always* possible to come up with a model that fits a given set of training data within reasonable error bounds. Indeed, we observed wide spread of optimized parameter values – all producing comparable RMSE – depending on their initial guess (5.3),

thus pointing to non-unique parameter estimation. The range of plausible optimized parameter estimates could be further extended by modifying the model discretization and/or amount of data available for calibration.

Choice of the accepted model depends on the model context. It is often possible to constrain the optimization within a physically sensible range of parameter values, thus *a priori* eliminating a number of implausible solutions. However, as we observed, unless the range of acceptable parameter values is very narrow, we are still facing a high number of plausible parameter combinations that fit the data comparatively well. Identifying the accepted model is partly a matter of modeler's experience and personal choice because given the uncertainty in data quality (measurement noise, uncertainty about exact sensor placement), the best fitting model (with the lowest RMSE or other criterion) is not necessarily the one pointing to the true/most realistic parameter values. In fact, it can well be expected that a dataset forward-calculated with the true set of parameter values would *not* produce the lowest RMSE when compared to field data containing noise.

We presented a comparatively simple (1D, homogeneous, 3-phase) model for heat transfer in a ground undergoing cycles of freezing and thawing. The model relies on a number of conceptual assumptions to maintain the parsimony. Nevertheless, it predicts temperature variation at our test site with satisfactory accuracy. Simplicity of the model is a benefit in that the requirements on input data are relatively low – only surface temperature timeseries (which are comparatively easy to measure or could be scaled down from more widely-available air temperature data), initial temperature distribution and bottom boundary condition are needed. On the other hand, we can expect that optimized parameter estimates will compensate for conceptual simplifications in the model.

Although we advocate for use of easy-to-measure ground surface temperatures to drive the model, we do recognize that these typically suffer from rapid fluctuations influenced by short-wave radiation. Using near-surface temperatures to drive the model instead (at ca. 10 cm depth) could improve performance in the upper portion of the modeled domain.

Real-world data inherently contain noise, both due to instrumental setup (precision of the sensors, drift in the sensor measurements) and physical conditions in the borehole (convection of fluids in the borehole, vertical displacement of thermistors as consequence of frost heave). An exhaustive analysis of the sum of these error contributions was outside of the scope of this study.

We saw that due to hysteretic nature of freeze-thaw processes, the heat model needs to be calibrated for freezing and thawing seasons separately. Relatively short timeseries of one freezing season were sufficient to reach a plausible parameter estimation; extended calibration dataset (including several freezing seasons from consecutive years) may provide more realistic parameter estimates, though at a cost of higher uncertainty.

Nicolsky et al. (2007) stressed the importance of good initial parameterization estimates when using gradient-search methods. Using their approach to determining

optimal initial parameter estimates that are likely in the basin of attraction of global minimum may help narrowing down plausible parameter combinations.

In the context of geotechnical and engineering applications, the actual true values of thermal parameters remain of interest, as they can be used further in geotechnical models. Further efforts in improving the structure and sensitivity of the model, constraining the optimization and including further independent validation will be required to validate the model in this context.

CHAPTER 6

Coupled thermo-geophysical inversion

Boreholes temperature measurements provide the most reliable information about ground thermal regime. However, they are geographically and temporally sparse, as installation and long-term operation of ground temperature monitoring network is demanding both financially and physically. In spite of direct information they provide, borehole records inform about discrete ground properties in one spatial dimension. Meanwhile ground thermal properties are known to be highly variable due to local conditions.

Surface geophysical measurements potentially provide an attractive way of informing permafrost (thermal) models. Depending on the geophysical method used, they can provide 2-3D picture of subsurface properties, and cover comparatively large areas. Repeated measurements may inform about in-situ processes, feeding into more accurate conceptual models.

Studies by Hauck et al. (2008) and Krautblatter et al. (2010) demonstrate that there is quantitative link between electrical and thermal properties of geological materials. However until now, geophysical data have not been used in fully coupled optimization scheme, to constrain estimation of thermal properties of ground.

In this chapter, we evaluate feasibility of calibrating ground thermal properties on surface time lapse geoelectrical measurements. Electrical properties of ground depend mainly on the amount of unfrozen water available to carry the current. This

unfrozen water content is temperature-dependent, and temperature at any depth depends on ground surface temperature and thermal properties. Quantitative comparison between ground temperature timeseries and resistivity timeseries over complete freeze-thaw cycles is expected to provide calibration of the relationships between the two petro-physical properties that can be further exploited for predictions regarding the ground thermal regime.

6.1 Coupled thermo-geophysical approach to heat model calibration

The coupled inversion approach builds upon an assumption that there is a quantitative link between ground temperature and ground electrical properties. The ground electrical properties depend on four main factors: soil mineralogical composition, soil porosity, fraction of unfrozen water content and geochemical composition of the pore water (e.g. Hoekstra et al. 1975; Friedman 2005). The unfrozen water is typically the only conducting phase in a soil. It is also the only component that substantially changes its volume fraction over the course of a year, due to temperature-dependent processes of freezing and thawing. Due to the zero-curtain effect, there is no single temperature value at which ground resistivity changes from *frozen* to *unfrozen* (Hauck, 2002; Doetsch et al., 2015). At a freezing point of the pore water, the fraction of unfrozen water changes steeply due to phase change between water and ice. Meanwhile the temperature remains constant for as long as the latent heat of fusion is assimilated (or extracted). Consequently, the unfrozen water content is the key variable that provides the link between temporal changes of ground temperature and changes in ground electrical resistivity.

The coupled inversion approach is an optimization/inversion algorithm. It aims to estimate soil properties (thermal and electrical) which will, with sufficient accuracy, reproduce the observed resistivity timeseries, given a certain surface temperature variation. The procedure is outlined in figure 6.1 and further detailed below.

The coupled model consists of two, essentially standalone, modules: a heat transport model and an electrical resistivity model. The 1D heat model calculates temperature distribution in the ground given a set of initial and boundary conditions, forcing ground surface temperatures and initial thermal parameters (chapter 5). The calculated temperature distribution is translated into a 1D multi-layer geoelectrical model of the ground. This is done by dividing the modeled domain into many equally spaced layers. For each layer of the resistivity model, the layer-representative temperature is found by interpolating between the nearest solutions of the heat model. For each layer-representative temperature, fractions of water, ice and rock are found using an empirical relation describing unfrozen water content in soils at subfreezing temperatures (equation 5.4). Effective bulk soil resistivity for the given model layer is calculated from specific resistivities of respective ground constituents by using a resis-

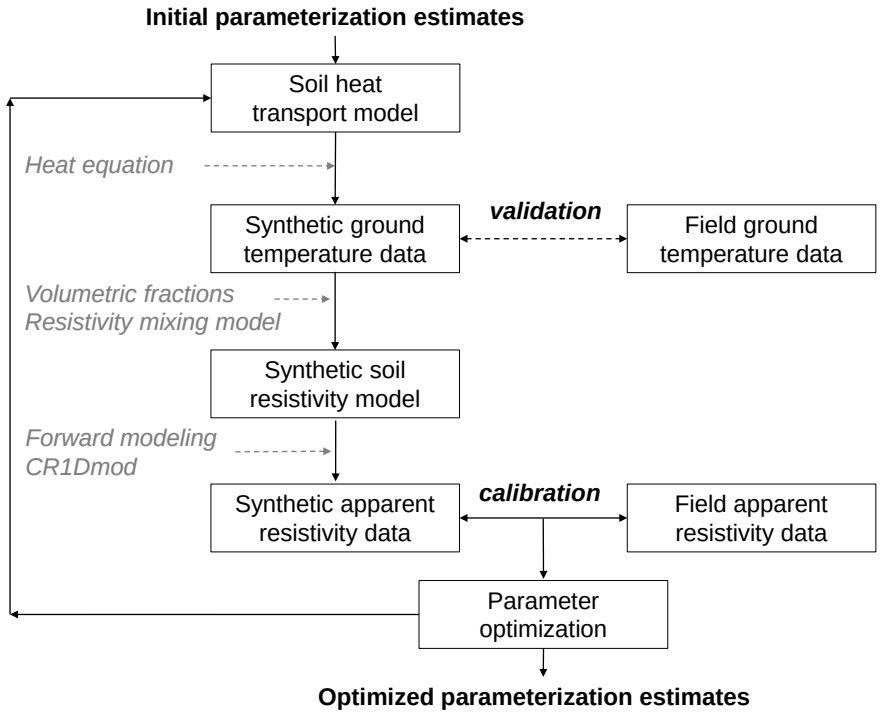

Figure 6.1: Flow diagram of the coupled thermo-geophysical inversion using ground surface temperature data as model input, and apparent resistivity data collected from surface of the ground for calibration. Note that only surface measurements are used to drive and calibrate the model; borehole temperatures may be used for model validation, however, they are not required for the optimization.

tivity mixing rule. From the geoelectrical model, forward apparent resistivity response is calculated by the CR1Dmod program (Ingeman-Nielsen and Baumgartner, 2006) using the same electrode configurations as on the field site. The calculated apparent resistivities are compared to the field geoelectrical measurements. The difference is then minimized by adjusting thermal parameters of the heat model from which the forward resistivities are calculated, and the specific resistivities of soil fractions. The final heat model calibration is validated by comparing the simulated ground temperature distribution to borehole temperature timeseries from the location of the time lapse ERT acquisitions.

The fundamental characteristic of our approach is the use of ***apparent resistivities*** *for calibration, instead of inverted resistivity models.*

The reason for using apparent resistivities is expectation that they introduce less additional uncertainty to the calibration in form of inherent inversion assumptions

and artifacts. Most importantly, the relationship translating certain ground electrical composition into apparent resistivity is unique and governed by equations for conservation of charge, Ohm's law and geometry of electrode configuration used to collect the resistivity data. As opposed to that, any inverted resistivity model is only one of a number of possible realizations that explains the measured apparent resistivity data acceptably well. The non-unique nature of inverted resistivity model thus provides less solid basis for quantitative calibration.

In the following sections, we outline and test the coupled inversion approach, and compare it with the traditional heat model calibration on borehole temperatures discussed in previous chapter. Section 6.2 explains the setup of the resistivity module of the coupled model. We review and evaluate two commonly used resistivity mixing relationships for calculation of effective bulk resistivity of three-phase soil. In section 6.3, we evaluate sensitivity of the coupled model to heat and resistivity parameters. In section 6.4 we perform calibration tests on synthetic data and in section 6.5, we apply the coupled inversion approach to field data. Advantages and limitations of the method are discussed in section 6.6.

Modeling and optimization framework is implemented in MATLAB, with the heat equation solver implemented in *Python* (refer to section 5.1.3 for details about implementation).

6.2 Resistivity model setup and validation

The geophysical part of the modeling framework consists of a 1D geoelectrical model with a large number of layers of equal thickness. In convergence testing, we determined that a model made of 128 layers within the 6 m deep domain produces convergent solution. A representative temperature is assigned to each layer based on interpolation from the nearest grid points of the heat model solution. Fractions of water, ice and soil minerals are calculated based on equations 5.2 and 5.4. The *effective bulk resistivity* is then calculated for each layer of the model by weighing the *specific resistivities* of the respective ground components in a resistivity mixing relation. The choice of the resistivity mixing relation is justified in section 6.2.1.

Based on the derived ground resistivity model, synthetic apparent resistivities are calculated by CR1Dmod code (Ingeman-Nielsen and Baumgartner, 2006), using the same electrode configuration as in the field acquisitions.

As the apparent resistivity field measurements launch every day at 18:00 UTC and last for up to 5.5 hours, heat model solutions at time steps between 18:00 – 00:00 UTC (16:00 – 22:00 Greenlandic time) every day are averaged to provide the most realistic temperature profile.

Parameter optimization is based on iterative non-linear least-squares formulation and uses the trust-region reflective algorithm – the same as in the case of heat model calibration (chapter 5, section 5.2).

Cost function is the sum of squared differences between logarithms of field-measured and forward-calculated *apparent resistivities*. Reason for using the log-transformed resistivities is that the problem becomes more linear and a more equally weighted fitting of the resistivity data is achieved. The cost function is minimized by adjusting thermal parameters of the heat model from which the forward resistivities are calculated. We use the root mean square error (RMSE) between simulated and field resistivities to evaluate the model fit and compare respective calibration runs.

6.2.1 Choice of resistivity mixing rule

Validation of the resistivity module essentially consists of validation of resistivity mixing relationship used to calculate effective resistivity model of a soil of a certain phase composition. The purpose is to confirm that the chosen relationship predicts bulk soil resistivity within acceptable error bounds. Good accuracy of resistivity mixing relation is crucial for success of the coupled inversion approach as it ultimately provides the calibration link between changing phase composition of a soil (temperature-dependent) and observed resistivity.

Number of mixing models is commonly used to relate specific resistivities of ground constituents and their volumetric fractions to the effective resistivity of bulk soil (for an overview, see e.g. Glover 2010). In this work, we compare two relationships: geometric mean and the Archie's law.

The traditional Archie's law (Archie, 1942) derives bulk resistivity of ground material based on material's porosity and resistivity of pore fluid:

$$\rho_e = \rho_w \eta^{-m} \phi^{-n} \tag{6.1}$$

where ρ_e is the effective resistivity of the bulk soil, ρ_w is the specific resistivity of the pore water, η is the porosity, ϕ is the unfrozen fraction of pore water and m and n are empirical coefficients.

The geometric mean model (e.g. Guéguen and Palciauskas (1994) estimates the effective bulk resistivity as the geometric mean of respective specific resistivities of ground components, weighted by their volumetric fractions:

$$\rho_e = \left(\prod_{i=1}^{n} \rho_i^{\theta_i} \right) \tag{6.2}$$

where ρ_i and θ_i are the specific resistivity and volumetric content of the i-*th* soil constituent respectively.

Without direct measurements of specific resistivities of ground constituents, we essentially have two ways of validating the resistivity mixing relationship on field measurements (both are schematically illustrated on figure 6.2):

1. *Effective resistivity* can be compared to the *inverted resistivity* (figure 6.2a). In this case, we calculate volumetric fractions of ground constituents based on

unfrozen water content (measured by the soil moisture sensor at 0.3 m depth) and equation 5.4. Resistivity mixing rule is used to estimate the bulk effective resistivity of the soil of given phase composition. The bulk effective resistivity derived from water content is then compared to the inverted resistivity extracted from inverted model layer closest to the depth of soil moisture sensor.

2. *Forward-calculated apparent resistivity* can be compared to the *field-measured apparent resistivity* (figure 6.2b). For the purpose of validation, we use temperature profile measured in borehole ILU2013-01 (chapter 2.3). The temperature distribution gives rise to a certain partitioning of ground constituents (equations 5.2 and 5.4), which in turn is used to calculate the effective ground resistivity model (similar as in the previous approach). The effective resistivity distribution is then used to forward-calculate the apparent resistivity response of the ground of the given composition, using the same electrode configuration as on a field site. The forward-calculated apparent resistivity is then compared to the field-measured resistivity.

The first approach is the more traditional way of using resistivity data in estimating ground ice/water content changes. For our purpose of parameter calibration, we expect this approach being less accurate. This is due to potential inversion-induced artifacts that cannot be explained by the resistivity mixing rules, and due to the fact that comparing indirect measurements from ground surface (resistivity) with point observations at a specific depth (temperature or moisture/ice content) inherently faces scale and resolution issues.

The second validation approach corresponds to the fully coupled inversion scheme, with the only difference that the initial temperature profile used to estimate phase composition of the ground is simulated by heat model (described in previous chapter 5), not taken from borehole measurements.

Performance of each of the resistivity mixing rules can be appreciated on figure 6.3 which shows comparison between measured resistivities (inverted and apparent) *vs.* synthetic resistivities computed by each mixing rule throughout one complete cycle of freezing and thawing 2014/2015. Measurements and simulations from depth of 0.3 m are extracted for the purpose of comparison.

Specific resistivities of soil constituents and values of Archie's coefficients used in plotting synthetic resistivity curves (in red) in figure 6.3 are result of non-linear least-squares fitting of synthetic resistivities to field measurements. Values of specific resistivities of water, ice and soil minerals used in geometric model: $\rho_w = 20\ \Omega$m, $\rho_i = 10^5 \Omega$m, $\rho_s = 6000\ \Omega$m. Values of Archie's coefficients: $m = 5.3, n = 3.5$. Corresponding mean deviation between simulated *vs.* measured resistivities is indicated as RMSE in figure 6.3.

General slope of initial resistivity increase upon freezing (from beginning of October to middle of November) is correctly reproduced by both resistivity models. The *geometric mean* model appears to slightly better follow the resistivity increase in the initial phase of freezing, however, it underestimates the resistivity throughout the

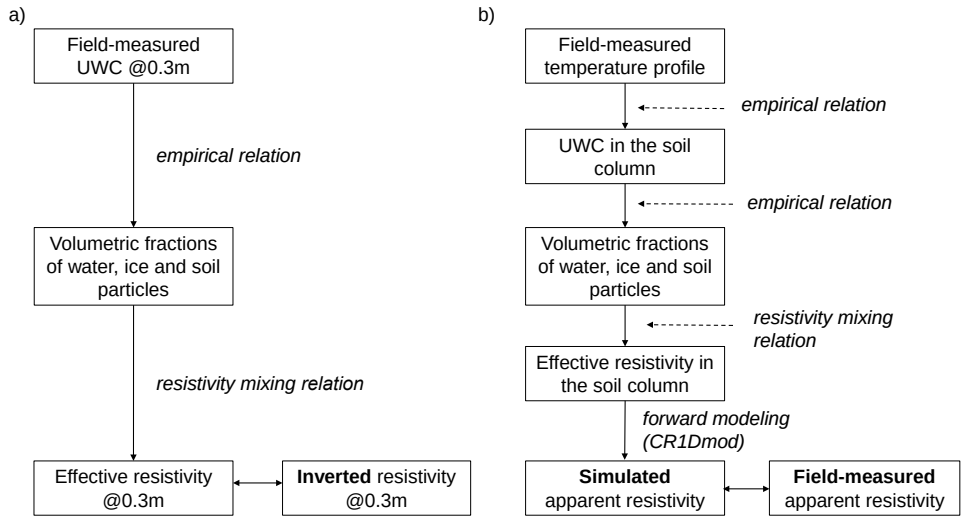

Figure 6.2: Two approaches to validation of the resistivity model and effective resistivity mixing relationship: (a) Validation on inverted resistivity model. Theoretical *effective resistivity* of the soil at 0.3 m depth is calculated from specific resistivities of ground constituents weighed by their volumetric fractions. The volumetric fractions are derived (equation 5.2 and 5.4) from unfrozen water content measurements by soil moisture sensor at 0.3 m. (b) Validation on apparent resistivity field measurements. The *synthetic apparent resistivity* is forward-calculated from effective resistivity model using the CR1Dmod program. The effective resistivity model is from ground temperature profile measured in borehole ILU2013-01 using equations 5.2 and 5.4.

entire year. On the other hand, the *Archie's law* is more successful in reproducing magnitude and variations of resistivity during frozen state (ca. between December – beginning of May). Neither of the models fully captures the extreme resistivity values during deeply frozen state. We speculate that variations of grounding resistances (chapter 3), not accounted for by the resistivity models, contributes to extreme expressions of the field resistivity during the coldest periods.

The average deviation between synthetic *vs.* field-measured resistivities is lower when comparing the apparent resistivities as opposed to inverted resistivities. This supports our choice of using **apparent resistivities** for calibration.

The **Archie's law** performs slightly better than geometric mean, as the average misfit between log-transformed field-measured and forward-calculated resistivities is smaller; however, the RMSE should not be the only factor in choice of the effective resistivity mixing rule. Sensitivity of the model output to change in its parameters is important, as it ultimately conditions whether certain parameters can be determined. Sensitivity of each of the mixing rules in the coupled model is discussed in following section 6.3.

Because of the hysteresis of ground resistivity and unfrozen water content (chap-

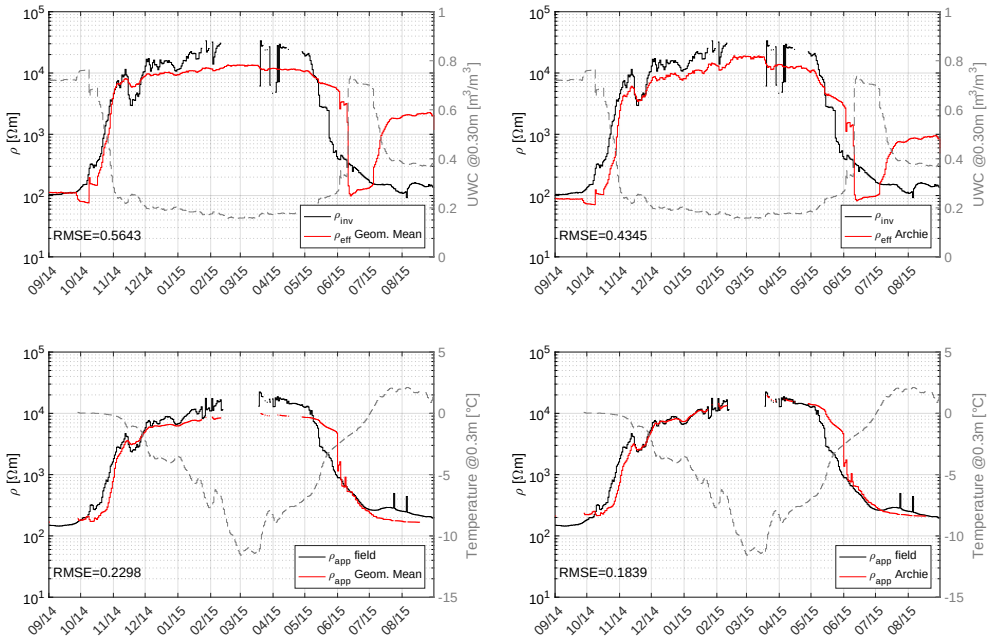

Figure 6.3: Validation of resistivity mixing relationship. RMSE is the root mean square error between logarithm of field-measured resistivities (apparent or inverted) and synthetic effective resistivities (calculated by Archie's law or geometric mean from volumetric fractions of ground constituents and their specific resistivities). The date ticks indicate the first day of every month. Upper subplots (a) and (b) correspond to the validation on field inverted resistivity (figure 6.2a), using either the geometric mean (a) or the Archie's law (b) to compute the synthetic effective resistivity. Lower subplots (c) and (d) correspond to the validation on field apparent resistivity (figure 6.2b) – the approach used in the coupled inversion. Again, we compare between the apparent resistivities resulting from effective resistivity model as calculated by the geometric mean (c) *vs.* Archie's law (d).

ter 4, see also (Tomaskovicova and Ingeman-Nielsen, 2016)), neither of the models succeeds in explaining abrupt resistivity decrease upon ground thawing (beginning of May). Resistivities in the thawing phase are one order of magnitude lower than resistivities in freezing phase at the same unfrozen water content (see chapter 4 and article in attachment C for reference). This is of course not accounted for by neither of the resistivity mixing rules, and results in both models overestimating the synthetic resistivities in the thawing phase. Portions of the resistivity data acquired for the ground above 0 °C can not be used for calibration, as the resistivity response is not directly governed by neither ground temperature nor the soil moisture variation.

In permafrost modeling applications, the thawing part of the resistivity curve is typically of greater interest. However, our results suggest that neither of the resistivity mixing relations tested captures the complexity of relationship between soil unfrozen

water content and resistivity during irreversible processes of phase change. As both resistivity models fit the freezing part of the curve reasonably well, we only use the freezing period in the proof of coupled inversion concept.

6.3 Sensitivity analysis

Sensitivity analysis, described in chapter 5.2, is repeated for the fully coupled optimization scheme. Again, model sensitivity to inputs changes with model discretization and parameter values in parameter vector. However, due to practicality, we only perform the sensitivity analysis with the initial and optimized parameterization estimates.

Both thermal and resistivity parameters are evaluated; as we recall, the synthetic, forward-calculated apparent resistivity is derived from volumetric fraction of respective soil phases, which are determined by soil temperature profile. Thus, success of the coupled optimization depends on sensitivity of the forward apparent resistivity calculation to change in the heat parameters [C, λ] as well as resistivity parameters [ρ, Archie's parameters m and n]. Parameters [α, β, T_f, η] describe the unfrozen water content variation with temperature below freezing point and thus are used in both heat and resistivity modules of the coupled scheme. Figure 6.4 shows change in simulated apparent resistivity (log-transformed) resulting from 10% change in each of the input parameters, respectively.

Resistivity model based on Archie's law (figure 6.4b) is overall more sensitive to changes in all input parameters. Porosity (η) is, again, the most influential parameter in the coupled scheme, as it was previously in the heat model alone (section 5.2). This makes sense, as the total volume and inter-connectedness of pores available for storage and movement of soil moisture determine resistance to current flow.

Similarly, parameters α and β describe unfrozen water content variation with temperature below the freezing point and thus have essential influence on apparent resistivity calculations.

Archie's parameters ρ_w, m and n are obviously of great importance for forward calculation of apparent resistivity.

Both resistivity mixing rules show very little sensitivity to changes in heat model input. Nevertheless, we will attempt to recover the thermal conductivity of soil minerals (λ_s), which is an important parameter for heat model predictions. The remaining heat model parameters have either less influence on heat model predictions, or they can be fixed according to well-documented table values (5.2).

Following the comparison of the two resistivity mixing relations in section 6.2.1 and results of sensitivity analysis, we choose the **Archie's law** for deriving effective resistivity model in the coupled inversion scheme. Consequently, we identify our target parameters for optimization will ideally be the following: λ_s, α, β, η, ρ_w and Archie's parameters m and n.

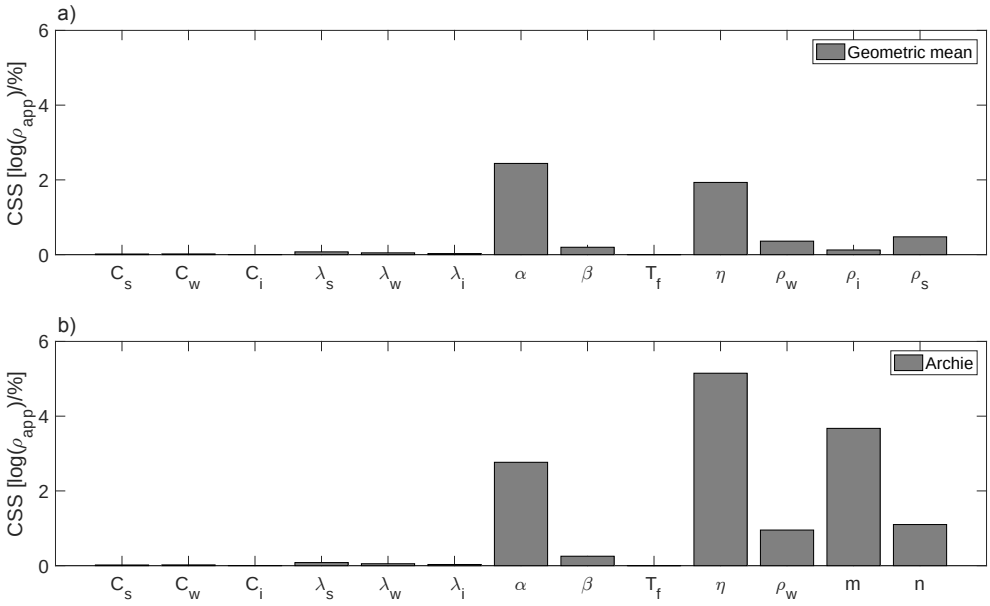

Figure 6.4: Composite scaled sensitivity (CSS) of heat and resistivity model parameters in the fully coupled inversion scheme. Both geometric mean and Archie's law resistivity mixing relationships are used to compare sensitivity of the coupled scheme using either of the models. The sensitivity is expressed as the change in logarithm of forward-calculated apparent resistivity following 10% change in the evaluated parameter. (a) CSS for parameters of the coupled inversion using the geometric mean resistivity mixing rule. (b) CSS for parameters of the coupled inversion using the Archie's law resistivity mixing rule.

6.4 Coupled inversion with synthetic data

We performed several optimization runs on synthetic data without noise, to get a feel for sensitivity of the optimization algorithm, correct optimization settings and identify number and combination of parameters that can be estimated at once. In the procedure, a set of *true* parameter values is used to produce *reference temperature field*, which in turn gives rise to synthetic effective resistivity model. From the ground resistivity model, *reference apparent resistivity* response is calculated. The true parameter value(s) are then perturbed by a random error coefficient ranging from $\pm 20 - 90\%$. We then aim to recover the true parameter values by updating the perturbed heat and resistivity parameters iteratively and comparing the forward-calculated synthetic apparent resistivity to the reference apparent resistivity. Optimization algorithm and convergence criteria are the same as described in analogous section about heat model testing 5.3.1.

Porosity (η) is the most sensitive parameter of the coupled model. The optimization algorithm converged to the true parameter value within 3 iterations. The

parameter was well-determined with narrow 95% confidence intervals.

Thermal conductivity of soil minerals (λ_s) is an essential parameter for heat model predictions, even though the coupled scheme appears to be very little sensitive to it. Nevertheless, in a single-parameter optimization on synthetic data without noise, the true parameter value was recovered accurately within four iterations.

Joint calibration of all of the *seven fitted parameters* at once [α, β, η, λ_s, ρ_w, m, n] produced very good fit between simulated and reference apparent resistivities, with final RMSE after optimization typically in the range of 10^{-3} – 10^{-2} corresponding to the convergence criteria (see section 5.2 for explanation of choice and values of convergence criteria). The optimization converges within 4 – 5 iterations. However, the very good fit results from optimized parameter estimates that are different from the true parameter values. Moreover, repeating the calibration from different starting points reveals that optimized parameter values depend on their initial estimates. In spite of non-unique determination of the fitted parameters, they all lie in physically plausible range.

We attempted to fix some of the less sensitive parameters (as per analysis in section 6.3) and run the synthetic optimization for 6 parameters (λ_s fixed) and 5 parameters (λ_s and β fixed) respectively. The optimization with 6 fitted parameters [α, β, η, ρ_w, m, n] produced slightly lower final RMSE in comparison to the optimization with 7 and 5 fitted parameters, however, it did not improve recovery of the true parameter values. Nevertheless, our synthetic tests confirmed that the optimization algorithm converges to a set of parameters producing very good fit (within convergence tolerances) to the training dataset.

In the following section, we attempt to estimate the real thermal and resistivity parameters of the ground in Ilulissat through fully coupled inversion approach and compare the result to calibration on borehole temperatures only.

6.5 Coupled inversion with field data

We applied the approach determined in synthetic study (section 6.4) to the optimization of thermal parameterization of heat model using only field apparent resistivity data collected from the surface.

Our fitted parameters in the optimization on field data are: α, β, η, ρ_w, m, n. We proceed with fixing the thermal conductivity of soil grains (λ_s) to value 1.70 W/m/K. We also fix the value of heat capacity of soil grains (C_s) to 3e^6 J/m^3/K (values from heat model calibration RMSE1, section 5.3.3).

The results are displayed on figure 6.5. The figure 6.5a shows the best fit of apparent resistivities after calibration on freezing season 2014/2015. The synthetic apparent resistivities in the crossplot were calculated with optimized parameter values that are listed in annotation of subplots a) (resistivity parameters) and b) (shared heat and resistivity model parameters). Although the fit of resistivities is not ideal, the obtained parameterization produces temperature field that fits the field-measured temperatures in freezing season 2014/2015 within ±0.66°(figure 6.5b).

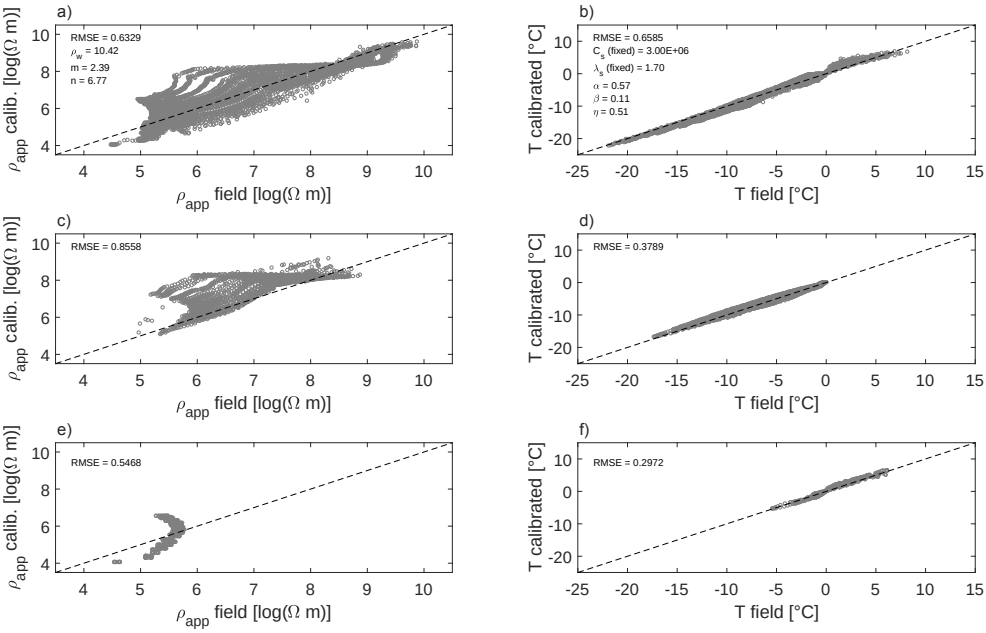

Figure 6.5: Calibration of heat model on apparent resistivities from freezing season 2014 –2015 (a and b) and validation of the optimized model on freezing seasons 2012 – 2013 (c and d) and 2013 – 2014 (e and f). The values of optimized thermal and resistivity model parameters are listed in annotations of plots a) and b).

To assess the predictive value of the model, we used the optimized parameterization estimates (values as listed in figure 6.5a and 6.5b) to forward-calculate the apparent resistivity distribution in freezing seasons 2012/2013 (figure 6.5c) and 2013/2014 respectively (figure 6.5e). We observe that the parameter values optimized on the freezing season 2014/2015 predict the field temperature measurements from freezing season 2012/2013 with residual error 0.38°(figure 6.5d). The field temperature measurements from freezing season 2013/2014 (only two months are available for comparison) are predicted with residual error 0.30°(figure 6.5f).

The residual error between field-measured and forward-calculated (with optimized parameters) temperature fields is smaller when using the coupled calibration approach, as opposed to the thermal optimization only (section 5.3.3). On the other hand, parameter values remain non-uniquely determined, with optimized values depending on the initial parameter estimates. Regardless, all the optimization runs come up with physically plausible parameter values and the forward-calculated temperature fields fit the training dataset with residual error around 0.6°.

6.6 Discussion and conclusions

Efforts using geophysical data to constrain other – especially hydrological – models are by now well documented. The coupling strategies vary, from constraining inversion and interpretation of the other models with inverted geophysical data (Doetsch et al., 2013), through structurally-coupled approaches (Gallardo and Meju, 2011; Lochbühler et al., 2013), to fully coupled inversion schemes using the geophysical data before inversion (Hinnell et al., 2010; Herckenrath et al., 2013a). The fully coupled approaches have been encouraged by some (Gallardo and Meju, 2011), as separate data inversions lead to inconsistent models for the same subsurface target. The fully coupled framework has been shown to improve accuracy and reduce uncertainty of prediction of hydrological parameters (Hinnell et al., 2010; Herckenrath et al., 2013b)

In permafrost *thermal* modeling, coupling approaches have been applied in essentially two ways: temperature-calibrated resistivity tomography has been used for quantitative estimation of ground ice and water content changes (Krautblatter et al., 2010), and inverted resistivity models have been used to constrain ground ice changes estimates (Hauck et al., 2008).

Our approach to coupled modeling revealed lack of adequate resistivity mixing relationship that would correctly translate phase composition of the ground into the effective resistivity model. Traditional resistivity mixing relationships do not account for hysteresis in variation of ground resistivity with unfrozen water content and temperature. The Archie's law applies when virtually all conductivity in a bulk soil can be attributed to the pore liquid. This condition is not entirely met in our field situation, as high clay content likely contributes to lowering the overall soil resistivity by surface conduction. We did tested a modification of Archie's law accounting for surface conduction of clays (e.g. Glover et al. (2000)); however, preliminary results did not justify proceeding with this version of relationship at the given point. Adaptation of the resistivity mixing relationship remains a possibility for improvement of performance of the coupled inversion framework.

The approach described in this work constitutes one of a number of possible ways of adding a constraining information directly to the process of estimation of heat model parameters. Primarily though, our aim was to investigate whether *surface measurements* can substitute the borehole information traditionally used for thermal calibration, and to what extent. The geoelectrical data were shown to contain constraining information for calibration of heat model. Even though we do not obtain an ideal resistivity model, the thermal calibration is useful. The fit of the resistivity-calibrated heat model is comparable to the fit of heat model calibrated on borehole temperature measurements.

As is the case with purely thermal inversion, the optimized parameter estimates displayed non-uniqueness in their determination. Depending on the context and intended application though, the predictive value of the coupled model is an encouraging result. Recognized equivalency issues affecting the resistivity part of the modeling framework, lack of more adequate resistivity mixing relationship and conceptual

simplifications of the heat model suggest a few immediate ways for improving the performance of the coupled inversion approach.

CHAPTER 7

Conclusions

This project was concerned with a wide range of challenges, spanning from improvement of field practice, through description and modeling of in-situ processes and relationships between environmental variables, to the use of monitoring data in thermal modeling and development of innovative coupled inversion approach.

In spite of this wide range of topics, all the chapters contribute to one story. The coupled modeling approach requires thorough understanding of in-situ processes and extensive calibration data. These could only be acquired by building and optimizing an innovative monitoring system that provided dense data of consistent quality. The amount and variety of data collected provided further insight into the in-situ processes and indicated a number of possible improvements for currently used modeling assumptions.

The following section 7.1 highlights contributions and novelties of this work, while section 7.2 suggests interesting future study directions and improvements.

7.1 Contributions and novelties

The main contributions of this thesis are the following:

1. **The longest-reported timeseries of time lapse electrical resistivity from high-latitude permafrost** We report the longest continued monitoring of ground electrical resistivity from an Arctic permafrost site, to date. At the same time, we present soil moisture content and temperature data that were quantitatively compared to the resistivity data. The importance of continuous, long-term time series for permafrost studies has been recognized previously. We confirmed that time series of complete freeze-thaw cycles with relatively dense sampling frequency are necessary to capture the complexity of the in-situ processes. This understanding is an inevitable precondition for guiding the choice of equations and target optimization parameters used in modeling such systems.

2. **Design, setup and successful operation of an automated ground resistivity monitoring system** We describe a ground resistivity measuring

system that, even though not manufactured for long-term time lapse acquisition, could be adapted to provide nearly continuous and complete data series, limited only by environmental factors (such as grounding resistances) rather than system issues. Since equipping the system with an on-site computer, automated data transmission and power backup, we were collecting uninterrupted daily measurements of ground apparent resistivity.

3. **The Focus-One protocol** We described a measurement protocol for estimating electrode grounding resistances of multi-electrode arrays used for ERT measurements. The protocol measures the single-electrode grounding resistance with accuracy of ±7 % for arrays of 30+ electrodes. Practical relevance of the protocol was demonstrated in several field studies, where the protocol helped to optimize electrode arrays for long-term monitoring projects (see next).

4. **Electrode design optimization for monitoring applications** The grounding resistance problem, although widely recognized, has not been previously studied under field conditions in a systematic way. Our set of laboratory and field experiments led to quantification of grounding resistances across a range of ground temperatures, lithologies and electrode shapes. Improvement achieved by each electrode shape was quantified and statistically evaluated. We formulated practical recommendations and provided tools for optimizing choice of electrodes during the design stage of a monitoring project.

5. **Timeseries of field-measured grounding resistances** While notoriously difficult to measure in the field, grounding resistances impact completeness and quality of monitoring data. Therefore reporting timeseries of grounding resistances over complete freeze-thaw cycles in three different periglacial areas provides valuable experience and reference for practicing geophysicists. We observed that electrodes are virtually never perfectly grounded and the additional grounding resistance may be up to 1 MΩ in the frozen period. This undermines the assumption that permanently placed sensors suffer no change of conditions of installation. Through a modeling study, we quantified that errors of up to 10% may be introduced to time lapse acquisitions depending on transmitted current and additional grounding resistance.

6. **Freeze-thaw hysteresis of unfrozen water content** Through in-situ measurements and modeling, we described irreversible relationship between soil unfrozen water content and ground temperature during cycles of freezing and thawing. Consistently higher unfrozen water contents were observed during freezing of the active layer than during thawing. This implies that the amount of unfrozen water in a system below the freezing point cannot be uniquely determined from ground temperature, and rather it depends on the history of the freeze-thaw cycle. While freezing is a slow process happening over time span of weeks (at a given depth, at this site), thawing of the same volume of soil is comparatively fast process. This knowledge is of great practical relevance

for permafrost modeling studies, as the rate of change and the total amount of unfrozen water are essential parameters controlling heat transfer in a ground undergoing phase change.

7. **Freeze-thaw hysteresis of ground electrical resistivity** Previously reported from laboratory experiments, we observed in-situ hysteresis of ground electrical resistivity in relation to unfrozen water content. Although a number of relationships quantitatively relates soil electrical properties to its water content and *vice-versa*, they do not take into account changes in pore-scale fluid distribution associated with saturation history. As the relationship between ground resistivity and unfrozen water content depends on history of the freeze-thaw cycle, in our experience, the resistivity mixing relationships only allow to reliably model the freezing part of the resistivity curve. This has implications for quantitative interpretation of resistivity models in terms of ground ice/water content changes.

8. **Simple heat transport model for active layer and permafrost** We build a comparatively simple, one-dimensional model for conductive heat transfer in a three-phase soil (grain, water, ice) undergoing cycles of freezing and thawing. The model reproduced calibration dataset (freezing season 2014/2015) with RMSE = 0.55 °C and predicted temperature variation in the two previous freezing seasons 2012/2013 and 2013/2014 within ±0.62 °C and ±0.32 °C respectively. Among the advantages of the model is low requirement on input data which are relatively easy to measure (ground surface temperatures). Known limitation is the number of assumptions used to construct the model. However, these are simplifications inherent to any model development following the principle of parsimony. Optimal parameter estimates can be expected to compensate for simplified model structure.

9. **Automated iterative parameter optimization** A high number of heat model and coupled model parameters would be inefficient to systematically adjust manually. A gradient-search algorithm has been shown to satisfactorily optimize parameter estimates in synthetic tests. In the tests with field data, the algorithm identified physically plausible parameter combinations while providing good fit to both training and testing datasets. Admittedly, the algorithm is susceptible to getting trapped in local minima and the optimized parameter estimates depend on initial parameter guesses, model discretization and amount of calibration data. We expect that this can be partly remedied by optimizing the initial parameter estimates, orthogonal validation methods and/or additional constraining information (such as resistivity data).

10. **Validation of resistivity mixing relationship for the effective resistivity of a multi-phase soil** Comparison of two commonly used resistivity mixing relationships revealed that the Archie's law is more suitable for simulating the effective ground resistivity based on ground phase composition at our site.

Due to the freeze-thaw resistivity hysteresis, the relationship only satisfactorily explains the freezing part of the yearly resistivity variation.

11. **Fully coupled inversion scheme using geoelectrical data for heat model calibration** The use of apparent resistivity data in fully coupled calibration of a heat model has not been documented so far in permafrost thermal modeling. In spite of a relatively poor fit of the resistivity model, the thermal calibration is useful. Calibration of thermal parameters on time lapse resistivities produced a fit comparable to the calibration on borehole temperatures. Thus we demonstrated that time lapse geoelectrical data contain information that can constrain the optimization of ground thermal parameters. In its current setup, the coupled inversion is not sensitive enough to some of the heat model parameters of interest. We expect that using alternative heat model formulations (use of 2-phase formulation (frozen *vs.* thawed phase) or use of thermal diffusivity instead of optimizing for thermal conductivity and heat capacity separately) could improve the sensitivity of the coupled model. Also, adding constraining information to the resistivity part of the inversion is expected to improve the equivalency problem which poses a serious complication at this site. Finally, increasing model complexity by accounting for heterogeneities is expected to lead to parameter estimates that not only have good predictive value, but also reflect the true parameter values for the given site.

7.2 Directions for future work

The results of this thesis point to a number of interesting challenges that deserve further attention and study.

Geoelectrical monitoring studies in their interpretations implicitly assume that conditions of electrode grounding do not affect quality and values of the acquired data. However, we observed that real-world electrodes are practically never perfectly grounded and grounding resistances influence the actual resistivity values measured. This is of particular concern in permafrost monitoring applications where grounding resistances vary greatly between summer and winter seasons. For improved quantitative interpretation of geoelectrical monitoring data, we see the benefit of integrating the grounding resistance information into the resistivity inversion algorithms.

Our investigation site in Ilulissat has proven to be a challenge in terms of interpretation of resistivity data. Equivalency and anisotropy issues complicated the inversion and interpretation of the resistivity models. Inversion algorithms supporting anisotropic conductivities could lead to more realistic resistivity models. Constraining the resistivity inversion (also in the coupled scheme), e.g. with another type of surface geophysical data, holds promising results in terms of reducing depth and resistivity exaggeration in the inverted models.

We identified a need for better resistivity mixing models relating soil phase distribution to the effective bulk resistivity for the purpose of more precise, quantita-

tive interpretations. Deeper insight into the pore-scale processes causing resistivity hysteresis could lead to improvement of the formulation of resistivity mixing relationships.

We have previously stated that the geology in Ilulissat is complicated by presence of residual salinity in the soil profile. This has not been reflected in the present study, mainly due to simplicity of the model used, and due to limited sensitivity of freezing point depression parameter in both the heat-only and the coupled calibration schemes. Modification of the unfrozen water content relationship and the resistivity mixing rule to make the model more sensitive and account for variation in salinity would nevertheless constitute a desired improvement and extend the range of application of the method.

One of the prime advantages of geophysical methods is their ability to map larger areas at relatively low time and financial cost. Therefore extending our coupled approach to 2 dimensions would be of great practical relevance for permafrost mapping efforts and monitoring applications. It is also expected to contribute to more cost- and time-efficient delineation of zones of thaw-sensitive permafrost for geotechnical and infrastructure planning applications. Last but not least, the calibrated thermal model can contribute to evaluation of impact of future climate scenarios on thermal regime and stability of ground affected by permafrost.

APPENDIX A

Effect of electrode shape on grounding resistances, Part 1 - The Focus-One protocol

GEOPHYSICS, VOL. 81, NO. 1 (JANUARY-FEBRUARY 2016); P. WA159–WA167, 5 FIGS., 1 TABLE.
10.1190/GEO2015-0484.1

Effect of electrode shape on grounding resistances — Part 1: The focus-one protocol

Thomas Ingeman-Nielsen[1], Soňa Tomaškovičová[1], and Torleif Dahlin[2]

ABSTRACT

Electrode grounding resistance is a major factor affecting measurement quality in electric resistivity tomography (ERT) measurements for cryospheric applications. Still, little information is available on grounding resistances in the geophysical literature, mainly because it is difficult to measure. The focus-one protocol is a new method for estimating single electrode grounding resistances by measuring the resistance between a single electrode in an ERT array and all the remaining electrodes connected in parallel. For large arrays, the measured resistance is dominated by the grounding resistance of the electrode under test, the focus electrode. We have developed an equivalent circuit model formulation for the resistance measured when applying the focus-one protocol. Our model depends on the individual grounding resistances of the electrodes of the array, the mutual resistances between electrodes, and the instrument input impedance. Using analytical formulations for the potentials around prolate and oblate spheroidal electrode models (as approximations for rod and plate electrodes), we have investigated the performance and accuracy of the focus-one protocol in estimating single-electrode grounding resistances. We also found that the focus-one protocol provided accurate estimations of electrode grounding resistances to within $\pm 7\%$ for arrays of 30 electrodes or more when the ratio of instrument input impedance to the half-space resistivity was 1000 m^{-1} or more. The focus-one protocol was of high practical value in field operations because it helped to optimize array installation, electrode design, and placement. The measured grounding resistances may also be included in future inversion schemes to improve data interpretation under difficult environmental conditions such as those encountered in cryospheric applications.

INTRODUCTION

Electrode grounding resistance is a major factor affecting the measurement quality in electric resistivity tomography (ERT) measurements. This was recognized in the early development and application of the resistivity method by, e.g., Rooney and Gish (1927), who report on high grounding resistances limiting the current injection and the sensitivity of their potential galvanometer. Such issues have continued to challenge generations of geophysicists because the limitations on total transmitted current lead to lower measured potentials and lower signal-to-noise levels (Dahlin and Loke, 1998; Dabas et al., 2000; Ishikawa, 2008; Doetsch et al., 2015). In severe cases, especially when ground freezing or drying is involved, grounding resistances may be so high that the transmitter circuitry loses the ability to properly regulate the current (or transmit at all) so that valid measurements cannot be obtained (Hilbich et al., 2009; Doetsch et al., 2015; Tomaškovičová et al., 2016).

Several techniques to reduce the grounding resistance problem have been reported. Enlarging the surface area of the electrodes in contact with the soil is a common strategy. It may be achieved by inserting the rod electrodes in the ground as deep as possible (Telford et al., 1990; Zonge et al., 2005), or using other electrode geometries, such as wire meshes (Zonge et al., 2005) or plates (Doetsch et al., 2015). Multiple electrodes may also be inserted in parallel (Reynolds, 1997; Kneisel and Hauck, 2008; Zonge et al., 2005). Electrodes may be watered with fresh or saline water (Telford et al., 1990; Reynolds, 1997; Zonge et al., 2005, Rosset et al., 2013) or conductive gels may be applied (Athanasiou et al., 2007), and detergents may be added to decrease water surface tension,

Manuscript received by the Editor 11 September 2015; revised manuscript received 7 October 2015; published online 29 January 2016.
[1]Technical University of Denmark, Department of Civil Engineering, Arctic Technology Centre, Lyngby, Denmark. E-mail: tin@byg.dtu.dk; soto@byg.dtu.dk.
[2]Lund University, Engineering Geology, Lund, Sweden. E-mail: torleif.dahlin@tg.lth.se.

thereby facilitating the wetting of electrode and grain surfaces (Zonge et al., 2005). Installing electrodes in clay or mud mixed with water helps to retain moisture over the course of measurements (Reynolds, 1997; Zonge et al., 2005). Measurements on rock may be performed by placing water-soaked sponges between the rock and the electrode (Kneisel and Hauck, 2008) or using expansion bolts as electrodes in holes drilled into the rock surface (Van Schoor and Binley, 2010).

Such recommendations typically originate from practical field experiences by practitioners working hard to alleviate the grounding-resistance-related problems, based on the theoretical understanding that electrode size and interfacial resistance are important factors.

In spite of the obvious significance of the problem, very little information is available in the geophysical literature about the grounding resistance of different electrode types and shapes. Calculation of the theoretical electrode grounding resistance is possible for simple electrode shapes through analytical formulations (Sunde, 1949; Wait, 1982; Ingeman-Nielsen and Tomaškovičová, personal communication, 2015) and for more complex electrode geometries by numerical modeling (Rücker and Günther, 2011).

Sunde (1949) describes a method to derive the single electrode grounding resistance based on the pairwise differential resistance measurements of three electrodes, provided that the electrodes are so distantly spaced that mutual resistance effects between the electrodes may be neglected. Using this approach, Hessler and Franzke (1958) measure the grounding resistances of large electrodes in a permafrost-affected area, and they observe up to three orders of magnitude difference in grounding resistance between the summer (thawed) and winter (frozen) season.

However for electrode layouts with short electrode spacings, such as those typically used in near-surface investigations for environmental or geotechnical projects, this method is not applicable. In practical field applications, electrode grounding is typically tested using a pairwise electrode contact test, which indicates whether current can be transmitted using a specific pair of electrodes. It also provides a circuit resistance that is indicative of the grounding resistances of the two electrodes involved, but, in general, the true single electrode grounding resistance cannot be measured.

In this paper, we present the focus-one measurement protocol, which may be used in field experiments to provide an estimate of the single-electrode grounding resistance for individual electrodes in multielectrode arrays used for ERT measurements. We derive the mathematical formulation of an equivalent electric circuit model of the focus-one measurement and use it to model the theoretical focus-one grounding resistances of synthetic multielectrode arrays with finite electrodes of different shapes. The purpose of the modeling is to evaluate the error of the grounding resistance measured using the focus-one protocol relative to the true single electrode grounding resistance, and thus, evaluate the applicability of the protocol to estimate grounding resistances of electrodes in a field setting.

The paper is the first part of a study concerned with the impact of grounding resistances on reliability of field ERT measurements. It provides the theoretical basis for the practical experiments reported in Tomaškovičová et al. (2016), in which we compare grounding resistance measurements of different electrode designs under varying environmental conditions.

DEFINITION OF GROUNDING AND MUTUAL RESISTANCE

The grounding resistance of an electrode $R_g(\Omega)$ is the potential at the electrode surface $U(\mathrm{V})$ divided by the current injected by that electrode $I(\mathrm{A})$ (Sunde, 1949; Wait, 1982; Hördt et al. 2013) as follows:

$$R_g = \frac{U}{I}. \tag{1}$$

When multiple electrodes are in use and transmitting current, the surface potential of a particular electrode is the combined potential field at that electrode caused by current injection at each electrode. In typical four-electrode resistivity measurements, two current electrodes are used, but in fact, current may flow into or out of the ground also through the potential electrodes, due to leakage currents through the instrument receiver circuitry. Thus, in the general case of N current-carrying electrodes (where $N \geq 1$), the grounding resistance of electrode i is (Sunde, 1949) as follows:

$$R_i = \frac{\sum_{n=1}^{N} U_{i,n}}{I_i} = \frac{\sum_{n=1}^{N} I_n R_{i,n}}{I_i}, \tag{2}$$

where $R_i(\Omega)$ is the grounding resistance of electrode i, $I_i(\mathrm{A})$ is the current injected by electrode i, and $U_{i,n}(\mathrm{V})$ is the potential observed at electrode i, due to the current injected at electrode n. The value

$$R_{i,j} = \frac{U_{i,j}}{I_j}, \quad i \neq j, \tag{3}$$

is called the mutual resistance at electrode i with respect to electrode j (Sunde, 1949) and represents the potential at electrode i due to the current injected at electrode j. When $i = j$, the value is simply the grounding resistance of electrode i in the absence of any other current-carrying electrode, and it is referred to as the single-electrode grounding resistance.

COMMON MODELS OF ELECTRODE GROUNDING RESISTANCE

In standard treatment of geoelectric data, electrodes are typically considered perfectly grounded infinitesimal points. However, available in the literature are analytical solutions for the potentials around a family of spheroidal electrodes: spherical (Sunde, 1949; Wait, 1982; Lile et al., 1997; Hördt et al. 2013), prolate (Wait, 1973, 1982; Igel, 2007; Rücker and Günther, 2011), and oblate spheroidal electrodes (Ingeman-Nielsen and Tomaškovičová, personal communication, 2015). The prolate and oblate spheroidal models are ellipsoids with rotational symmetry around the major and minor axes, respectively, resulting in near-rod-shaped electrodes (prolate) and pill-shaped electrodes (oblate) (see Figure 1).

The potentials around any of the spheroidal type electrodes can be summarized in the following equation (Ingeman-Nielsen and Tomaškovičová, personal communication, 2015):

$$U(x,y,z) = \frac{\rho I}{k\pi r'},$$
$$k = \begin{cases} 2 & \text{for a homogeneous half-space} \\ 4 & \text{for a homogeneous full-space} \end{cases}, \quad (4)$$

where $\rho(\Omega\text{m})$ is the resistivity of the embedding medium and $r'(\text{m})$ is the equivalent distance. The equivalent distance is the distance from an imaginary point electrode at which the potential would be the same as at the observation point. Like theoretical point electrodes, spherical electrodes give rise to spherical isopotential surfaces. Thus, for a spherical electrode, the equivalent distance is just the distance from the center of the spherical electrode to the point of observation ($r' = r$). Prolate and oblate spheroidal electrodes give rise to prolate and oblate spheroidal isopotential surfaces (which become increasingly spherical with increasing distance from the electrode), and the equivalent distances r' for such electrodes are summarized in Table 1 according to the information from Wait (1982) and Ingeman-Nielsen and Tomaškovičová (personal communication, 2015).

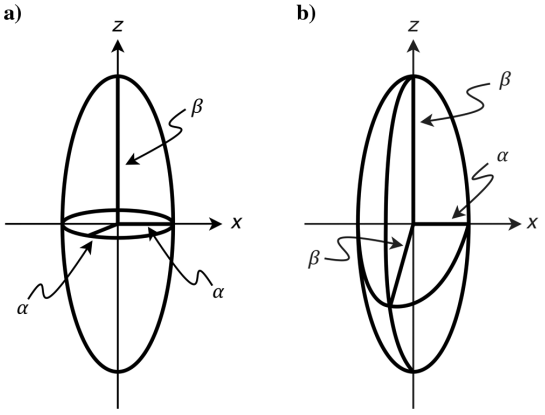

Figure 1. Illustration of the geometry of (a) prolate and (b) oblate spheroidal electrode models. They are spheroids (two axes of equal length) with rotational symmetry about the minor α and major β axis, respectively.

The surface potential of the electrode may be found by specifying the minor or major axis length of the spheroid as the x or z coordinate, taking into account the appropriate axis of rotational symmetry. For example, the spheroidal coordinate describing the surface of a prolate spheroidal electrode with rotational symmetry around the z-axis is $\eta_e = \beta/f$, where f is the semifocal distance ($f = \sqrt{\beta^2 - \alpha^2}$), β is the major axis length, and α is the minor axis length of the spheroid describing the electrode surface. Potentials for electrodes oriented with rotational symmetry around a different axis than that specified in Table 1 may be obtained by simple Cartesian coordinate transformation.

Following the derivations of Wait (1982) and Ingeman-Nielsen and Tomaškovičová (personal communication, 2015), the electrode grounding resistance of a spheroidal electrode may thus be described by the following equation:

$$R_g = R_m + R_a, \qquad R_m = \frac{\rho}{k\pi r'_e} \quad (5)$$

where r'_e is the equivalent distance from the electrode center to the surface of the electrode, also referred to as the equivalent radius of the electrode. The first term thus describes the effect of the geometry of the electrode and properties of the embedding medium $R_m(\Omega)$. The second term $R_a(\Omega)$ is an additional resistance, which may comprise an interfacial resistance component between electrode and soil, and a near-zone anomalous resistivity contribution. The value R_a may be a positive or negative term, depending on the resistivity of the anomalous zone (higher or lower than that of the embedding medium), and it may represent the change in grounding resistance from, e.g., watering of the electrode or preferential freezing or drying around the electrode. If R_a is zero, we consider the electrode to be perfectly grounded.

Mutual resistances $R_{i,j}(i \neq j)$ between spheroidal electrodes embedded in a full space may be calculated using the potential of equation 4. In this case, $r' = r'_{i,j}$ is the equivalent distance between the centers of the two electrodes $r'_{i,j}$ (Sunde, 1949), when the anomalous zones around the electrodes are small compared with the distance between them as follows:

$$R_{i,j} = \frac{U_{i,j}}{I_j} = \frac{\rho}{k\pi r'_{i,j}} \quad (6)$$

Table 1. Equivalent radius for prolate and oblate spheroidal electrodes; f is the semi focal distance $f = \sqrt{\beta^2 - \alpha^2}$, where β is the length of the major axis and α is the length of the minor axis of the electrode; i is the imaginary unit.

	Prolate spheroidal electrode	Oblate spheroidal electrode
Rotational symmetry	z-axis	x-axis
Equivalent radius	$r' = \frac{f}{Q_0(\eta)} = \frac{2f}{\ln(\frac{\eta+1}{\eta-1})}$	$r' = \frac{f}{iQ_0(i\zeta)} = \frac{2f}{i\ln(\frac{i\zeta+1}{i\zeta-1})}$
Spheroidal parameter ($y = 0$)	$\eta = \frac{\sqrt{x^2+(z+f)^2}+\sqrt{x^2+(z-f)^2}}{2f}$	$\zeta = \sqrt{\frac{\left(\sqrt{x^2+(z-f)^2}+\sqrt{x^2+(z+f)^2}\right)^2}{4f^2} - 1}$
Spheroidal parameter ($x = 0$, $y = 0$)	$\eta = \frac{z}{f}$	$\zeta = \sqrt{\frac{z}{2f^2} - 1}$
Spheroidal parameter ($z = 0$, $y = 0$)	$\eta = \sqrt{1 + \frac{x^2}{f^2}}$	$\zeta = \frac{x}{f}$

With this expression, the shape and size of the transmitting electrode j are taken into consideration, whereas the receiving electrode i is considered as an infinitesimal point. This approximation is acceptable when the distance between electrodes is large compared with their size (Ingeman-Nielsen and Tomaškovičová, personal communication, 2015).

THE FOCUS-ONE MEASUREMENT

Measuring the true single-electrode grounding resistance is not possible in practice, and only differential measurements can be performed. However, the focus-one electrode test protocol is a recent development available in commercial instruments from ABEM Instruments AB (P. Hedblom, personal communication, 2015), in which each electrode in an array is tested against all the remaining electrodes in parallel. The focus-one measurement is effectively a two-electrode measurement — current is transmitted across the same electrodes because they are used to measure the potential difference. However, the grounding resistance of half of the circuit is significantly reduced by connecting all electrodes in the array in parallel, except for the electrode under test (the focus electrode). This way, the measurement is dominated by the grounding resistance of the focus electrode. The setup is sketched in Figure 2 for an array of N electrodes with electrode n as the focus electrode. Obviously, for $N = 2$, this setup reduces to a pairwise electrode test. We present here a mathematical formulation of the circuit model of the focus-one measurement for the purpose of evaluating the focus-one resistance responses. This allows us to assert the difference between the measured focus-one resistance and the true single-electrode grounding resistance through forward modeling, while taking into account any leakage current caused by the finite internal resistance of the instrument (the input impedance).

We set up a system of linear equations to find the individual electrode currents and relevant potentials measured by the instrument. We find that, for each electrode:

$$U_i = \sum_{j=1}^{N} I_j R_{i,j} \Leftrightarrow \left(\sum_{j=1}^{N} I_j R_{i,j}\right) - U_i = 0. \tag{7}$$

For the currents passing through the electrodes and instrument internal resistance, we may write as follows:

$$I_1 + \cdots + I_{n-1} + I_{n+1} + \cdots + I_N = -I_n, \tag{8}$$

$$I = -I_n + I_v, \tag{9}$$

where $I_v(\mathrm{A})$ is the leakage current through internal resistance $R_v(\Omega)$ of the instrument. Finally, for the measured potentials:

$$I_v R_v - U_A + U_B = 0, \tag{10}$$

where $U_B(\mathrm{V})$ is the potential at the focus electrode n and U_A is the potential of the remaining $N - 1$ electrodes, assuming perfectly conducting wires connect the electrodes and instrument.

Equations 7–10 can be expressed in matrix notation as follows:

$$\begin{bmatrix}
R_{1,1} & \cdots & R_{1,n-1} & R_{1,n} & R_{1,n+1} & \cdots & R_{1,N} & 0 & -1 & 0 \\
\vdots & & \vdots & \vdots & \vdots & & \vdots & \vdots & \vdots & \vdots \\
R_{n-1,1} & \cdots & R_{n-1,n-1} & R_{n-1,n} & R_{n-1,n+1} & \cdots & R_{n-1,N} & 0 & -1 & 0 \\
R_{n,1} & \cdots & R_{n,n-1} & R_{n,n} & R_{n,n+1} & \cdots & R_{n,N} & 0 & 0 & -1 \\
R_{n+1,1} & \cdots & R_{n+1,n-1} & R_{n+1,n} & R_{n+1,n+1} & \cdots & R_{n+1,N} & 0 & -1 & 0 \\
\vdots & & \vdots & \vdots & \vdots & & \vdots & \vdots & \vdots & \vdots \\
R_{N,1} & \cdots & R_{N,n-1} & R_{N,n} & R_{N,n+1} & \cdots & R_{N,N} & 0 & -1 & 0 \\
0 & \cdots & 0 & 0 & 0 & \cdots & 0 & R_v & -1 & 1 \\
1 & \cdots & 1 & 1 & 1 & \cdots & 1 & 0 & 0 & 0 \\
1 & \cdots & 1 & 0 & 1 & \cdots & 1 & 1 & 0 & 0
\end{bmatrix}
\cdot
\begin{bmatrix}
I_1 \\ \vdots \\ I_{n-1} \\ I_n \\ I_{n+1} \\ \vdots \\ I_N \\ I_v \\ U_A \\ U_B
\end{bmatrix}
=
\begin{bmatrix}
0 \\ \vdots \\ 0 \\ 0 \\ 0 \\ \vdots \\ 0 \\ 0 \\ 0 \\ I
\end{bmatrix}. \tag{11}$$

Equation 11 is of the form $\underline{\underline{\mathbf{A}}}\mathbf{x} = \mathbf{b}$ and can be solved as $\mathbf{x} = \underline{\underline{\mathbf{A}}}^{-1}\mathbf{b}$. After solution, the solution vector $\mathbf{x}$ holds the currents transmitted by the individual electrodes I_i, the leakage current through the instrument I_v, and the two potentials U_A and U_B. The measured focus-one resistance may be calculated as follows:

$$R = \frac{U_A - U_B}{I}. \tag{12}$$

In the simplest case in which the layout consists of only two electrodes ($N = 2$), the measured resistance reduces to the simple representation as follows:

$$R = (R_{1,1} - R_{1,2} - R_{2,1} + R_{2,2}) \times \frac{R_v}{R_{1,1} - R_{1,2} - R_{2,1} + R_{2,2} + R_v}. \tag{13}$$

The first factor in equation 13 represents the ideal circuit resistance. The second term represents the effect of current leakage through the instrument, and it is equivalent to the system factor introduced by Ingeman-Nielsen and Tomaškovičová (personal communication, 2015). For identical electrodes in a homogeneous medium (half- or full-space), the mutual and grounding resistances are linearly dependent on the medium resistivity, and the system factor may be represented as follows:

$$F_s = \frac{R_v/\rho}{K + R_v/\rho}, \tag{14}$$

where K is a term that depends only on the electrode shape and layout geometry. From this formulation, we observe that the measured resistance scales with the ratio of instrument input impedance to medium resistivity R_v/ρ. Through numerical modeling of layouts with up to 1000 electrodes, we have confirmed this observation for the focus-one protocol in general.

Whenever electrodes are identical in shape and properties or distantly spaced, the reciprocity principle ($R_{i,j} = R_{j,i}$) may be applied in equations 11 and 13 to reduce the computational effort.

MODELING RESULTS

Focus-one resistance errors for perfectly grounded electrodes

The derivation has been used to investigate the theoretical errors in measured focus-one resistance relative to the true single-electrode grounding resistance for arrays with three different electrode geometries (see Figure 3): (1) prolate spheroidal electrodes ($\alpha = 0.5$ cm, $\beta = 10$ cm) inserted vertically (major axis) into a homogeneous half-space, (2) oblate spheroidal electrodes ($\alpha = 0.5$ mm, $\beta = 8$ cm) inserted vertically into a homogeneous half-space, with the minor axis oriented in the length direction of the electrode layout, and (3) buried horizontal prolate spheroidal

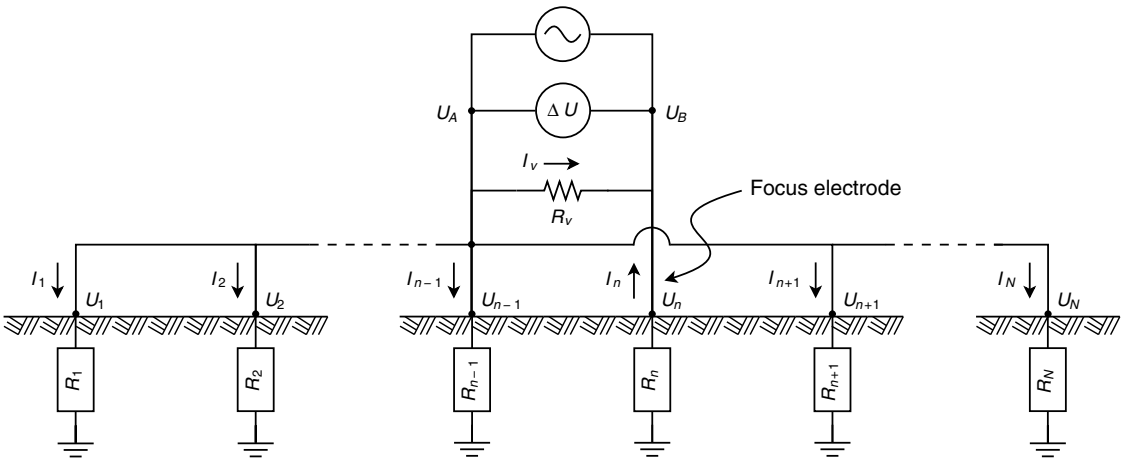

Figure 2. Equivalent circuit diagram of the focus-one measurement over an array of N electrodes with electrode n as the focus electrode. Mutual effects between electrodes are not represented.

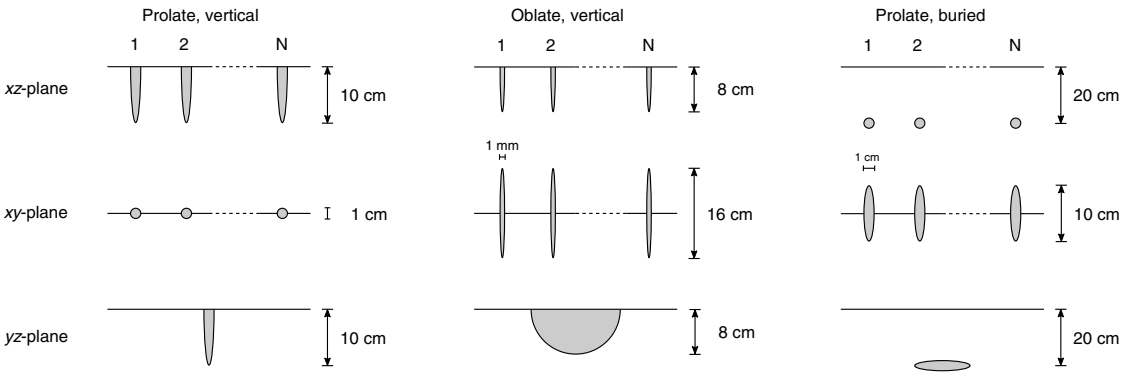

Figure 3. The electrode arrays investigated consist of N electrodes equidistantly positioned along the x-axis. Three electrode geometries are investigated: (1) vertical prolate spheroidal electrodes with the major axis in the z-direction, (2) vertical oblate spheroidal electrodes with the minor axis in the x-direction, and (3) buried prolate spheroidal electrodes with the major axis in the y-direction (perpendicular to the array direction). The figure is not to scale.

electrodes ($\alpha = 0.5$ cm, $\beta = 5$ cm) with the major axis oriented in the y-direction (perpendicular to the electrode layout) and buried at a depth of 0.2 m. In the case of buried electrodes, grounding resistances are calculated by introducing imaginary image electrodes above the ground surface (Sunde, 1949; Daniels, 1978). Modeling results are presented in Figure 4 as a function of the number of electrodes in the layout (electrode count, N) for different choices of focus electrode, electrode spacing, and R_v/ρ, whereas all electrodes are considered perfectly grounded. The calculated focus-one to single-rod resistance errors are plotted as absolute values ($|R/R_g^{N=1} - 1|$) to allow logarithmic axes.

We observe that the measured focus-one resistance is close to twice the single electrode grounding resistance when a two-electrode setup is measured, and it decreases with increasing electrode count as expected. For layouts with relatively small electrode spacing, the measured focus-one resistance actually becomes less than the single-electrode grounding resistance (the error is negative) for sufficiently large electrode counts due to the mutual resistance effects.

The error depends on the choice of focus electrode (see Figure 4a and 4b). Electrodes at the ends of the layout are less affected by mutual effects, and thus the measured focus-one resistance is less reduced for larger electrode counts. This edge effect is quickly reduced as the focus electrode is moved toward the center of the layout. This is clear from the relatively small change in error observed when comparing the center electrode with an electrode at a distance of one-tenth of the total electrode array length.

The measured error is strongly dependent on the chosen electrode separation. For large separations, the mutual effects are insignificant and the error simply decreases with the increasing electrode count. Mutual effects become increasingly important for short electrode spacings causing the sign change of the error to occur at smaller electrode counts. This effect is more pronounced for oblate than for prolate spheroidal electrodes as shown in Figure 4c and 4d.

Finally, the error depends on the ratio of instrument input impedance to half-space resistivity. For smaller ratios, the reduction in measured focus-one resistance increases, the electrode count needed to cause the sign change in the error is reduced, and the absolute value of the error at large electrode counts is increased. This effect is more pronounced for prolate than oblate spheroidal electrodes (see Figure 4e and 4f).

Although burial of the electrodes effectively reduces the theoretical single-electrode grounding resistance, the modeling showed that the change in the focus-one resistance error was minimal at less than 1% (results not shown).

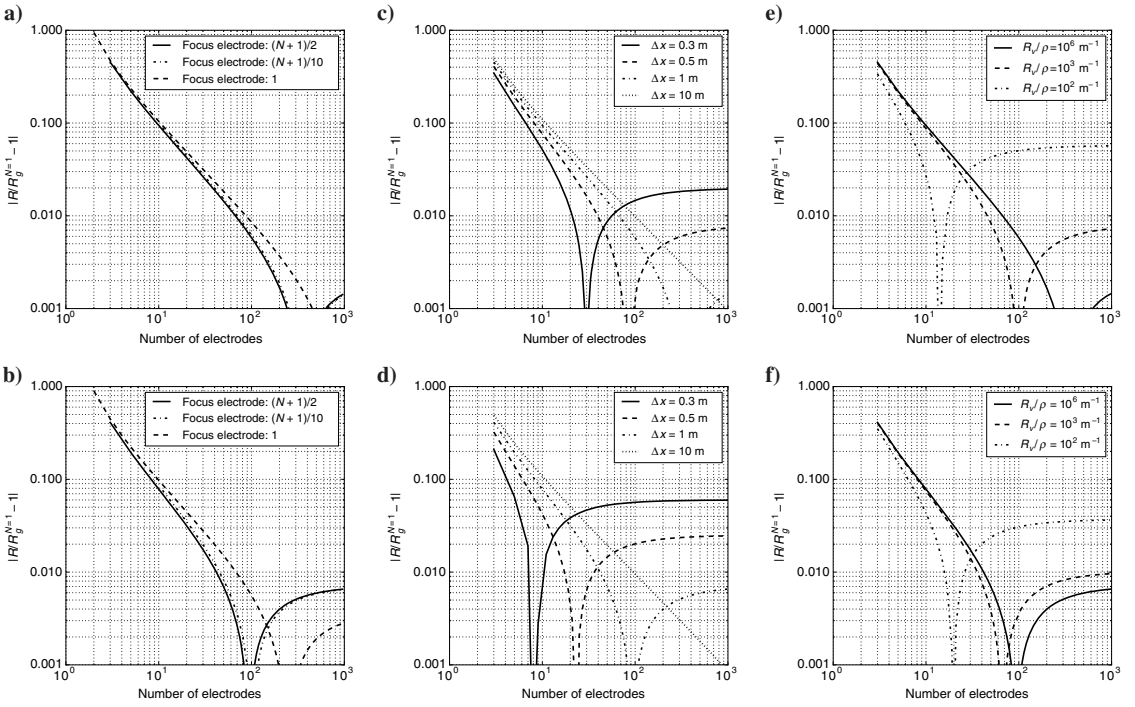

Figure 4. Absolute value of the error in measured focus-one resistance to single electrode grounding resistance for prolate ($\alpha = 0.5$ cm, $\beta = 10$ cm, plots a, c, and e) and oblate spheroidal electrodes ($\alpha = 0.5$ mm, $\beta = 8$ cm, plots b, d, and f). Plots (a and b) show errors for different choices of focus electrode using an electrode spacing of 1 m and infinite instrument input impedance. Plots (c and d) show errors for different choices of electrode spacing using a focus electrode at the center of the layout and infinite input impedance. Plots (e and f) show errors for different values of the ratio R_v/ρ, using a focus electrode at the center of the layout and an electrode spacing of 1 m. All electrodes are considered perfectly grounded. Note that the plots show the absolute value of the error, which is always positive for small electrode counts and may turn negative for large counts.

Effect of additional grounding resistance on focus-one resistance

The effect of additional grounding resistance has been studied under the assumption that the additional resistances of all electrodes in a layout are lognormally distributed with a scale e^{μ} and shape σ such that $\log_e(R_g)$ is normally distributed with mean μ and standard deviation σ.

For each choice of electrode count from 2 to 1000, we report the mean and standard deviation of 1000 repeated calculations of the focus-one resistance. These repetitions use random sampling of a specific lognormal distribution for the additional resistance of the (nonfocus) electrodes. Based on the field observations by Tomaškovičová et al. (2016), we chose three values of e^{μ} at [3, 30, and 300 kΩ] and $\sigma = 0.4$. For each distribution, we studied a focus electrode at the center of the array with additional resistance R_a equal to $e^{\mu-2\sigma}$, e^{μ}, and $e^{\mu+2\sigma}$, (see Figure 5a).

We find that when R_a is small compared with R_m (the contribution of the embedding media; see equation 5), the errors induced by the additional grounding resistance are insignificant and the total focus-one resistance error is similar to the perfectly grounded case. Because R_a is increased, the measured focus-one resistance error (mean of 1000 repeated calculations) depends mainly on the additional grounding resistance of the focus electrode. A focus electrode additional resistance of less than e^{μ} results in larger errors (fewer negative for high electrode counts), whereas a focus electrode additional resistance larger than e^{μ} results in smaller errors (more negative for high electrode counts). The variation observed due to the repeated random sampling for electrode additional resistances is larger for layouts with few electrodes and decreases with an increasing electrode count. As an example, results are shown in Figure 5b for prolate spheroidal electrodes ($\alpha = 0.5$ cm, $\beta = 10$ cm) at the surface of a homogeneous half-space of 10,000 Ωm for an instrument input impedance of 10 MΩ and an electrode spacing of 1 m.

Our complete model suite included prolate and oblate electrodes at the surface of a half-space and prolate electrodes buried at a depth of 20 cm. Electrode dimensions and geometry were the same as previously described. Electrode separations varied from 0.3 to 1 m, and the ratio R_v/ρ varied between 300 and 10^5 m^{-1}. Figure 5c shows the first and 99th percentile errors of the modeled focus-one resistances relative to the single-electrode grounding resistance for arrays with electrode counts from three to 1000 and varying values of the R_v/ρ ratio. The maximum error observed is better than ±7% across all model scenarios for arrays of 30 electrodes or more, provided R_v/ρ ratio is larger than 1000 m^{-1}. However, for longer electrode arrays (larger electrode counts), the grounding resistance is more likely to be underestimated than overestimated.

THE EFFECT OF SQUARE AND CYLINDRICAL ELECTRODES

Using prolate and oblate electrode models have allowed us to use fast and simple analytical solutions for the modeling exercises. For practical reasons in field surveys, however, the electrodes would typically be cylindrical rods or square plates rather than prolate and oblate spheroids.

To evaluate the error introduced by the spheroidal approximation, we have used COMSOL Multiphysics to produce numerical models of a square plate of similar areal extent as the oblate model in the presented modeling, and a cylindrical rod of the same length as the prolate model was used. Both were inserted vertically into a homogeneous half-space.

The square electrode modeled had dimensions of $10 \times 10 \times 0.1$ cm ($h \times w \times t$), and the surface potential was 6% lower than that of the equivalent oblate spheroidal model ($\alpha = t$ and $\beta = \sqrt{\pi \times h \times w}$), which translates directly to a 6.0% error in single electrode grounding resistance. At 0.3 m distance from the electrode surface (perpendicular to the plate surface and at the ground surface), the difference in potential was less than 0.8%.

The cylindrical rod electrode was 1 cm in diameter d, 10 cm long l, and it was conical at the lower 2 cm, which is customary for ease of installation. The surface potential was 5.7% lower than that of the equivalent prolate spheroidal model ($\alpha = d/2$ and $\beta = l$). At 0.3 m distance from the electrode surface (at the ground surface), the difference in potential was less than 0.5%.

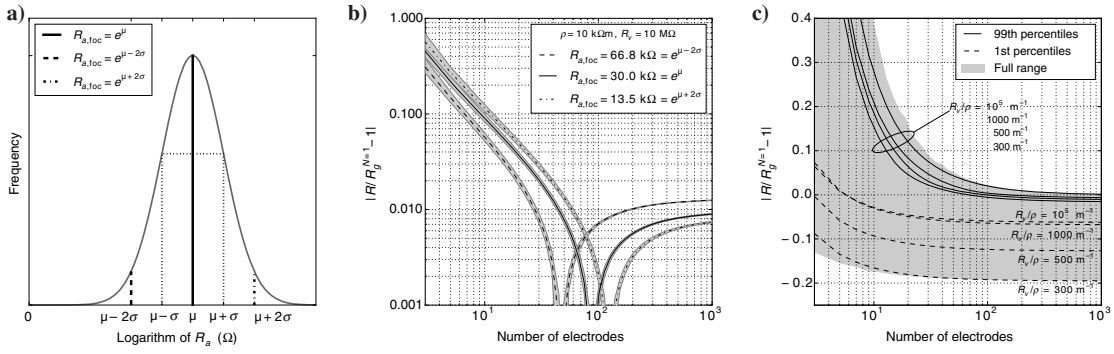

Figure 5. Examples of the error in modeled focus-one resistance relative to true single-electrode grounding resistance, when the additional grounding resistances of the layout electrodes are assumed to follow a lognormal distribution. Panel (a) shows the three choices of focus electrode additional resistance modeled for each distribution. (b) Example of model results for prolate spheroidal electrodes ($\alpha = 0.5$ cm, $\beta = 10$ cm) at the surface of a homogeneous half-space. The black lines are 50th percentiles, and the shaded areas represent the 5th to 95th percentiles of the 1000 repetitions for each array size. (c) First and 99th percentiles for different values of R_v/ρ and max and min of the full range of models, illustrating the accuracy of the focus-one measurement for arrays of different electrode counts.

The numerical model was also tested with oblate and prolate electrode models, and we found a numerical precision of $\pm 0.3\%$ of the analytically calculated potential. Furthermore, we calculated the responses of the square and cylindrical models for three different half-space resistivities and confirmed that the potential fields of these electrode shapes also depend linearly on the half-space resistivity.

The focus-one to true single-electrode grounding resistance ratio ($R/R_g^{N=1} - 1$) used to plot the modeling results in Figures 4 and 5 is slightly affected by the spheroidal assumptions. Considering the relatively severe case of arrays with electrode spacings of 0.3 m, a half-space resistivity of 10 kΩm, and an instrument input impedance of 1 MΩ ($R_v/\rho = 100$ m^{-1}), the ratios based on the oblate and square electrode models typically differ by less than ± 0.005 or 0.5% points. For layouts with very few electrodes, the differences may amount to as much as $\pm 1.5\%$ points. Based on these numerical simulations, we therefore conclude that the errors introduced by the spheroidal assumptions are so small that they have no practical significance.

THE EFFECT OF FINITE RECEIVER ELECTRODES

The present modeling considers the electrode shape and size when calculating potential fields originating from current injection of an electrode. However, in the calculation of mutual resistances, the receiver electrode is considered as a point electrode. The physical size and shape of receiver electrodes and the perturbation of the potential field caused by their presence are thus neglected. Such effects are discussed by Rücker and Günther (2011) and Ingeman-Nielsen and Tomaškovičová (personal communication, 2015), who find that the approximation is valid for electrodes that are small when compared with their separation. This condition is typically met in an array of equidistant electrodes, except possibly for neighboring electrodes. Thus, for arrays of many electrodes, we expect the effects to be insignificant. The mathematical formulation presented is general and depends on the calculated grounding and mutual resistances. These could be provided by any suitable forward modeling scheme, e.g. the numerical scheme presented by Rücker and Günther (2011), which takes the mentioned electrode effects into account at the expense of greater computational effort.

CONCLUSION

In this paper, we have presented the focus-one protocol for estimating electrode grounding resistances of multielectrode arrays used for ERT measurements. In the focus-one measurement, the resistance is measured between one single electrode (the focus electrode) and all the remaining electrodes connected in parallel. In this way, the measured resistance is dominated by, and thus, provides an estimate of the grounding resistance of the focus electrode.

We have presented a general mathematical formulation of the measured circuit resistance, taking into account the instrument input impedance and mutual effects between the electrodes of the array. Based on this formulation, the performance of the focus-one protocol was investigated using prolate and oblate spheroidal models as approximations for rod and plate electrodes inserted vertically at the surface of a homogeneous half-space.

We found that the deviations of the measured focus-one resistance compared with the true single electrode grounding resistance may be positive and negative; i.e., the focus-one resistance may be larger or smaller than the true single electrode grounding resistance, depending mainly on the mutual effects between electrodes. The largest absolute deviations occur for low electrode separations, low ratio of instrument input impedance to half-space resistivity (R_v/ρ), and high-focus electrode grounding resistance. However, for $R_v/\rho \geq 1000$ m^{-1}, the focus-one measurement typically provides an accurate estimate of the true single-electrode grounding resistance to within $\pm 7\%$ for arrays of 30 electrodes or more.

We attribute the focus-one protocol great practical relevance as a fast method to evaluate electrode grounding resistances in field operations and a tool to optimize array installation, electrode design, and eventually the quality of the collected data. We also foresee the use of focus-one resistances in future inversion schemes that may take instrument input impedance and electrode grounding resistances into account as a tool to improve inversion quality under difficult environmental conditions, such as those encountered in cryospheric applications.

ACKNOWLEDGMENTS

The focus-one protocol discussed in this paper was invented by P. Hedblom of ABEM Instruments AB. We wish to thank him for fruitful discussions about the implementation of the protocol in their current instrumentation.

REFERENCES

Athanasiou, E. N., P. I. Tsourlos, G. N. Vargemezis, C. B. Papazachos, and G. N. Tsokas, 2007, Non-destructive DC resistivity surveying using flat-base electrodes: Near Surface Geophysics, **5**, 263–272, doi: 10.3997/1873-0604.2007008.

Dabas, M., A. Hesse, and J. Tabbagh, 2000, Experimental resistivity survey at Wroxeter archaeological site with a fast and light recording device: Archaeological Prospection, **7**, 107–118, doi: 10.1002/1099-0763(200006)7:2<107::AID-ARP138>3.3.CO;2-S.

Dahlin, T., and M. H. Loke, 1998, Resolution of 2D Wenner resistivity imaging as assessed by numerical modelling: Journal of Applied Geophysics, **38**, 237–249, doi: 10.1016/S0926-9851(97)00030-X.

Daniels, J. J., 1978, Interpretation of buried electrode resistivity data using a layered earth model: Geophysics, **43**, 988–1001, doi: 10.1190/1.1440878.

Doetsch, J., T. Ingeman-Nielsen, A. V. Christiansen, G. Fiandaca, E. Auken, and B. Elberling, 2015, Direct current (DC) resistivity and induced polarization (IP) monitoring of active layer dynamics at high temporal resolution: Cold Regions Science and Technology, **119**, 16–28, doi: 10.1016/j.coldregions.2015.07.002.

Hessler, V. P., and A. R. Franzke, 1958, Earth-potential electrodes in permafrost and tundra: Arctic, **11**, 211–217, doi: 10.14430/arctic3746.

Hilbich, C., L. Marescot, C. Hauck, M. H. Loke, and R. Mäusbacher, 2009, Applicability of electrical resistivity tomography monitoring to coarse blocky and ice-rich permafrost landforms: Permafrost and Periglacial Processes, **20**, 269–284, doi: 10.1002/ppp.v20:3.

Hördt, A., P. Weidelt, and A. Przyklenk, 2013, Contact impedance of grounded and capacitive electrodes: Geophysical Journal International, **193**, 187–196, doi: 10.1093/gji/ggs091.

Igel, J., 2007, On the small-scale variability of electrical soil properties and its influence on geophysical measurements: Ph.D. dissertation, University of Frankfurt/Main.

Ishikawa, M., 2008, ERT imaging for frozen ground detection, *in* C. Hauck, and C. Kneisel, eds., Applied geophysics in periglacial environments: Cambridge University Press, 109–117.

Kneisel, C., and C. Hauck, 2008, Electrical methods, *in* C. Hauck, and C. Kneisel, eds., Applied geophysics in periglacial environments: Cambridge University Press, 3–27.

Lile, O. B., M. Morris, and J. S. Rønning, 1997, Estimating groundwater flow velocity from changes in contact resistance during a saltwater tracer experiment: Journal of Applied Geophysics, **38**, 105–114, doi: 10.1016/S0926-9851(97)00018-9.

Reynolds, J. M., 1997, An introduction to applied and environmental geophysics: Wiley.

Rooney, W. J., and O. H. Gish, 1927, Results of earth-resistivity surveys near Watheroo, Western Australia, and at Ebro, Spain: Terrestrial Magnetism and Atmospheric Electricity, **32**, 49–63, doi: 10.1029/TE032i002p00049.

Rosset, E., C. Hilbich, S. Schneider, and C. Hauck, 2013, Automatic filtering of ERT monitoring data in mountain permafrost: Near Surface Geophysics, **11**, 423–433, doi: 10.3997/1873-0604.2013003.
Rücker, C., and T. Günther, 2011, The simulation of finite ERT electrodes using the complete electrode model: Geophysics, **76**, no. 4, F227–F238, doi: 10.1190/1.3581356.
Sunde, E. D., 1949, Earth conduction effects in transmission systems: Dover Van Nostrand Company Inc.
Telford, W. M., L. P. Geldart, and R. E. Sheriff, 1990, Applied geophysics: Syndicate of the University of Cambridge.
Tomaškovičová, S., T. Ingeman-Nielsen, A. V. Christiansen, I. Brandt, T. Dahlin, and B. Elberling, 2016, Effect of electrode shape on grounding resistances. Part 1: Experimental results and cryospheric monitoring: Geophysics, **81**, this issue, doi: 10.1190/GEO2015-0148.1.
Van Schoor, M., and A. Binley, 2010, In-mine (tunnel-to-tunnel) electrical resistance tomography in South African platinum mines: Near Surface Geophysics, **8**, 563–574, doi: 10.3997/1873-0604.2010021.
Wait, J. R., 1973, Resistance of earth electrodes: Electronics Letters, **9**, 90–91, doi: 10.1049/el:19730068.
Wait, J. R., 1982, Geo-electromagnetism: Academic Press.
Zonge, K., J. Wynn, and S. Urquhart, 2005, Resistivity, induced polarization and complex resistivity, *in* D. K. Butler, ed., Near-surface geophysics: SEG, 265–300.

APPENDIX B

Effect of electrode shape on grounding resistances, Part 2 - Experimental results and cryospheric monitoring

GEOPHYSICS, VOL. 81, NO. 1 (JANUARY-FEBRUARY 2016); P. WA169–WA182, 10 FIGS., 4 TABLES.
10.1190/GEO2015-0148.1

Effect of electrode shape on grounding resistances — Part 2: Experimental results and cryospheric monitoring

Soňa Tomaškovičová[1], Thomas Ingeman-Nielsen[1], Anders V. Christiansen[2], Inooraq Brandt[3], Torleif Dahlin[4], and Bo Elberling[5]

ABSTRACT

Although electric resistivity tomography (ERT) is now regarded as a standard tool in permafrost monitoring, high grounding resistances continue to limit the acquisition of time series over complete freeze-thaw cycles. In an attempt to alleviate the grounding resistance problem, we have tested three electrode designs featuring increasing sizes and surface area, in the laboratory and at three different field sites in Greenland. Grounding resistance measurements showed that changing the electrode shape (using plates instead of rods) reduced the grounding resistances at all sites by 28%–69% during unfrozen and frozen ground conditions. Using meshes instead of plates (the same rectangular shape and a larger effective surface area) further improved the grounding resistances by 29%–37% in winter. Replacement of rod electrodes of one entire permanent permafrost monitoring array by meshes resulted in an immediate reduction of the average grounding resistance by 73% from 1.5 to 0.4 kΩ (unfrozen conditions); in addition, the length of the acquisition period during the winter season was markedly prolonged. Grounding resistance time series from the three ERT monitoring stations in Greenland showed that the electrodes were rarely perfectly grounded and that grounding resistances exceeding 1 MΩ may occur in severe cases. We concluded that the temperature, electrode shape, and lithology at the sites have a marked impact on electrode performance. Choosing an optimized electrode design may be the deciding factor for successful data acquisition, and should therefore be considered when planning a long-term monitoring project.

INTRODUCTION

The problem of obtaining good ground contact is well-known to most practicing field geophysicists working with electric resistivity tomography (ERT). Because field transmitters are capable of supplying certain maximum potential difference to drive the current, the electrode grounding resistance may become the limiting factor of successful ERT surveys. However, stepping down to transmission of lower currents negatively affects the signal-to-noise ratio (S/N), with implications for data quality. Several authors have argued that high grounding resistances reduced the quality of measurements (Dabas et al., 2000; Baines et al., 2002; Lundström et al., 2009; Hilbich et al., 2011; Rosset et al., 2013) using it as an indicator of data quality in some cases (Branco et al., 2013).

ERT is particularly suitable for monitoring applications due to its repeatability, relative speed of acquisition, and comparatively ease of data processing. It has become a standard tool in frozen ground research, thanks to its multiple advantages over conventional permafrost monitoring approaches (Scott et al., 1990; Vonder Mühll et al., 2001; Hauck and Vonder Mühll, 2003; Kneisel and Hauck, 2008; Hilbich et al., 2011). It is relatively cost efficient and logistically more convenient than drilling. It has the advantage of providing 2D or 3D spatial variability, as opposed to 1D information inferred from temperature boreholes. It can be operated in auto-

Manuscript received by the Editor 6 March 2015; revised manuscript received 11 September 2015; published online 12 January 2016.
[1]Technical University of Denmark, Department of Civil Engineering, Arctic Technology Centre, Lyngby, Denmark. E-mail: soto@byg.dtu.dk; tin@byg.dtu.dk.
[2]Aarhus University, Department of Geoscience, Aarhus, Denmark. E-mail: anders.vest@geo.au.dk.
[3]Orbicon Greenland, Nuuk, Greenland. E-mail: inbr@orbicon.gl.
[4]Lund University, Engineering Geology, Lund, Sweden. E-mail: torleif.dahlin@tg.lth.se.
[5]University of Copenhagen, Department of Geosciences and Natural Resource Management, Center for Permafrost (CENPERM), Copenhagen, Denmark. E-mail: be@ign.ku.dk.

mated mode, which makes it relevant in remote and inaccessible areas as in the Arctic. Not least, its high sensitivity to phase change between water and ice makes it capable of distinguishing unfrozen water content at subzero temperatures. This implies that time-lapse ERT is capable of detecting ground thawing far before any temperature logs can do so, particularly in warm permafrost near 0°C (Kneisel, 2006; Hilbich et al., 2011). This makes ERT monitoring a valuable tool in assessing the effect of climate warming on the distribution of soil unfrozen water in cold regions.

However, in monitoring applications, the requirements on data quality are high because relative changes of ground resistivity should reflect environmental processes of interest, rather than noise resulting from, among other factors, changing grounding resistances. And yet, extremely high grounding resistances encountered over the freezing periods not only substantially compromise the data quality, but more often than not, they limit the possibility of data acquisition to summer months. Consequently, comparison of temporally sparse ERT data with long-term climate records becomes a challenging task (Hilbich et al., 2011).

In ERT surveying, a few techniques to alleviate the grounding resistance problem have been proposed. Enlarging the surface area of the electrodes in contact with the soil is a common strategy. This can be achieved by inserting the electrodes in the ground as deep as possible (Telford et al., 1990; Zonge et al., 2005), or inserting multiple electrodes in parallel (Reynolds, 1997; Zonge et al., 2005; Kneisel and Hauck, 2008; Rosset et al., 2013). For the purpose of facilitating the current flow from the electrode to the ground, electrodes may be watered with fresh or saline water (Telford et al., 1990; Reynolds, 1997; Zonge et al., 2005) or a conductive gel may be applied (Athanasiou et al., 2007). In arid regions, adding detergents helps to decrease the water surface tension thus improving the wetting of electrode and grain surfaces (Zonge et al., 2005). Measurements on rock may be facilitated by placing water-soaked sponges between the rock and the electrode (Kneisel and Hauck, 2008). Installing the electrodes in clay or mud mixed with water helps to retain moisture over the course of the measurements (Reynolds, 1997; Zonge et al., 2005).

Nonetheless, in automated ERT monitoring, it is mostly too labor intensive, if not impossible, to check and adjust the electrode contact before every measurement launch. Not least, because monitoring projects often span several seasons, the quality of electrode grounding will necessarily vary as result of changing environmental conditions in the ground. Consequently, an array that performs very well in the summer/humid season might become impossible to measure in the winter/dry season. This is particularly the case in cryospheric applications, in which the ERT method typically suffers from high grounding resistances for substantial portions of the year. These limitations require the foreseeable issues to be addressed during the design phase of a monitoring project. As pointed out by LaBrecque and Daily (2008), electrodes are a primary source of errors in resistivity measurement systems. Thus, optimization of electrode design is an essential part of such preparations.

The aim of this study is to improve our understanding of properties and processes affecting the grounding resistance of real electrodes and provide quantitative information on the range of grounding resistances that may occur during ERT monitoring in permafrost areas and other cryospheric applications. We present results of field and laboratory experiments documenting the performance of three electrode types of different size, shape, and surface area under various ground temperature conditions at three field sites of different lithology. We also provide grounding resistance time series measured at three active or past monitoring stations in Greenland, and we attempt to separate the contributions of different processes to the observed grounding resistances.

This is the second of two papers describing our study of electrode grounding resistances. The first paper presents the theoretical basis of the study and the focus-one protocol used for measuring grounding resistances of ERT array electrodes (Ingeman-Nielsen et al., 2016).

Definition of grounding resistance

The grounding resistance R_g (Ω) of an electrode is defined as the potential U (V) at the electrode surface (relative to zero potential at infinite distance) divided by the current I (A) injected by the electrode into the medium in which it is embedded (Sunde, 1949; Wait, 1982; Hördt et al., 2013):

$$R_g = \frac{U}{I}. \tag{1}$$

T. Ingeman-Nielsen and S. Tomaškovičová (personal communication, 2015) and Ingeman-Nielsen et al. (2016) present a framework for calculating the theoretical grounding resistance for rod and plate electrodes. According to their derivations, the grounding resistance of an electrode may be represented as follows:

$$R_g = R_m + R_a, \tag{2}$$

where R_m (Ω) represents the effect of the geometry of the electrode and properties of the embedding medium (the ground resistivity). The second term R_a (Ω) is an additional resistance, which may comprise an interfacial resistance component at the electrode-soil interface and a near-zone anomalous resistivity contribution. The anomalous zone is linked to the disturbance created by the planting and treatment (e.g., watering) of the electrode and possible interaction, such as preferential drying or freezing around the electrode. The additional resistance R_a may be positive or negative depending on the resistivity of the anomalous zone and magnitude of the interfacial component (always positive). If R_a is zero, we consider the electrode *perfectly grounded*.

In practical field applications, measuring the single-electrode grounding resistance is not possible because only differential measurements can be performed. However, the focus-one protocol (Ingeman-Nielsen et al., 2016) provides a convenient way to approximate the grounding resistance of each electrode in a multi-electrode array. The focus-one protocol consists of a sequence of measurements, in which the resistance of each electrode is measured in turn against all the remaining electrodes in parallel. It is essentially a "two-electrode" measurement, transmitting current and measuring the potential difference on the same set of electrodes. However, the grounding resistance of one side of the circuit is effectively reduced by connecting many electrodes in parallel, and the measured circuit resistance therefore approximates the single-electrode resistance of the *focus electrode*. Through numerical modeling, Ingeman-Nielsen et al. (2016) show that the measured focus-one resistances are typically within ±7% (or better) of the true single rod grounding resistances for arrays of more than 30 electrodes,

provided that the internal resistance of the instrument is on the order of 10 MΩ or higher.

MATERIALS AND METHODS

With our focus on electrodes as an important source of error, we studied improvements that can be achieved under various ground conditions by using alternative electrode designs. Three types of data are evaluated in this study as follows:

1) Temperature-controlled laboratory experiment: A feasibility study focused on temperature influence on grounding resistances of four electrode configurations.
2) Field comparison of electrode types: Three test sites of different lithology were equipped, each with short arrays of three different electrode designs, and grounding resistances was measured across seasons.
3) Authentic field monitoring applications: Changes of grounding resistance have been monitored at three semipermanent ERT monitoring sites, each equipped with electrodes of a different design. The performance of the arrays is assessed by comparing the grounding resistances and the length of the measurements season. Grounding resistance changes due to the use of two alternative electrode designs are quantified at one of the sites.

Throughout the paper, measurement results are represented as mean ± standard deviation whenever relevant and when multiple measurements or repetitions are available.

Electrodes

The electrode designs chosen for testing were short-rod electrodes, square-plate electrodes, and square-mesh electrodes (see Figure 1). The electrodes were chosen to allow a study of the effect of shape and size (comparing rods and plates) and the effect of increasing surface area of similarly shaped electrodes (comparing plates and meshes). All electrodes were made of stainless steel to reduce the influence of material properties, and their dimensions and properties are listed in Table 1. The mesh electrodes were composed of four layers of stainless steel wire mesh with a thread diameter of 1 mm and a mesh density of 3.86 per centimeter. All electrodes were connected to the measurement instrumentation by copper wire attached to the electrodes with nuts and bolts, as visible in detail in Figure 1c.

Temperature-controlled laboratory experiment

In an attempt to separate temperature effects (ground freezing/thawing) on grounding resistances from other environmental factors, we conducted a laboratory experiment in a temperature-controlled climate chamber, measuring the resistance of individual electrodes in small buckets at different temperatures.

Thirty-two plastic buckets (diameter: 26.9 cm [top]/23 cm [bottom] and height 23.6 cm) were lined with aluminum foil and filled with a silty clay material from Kangerlussuaq, west Greenland. The silty clay material was thoroughly homogenized in a large industrial mixer, whereas distilled water was added to make up for moisture loss during storage. Approximately 8 kg of the silty clay was placed in each bucket. The final gravimetric water content was measured by oven drying of three samples from each bucket. The gravimetric water content in all the buckets varied in a range between 37.6% and 43.4% with a mean and standard deviation of 40.1 ± 1.5%.

The buckets were arranged in four rows and eight columns. The first row contained eight horizontally oriented rod electrodes, the second row contained vertically oriented plate electrodes, the third

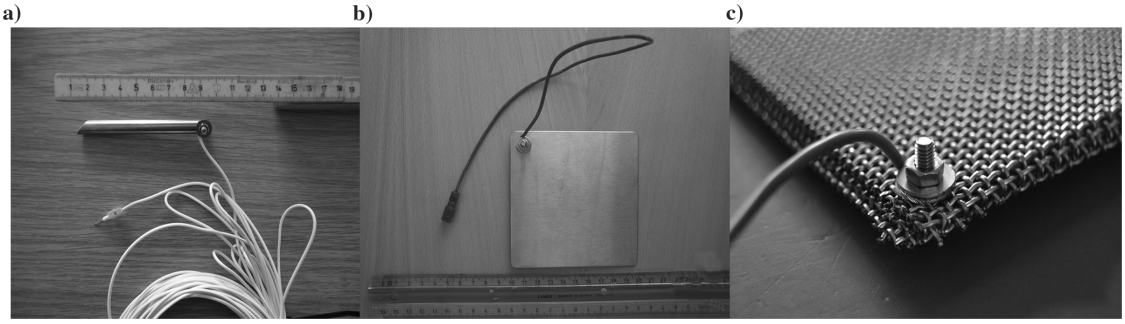

Figure 1. Electrode designs tested: (a) rod electrode with attached copper cable, (b) plate electrode, and (c) mesh electrode.

Table 1. Properties of the physical electrodes used in field and laboratory testing.

	Rods	Plates	Meshes
Dimensions	$\phi = 1.0$ cm, $L = 8.0$ cm	$10 \times 10 \times 0.1$ cm ($h \times w \times t$)	$10 \times 10 \times 0.6$ cm ($h \times w \times t$)
Estimated effective surface area	27 cm^2	204 cm^2	985 cm^2
Material	Stainless steel	Stainless steel	Stainless steel

row contained horizontally oriented plate electrodes (Figure 2b), and the fourth row contained vertically placed mesh electrodes. The total height of the clay mixture in each bucket was approximately 15 cm. The vertically placed electrodes were covered by 1 cm, and the horizontally placed ones by 5 cm of clay mixture. To take full advantage of the large effective surface area of the mesh electrodes, the mesh openings were filled with the clay mixture before installation.

Insulated copper wires were attached to each electrode with a nut and bolt, and, similarly, wires were attached to the aluminum foil lining of each bucket. During measurements, the wires from a specific electrode and the aluminum-foil lining of the corresponding bucket were connected to the two terminals of the instrument and used for simultaneous current injection and potential measurement. The lining thus functioned as a very large electrode ensuring that the resistance between the two terminals of the instrument was primarily controlled by the properties of the single rod, plate, or mesh electrode installed in the bucket.

A thermistor was placed in the first bucket of each row to measure the temperature of the soil in the bucket. Finally, a lid was placed on each bucket to reduce moisture loss during the experiment.

The buckets were placed on Styrofoam pads, and isolating material was placed around and between the buckets to encourage a one-sided freezing pattern (Figure 2a). The buckets were placed in a climate chamber in which they rested for 24 h before the testing began. In the following days, three sets of measurements were performed at -1.4 ± 0.3°C, -14.3 ± 0.6°C, and finally at 19.9 ± 0.8°C. A resting period of 24 h after each temperature step allowed the temperature within the buckets to stabilize.

We measured the total circuit resistance of each bucket using an ABEM Terrameter SAS 1000, using a current of 1 mA with a 100% duty cycle square waveform and a period of 1 s. Voltage measurements were acquired over the last 0.3 s of each on time, and results of five periods were averaged. The results of this experiment are reported in the "Results: Temperature-controlled laboratory experiment" subsection.

Description of selected field sites

Three sites in central west Greenland were selected for testing of the electrode designs under realistic field conditions. The sites were selected based on the availability of current or past ERT time-lapse monitoring data.

The Qeqertarsuaq site (69° 15′N, 53° 30′W, 30 m above sea level) is located at Østerlien, near the Arctic Station on Qeqertarsuaq/Disko Island in a tundra landscape/environment. Disko Island is located in the transitional zone between the Low and High Arctic. According to meteorologic data of nearby Arctic Station (Hansen et al., 2006), mean air temperatures of the warmest (July) and the coldest (February to March) months are 7.1°C and −16.0°C, respectively. The mean annual soil temperature at 5 cm depth is −1.9°C. Accordingly, the site is located in the discontinuous permafrost zone, and no permafrost was observed from ground temperature measurements at the actual site location to a depth of 3.5 m. The study site is situated in a bedrock valley filled with loose Holocene sands and gravels with a typical topsoil thickness of 5–10 cm. The crystalline basement (granite) and Tertiary breccia plateau basalts are visible in outcrops around the area. Among other important environmental parameters, air and soil temperature and soil moisture content are recorded at the site.

The Ilulissat site (69° 14′N, 51° 3′W, 33 m above sea level) is situated near the airport of the town of Ilulissat on the mainland in the inner part of the Disko Bay. The site is located in the continuous permafrost zone (Brown et al., 1998), and the mean annual air temperature (MAAT) is −5.1°C (2003–2012, data from Cappelen, 2013, Danish Meteorological Institute, tech. rept. 3-11). The active layer thickness at the site is approximately 80 cm, below which ice-rich permafrost is found. The sediment cover consists of postglacial silt and clay marine deposits. These deposits are fully leached in the upper part, with the residual salinity increasing with depth, causing the deeper parts of the soil profile to be technically unfrozen due to the freezing point depression. Gneiss bedrock is encountered at the site at a 7 m depth. Unfrozen soil water content in the active layer in the thawed period ranges from 60% to 70% at nearly full saturation.

The Sisimiut site (66° 56′N, 53° 36′W, approximately 48 m above sea level) is located in a valley east of the town of Sisimiut. The area is affected by discontinuous permafrost (Brown et al., 1998) with an MAAT of −1.1°C (2003–2012, data from Cappelen, 2013, Danish Meteorological Institute, tech. rept. 3-11). The top part of the sedimentary sequence is dominated by sandy freshwater deposits underlain by postglacial marine clayey silt deposits (Ingeman-Nielsen, 2005). The topsoil thickness is typically less than 5 cm. The area is shaded by a large mountain ridge to the south, causing the site location to be expectedly colder than the meteorologic data from the town station indicates (located near the coast a few kilometers from the site). The active-layer thickness is approximately 1.0 m at the site, which is well-drained and slightly elevated, causing little snow to accumulate in winter. However, the active-layer thickness varies in the immediate surroundings, depending on peat and topsoil thicknesses, lithology, and drainage conditions, which all show considerable variability.

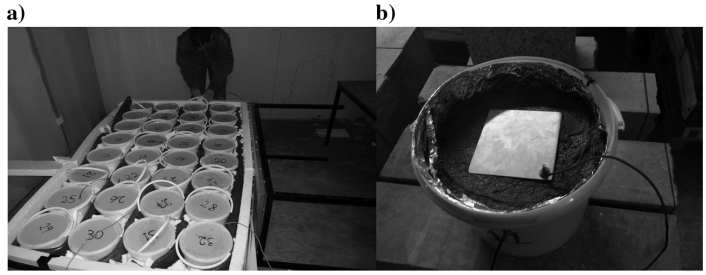

Figure 2. Temperature-controlled laboratory experiment setup: (a) arrangement of 32 buckets with test electrodes in a cold chamber and (b) placement of the horizontal plate electrode in an aluminum-foil-lined plastic bucket filled with the clay mixture and covered by 5 cm of clay material.

Electrode field experiment setup and measurement procedure

Experimental test sites were established at each of the three monitoring field sites for testing the three different electrode designs under different soil conditions. At each site, three arrays of 10 mesh electrodes, 10 plate electrodes, and 10 rod electrodes were installed. Mesh and plate electrodes were installed vertically in the ground so that the plane defined by the electrode is perpendicular to an imaginary line connecting the centers of all electrodes of that type. If the nature of the soil allowed, the mesh openings of the mesh electrodes were filled with local material (Figure 3c). Rod electrodes were installed with the rod length axis in the horizontal direction and perpendicular to an imaginary line connecting the rod electrodes. All electrodes of the same kind were spaced 30 cm apart; the arrays of respective electrode types were likewise spaced 30 cm apart. If the center of the first mesh electrode was at (0.0, 0.0) m, the center of the last rod electrode thus was at (2.70, 0.60) m (Figure 3a).

The electrodes were buried at a depth of 5–10 cm, depending on the conditions of the field site, to protect them from damage and removal by animals, and for ensuring installation in actual soil (and not debris and mosses at the surface).

Grounding resistances of the electrodes at all three sites were measured in summer, fall, and winter 2013/2014. The individual electrode grounding resistances were measured using the focus-one protocol for each of the three arrays in turn, using an ABEM Terrameter SAS 1000 or an ABEM Terrameter LS, depending on availability. The current during grounding resistance measurements was fixed at 1 mA, using a 100% duty cycle square waveform with a period of 1 s. Voltage measurements were acquired over the last 0.3 s of each on time, and the results of five periods were averaged. The results of these experiments are reported in the "Results: Electrode field experiment" subsection.

Long-term monitoring arrays

At the Qeqertarsuaq site, the ERT monitoring station was set up in July 2013 and scheduled to collect several resistivity profiles a day throughout the freezing season until the end of February 2014 (Doetsch et al., 2015). The monitoring was carried out on two parallel lines (2 m apart) with 64 electrodes each (although Doetsch et al. [2015] report data from only one of the two lines), electrode spacing 0.5 m for the 42 electrodes at the center of each line, and 2 m spacing for the electrodes at the ends of the layouts. The arrays were installed using stainless steel plate electrodes with dimensions of $10 \times 10 \times 0.6$ cm, buried at a 5–10-cm depth. The site was instrumented with an ABEM Terrameter LS and an external switchbox ABEM ES10-64 and connected to the Internet for remote control, data download, and monitoring of system conditions. The automated data acquisition program was initially set to collect 7359 resistivity measurements per day using all 128 electrodes, but the sequence had to be reduced after ground freezing commenced due to problems of increasing grounding resistance. After the reduction, 1464 measurements were collected per day using only one array, and 0.5 m spaced electrodes. The grounding resistances of all electrodes were measured daily using the focus-one protocol throughout the entire acquisition period.

The monitoring station at Ilulissat was set up in August 2012 and comprised an array of 64 electrodes with uniform spacing of 0.5 m. The station was equipped with an ABEM Terrameter SAS 1000 and an external switchbox ABEM ES10-64, and it was scheduled to measure 1625 resistivity measurements once a day. Initially, the station was operating in time-lapse mode with no possibility of remote control. Due to instrument limitations, repeated electrode grounding measurements could not be scheduled in the time-lapse mode, and thus they were only collected upon site visits. In February 2014, the station was upgraded for remote control and data transmission. This upgrade also allowed daily measurements of electrode grounding

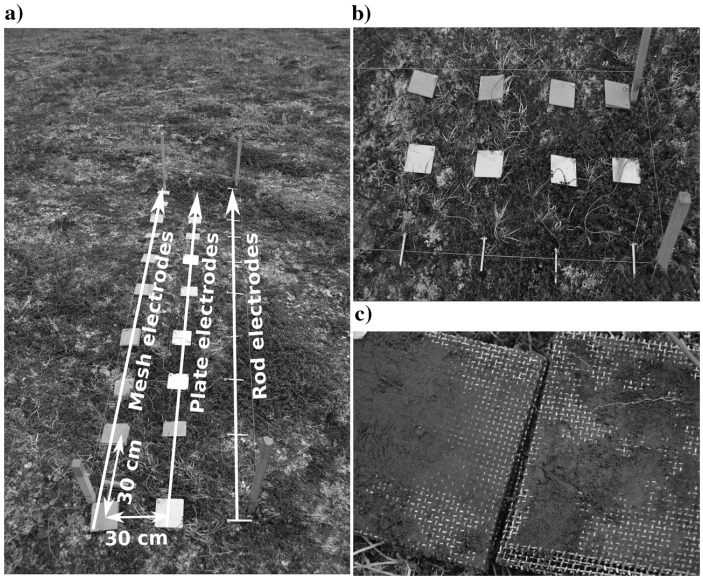

Figure 3. (a) Layout of the electrode field test site indicating electrodes placement and spacing between electrodes, (b) detail of the electrode arrangement, and (c) mesh openings were filled with local soil to take advantage of the increased surface area.

resistance using the focus-one protocol. Initially, the station was equipped with stainless steel rod electrodes (length 8 cm and diameter 1 cm). However, after encountering contact problems relating to ground freezing in late December 2012, all electrodes were replaced by mesh electrodes with dimensions $10 \times 10 \times 0.6$ cm in August 2013.

At Sisimiut, the monitoring array was installed in July 2010. It comprised an array of 64 electrodes with uniform spacing of 0.5 m. The electrodes were stainless steel rods (length 10 cm and diameter 1 cm) buried at a depth of 5–10 cm, oriented horizontally, and with the long axis perpendicular to the array. The array was measured using an ABEM Terrameter LS (using the internal 64-electrode switchbox), but because the site had no power-line access, measurements were initiated manually at irregular intervals. Over the fall, the array was measured several times per week, whereas in the winter months of 2010/2011, intervals increased to monthly or bimonthly. Typically protocols of approximately 2000 resistivity measurements were used, but in winter, electrodes were affected by high grounding resistances, significantly reducing the number of measurements (unique four-electrode combinations) that could actually be collected. Electrode grounding resistance measurements were collected using the focus-one protocol before each data acquisition, and they are thus available at the same temporal intervals. The results of these monitoring experiments are reported in the "Results: Monitoring applications" subsection.

RESULTS

Temperature-controlled laboratory experiment

The results of the temperature-controlled laboratory experiments are summarized in Table 2 and visualized with box plots in Figure 4. A pronounced increase in the total circuit resistance is observed due to freezing. The change is approximately two orders of magnitude between the warmest (+19.9°C) and coldest (−14.3°C) temperatures. At all three temperatures tested, the choice of electrode seems to affect the total circuit resistance, with rods performing the worst (largest resistances and variance); followed by horizontal plates; vertical plates; and finally meshes, which exhibit the lowest measured circuit resistances among all electrodes. The mesh electrodes also exhibit the lowest variation in circuit resistance at all temperatures, although the variation is larger at subzero temperatures for all types of electrodes.

To test the significance of these observations, we have applied a two-way analysis of variance (ANOVA) to the data (Montgomery, 1997), treating the electrode types and temperatures as categorical factors and assuming a log-normal distribution of resistances. We conclude that the main effects of the electrode type and temperature are statistically significant and that there is also significant interaction between electrode type and temperature. On this basis, we applied Tukey's range test (Tukey, 1949) to compare the means of the effects of electrode type at each temperature. The means are all

Table 2. Averages (arithmetic) and standard deviations of total circuit resistances measured in the laboratory experiment at three different temperatures on three electrode types (four configurations), along with the number of involved measurements. Here, *N* refers to the number of electrodes (buckets) that were included in averaging; H and V signify a horizontal and vertical orientation of the plates, respectively.

Temperature	Rods (kΩ)		Plates H (kΩ)		Plates V (kΩ)		Meshes (kΩ)	
$+19.9 \pm 0.8$°C	0.3 ± 0.04	($N = 6$)	0.1 ± 0.01	($N = 5$)	0.1 ± 0.01	($N = 6$)	0.1 ± 0.01	($N = 6$)
-1.4 ± 0.3°C	1.8 ± 0.7	($N = 8$)	1.2 ± 0.2	($N = 7$)	1.0 ± 0.4	($N = 8$)	0.6 ± 0.1	($N = 8$)
-14.3 ± 0.6°C	23.3 ± 7.5	($N = 8$)	19.6 ± 4.9	($N = 8$)	14.7 ± 6.4	($N = 8$)	9.0 ± 2.1	($N = 8$)

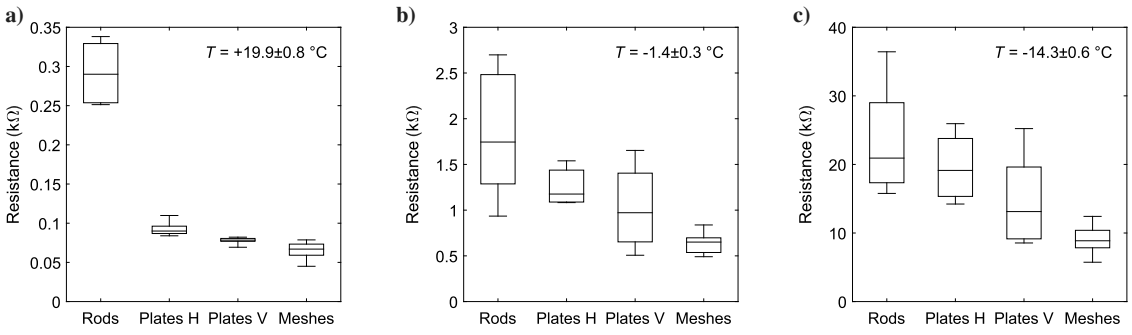

Figure 4. Box plots showing the variation in measured focus-one resistance for eight electrodes of each kind/orientation. The height of the box represents the interquartile range of the data set, and it extends from the 25th to 75th percentile. The horizontal bar within the box indicates the median value, and the whiskers extend to the maximum and minimum (average) values recorded for the given electrode type. The H and V signify the horizontal and vertical orientation of the plates, respectively. The actual number of electrodes involved in plotting each box plot is specified in Table 2.

significantly different ($p < 0.01$) except the means of the rods and horizontal plates at the coldest temperature, which did not differ significantly ($p > 0.05$).

It should be noted that due to the different shapes and orientations of the electrodes and the limited size of the buckets, it cannot be ruled out that some of the variation in total circuit resistance could be explained by variations in current flow patterns that would not be observed in a field setup. For the same reason, the values obtained in the experiment are not applicable to field situations. Nevertheless, because the vertically oriented plates and the meshes have similar shapes and orientations in the buckets, the observed difference between these electrode types can be considered conclusive, and similar effects would be expected in the field.

Ice buildup around electrodes

At the lowest temperature −14.9°C, we selected two buckets of each electrode configuration and cut them in half to visually inspect the effect of freezing processes in the soil around the electrodes. During ground freezing, pore water may migrate to the freezing front and create ice lenses (e.g., Arenson et al., 2005) that could affect the performance of the electrodes. The images in Figure 5 show preferential ice buildup around the metal electrodes, most severely around the plate electrodes. Especially, the horizontally oriented plate shown in Figure 5b has accommodated the growth of a horizontal ice lens immediately above the electrode, effectively isolating one side of it from the surrounding soil, and arguably contributing to the poor performance of horizontal plates. We did not observe significant ice buildup around the rod and mesh electrodes. The size of the rods and construction of the meshes possibly result in a smaller perturbation of the temperature field as compared with the solid plates, which could explain the lower affinity for ice buildup.

Electrode field experiment

Data collected at the three field test sites are summarized in Table 3 and visualized in box plots in Figure 6. The standard deviation of repeated measurements at a particular electrode was typically less than 3% of the measured resistance value. These averaged resistances were used to plot and calculate the general statistics.

The data agree with the findings of the laboratory experiment, with rods generally showing higher focus-one resistances than plates, which in turn have higher focus-one resistances than mesh electrodes. We also observe a strong temperature effect (effect of ground freezing), with focus-one resistances increasing by two to three orders of magnitude between unfrozen and coldest (frozen) conditions. Notably, on the site visit at Sisimiut in March 2014, grounding resistances of all electrodes of the rod type had grown so high that the instrument was incapable of measuring the focus-one resistances (indicating individual grounding resistances larger than approximately 1.2 MΩ). Similarly, approximately half of the mesh and plate electrodes could not be measured.

Because with the laboratory results, a two-way ANOVA has been applied to the data from each of the three sites, treating electrode types and temperatures as categorical factors and assuming a log-normal distribution of measured focus-one resistances. For all sites, we conclude that the main effects of electrode type and temperature are statistically significant and that there is also significant interaction between electrode type and temperature. On this basis, we applied Tukey's range test to compare the means of the effects of electrode type, and we conclude that the rods have significantly higher ($p < 0.01$) grounding resistance than plates and meshes at all temperatures and all sites (except Sisimiut in March, where no statistics could be calculated).

In Ilulissat and Qeqertarsuaq, the focus-one resistance of meshes is significantly lower ($p < 0.01$) than that of the plates at subzero temperatures in October 2013 and February 2014. However, the difference is not significant ($p > 0.05$) in the summer, when the ground is thawed. At the Sisimiut site, the meshes and plates cannot be considered significantly different ($p > 0.05$) at any time of year.

Based on these results, we conclude that mesh electrodes are a significant improvement over other electrode types at two out of three test sites (Ilulissat and Qeqertarsuaq). The rods show the high-

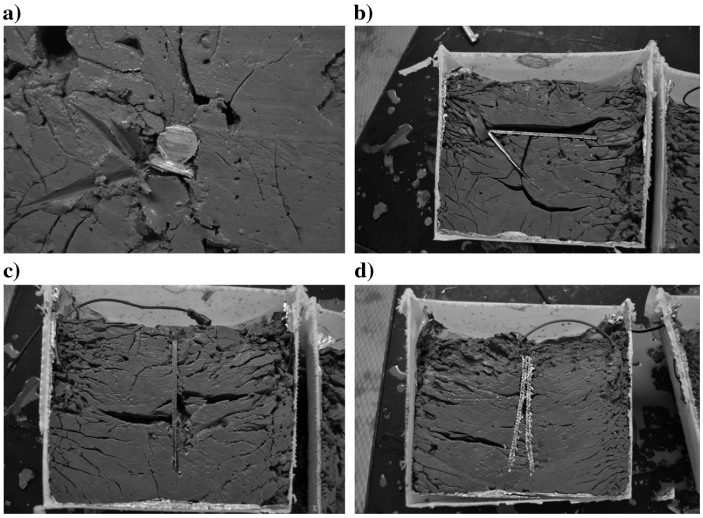

Figure 5. Photos of buckets with the four electrode configurations tested: (a) horizontally oriented rods, (b) horizontally oriented plates, (c) vertically oriented plates, and (d) vertically oriented meshes. Buckets were cut open while deep frozen at −14.9°C, to observe the effect of ice buildup around the electrodes. The ice has melted during the cutting, but the cryo patterns have been preserved as voids, observable as black areas in the images. The preferential freezing patterns particularly affect the plate electrodes of both configurations and are suspected to be a main factor in their decreased electrode performance at subzero temperatures.

est grounding resistances at all sites and all times of year. This includes Sisimiut in March, where the number of electrodes that could not be measured is used as an indication of electrode performance. The performance differences seem related to site conditions, where Sisimiut is seen to exhibit markedly higher grounding resistances, even in summer, compared with the other sites. This difference is believed to be related to lithology and drainage conditions at the site, but possibly also to the ground temperature regime and permafrost conditions, which would affect the overall half-space resistivity, and thus the embedding medium contribution to the grounding resistance.

Monitoring applications

At the ERT monitoring site in Ilulissat, we first experienced the severe effects of extremely high grounding resistances following the onset of the ground freezing in October 2012. Although no direct measurements of grounding resistances are available from that period, records show that transmitted current was decreasing and the number of daily resistivity measurements that could be collected was decreasing, suggesting increasing grounding resistances. By the end of November, approximately a month after the ground freezing had begun, the grounding resistances reached magnitudes that made it impossible for the SAS 1000 instrument to transmit even the lowest current (1 mA). By the end of December 2012, the ground freezing progressed to a point at which 98% of the daily resistivity measurements could not be measured (see Figure 8).

The success of the laboratory experiments prompted us to replace the rod electrodes by mesh electrodes during the site visit in August 2013. The grounding resistances of rods were recorded on the last day these were in the ground. On the following day (day 1), the rod electrodes were replaced by mesh electrodes. The grounding resistances of the new mesh electrodes were measured on the day of replacement and for 10 consecutive days. Because there was no rainfall event or distinctive temperature change over this period, we consider the environmental conditions for both electrode types to be comparable. We observed immediate and significant (t-test, $p < 0.01$) improvement of grounding resistance following the electrode replacement because the average grounding resistance dropped from 1.5 ± 0.9 kΩ for rods to 0.4 ± 0.1 kΩ for meshes; see Figure 7a. Comparison of the grounding resistances of the two types of electrodes on 29 April 2013 (rods) and 29 April 2014 (meshes) also reveals a significant (t-test, $p < 0.01$) reduction in grounding resistances of the monitoring array, with an average grounding resistance of 25.2 ± 11.4 kΩ for the 64 mesh electrodes (2014), as opposed to 64.1 ± 32.1 kΩ for the rod electrodes (2013), under similar ground temperature conditions (Figure 7b).

Figure 8b shows the number of collected resistivity measurements per day over the entire period that the Ilulissat station has been operational. Although the array was equipped with rod electrodes (the dark gray shading), the onset of freezing was followed by a substantial decrease in the number of daily resistivity measurements collected. When the ground temperature reached approximately −15°C in the beginning of January, the number of measurements had dropped to only 31 records per day. Although the exact grounding resistance values of the monitoring array electrodes from that period are unavailable, the corresponding grounding resistances measured for the short test arrays (see Figure 6 and Table 3) indicate a plausible range of 0.l–0.2 MΩ.

Performance of the array dramatically improved following the electrode replacement in August 2013. Since then, we were able to collect nearly complete data sets throughout the entire winter season, with at most 52 resistivity measurements skipped on a single day. Still, operation of the station was seriously affected by instrument software problems with large data gaps as a result. The station upgrade for remote control and data download completed in February 2014 has significantly reduced station downtime. As an added benefit, we have been able to measure the focus-one resistance of all electrodes at the site on a daily basis.

Table 3. Averages (arithmetic) and standard deviations of grounding resistances measured across seasons at three field experimental sites, along with the number of involved measurements. The *n* specifies the number of measurement repeats collected for each focus electrode, whereas *N* refers to the number of electrodes of the given type that could actually be measured; "n.m." (not measured) indicates that no electrodes of the given type could be measured due to high grounding resistances.

Time	Location	Rods (kΩ)		Plates (kΩ)		Meshes (kΩ)		Soil temperature at 10 cm
July/August 2013 ($n = 5$)	Qeqertarsuaq	1.8 ± 0.2	($N = 10$)	1.3 ± 0.2	($N = 10$)	1.2 ± 0.2	($N = 10$)	+8.8°C
	Ilulissat	1.2 ± 0.1	($N = 10$)	0.6 ± 0.1	($N = 10$)	0.6 ± 0.1	($N = 10$)	+9.5°C[6]
	Sisimiut	16.6 ± 4.9	($N = 10$)	9.2 ± 2.4	($N = 10$)	6.9 ± 1.3	($N = 10$)	+3.8°C[7]
October 2013 ($n = 5$)	Qeqertarsuaq	15.8 ± 3.1	($N = 10$)	4.9 ± 1.1	($N = 10$)	3.3 ± 1.0	($N = 10$)	−0.3°C
	Ilulissat	31.0 ± 4.4	($N = 10$)	17.7 ± 3.0	($N = 10$)	12.6 ± 2.6	($N = 10$)	−2.6°C
	Sisimiut	285.6 ± 56.5	($N = 7$)	162.6 ± 42.7	($N = 10$)	177.1 ± 44.4	($N = 9$)	−0.3°C
February/March 2014 ($n = 5$)	Qeqertarsuaq	1055.3 ± 65.3	($N = 4$)	555.4 ± 121.9	($N = 10$)	351.2 ± 48.8	($N = 10$)	−10.1°C
	Ilulissat	144.5 ± 26.4	($N = 10$)	97.7 ± 17.1	($N = 10$)	65.8 ± 11.4	($N = 10$)	−10.4°C
	Sisimiut	n.m.	($N = 0$)	1055.5 ± 111.3	($N = 4$)	1171.4 ± 132.6	($N = 5$)	−9.9°C)[8]

[6]Temperature obtained three days after electrode measurements due to data logger malfunction.
[7]Average temperature of the month of August due to data logger malfunction in the days around electrode measurement.
[8]Average ground surface temperature on the day of electrode measurements.

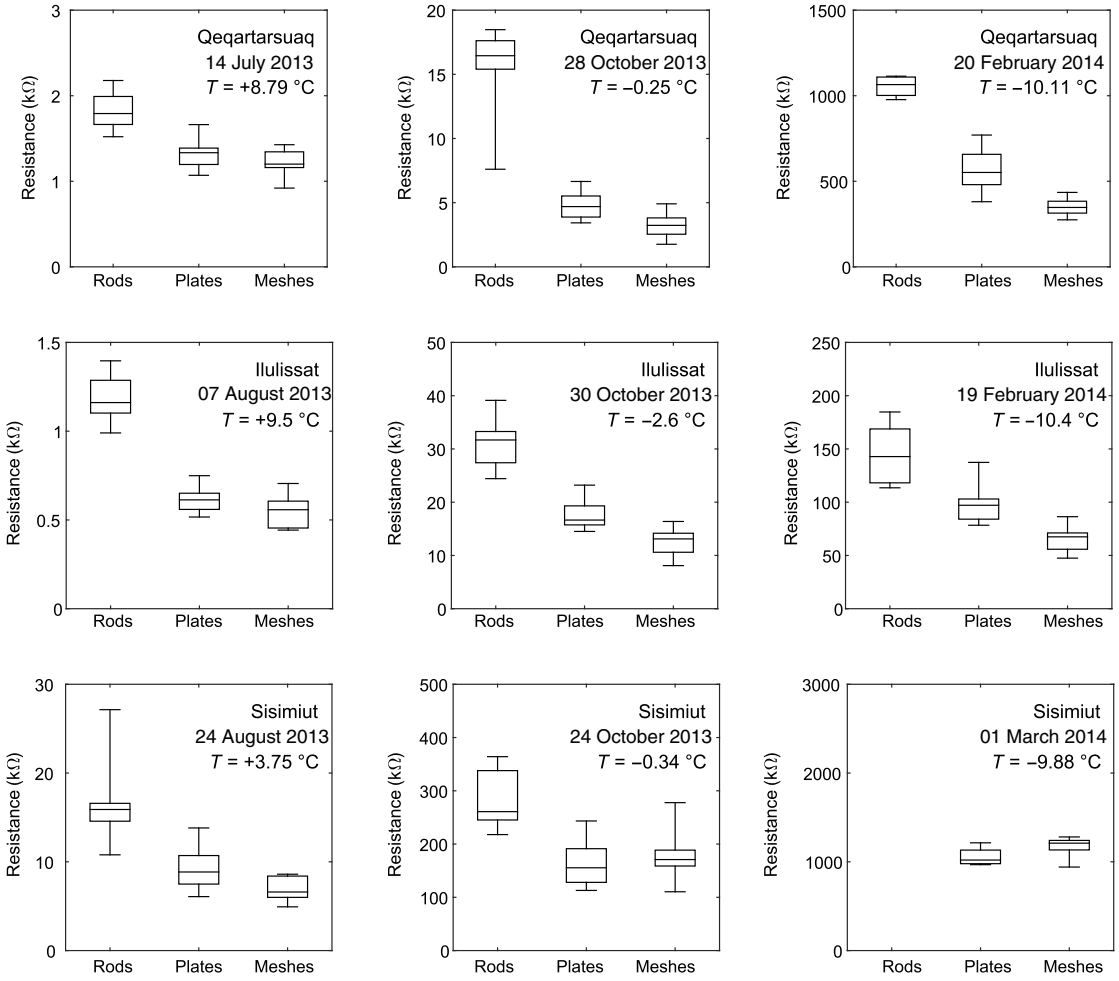

Figure 6. Box plots showing the variation in measured focus-one resistance for the three type of electrodes at the three field test sites. The height of the box portion represents the interquartile range, and the horizontal bar represents the median value. The whiskers extend to the maximum and minimum (average) values recorded for the given electrode type. The actual number of measurements involved in each box plot may be obtained from Table 3.

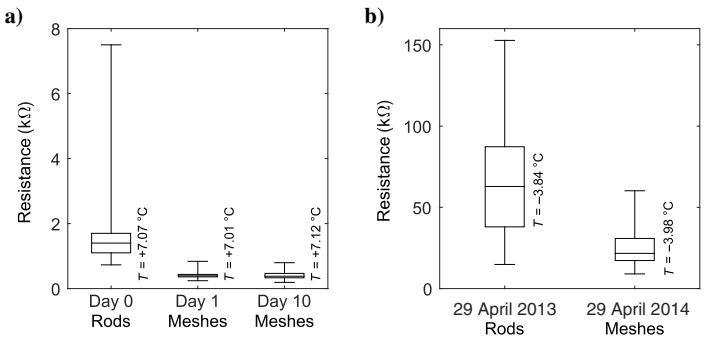

Figure 7. Comparison of electrode focus-one resistances for rod and mesh electrodes following the replacement at the Ilulissat monitoring station: (a) immediate reduction of grounding resistances following replacement of rod electrodes by mesh electrodes on 1 August 2013 (day 1) and (b) comparison of grounding resistances of rod versus mesh electrodes on the same day of the years 2013 and 2014. The height of the boxes represents the interquartile range, and the horizontal bar represents the median value. The ends of the whiskers extend to the maximum and minimum (average) values recorded for the given data set. Ground temperatures are measured at a 20 cm depth.

Grounding resistance time series

Figure 9a–9c shows a time series of focus-one resistances collected at the three monitoring sites in Qeqertarsuaq (plate electrodes), Sisimiut (rod electrodes), and Ilulissat (mesh electrodes).

The measured focus-one resistances were observed to be log-normal distributed at all sites, thus supporting the assumptions made in the statistical analysis of laboratory and field experiments. The observation is illustrated by histograms of the focus-one resistances observed at the Ilulissat monitoring site in summer and winter (see Figure 9d). The winter distribution exhibits a more regular bell shape than the summer distribution. The difference is linked to the change in the physical state of the soil over the seasons. In summer, the soil is unfrozen, and environmental parameters, such as temperature and soil moisture content, may change rapidly due to, e.g., precipitation or drought. Such events significantly affect the measured grounding resistances. In winter, however, the ground is frozen, and a change in moisture content and resistivity is linked mainly to the diurnal variations in temperature and thus plays a less significant role.

At the Ilulissat site, focus-one resistances range in summer from 0.19 to 1.4 kΩ, with a geometric mean (scale, e^{μ}) of 0.48 kΩ and a shape factor (σ) of 0.4. In winter, the measured resistances increase by approximately two orders of magnitude, ranging from 9.3 to 180 kΩ with a mean of 33 kΩ and a shape factor of 0.5.

At Qeqertarsuaq, the time series covers one freeze-up period. The measured focus-one resistances are very stable in summer ranging from 1.6 to 8.1 kΩ with a geometric mean of 2.6 kΩ and a shape factor of 0.2. In winter, the focus-one resistances are also around two orders of magnitude higher, ranging from 110 to 1.2 MΩ with a geometric mean of 344 kΩ and a shape factor of 0.4. The 1.2 MΩ is close to the upper limit of the instrument measurement range, some electrodes were indeed not measurable, and resistivity measurements suffered significantly from the high grounding resistances (see details in Doetsch et al., 2015).

The Sisimiut time series is sparse due to manual data collection, and it covers only a fall/winter season. The winter focus-one measurements range from 18 to 1.2 MΩ with a geometric mean of 203 kΩ and a shape factor of 1.0. At this site, resistivity measurements were also significantly affected by the high grounding resistances, sometimes to a point where measurements were not possible.

In an attempt at evaluating the relative contribution of the geometric effects (perfect grounding) and additional grounding resistance, we have calculated for each site the theoretical perfect single-electrode grounding resistances of equivalent spheroidal electrode models. Spheroids are ellipsoids of revolution, and their surface potential, and thus the grounding resistance, may be calculated using simple analytical expressions given by Ingeman-Nielsen et al. (2016) and T. Ingeman-Nielsen and S. Tomaškovičová (personal communication, 2015), under the assumption that the ground is a homogeneous half-space. We approximated the rod electrodes by a prolate spheroidal model of similar length and radius, and we approximated the plate and mesh electrodes by oblate spheroidal models of similar thickness and areal extent ($\beta = \sqrt{s^2/\pi}$, where s is the plate side length and β is the oblate spheroid major axis); see Figure 10. The grounding resistances of electrodes under perfectly grounded conditions are proportional to the resistivity of the half-space into which they are inserted (Ingeman-Nielsen et al., 2016), and the proportionality factors we have calculated for the electrodes used in this study are listed in Table 4 together with the properties of the spheroidal models applied.

To obtain a time series of equivalent half-space resistivities for each site, we used the normal four-electrode apparent resistivity measurements obtained during automated ERT measurements and calculated weighted averages on a daily basis. The theoretical

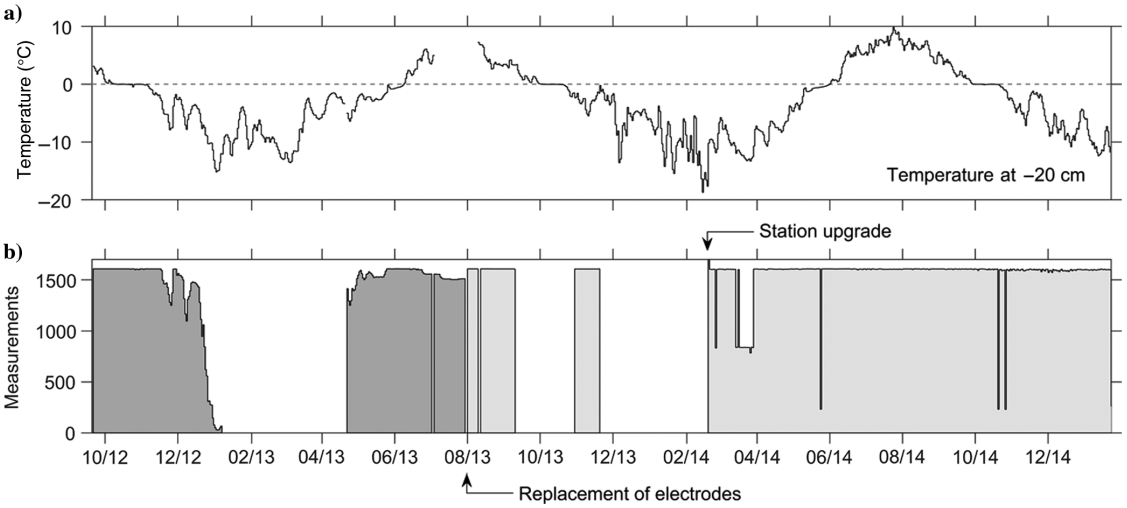

Figure 8. (a) Average daily ground temperature at 20 cm depth at the ERT monitoring site in Ilulissat between 21 September 2012 and 22 January 2015 and (b) the number of collected resistivity measurements on a daily basis. Date ticks indicate the first day of every second month. The dark-gray shading indicates rod electrodes, and the light-gray shading indicates mesh electrodes. A complete day record comprises 1625 measurements. The periods with zero records (such as from 7 January 2013 to 22 April 2013) are due to the Terrameter software malfunction. After the station was upgraded to remote control (19 February 2014), we have not experienced a complete software failure.

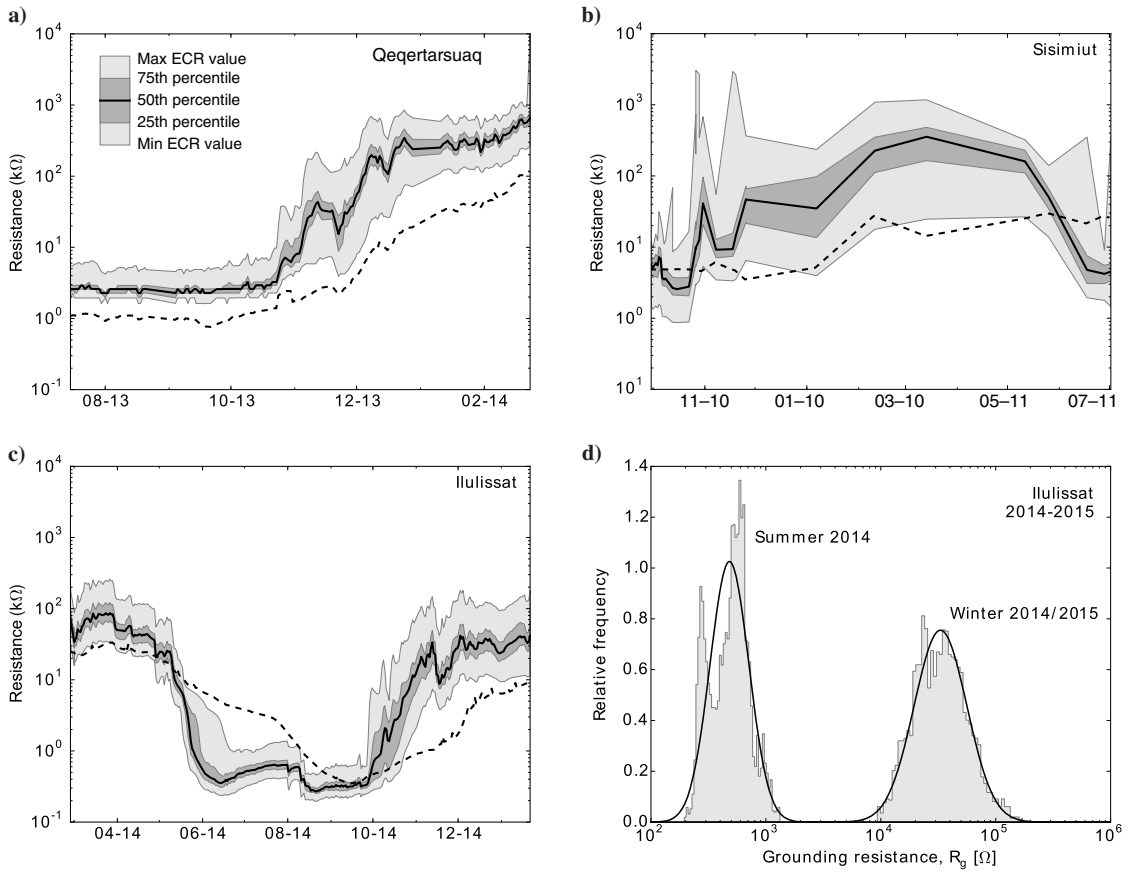

Figure 9. Time series of measured focus-one resistances (grounding resistances) for the monitoring stations in (a) Qeqertarsuaq, (b) Sisimiut, and (c) Ilulissat. The plots show mean array grounding resistance (the solid black line), 25th and 75th percentiles (the dark-gray shading), and maximum and minimum measured values (the light-gray shading). The plots also show the theoretical grounding resistance of a perfectly grounded electrode using estimated half-space resistivities based on the measured average daily apparent resistivities for each profile (dashed black line). The histograms in panel (d) illustrate the log-normal distribution of grounding resistances observed in Ilulissat in summer (1 July 2014 to 1 September 2014) and winter (1 December 2014 to 31 January 2015).

Table 4. Properties of physical electrodes used in monitoring applications and the equivalent spheroidal electrode models used in interpretation.

	Rods	Plates	Meshes
Installed at locality	Sisimiut	Qeqertarsuaq	Ilulissat
Electrode dimensions	$\phi = 1.0$ cm, $L = 10.0$ cm	$10 \times 10 \times 0.6$ cm ($h \times w \times t$)	$10 \times 10 \times 0.6$ cm ($h \times w \times t$)
Burial depth	−0.1 m	−0.1 m	−0.2 m
Model type	Prolate spheroid	Oblate spheroid	Oblate spheroid
Model dimensions	$\alpha = 0.5$ cm, $\beta = 5$ cm	$\alpha = 3$ mm, $\beta = 5.6$ cm	$\alpha = 3$ mm, $\beta = 5.6$ cm
Rotational symmetry around	y-axis	x-axis	x-axis
Grounding resistance	$5.182\ \mathrm{m}^{-1} \cdot \rho$	$2.551\ \mathrm{m}^{-1} \cdot \rho$	$2.344\ \mathrm{m}^{-1} \cdot \rho$

perfect grounding resistances were then calculated by multiplying the daily time series of half-space resistivities for a particular site by the appropriate proportionality constant listed in Table 4. These time series are included in the plots in Figure 9a–9c as dashed lines.

Obviously, using a homogeneous half-space resistivity is not very appropriate in a setting in which top-down freezing and thawing cause a layered earth structure with large resistivity contrasts. The problem is most clearly visible in the Ilulissat data, in which focus-one resistances drop as the ground thaws, but the estimated perfect grounding resistance only drops gradually over the summer because the thawing progresses and affects a larger part of the resistivity measurements used for the half-space approximation. This indicates that the focus-one protocol is highly sensitive to 2D and 3D ground resistivity variations.

At the Qeqertarsuaq site, the estimated perfect grounding resistance is consistently lower than the observed focus-one resistances, typically by a factor of two or more to the best grounded electrodes. At the Ilulissat and Sisimiut sites, however, during some parts of the year, the estimated perfect grounding resistance is approximately coincident with the minimum measured focus-one resistance. Furthermore, the estimated perfect grounding resistance never reaches the very high resistance values measured at some electrodes in wintertime.

Therefore, it seems an appropriate first approximation to consider the best grounded electrode of the layout to be perfectly grounded and consider the span of focus-one resistances on any given day as a conservative estimation of the additional grounding resistance. Thereby, we implicitly assume the half-space properties to be invariable along the layout and the additional grounding resistance R_a to be positively valued.

Under these assumptions, the additional grounding resistances in summer range from 0 to 1.2 kΩ and 6.5 kΩ at the Ilulissat and Qeqertarsuaq sites, respectively. The estimated additional grounding resistance in winter is up to three orders of magnitude larger, ranging from 0 to 170 kΩ at the Ilulissat monitoring station and up to more than 1 MΩ at the Qeqertarsuaq and Sisimiut monitoring stations.

DISCUSSION

There is a clear benefit in focusing on the evaluation of grounding resistance data from Arctic tundra landscapes. The environmental settings give rise to some of the most extreme conditions for ERT; on the one hand, the thawed, moisture-saturated ground provides very favorable conditions for good grounding of electrodes in the summer season. On the other hand, extremely high grounding resistances encountered upon ground freezing make it difficult to carry out surveys and monitoring projects throughout the winter. The challenge is to design a monitoring array that can sustain and perform in both extreme scenarios.

The problem of high grounding resistances is threefold. The most immediate problem concerns the total resistive load of the current transmission circuit. High loads require high supply voltages to drive even small currents, and they may challenge the ability of the acquisition system to stabilize the transmitted currents (Doetsch et al., 2015). The result may be noisy measurements, if measuring is at all possible. If the transmitted current is correctly stabilized, very high grounding resistances of the current electrodes may result in small transmitted currents and correspondingly lower signal levels at the receiver (depending on the ground resistivity structure), causing increased S/N, as pointed out in an early study by Rooney and Gish (1927). The third issue relates to leakage currents through the receiver circuitry at high grounding resistances of the receiver electrodes. LaBrecque et al. (2007) present a simple model using a grounding resistance of 10 kΩ and internal instrument resistance of 10 MΩ. They conclude that the combination results in errors of approximately 0.2% in measured voltages and thus apparent resistivities. Through a more complex model, which takes into account the size, shape, and positioning of the electrodes, T. Ingeman-Nielsen and S. Tomaškovičová (personal communication, 2015) describe systematic measurement errors due to receiver electrode grounding resistances. According to their model, grounding resistances in the upper range of values observed in this study would lead to errors in resistivity measurements on the order of 10% or more at receiver input impedances of around 10 MΩ. Choosing an optimized electrode design for ERT studies in cold regions could therefore not only prolong the period of acquisition but also improve the quality of measurements and accuracy of interpretations.

For this study, we used two different types of instruments. The ABEM Terrameter SAS 1000 has a fixed receiver input impedance of 10 MΩ, whereas the ABEM Terrameter LS has a receiver input impedance ranging from 200 MΩ at the highest gain setting (±2.5 V) to 20 MΩ at the lowest gain setting (±600 V). For normal resistivity measurements, these are the values to consider. However, when doing focus-one measurements, typically the receiver circuitry is connected in parallel with the transmitter circuitry, and thus any impedance associated with the current transmission circuitry needs to be taken into account. The SAS 1000 instrument transmission circuitry has very high (but unspecified) impedance (P. Hedblom, personal communication, 2015). The effective impedance of the instrument is therefore assumed close to 10 MΩ when doing focus-one measurements with current and potential terminals connected in parallel. The Terrameter LS, however, has separate monitoring channels permanently connected to the transmission circuitry and a resulting effective impedance of 6 MΩ or greater (depending on the gain). Thus, based on the findings of Ingeman-Nielsen

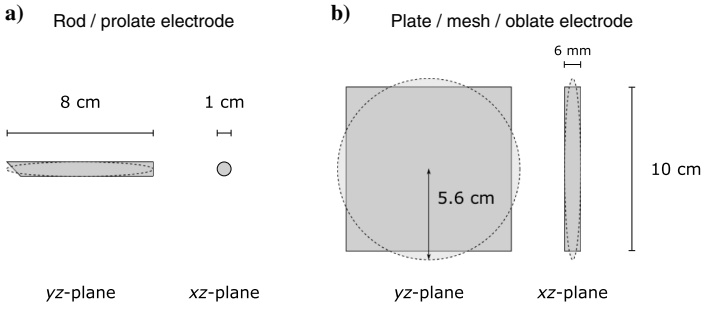

Figure 10. Schematic representation of electrode types and equivalent spheroidal models: (a) the rod electrodes are approximated by prolate spheroids of the same length and (b) the plate and mesh electrodes are approximated by oblate spheroids with similar areal extent and thickness. The coordinate system is oriented such that the electrode array direction is along the x-axis.

et al. (2016), the focus-one measurements collected with the two instruments are typically accurate to within ±7% and ±12% (focus-one resistances typically underestimated), SAS 1000 and LS, respectively, for the monitoring arrays of 64 electrodes or more, and to within ±19% and ±21% (focus-one resistances typically overestimated) for the short 10-electrode arrays. These specified ranges correspond to R_v/ρ ratios of 1000 and 500 m^{-1}, for the SAS 1000 and LS instruments, respectively.

Although automated profile focus-one measurements with the SAS 1000 are performed using the calibrated standard measurement channel, the current Terrameter LS firmware uses an uncalibrated internal transmitter monitoring channel (P. Hedblom, personal communication, 2015). Analysis of the full time series of resistivity measurements from Qeqertarsuaq indicates that the uncalibrated channel voltage measurement is typically within ±10% of the voltage measured by a calibrated monitoring channel. This additional measurement uncertainty relates only to the automated grounding resistance measurement time series from Qeqertarsuaq. The short array electrode field tests are measured manually using the standard measurement channel and are therefore not affected.

Understanding the changes of grounding resistances in cold regions requires insight into processes that condition the resistivity of half-space and a possible alteration zone around the electrode. The bulk ground resistivity depends on four main factors: soil mineralogic composition, porosity, fraction of unfrozen pore water, and geochemical composition of the pore water (e.g., Hoekstra et al., 1975; Friedman, 2005). An aqueous solution is, in most cases, the only conducting phase in the soil. In practice, it is also the only phase that substantially changes proportions over the course of a year. The processes of drying out and freezing (fall/winter) and thawing and infiltration (spring/summer) control not only the moisture content but also concentration of solutes in the unfrozen pore water.

When trying to evaluate the contribution of respective environmental effects in field experiments, it is impossible to properly control the numerous factors influencing ground resistivity. However, the experiment we conducted in the laboratory allowed us to control some of the most important factors, such as soil type, soil moisture content, and temperature. Due to the scale of the experiment, the laboratory results are not quantitatively comparable to field results. The geometric effects of the small buckets alter the current paths and impact of the embedding medium. Indeed, the grounding resistances measured in the field were typically several orders of magnitude higher than values obtained at similar temperatures in the laboratory. Nevertheless, the experiments in the controlled environment allowed us to qualitatively confirm the findings of the field observations and observing the cryostructure occurring around electrodes.

The horizontally oriented plate electrodes were included in the laboratory tests based on a recommendation (T. Dahlin, personal communication, 2013) that such an electrode configuration had been successfully implemented in a monitoring system under temperate conditions to improve moisture retention around the electrodes and thus decrease grounding resistances. The effect under frozen conditions, however, proved opposite due to preferential ice buildup around the electrode, and thus it was decided not to consider that electrode configuration for long-term field experiments in the Arctic. Although increasing the size of electrodes reduces the grounding resistance, it may also inflict geometric errors on resistivity measurements, especially when electrode separations are short (Igel, 2007). This effect has not been investigated in the current study.

CONCLUSIONS

It is widely recognized that high grounding resistances negatively influence ERT acquisitions in terms of the amount and quality of measured data. In monitoring applications in cold climates, the grounding resistance becomes the limiting factor of successful acquisition of meaningfully long time series, and high grounding resistances often restrict the measurements to the short summer season. We found that modifications to the electrode design bring significant ($p < 0.01$) improvements to the performance of an ERT array that operates under ground freezing conditions.

Our 3^3 factorial field experiment (three sites, three electrode types, and three seasons) provides a thorough and coherent analysis of electrode performance under realistic field conditions. It addresses the main effect of electrode size by testing rod electrodes against two similarly sized square electrodes (plates and meshes). It also considers the surface area and alteration zone effects, by comparing electrodes of similar size, but different surface area and construction design (plates and meshes). Finally, lithologic/resistivity effects are treated by repeating the same experiments at multiple sites and multiple seasons.

We conclude that increasing the electrode size (using plates or meshes instead of rods) significantly ($p < 0.01$) reduces the grounding resistance (by 28%–69%) at all sites and all seasons (thawed and frozen ground conditions). Furthermore, changing the electrode construction from plates to meshes further improves the grounding resistance in winter (frozen ground conditions) by 29%–37% at two out of three sites. At the Sisimiut site, plate and mesh electrodes performed equally well.

As the plate and mesh electrodes are similarly shaped, the main difference is in the effective surface area of the electrodes, which is five times larger for the mesh electrodes. The increased effective surface area seems to be an advantage when the electrodes are inserted or buried in fine-grained mineral or organic soils with some cohesive properties, in which the soil may fill the mesh openings. In coarser grained soils under well-drained conditions, it is unlikely that full advantage is taken of the larger surface area, which is probably the reason mesh electrodes did not constitute an improvement over plate electrodes at the Sisimiut site. The mesh electrodes may even provide less surface area than the plates if placed on hard surfaces such as rock outcrops, unless a wetting or contact agent such as moist clay, mud, or a sponge is used as part of the installation.

We speculate that the thermal properties of electrodes also play a role in the performance of the electrodes in cryospheric applications. Preferential freezing around the electrodes due to the changing heat flow in the soil caused by heat conduction through the electrode may counteract the benefit of increasing the size of massive electrodes. This would be a significant process in fine-grained soils in which capillary forces could result in vertical and horizontal moisture transport and ice buildup during ground freezing, as indicated by the cryostructure observed around plate electrodes in the laboratory experiment.

In spite of these reservations, the advantage of applying an optimized electrode design is documented at the Ilulissat permanent ERT monitoring station. The replacement of 64 rod electrodes by mesh electrodes resulted in an immediate reduction in the average grounding resistance by 73%, from 1.5 to 0.4 kΩ. Compa-

rable winter grounding resistances improved by 61%, from an average of 64.1 to 25.2 kΩ.

Time series of focus-one grounding resistances from long-term monitoring arrays at the three field sites document that grounding resistances are lognormally distributed and correlated to temperature (ground freezing). Summer grounding resistances at Ilulissat and Qeqertarsuaq monitoring stations range from 0.2 to 8.1 kΩ and may increase by more than two orders of magnitude upon ground freezing. Values of more than 1 MΩ were observed at the Qeqertarsuaq and Sisimiut monitoring stations. These observations support the conclusion that choosing an optimized electrode design, in this case the mesh electrodes, may make the difference between being able to collect measurements or not during the most challenging parts of the year.

With this paper, we present the first complete and coherent study of electrode grounding resistances under adverse environmental conditions, and we document the range of contact resistance values that can be expected in field situations in cold climates. We also quantitatively demonstrate the general understanding that increasing the electrode size and surface area decreases the electrode grounding resistance.

We expect the insight provided in this study to pave the way for future improvement in acquisition systems designed for proper monitoring of grounding resistances and improved accuracy in standard resistivity and IP measurements. This is of particular importance in monitoring applications in which minute changes in the resistivity structure are of interest. To enhance resolution and applicability of the ERT method and to improve our chances of correct data interpretation, we also see a need to incorporate the grounding resistance information into the data processing and inversion algorithms.

ACKNOWLEDGMENTS

Funding for this study was provided to B. Elberling by the Danish National Research Foundation (CENPERM DNRF100) and is part of a larger research program at 10 sites in Greenland. The authors would like to thank the Arctic Station for supplying a logistical platform and the permits for the work in Qeqertarsuaq and N. Foged for his help with calibrating instruments. We also wish to thank R. Nielsen, S. Mulvad, K. Trabjerg, S. Høgsholt, and M.T. Christensen for their contribution to the field and laboratory work.

REFERENCES

Arenson, L., D. Xia, D. Sego, and K. Biggar, 2005, Brine and unfrozen water migration during the freezing of Devon silt: Proceedings of the 4th Biennial Workshop on Assessment and Remediation of Contaminated Sites in Arctic and Cold Climates, 35–44.

Athanasiou, E. N., P. I. Tsourlos, G. N. Vargemezis, C. B. Papazachos, and G. N. Tsokas, 2007, Non-destructive DC resistivity surveying using flat-base electrodes: Near Surface Geophysics, **5**, 263–272, doi: 10.3997/1873-0604.2007008.

Baines, D., D. G. Smith, D. G. Froese, P. Bauman, and G. Nimeck, 2002, Electrical resistivity ground imaging (ERGI): A new tool for mapping the lithology and geometry of channel-belts and valley-fills: Sedimentology, **49**, 441–449, doi: 10.1046/j.1365-3091.2002.00453.x.

Branco, R. M. G. C., A. N. Amorim, J. A. Martins, S. B. Lima, N. C. Pedrosa, N. C. C. Vieira, and K. M. L. Oliveira, 2013, 2D/3D electrical resistivity tomography (ERT) applied to preliminary economic/geoelectrical evaluation of Jandaira and Açu Formations in the SW border of Potiguar Basin, Rio Grande do Norte, Brazil: 13th International Congress of the Brazilian Geophysical Society and EXPOGEF, Extended Abstracts, 574–577.

Brown, J., O. J. Ferrians, Jr., J. A. Heginbottom, and E. S. Melnikov, 1998, Circum-Arctic map of permafrost and ground ice conditions: National Snow and Ice Data Center, digital media, http://nsidc.org/data/docs/fgdc/ggd318_map_circumarctic/, accessed February 2015.

Dabas, M., A. Hesse, and J. Tabbagh, 2000, Experimental resistivity survey at Wroxeter archaeological site with a fast and light recording device: Archaeological Prospection, **7**, 107–118, doi: 10.1002/1099-0763(200006)7:2<107::AID-ARP138>3.0.CO;2-0.

Doetsch, J., T. Ingeman-Nielsen, A. V. Christiansen, G. Fiandaca, E. Auken, and B. Elberling, 2015, Direct current (DC) resistivity and induced polarization (IP) monitoring of active layer dynamics at high temporal resolution: Cold Regions Science and Technology, **119**, 16–28, doi: 10.1016/j.coldregions.2015.07.002.

Friedman, S., 2005, Soil properties influencing apparent electrical conductivity: A review: Computers and Electronics in Agriculture, **46**, 45–70, doi: 10.1016/j.compag.2004.11.001.

Hansen, B. U., B. Elberling, O. Humlum, and N. Nielsen, 2006, Meteorological trends (1991–2004) at Arctic Station, Central West Greenland (69° 15′N) in a 130 years perspective: Danish Journal of Geography, **106**, 45–55, doi: 10.1080/00167223.2006.10649544.

Hauck, C., and D. Vonder Mühll, 2003, Permafrost monitoring using time-lapse resistivity tomography, *in* M. Phillips, S. M. Springman, and L. U. Arenson, eds., Permafrost: Swets & Zeitlinger, 361–366.

Hilbich, C., C. Fuss, and C. Hauck, 2011, Automated time-lapse ERT for improved process analysis and monitoring of frozen ground: Permafrost and Periglacial Processes, **22**, 306–319, doi: 10.1002/ppp.732.

Hoekstra, P., P. Sellmann, and A. Delaney, 1975, Ground and airborne resistivity surveys of permafrost near Fairbanks, Alaska: Geophysics, **40**, 641–656, doi: 10.1190/1.1440555.

Hördt, A., P. Weidelt, and A. Przyklenk, 2013, Contact impedance of grounded and capacitive electrodes: Geophysical Journal International, **193**, 187–196, doi: 10.1093/gji/ggs091.

Igel, J., 2007, On the small-scale variability of electrical soil properties and its influence on geophysical measurements: Ph.D. dissertation, University of Frankfurt/Main.

Ingeman-Nielsen, T., 2005, Geophysical techniques applied to permafrost investigations in Greenland: Ph.D. dissertation, Technical University of Denmark.

Ingeman-Nielsen, T., S. Tomaškovičová, and T. Dahlin, 2016, Effect of electrode shape on grounding resistances — Part 1: The focus-one protocol: Geophysics, **80**, this issue, doi: 10.1190/geo2015-0484.1.

Kneisel, C., 2006, Assessment of subsurface lithology in mountain environments using 2D resistivity imaging: Geomorphology, **80**, 32–44, doi: 10.1016/j.geomorph.2005.09.012.

Kneisel, C., and C. Hauck, 2008, Electrical methods, *in* C. Hauck, and C. Kneisel, eds., Applied geophysics in periglacial environments: Cambridge University Press, 3–27.

LaBrecque, D., and D. Daily, 2008, Assessment of measurement errors for galvanic-resistivity electrodes of different composition: Geophysics, **73**, no. 2, F55–F64, doi: 10.1190/1.2823457.

LaBrecque, D., W. Daily, and P. Atkins, 2007, Systematic errors in resistivity measurement systems: Proceedings of the 20th Symposium on the Application of Geophysics to Engineering and Environmental Problems, EEGS, 1153–1160.

Lundström, K., R. Larsson, and T. Dahlin, 2009, Mapping of quick clay formations using geotechnical and geophysical methods: Landslides, **6**, 1–15, doi: 10.1007/s10346-009-0144-9.

Montgomery, D. C., 1997, Design and analysis of experiments: John Wiley & Sons.

Reynolds, J. M., 1997, An introduction to applied and environmental geophysics: Wiley.

Rooney, W. J., and O. H. Gish, 1927, Results of earth-resistivity surveys near Watheroo, Western Australia, and at Ebro, Spain: Terrestrial Magnetism and Atmospheric Electricity, **32**, 49–63, doi: 10.1029/TE032i002p00049.

Rosset, E., C. Hilbich, S. Schneider, and C. Hauck, 2013, Automatic filtering of ERT monitoring data in mountain permafrost: Near Surface Geophysics, **11**, 423–433, doi: 10.3997/1873-0604.2013003.

Scott, W., P. Sellmann, and J. Hunter, 1990, Geophysics in the study of permafrost, *in* S. Ward, ed., Geotechnical and environmental geophysics: SEG, 355–384.

Sunde, E. D., 1949, Earth conduction effects in transmission systems: Dover Van Nostrand Company Inc..

Telford, W. M., L. P. Geldart, and R. E. Sheriff, 1990, Applied geophysics: Cambridge University Press.

Tukey, J. W., 1949, Comparing individual means in the analysis of variance: Biometrics, **5**, no. 2, 99–114, doi: 10.2307/3001913.

Vonder Mühll, D., C. Hauck, H. Gubler, R. McDonald, and N. Russill, 2001, New geophysical methods of investigating the nature and distribution of mountain permafrost with special reference to radiometry techniques: Permafrost and Periglacial Processes, **12**, 27–38, doi: 10.1002/ppp.382.

Wait, J. R., 1982, Geo-electromagnetism: Academic Press.

Zonge, K., J. Wynn, and S. Urquhart, 2005, Resistivity, induced polarization and complex resistivity, *in* D. K. Butler, ed., Near-surface geophysics: SEG, 265–300.

APPENDIX C

Automated monitoring of resistivity, moisture and temperature regimes in fine-grained permafrost soils in Ilulissat, West Greenland

Automated monitoring of the resistivity, moisture and temperature regimes in fine-grained permafrost soils in Ilulissat, West Greenland

Sonia Tomaskovicova[a], Thomas Ingeman-Nielsen[a]

[a] *DTU Civil Engineering, Technical University of Denmark, Kongens Lyngby, Denmark.*

Abstract

This article describes presently the longest timeseries of ground temperature, unfrozen water content and resistivity from high-latitude permafrost. Monitoring station in Ilulissat, West Greenland, was established in August 2012, in a sedimentary basin filled with fine-grained marine deposits – a common, frost-susceptible sediment type found along the west Greenlandic coast, complicating sustainable infrastructure design and maintenance. Automated resistivity measuring system was designed and optimized for time lapse acquisitions in this environment characterized by extremely variable electrode grounding conditions between thawed *vs.* frozen season. Monitoring data analyzed in this article were collected between September 2012 and October 2015. Good completeness of the records allowed to map in-situ processes conditioning thermal regime of active layer and permafrost in fine-grained sedimentary setting. We observed that temperature-dependent ground physical properties depend on whether a certain ground thermal and saturation state was reached by freezing or thawing. Consistently higher soil unfrozen water contents were observed during freezing of the active layer than during thawing. The freeze-thaw water content hysteresis has implications for modeling of heat transfer in a soil, as the amount of unfrozen water is one of the key parameters influencing bulk ground thermal properties. Hysteresis was also observed in the relationship between ground electrical resistivity and unfrozen water content, where resistivity during freezing is consistently higher than during thawing. Consequently, traditional resistivity mixing relations deriving bulk soil electrical resistivity from unfrozen water content do not entirely explain complexity of the relationship. This complicates quantitative interpretation of ground resistivity changes in terms of ground temperature and ice content changes.

Keywords: geoelectrical monitoring, unfrozen water content monitoring, freeze-thaw hysteresis, saline permafrost, ground thermal regime,

1 INTRODUCTION

Geophysical monitoring has been steadily gaining popularity in permafrost studies. Long-term monitoring provides improved in-situ process understanding - a knowledge ultimately necessary for more reliable modeling and prediction of climate change impacts on the Arctic regions (Hilbich et al., 2011).

Particularly in warm and/or saline permafrost, temperature boreholes do not reliably reflect ground stability changes. In warm permafrost, where mean annual ground temperature is near 0 °C, the zero-curtain effect masks potentially ongoing ground thawing. Residual salinity in partially-leached or unleached marine sediments causes a freezing-point depression and a general increase in unfrozen water content. Consequently, the soils may behave as unfrozen or partly frozen even at subzero temperatures.

Applications in mountain permafrost (Hilbich et al., 2008), rock walls (Krautblatter and Hauck, 2007) and high-latitude permafrost (Doetsch et al., 2015) prove that the electrical resistivity tomography (ERT) is well-suited for monitoring temporal changes in unfrozen water content. Surface geoelectrical measurements thus provide an attractive way of informing permafrost models. Studies by Hauck et al. (2008) and

Email address: soto@byg.dtu.dk (Sonia Tomaskovicova)

Krautblatter et al. (2010) demonstrate that there is a quantitative link between electrical and thermal properties of geological materials. Calibration of this link necessitates thorough understanding of petrophysical relationships and availability of data with sufficient level of detail spanning several freeze-thaw cycles.

While logistically comparatively convenient, deployment of ERT in harsh periglacial areas is facing numerous challenges. Among them remoteness of the monitoring sites and associated powering and data access issues, as well as extreme grounding resistances during the winter season complicate acquisition of timeseries over complete freeze-thaw cycles (Tomaskovicova et al., 2016).

In an effort to overcome these challenges, permafrost monitoring station in Ilulissat was designed with the primary aim to acquire geoelectrical calibration data for a coupled model of heat transfer in permafrost (Tomaskovicova et al., 2012). Additional environmental parameters were monitored to enable validation of the model, including ground temperatures, soil moisture, snow depth and soil thermal properties. Considering practical as well as scientific aspects, the aims of this study were following:

- to gain and share experience with design and long-term operation of a monitoring station in high-latitude fine-grained permafrost. Attention is paid to description of technical details of the resistivity system that is able to withstand harsh and variable environmental conditions and allows for safe data storage and unrestricted access;
- to describe in-situ processes conditioning thermal regime of a ground undergoing cycles of freezing and thawing;
- to quantitatively describe relationships between ground temperature, moisture content and electrical resistivity with the prospect of using them in thermal modeling;

The remainder of this article is structured as follows: section 2 introduces the monitoring field site. Section 3 provides details about components of the station and technical challenges linked to automated monitoring. Section 4 explains the process of inversion of geoelectrical data. In sections 5 and 6 respectively, we present and discuss results. Conclusions and recommendations are given in section 7.

2 ILULISSAT SITE DESCRIPTION

The monitoring site is situated near the airport in Ilulissat (69°14′ N, 51°3′ W,33 m above sea level), on the mainland in the inner part of the Disko Bay (figure 1). The mean annual air temperature between 2003 – 2012 was −5.1 °C (data from Cappelen, 2013). The site is located in the continuous permafrost zone (Brown et al. 1998).

At the time of the last glacial maximum (approximately 25 000 years before present (BP), Weichsel/Wisconsin glaciation), Greenland was covered by the Greenland Ice Sheet. According to Bennike and Björck (2002), the innermost part of the bay near Ilulissat was not deglaciated before 9600 years BP. Following the retreat of the ice sheets, marine transgression resulted in the deposition of fine-grained marine sediments at relatively high sea levels of $>$ 50 m above present. Most soil formations thus relate to the last Weichselian/Wisconsin glaciation and to the Holocene deglaciation. Onshore, the most important deposits are local side moraines and glacio-marine clay and silt sediments overlain by Holocene solifluction deposits and topsoil in form of only slightly decomposed peat (Ingeman-Nielsen et al., 2008).

Interaction between eustatic changes and isostatic uplift raised the area above sea level about 5000 years ago (Rasch (2000)), exposing the sediments to percolation of precipitation, and possibly groundwater flow. This resulted in depletion of salts in the upper part of the soil profile. At the end of the Holocene optimum (after 5000 years BP), climate allowed permafrost to develop as seen today (Dahl-Jensen et al., 1998; Hammer et al., 2001), effectively stopping the depletion process. The sediments have been exposed to the consolidation and fracturing phenomena caused by ice lens formation in fine-grained sediments (Foged, 1979). In Ilulissat, this history resulted in a complex profile consisting of an upper leached, ice-rich part of the permafrost and a lower (partly) unleached zone with high unfrozen water content and low or no ice content (Ingeman-Nielsen et al., 2008, 2010). Differences in residual salinity strongly affect the freezing

Figure 1: Position of Ilulissat on the map of Greenland and location of the field site east of the Ilulissat airport.

temperature of the sediments and, in combination with the local ground thermal regime, affect the presence and distribution of ice features in the soil profile.

Geological and geophysical model of the area – based on borehole information from 1970' – is presented on figure 2.

The active layer thickness at the site is approximately 90 cm, below which ca. 2-3 meters of ice-rich permafrost are found. Deeper parts of the soil profile are, however, technically unfrozen, in spite of measured ground temperatures around −3.1 °C. The cause is the pore water, which gradually changes from freshwater to seawater, with concentration of Cl^- ions up to 19‰below 4 m depth (Foged and Ingeman-Nielsen, 2008). Theoretical freezing point depression of the clay formations was calculated based on pure NaCl solution of the same chloride concentration; it ranges from −1 °C to −3.5 °C depending on the depth – and salinity concentration – in the profile. The bedrock is encountered at the site at 7 m depth and it consists of Nagsugtoquidian gneisses with amphibolitic bands affected by a series of fault and fracture systems, most importantly in NW-SE direction (Ingeman-Nielsen et al., 2008).

Alternating layers of highly contrasting resistivities result in a complicated geophysical model. Expected resistivity values, based on vertical electrical sounding curves from 1970' (Foged and Ingeman-Nielsen, 2008), are included on figure 2. Additionally, ice segregation at the top of permafrost and formation of ice lenses (figure 14) contributes to anisotropic soil electrical properties (e.g. Telford et al. (1990)).

3 AUTOMATED MONITORING STATION

The monitoring station in Ilulissat was first set up in August 2012 (overview of the installation in figure 3). The main purpose of the station has been to acquire time-lapse measurements of ground electrical resistivity for calibration of a heat transport model (Tomaskovicova et al., 2012). Additional environmental parameters were monitored to enable validation of the model, including air and ground temperatures, soil moisture, snow depth and soil thermal properties.

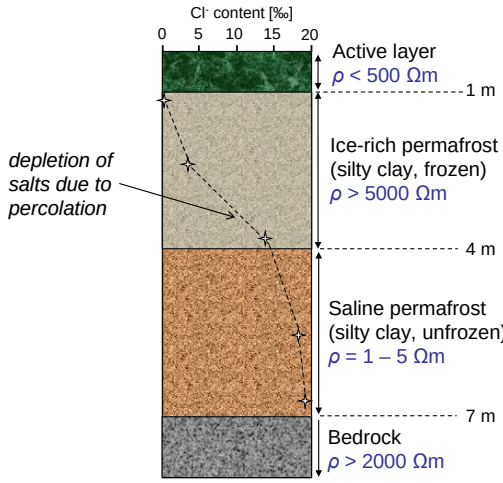

Figure 2: Schematic representation of geological profile in Ilulissat (adapted from Foged and Ingeman-Nielsen (2008)). Active layer thickness reaches 0.9 – 1 m, below which 2-3 m of ice-rich permafrost are found. The deeper sediments are technically unfrozen in spite of ground temperatures below 0 °C, as salinity content in pore water gradually increases and causes freezing point depression. Alternating layers of low and high resistivities (active layer – ice-rich permafrost – saline permafrost – bedrock) result in a complicated geophysical model.

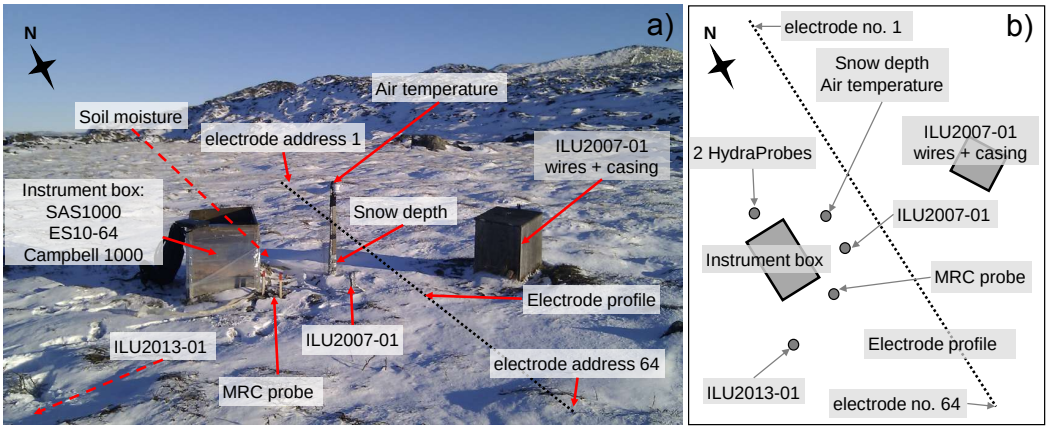

Figure 3: Components of the monitoring station in Ilulissat. (a) View of the station towards north, with Ilulissat airport to the left; (b) top-view drawing of the site (the drawing is not to scale). 'Electrode 1' and 'electrode 64' refer to the electrode address in the acquisition protocol.

In the following sections 3.1 through 3.3, we detail the setup, specifications and periods of operation of respective components of the automated station (for overview, see table 1 and figure 4). For detailed photos of the instrumentation in-situ, refer to figure 5.

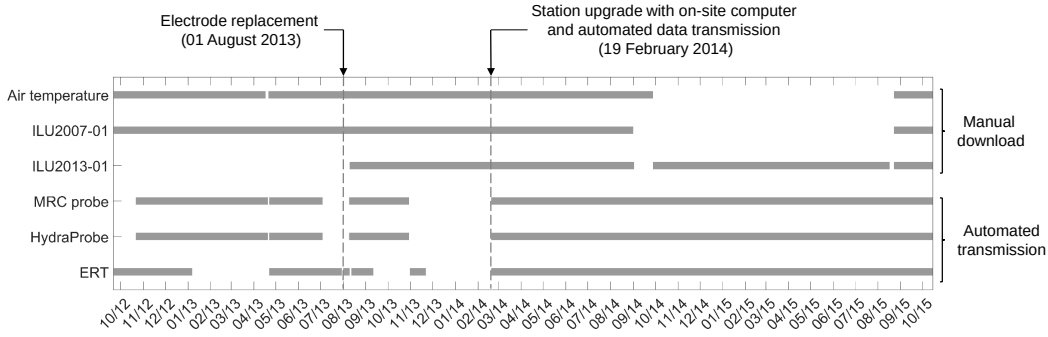

Figure 4: Overview of timeseries of collected data from respective sensors (grey line) with gaps indicating periods with missing data. Station upgrade events in 2013 and 2014 are noted. *Automated data transmission* points to the data that are backed up and transmitted via cellular modem to the university server. Date ticks indicate the first day of every month.

3.1. Air and ground temperature measurements

Air temperature is measured on a mast 1.1 m above ground surface. The sensor is placed inside a radiation shield and logs air temperature every 3 hours. On the same mast, five thermistors placed at heights 0, 0.03, 0.06, 0.1, 0.15, 0.2, 0.3 m from the ground surface provide indirect indication of snow depth.

Ground temperatures are measured at three locations, see figure 3. Borehole ILU2007-01, 4 m deep, was drilled in 2007 and instrumented with two HOBO U12-008 dataloggers and eight thermistors. Severe frost heave (26 cm between 2007 – 2013) has affected the plastic casing of the borehole and two sensors (at 1 m and 3 m depth) broke during the winter of 2012. Therefore, borehole ILU2013-01 was drilled in August 2013 and instrumented down to 6 m depth with a total of 12 thermistors. For details about placement of the thermistors refer to table 1.

Detailed soil temperatures are also measured in the active layer and at the top of the ice-rich permafrost using a 1.5 m long thermistor string with thermistors spaced by 10 cm. The thermistors are encased in a rigid tube (MRC probe) which includes and internal multiplexor that allows simple connection to a Campbell datalogger.

3.2. In-situ unfrozen water content measurements

The dielectric permittivity of the soil is measured through frequency-domain reflectometry (FDR) using two Stevens® HydraProbe® II sensors (*soil moisture probes*) connected to the CR1000 datalogger using the SDI-12 protocol. The probes are installed at depths of 0.30 and 0.55 meters (figure 5b). The measured dielectric permittivities are stored by the datalogger and converted to bulk soil volumetric unfrozen water contents during data processing using a conversion equation established for a similar clay soil from Kangerlussuaq, Greenland (Agergaard and Ingeman-Nielsen 2011):

$$UWC = 0.165 \times \sqrt{E_{r(TC)}} - 0.239 \quad , \tag{1}$$

where ($E_{r(TC)}$) is the temperature-corrected real part of the dielectric permittivity.

The measurements of both soil moisture probes confirm the same water content tendencies. For the sake of brevity, in the following text, we focus on discussing quantitative results from the upper sensor (at 0.3 m) only.

Table 1: Monitoring station components, measured parameters, sampling points and sampling frequencies.

Parameter measured	**Instrument/Sensor**	**Sampling points/Depths**	**Sampling frequency**
Ground resistivity	SAS1000 resistivity meter + ES10-64 electrode selector	64 electrodes, 0.5m spacing, 1625 configurations	24 h
Temperature to 1.5 m depth	MRC thermistor string	16 thermistors spaced by 10 cm between 0.0 – 1.5 m b.g.s.	3 h
Temperature to 4 m depth (borehole ILU2007-01)	HOBO U12-008 loggers with TMC-HD sensors	0, 0.25, 0.5, 0.75, 1, 2, 3, 4 m	3 h
Temperature to 6 m depth (borehole ILU2013-01)	HOBO U12-008 loggers with TMC-HD sensors	0, 0.25, 0.50, 0.75, 1.00, 1.25, 1.50, 2.00, 3.00, 4.00, 5.00, 6.0 0m	3 h
Unfrozen water content	Stevens Hydra Probe II SDI-12 sensors	at 0.3 and 0.55 m depth	3 h
Thermal conductivity	East 30 thermal properties probe	at 0.3 and 0.55 m depth	3 h
Air temperature	HOBO U12-008 logger with TMC-HD sensor	1.1m above ground surface, in a radiation shield	3 h

3.3. Automated resistivity monitoring system

The ERT instrumentation consists of an ABEM SAS1000 resistivity meter and an external electrode selector ABEM ES10-64. The ERT array is equipped with 64 electrodes equidistantly spaced by 0.5 m and buried at a depth of 10 to 20 cm. The burial protects the electrodes and cables from damage and removal by animals, and ensures electrode installation in the clay soil below the organic surface layer. Each of the 64 electrodes of the array is connected to the electrode selector by a coated copper cable (figure 5c-f).

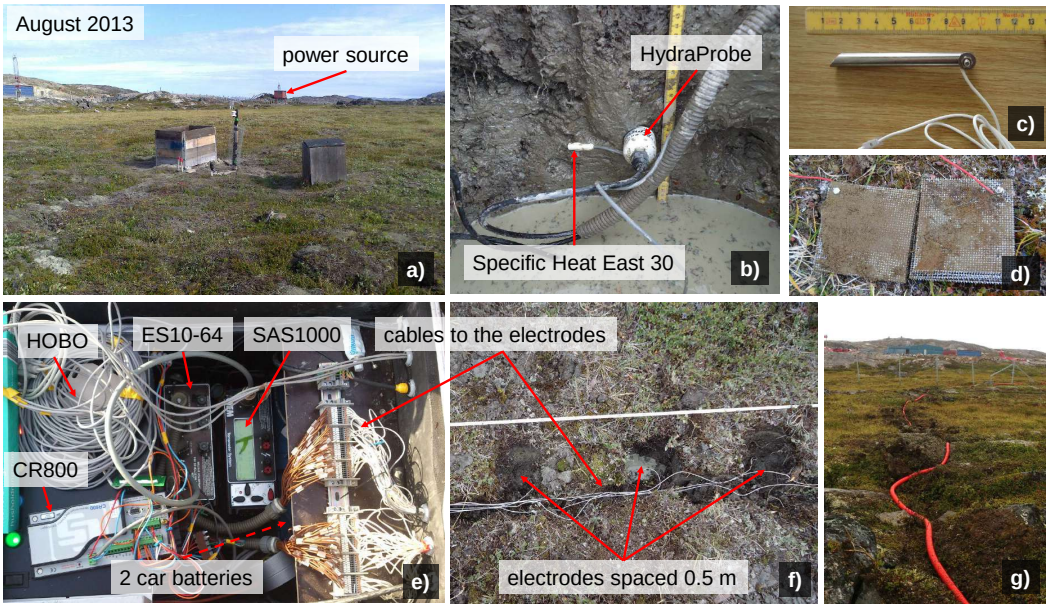

Figure 5: Details of the monitoring station. (a) View of the station towards the North in summer, with Ilulissat airport in the background; *power source* refers to the airport facility providing electricity to the station. (b) Detailed view of soil moisture probe and thermal properties probe. (c) Detail of the rod electrode, installed in August 2012. (d) Detail of the mesh electrode, mesh openings saturated with soil, installed in August 2013. (e) View inside the aluminium instrumentation box housing resistivity meter, power-supply unit (PSU), some of the HOBO dataloggers and Campbell datalogger (CR800 was upgraded to CR1000 in February 2014). White cables leading to electrodes of the ERT array are connected inside the box to ES10-64 via two multipin connectors. (f) Cable system leading from the instrument box to each of the electrode of the array, spaced 0.5 m. (g) Laying the power cable before burying it in the ground, view towards the East with Ilulissat airport fence and parking area in the background.

The ERT array was first equipped with 8 cm-long rod-shaped stainless steel electrodes (figure 5c). Over the first winter 2012/2013, a drastic increase of ground resistivity following ground freezing gradually made it impossible for the resistivity meter to transmit even very low currents (1 mA). In August 2013, we replaced the rod-shaped electrodes with square stainless steel mesh electrodes (figure 5d, for detailed discussion of electrode experiments see Tomaskovicova et al., 2016) which resulted in a 61% reduction of winter grounding resistances. After the replacement, the daily time lapse resistivity acquisition could be conducted throughout the entire winter seasons, and subsequent data gaps were due to terrameter software malfunction, rather than to grounding resistance issues. Choosing an optimized electrode design thus proved to be one of the key factors for the success of the resistivity monitoring station.

Remote control and data transmission.

Between August 2012 and February 2014, resistivity data could only be downloaded during station visits, usually once or twice per year. The resistivity meter, not designed for long-term time lapse

acquisitions, was prone to system errors that would require manual restart. This, in addition to the extreme grounding resistances affecting the rod electrodes in the first year, caused repeated station malfunctions and consequently long gaps in data collection.

The instability of the setup led us to schedule a major station upgrade at a site visit in February 2014. A low-power PC and cellular modem was installed (see figure 6) with the purpose of:

- Controlling the collection and storage of resistivity data
- Retrieving and storing measurements of ground temperature, unfrozen water content and thermal properties measured by the Campbell datalogger.
- Synchronizing collected data with the University server on a daily basis
- Allowing remote connections to the system for maintenance and reprogramming.

The PC communicates separately with the resistivity meter and electrode selector through serial connections. An in-house code is used to control the collection of the focus-one grounding resistances (Ingeman-Nielsen et al., 2016) of every electrode in the resistivity array, while the software ERIC (Torleif Dahlin, 2014, Pers. Comm.) is used to control the collection of regular four-electrode measurements. Data is transmitted to the server on a daily schedule using the *rsync* protocol over an *SSH*-connection; a simple solution which ensures the synchronization of all data (even after extended periods with no cellular connectivity) while allowing partial transfers and data compression to ensure minimal data charges. In order to allow recovery from potential software malfunction, the PC is programmed to reboot everyday at midnight. This setup has effectively reduced the station's downtime and result in greater data security through regular data upload to permanent storage.

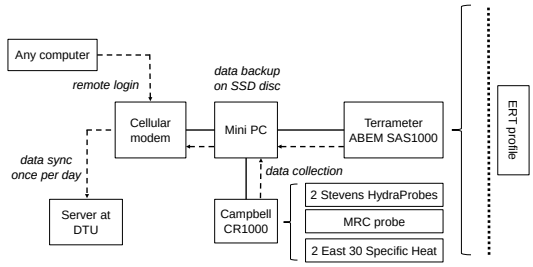

Figure 6: Layout of the automated data collection and transmission system. 64 equidistant electrodes of the ERT array are connected to an ABEM SAS1000 resisitivity meter via electrode selector ES10-64. Resistivity data collection is controlled by an on-site mini-PC, which also collects data from the Campbell datalogger measuring ground temperatures, unfrozen water content and thermal properties. The data is transmitted over a cellular modem to permanent storage at the University server.

Powering considerations

Power consumption of the resistivity system was estimated from the manufacturer's specifications. Based on 18.6 hours of standby time and 5.4 hours of acquisition time per day, the theoretical maximum power consumption of the resistivity system alone amounted to 931 Wh/day. This scenario applies to periods where maximum output voltage (400 V) would be required to complete the measurement cycle, and does not include the consumption of other elements of the station, such as PC, modem, dataloggers and battery-backup.

To ensure sufficient power for continuous operation, the station is connected to a 230 V power outlet at the nearest Ilulissat airport facility (figure 5a), using 270 meters-long double-sheathed round 3-core cable. The cable is housed in a corrugated plastic pipe and buried in average 30 cm below ground surface (figure 5g).

Power is supplied to the PC, resistivity instrumentation and datalogger by a custom-built power-supply unit (PSU) which controls the alternate supply from and charging of two 12 V, 60 Ah lead-acid batteries to ensure uninterrupted operation even during power outages.

All instrumentation is housed in a lockable aluminum box placed on a wooden pallet, to avoid disturbance of current paths in the ground.

The airport authorities provided us with readings of the actual power consumption of the station in its first year of operation. The maximum consumption was 30 kWh per month (during each October and November 2012). Over the summer months July-August 2013, the station power consumption was on average 25 kWh per month.

Acquisition protocol

The ERT system collects ground resistivity measurements in a total of 1625 4-electrode (quadrupole) configurations, once every 24 hours. 1392 measurements in **Gradient** configuration provide robust measurements with good depth of penetration (Dahlin and Zhou, 2006) for 2D visualization of freezing pattern.

Additionally, we configured a pseudo-1D **Wenner-Schlumberger** protocol, consisting of 233 electrode configurations with 33 vertical focus *pseudo-depths* (depths of maximum vertical sensitivity) and horizontal focus on the central 4 meters of the ERT profile (between 14.25 - 18.25 m relative to the total profile length of 31.5 m, see figure 7). The narrow horizontal focus of this protocol provides denser data coverage – and thus better chance for comparison – in the immediate vicinity of the borehole temperature installation.

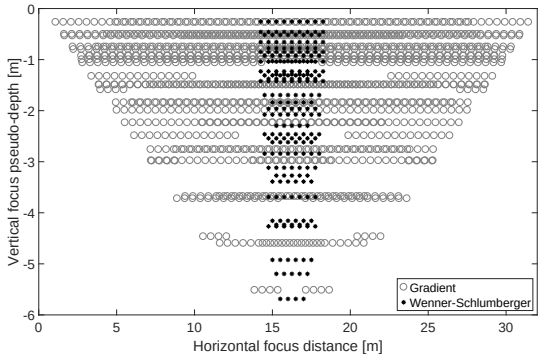

Figure 7: Visualization of focus points of combined measurement protocol consisting of Gradient and Wenner-Schlumberger protocols. The x-axis shows lateral focus distance while the y-axis shows the maximum vertical sensitivity (focus pseudo-depth) of each quadrupole configuration.

Resistivity data quality

Large amounts of data (up to 1625 records every 24 hours) rely on automated filtering procedures to detect and remove measurement errors. In our records, errors usually appeared as negative resistivity readings, high-value outliers and records skipped due to high grounding resistance.

We applied first two steps of the three-step filtering procedure described by Rosset et al. (2013). The technical and magnitude filter together removed up to 8 % of the Schlumberger and 10 % of the Gradient datapoints while the array was equipped with the rod-shaped electrodes. After the electrode replacement and improvement of electrode grounding, only 0.6 % of Schlumberger and 2 % Gradient records had to be discarded.

4 INVERSION OF THE RESISTIVITY DATA

The two-step filtered Gradient datasets were inverted using the RES2DINV inversion program using robust inversion scheme, refined model discretization, reduction of edge effects and increasing damping factor with depth (Loke, 1999). For consistency, we compared the seventh iteration of each inversion.

The 2D-inversions confirm horizontally-layered ground structure as inferred from boreholes, with uniform top-down freezing pattern (figure 8). Changes in resistivity in the top of the profile correspond well to the ground temperature and unfrozen water content variation due to freeze-thaw processes in the active layer. Minimum inverted resistivities range from 20 Ωm to 100 Ωm throughout September, while maximum winter values reach up to 10^4 Ωm in March – April. However, maximum thickness of the active layer (up to 0.9 m at the beginning of September) is not properly resolved. This is likely due to resolution problem - in spite of 0.5 m electrode spacing, limited data coverage in the topmost model layers does not allow proper resolution of resistivities and thicknesses in the top of active layer. Another problem arises in the depth of the model below 4 m, where 2 orders of magnitude of resistivity increase between summer and winter (from 20 to 2000 Ωm) cannot be explained by ground temperature variation. The mean annual ground temperature at the depth of 4 m is −3.05 °C, with yearly amplitude of only 0.33°. Exaggerated resistivity variation in the depth below 4 m is thus likely result of equivalency issues (e.g. Maillet (1947)) caused by complex geophysical model of alternating layers of high- and low-resistivity (figure 2).

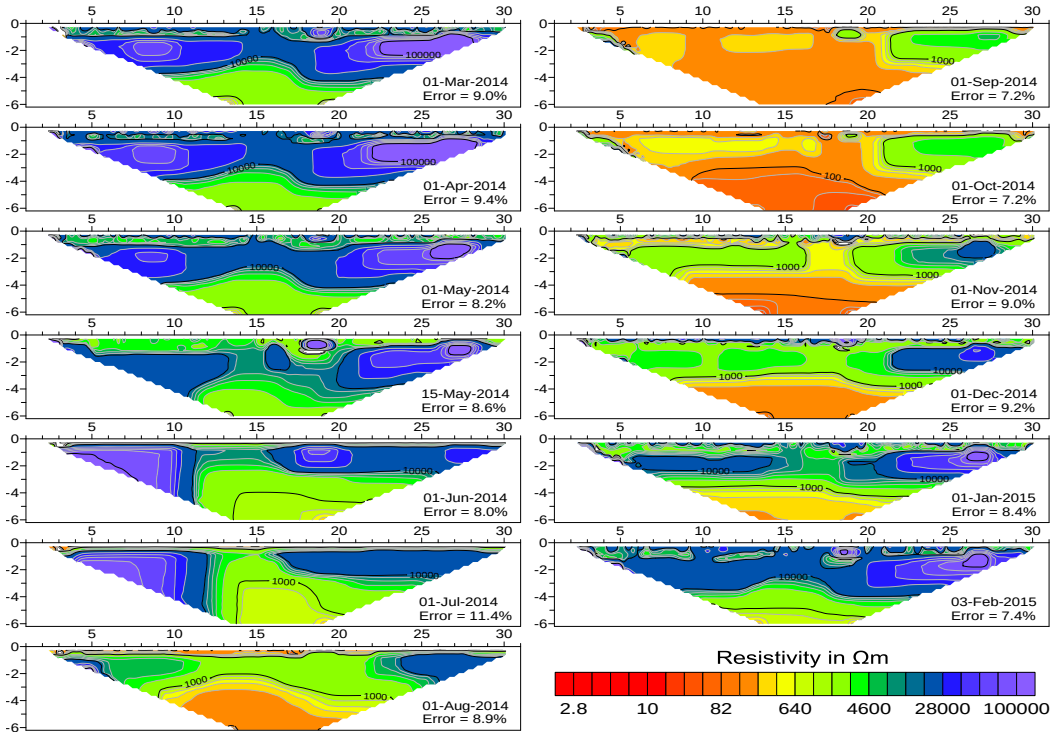

Figure 8: Inversions of time lapse Gradient data illustrate resolution and equivalency problems in interpretation of 2D acquisitions. Plots show evolution of ground resistivity throughout one year between 1st March 2014 – 1st February 2015. While the variation of resistivity in the upper 2 m can be attributed to ground temperature variation and freezing/thawing of soil moisture, same explanation does not hold for model layers below, where the ground is permanently frozen and temperature variation is minimal. Nevertheless the inverted models support assumption about ground structure with little horizontal variation and top-down freezing pattern, thus justifying the use of 1D-modeling in further processing and interpretation.

Aiming to produce resistivity models depicting more plausible resistivity variation, we focus in the following on 1D-inversions of the Wenner-Schlumberger acquisitions. 1D modeling allows for better control over the inversion process by constraining model geometry and resistivity variation in selected model layers. We fixed resistivities in the bottom of the modeled domain (where little to no resistivity variation is expected), thus forcing the inversion process to come up with more realistic resistivity values for upper model layers (corresponding to active layer and top of permafrost). Changing the fixed resistivity values below 4 m depth had no influence on quality of the model fit; however, it was important to fix the bottom resistivities to realistic values as they influence forward calculation of resistivities in upper model layers. Thus, Schlumberger soundings from the same location from years 1979 and 2007 with AB/2 electrode separation of up to 150 m were used to constrain resistivity values for the layers below 2 m depth. A resistivity distribution below 2 m that satisfied both the time lapse Wenner-Schlumberger datasets, as well as the Schlumberger soundings from 1979 and 2007, was consequently used in all of the starting models. Using more than 12 layers did not improve the inverted model fit. Initial resistivity distribution for layers in upper 2 m was based on daily averages of apparent resistivity at the corresponding pseudo-depth, so the initial model changed daily. Initial model setup for 1D-inversions is detailed on figure 9.

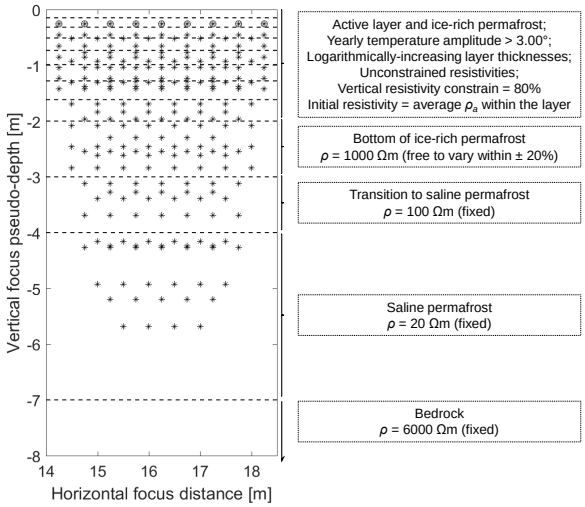

Figure 9: Initial model for 1D inversions. Star markers indicate points of maximum sensitivity of each of the Wenner-Schlumberger quadrupole configurations. Measurements at each vertical pseudo-depth (depth of maximum sensitivity of a given electrode configuration) were averaged, with standard deviation used as measurement error, resulting in a pseudo-1D dataset. Initial model for each inversion had the same geometry and constrains, but different initial resistivity distribution in the upper 2 m. Choice of depths and thicknesses of model layers was based on borehole information. The model consisted of 11 layers of fixed depths and thicknesses, with the 12^{th} layer extending to infinite depth. The model implicitly includes an air layer above the topmost ground layer. In the upper 2 m, layer boundaries were fixed at logarithmically increasing intervals. Initial resistivity values for each of these layers were specified as average apparent resistivities at the focus pseudo-depth closest to center of the given model layer. As an example, the initial resistivity value for model layers 1 and 2 is given by the average apparent resistivity at the topmost vertical focus pseudo-depth (encircled star markers). The resistivities in the upper 2 m of the model were allowed to vary freely during inversion, while vertical resistivity variation between neighboring model layers was limited to 80%. Initial/fixed resistivities of the layers below 2 m depth were determined by forward modeling and matching of simulated sounding curves to VES investigations from summer 1979 and 2007. The resistivity distribution below 2 m that satisfied data from 1979, 2007, as well as time lapse data from 2012-2015, was used for fixing resistivities in the lower layers of the model.

5 RESULTS

In the following sections, we present the results of monitoring from 21. September 2012 to 15. October 2015. Figure 10 provides an overview of the raw data considered in our interpretations. The air temperature data (10a) advise about the meteorological conditions at the site. The ground temperature (10b), soil moisture (10c) and resistivity (10d) data are then interpreted jointly to highlight the relationships between the processes.

5.1. In-situ unfrozen water content and freeze-thaw hysteresis

The unfrozen water content measurements (figure 10b) are strongly influenced by atmospheric conditions and exhibit a seasonal pattern. The maximum volumetric water content of approximately 70% at 0.3 m depth is measured in the middle of June and again at the beginning of September. Between the two maxima, increased water circulation and soil drying drive water content variation independently of the ground temperature. Zero-curtain is observed from beginning of October at 0.3 m depth, and lasts for approximately 4 weeks; meanwhile the unfrozen water content decreases steadily. From the onset of freezing down to ground temperature of $-4\,°C$, the volumetric unfrozen water content decreases from 70% to 25%. The minimum observed winter temperature at 0.3 metre depth is $-17\,°C$ and the corresponding minimum water content is 18%.

Unfrozen water content dynamics is distinctly different between periods of ground freezing and thawing. Freezing is a slow process, while thawing of the same volume of water is comparatively faster. Water content during freezing is consistently higher than during thawing at the same ground temperature (figure 11a). Different freezing/thawing patterns can be observed even during events of partial thawing during frozen season. Nevertheless, the freezing and thawing patterns respectively remain the same every year (figure 11b, c). No significant inter-annual changes in total unfrozen water content levels were observed during the three years of monitoring.

Complexity of phase change processes can only be captured by high sampling frequency. Notably during thawing, the freeze-thaw hysteresis can only be clearly resolved if up to eight water content measurements per day are available.

Ground temperature vs. unfrozen water content relationship

It has been well established (Lovell, 1957; Romanovsky et al., 2000; Nicolsky et al., 2007) that at full saturation, UWC can be derived from soil temperature (T) using the empirical relationship:

$$\theta = \eta \cdot \phi, \quad \phi = \begin{cases} S & T \geq T^* \\ \alpha |T_f - T|^{-\beta} & T < T^* \end{cases}, \tag{2}$$

where θ is the volumetric unfrozen water content of the bulk soil $[m^3_{water}/m^3_{soil}]$, η is the porosity $[m^3_{voids}/m^3_{soil}]$, ϕ is the volumetric unfrozen pore water fraction $[m^3_{water}/m^3_{voids}]$, S is the water saturation $[m^3_{water}/m^3_{voids}]$ (assumed unity in this study) and α and β are empirical constants describing intrinsic freezing characteristics of the given soil. T^* is the effective freezing point of the sample - the lowest temperature at which all the water in the sample is unfrozen ($\phi = S$), and is given by:

$$T^* = T_f - \left(\frac{S}{\alpha}\right)^{-\frac{1}{\beta}}, \tag{3}$$

where T_f is the freezing point of the pore water as a free substance.

We used the equations 2 and 3 to model the volumetric unfrozen water content using soil temperature measurements from soil moisture probes as input. Due to the freeze-thaw hysteresis, two sets of parameters – $[\alpha_f, \beta_f]$ for freezing and $[\alpha_t, \beta_t]$ for thawing – are needed to describe the water content variation accurately. Based on three freeze-thaw cycles, we defined the freezing season as starting when the maximum active layer thickness is reached (beginning of September) and ending when the lowest ground temperatures are recorded

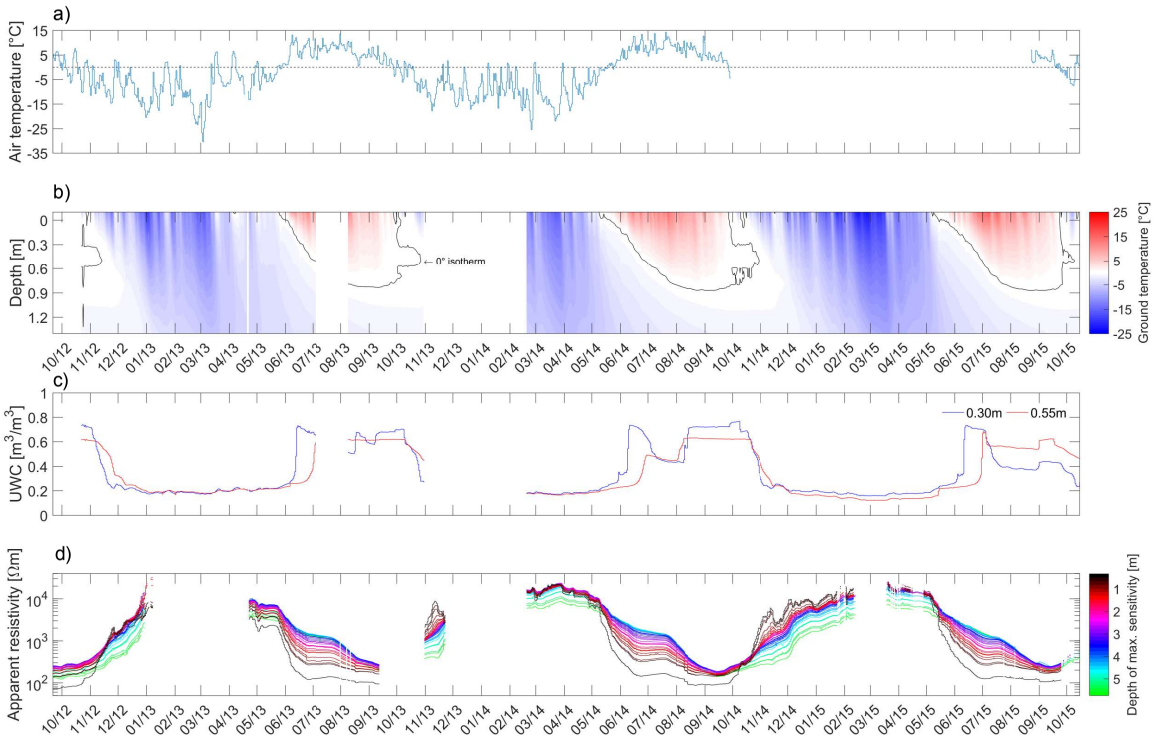

Figure 10: Timeseries of all the raw monitoring data. Note the different depth scale for figures c) and d). (a) Air temperature, daily averages of 8 records. (b) Ground temperature from MRC probe, daily averages of 8 records at 16 depths. (c) Unfrozen water content from two HydraProbe sensors placed at two depths in the active layer, daily averages of 8 records. (d) Apparent resistivity from the Wenner-Schlumberger configuration. Up to nine 4-electrode measurements at each focus pseudo-depth were averaged and are distinguished by the color gradient.

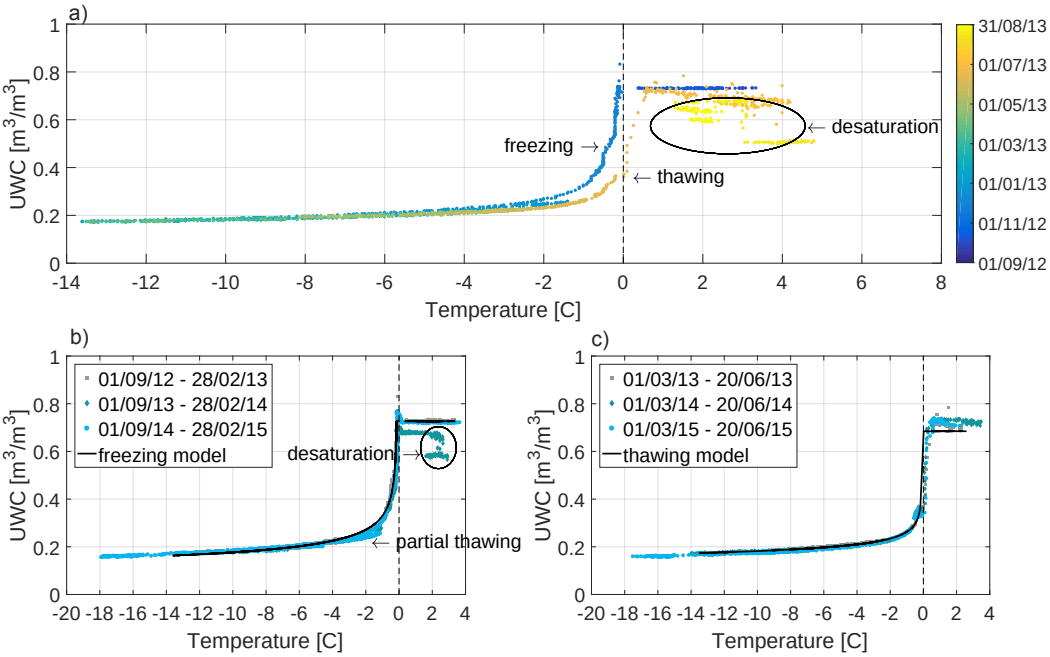

Figure 11: a) Field measurements (8 records/day, at 0.3 m depth) between 1st September 2012 and 31st August 2013 show the in-situ hysteretic variation of UWC during a course of one year. Desaturation due to water runoff and drying is observed after complete ground thawing at the given depth (after ca 25th June). b) The UWC follows the same freezing pattern year after year, as concluded from three consecutive freezing periods (1st September - 28th February, years 2012/2013 - 2014/2015). The freezing curve can be modeled with a set of soil-specific parameters $[a_{freeze}, b_{freeze}]$. Partial thawing is observed when the ground temperature fluctuates below 0°C. The slope of this partial thawing curve is the same as slope of the full thawing curve. c) UWC during thawing (1st March - 25th June, years 2013-2015) during the three consecutive thawing periods can be modeled with a set of soil-specific thawing parameters $[a_{thaw}, b_{thaw}]$.

(end of February). In the thawing season, only days with ground temperature below freezing point at a given depth are used for calibration.

We used the freezing season 2012/2013 and thawing season in 2013 to find the two sets of parameters $[\alpha_f, \beta_f]$ and $[\alpha_t, \beta_t]$ (table 5.1). The α and β parameters were calibrated in nonlinear least-squares fitting, with the cost function being the sum of squared differences between measured and modeled unfrozen water content. On figures 11b and 11c, we can appreciate the fit of modeled freezing and thawing curves to the water content measurements from three freezing and thawing seasons. The model is calibrated on the freeze-thaw period 2012/2013 and predicts water content variation in the following two years 2013/2014 and 2014/2015 within 5%.

Table 2: Unfrozen water content parameters, calibration for freezing and thawing periods separately. Table shows the optimal parameter estimates with 95% confidence intervals.

Freezing (1^{st} Sep. - 28^{th} Feb.)		Thawing (1^{st} Mar. - 20^{th} Jun.)	
porosity	0.73 ± 0.0018	porosity	0.69 ± 0.0047
α_f	0.44 ± 0.0031	α_t	0.38 ± 0.0084
β_f	0.26 ± 0.0039	β_t	0.15 ± 0.013
RMSE	0.014	RMSE	0.025

5.2. Analysis of apparent resistivity

According to Hilbich et al. (2011), analyzing apparent resistivity data prior to inverting them may improve interpretation of fast temporal changes of ground resistivity close to the surface. These fast changes otherwise tend to create inversion artifacts that complicate interpretation of results after inversion.

Figure 10d shows the evolution of daily average apparent resistivity values at each of the 33 pseudo-depths of the filtered Wenner-Schlumberger protocol. While the timeseries of just three years are too short to identify inter-annual tendencies, daily and seasonal changes are clearly reflected in the apparent resistivity data. Variations in ground temperature and water content in the active layer are mirrored in acquisitions by electrode configurations with the highest vertical sensitivity in the depths of less than 1 m. Below 4 m, large resistivity variations (nearly 2 orders of magnitude between summer low and winter high, figure 12d) are unexpected, considering the minimal temperature variation, with yearly amplitude of <0.1°C.

5.3. Analysis of inverted resistivity

Timeseries of inverted resistivity soundings (figure 12c) clearly reflect processes of ground freezing and thawing. In summer, the inverted model suggests very low resistivities of the active layer in the order of 20 - 100 Ωm. The low-resistivity anomaly in August - October extends well below 1 m depth while based on ground temperature data (figure 12b), the thaw front does not exceed 0.9 m. As with the apparent resistivities (section 5.2), this overestimation of ground model parameters is likely due to the effects of equivalency and anisotropy. The zero-curtain period during freezing typically lasts for up to 30 days during the month of October. The decrease of unfrozen water content during the isothermal process of latent heat extraction causes a sharp increase of ground resistivity by two orders of magnitude, from approximately 20 Ωm to approximately 2 kΩm. The resistivity changes associated with the zero-curtain effect are observed deeper in the inverted models than where phase change is actually occurring based on the temperature record (between 0.7 - 1 m instead between 0.5 - 0.7 m). In winter, resistivities in the top-most model layer reach the order of 10^4 Ωm.

The resistivity soundings successfully register several warmer events during the freezing period when ground temperature is overall below 0 °C. An example is a warmer period lasting for approximately 10 days in November 2014. The ground temperature increase from −4.3 °C to −1.2 °C at 0.3 m depth causes partial thawing and unfrozen water content increase from 22% to 26%. This is reflected by inverted resistivities dropping from 5.5 kΩm to 1.3 kΩm in the top 30 cm of the inverted model. These observations evidence

that the resistivity soundings are very sensitive to sub-zero water content changes in the ground and can therefore successfully identify ongoing thawing in warm permafrost.

Occasional water infiltration and percolation during thawing period and summer months does not noticeably influence the inverted resistivity models, likely due to a high saturation and low hydraulic conductivity of the clayey soil at the site.

5.4. Inverted resistivity, ground temperature and unfrozen water content relationships

We compared the inverted resistivity timeseries from the 2nd model layer (depth $\approx$ 0.15 - 0.32 m) to temperature and unfrozen water content measurements from soil moisture sensor at 0.3 m depth. The rate of resistivity increase during the zero-curtain periods and initial phase of ground **freezing** corresponds well to the unfrozen water content decrease (figure 13). From the onset of freezing to a ground temperature of $-4\,°C$ the volumetric water content is reduced by 45% at 0.3 m depth. This is accompanied by an increase in ground resistivity by two orders of magnitude, from $10^2\,\Omega$m to $10^4\,\Omega$m, within a period of four weeks. Resistivity at the lowest measured ground temperatures ($-17\,°C$ at 0.3 m depth, while corresponding minimum water content is 18%) could not be measured due to high electrode grounding resistances reaching up to 170 kΩ. However, the maximum recorded resistivities are in the range of $10^4\,\Omega$m at a ground temperature of $-10\,°C$. While there is a good correlation between fluctuations of resistivity and unfrozen water content in the frozen period, amplitudes of the resistivity fluctuations are larger than those of the unfrozen water (figure 13b). We speculate that variation in the electrode grounding resistances (correlated with surface temperature) (Tomaskovicova et al., 2016) contributes to larger amplitude excursions of the observed resistivities.

During **thawing**, the rate of decrease in ground resistivity is faster than the corresponding increase in unfrozen water content. Consequently, for comparable water contents, the resistivity observed during thawing is one order of magnitude *lower* than the resistivity during freezing (figure 13b). These observation suggest hysteresis in unfrozen water content-electrical resistivity relationship that is further addressed in Discussion (section 6). In mid-June, when frost table progressed below the soil moisture probe, the electrical resistivity further slightly decreases while the water content decreases. This may be an inversion artifact, as the distance to the high contrast layer boundary is increased.

6 DISCUSSION

Discussion is divided into two sections due to the scope of this study involving both technical details of the monitoring installation and description of environmental processes. First, we address challenges and practical solutions related to data acquisition and processing (6.1). Next, we discuss the in-situ processes and relationships between observed parameters (6.2).

6.1. Data acquisition and processing

Among the most important considerations for a **successful design of a monitoring project** in a remote area are:

1. **Power supply and backup** The high power consumption of our monitoring system would have been difficult to accommodate using alternative energy sources at this particular site, given the limited to no solar irradiation and risk of icing on wind turbine blades during the most power-demanding winter months. Connection to the power-grid was luckily possible close to the site, and backup battery packs ensured smooth operation through occasional power outages.

2. **Optimization of electrode design** At this particular monitoring site, the mesh electrodes proved to be a significant improvement over the originally-devised rod electrodes. Previous investigations have documented that the choice and effect of different electrode designs depend on the site conditions, in particular the lithology (Tomaskovicova et al., 2016).

3. **Data backup, transmission and remote control** Access to the system in between site visits not only allows for data backup and continuous analysis, but also for identification of errors, remote reprogramming and better planning of maintenance tasks during site visits.

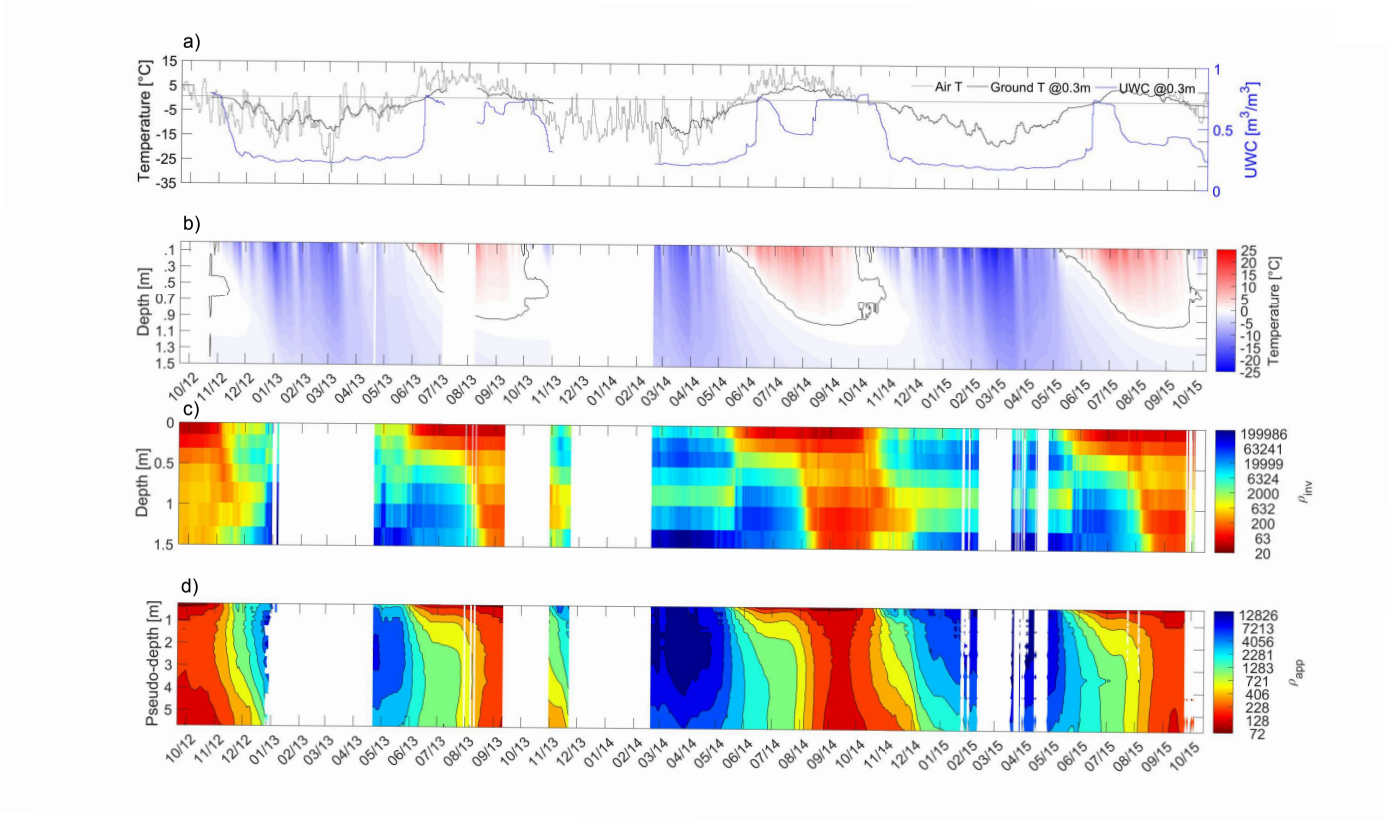

Figure 12: (a) Timeseries of air temperature, ground temperature (from soil moisture sensor) with unfrozen water content at 0.3 m depth. (b) Timeseries of ground temperature profiles down to 1.5 meters depth, data from MRC probe. (c) Timeseries of inverted 1D resistivity soundings measured by the Wenner-Schlumberger protocol. The plot is zoomed to the upper 1.5 meters of the profile to highlight the resistivity changes in the active layer. (d) Timeseries of apparent resistivity soundings. The apparent resistivity value for each day for every vertical focus pseudo-depth is averaged from up to nine acquisitions at that depth level. Date ticks indicate the first day of every month.

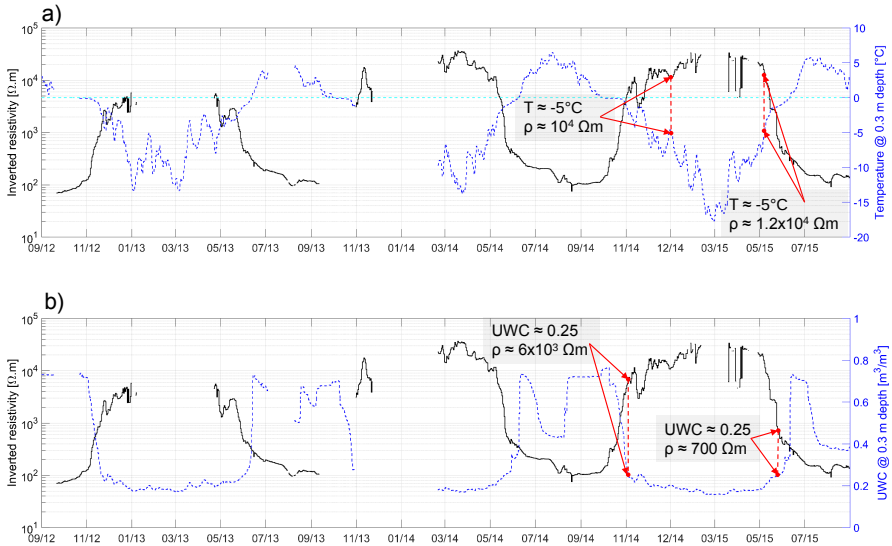

Figure 13: Timeseries of inverted resistivity from the 2nd model layer between 0.15 and 0.32 m compared with (a) the ground temperature and (b) unfrozen water content at 0.3 m depth (both daily averages of 8 measurements from soil moisture sensor). The dependence of inverted resistivity on water content (b) exhibits strong hysteresis effects, with resistivity during freezing one order of magnitude higher than during thawing at the same unfrozen water content (example November 2014 vs. May 2015). Comparison of inverted resistivity with ground temperature shows more proportional relationship (a), with resistivities in the order of $10^4\,\Omega$m at $-5\,^{\circ}$C during both freezing and thawing (example December 2014 vs. May 2015).

The main advantage of time-lapse monitoring with permanently installed electrodes is that the location of the electrodes can be considered constant. Consequently, smaller changes in the measured properties should be observable and linked to ongoing environmental processes. However in reality, the installations may still undergo changes that do not directly relate to the processes under investigation, especially if the monitoring project spans several seasons. For example, the **electrode grounding resistances** are affected by half-space resistivity distribution as well as changes in resistivity in the alteration zone in the immediate vicinity of the electrodes, and can amount up to approximately 170 kΩ in frozen soil conditions at the Ilulissat site. Depending on ERT system specifications, this magnitude of grounding resistances can lead to errors in resistivity measurements as large as 10% (Tomaskovicova et al., 2016). In addition to temperature-dependent grounding resistances, the soil structure around the electrodes changes with repeated cycles of freezing and thawing. As reported from laboratory experiments, ice buildup around the electrodes may effectively isolate some of them from the surrounding soil.

Inversion of the ERT acquisitions in this particular geological setting was seriously affected by **equivalency and anisotropy**. The source of anisotropy is notably the ice-rich layer observed in the top part of the permafrost. A drilling campaign in August 2013 close to the ERT profile confirmed the presence of thick and irregularly oriented ice lenses at the depth between 1.0 - 1.5 m (figure 14).

Figure 14: Ice-rich permafrost sample, 26 cm long, extracted from the depth between 1.19 - 1.45 m ca. 20 m east of the ERT profile. Back-lit photo highlights presence of nearly pure ice at the top of permafrost (photo: L. Lindhardt Pedersen).

A consequence of anisotropy is equivalency (Maillet, 1947; Parasnis, 2012). Due to the extremely resistive ice-rich layer, thicknesses as well as resistivities of the underlying low-resistivity saline permafrost were not properly resolved. The ambiguity of interpretation can be only partially resolved by using knowledge of geology of the area, and when available, using data in different measurement configuration for constraining the inversion. Our experience highlights the importance of critical interpretation of inverted resistivity models from permafrost settings.

6.2. In-situ processes

The **unfrozen water content hysteresis** is well-known in soil science where it is usually associated with water retention curves and processes of wetting and drying. The amount of liquid retained in a porous medium is not uniquely defined by the value of matric potential but is also dependent on the "history" of wetting and drying. Among the most important explanations of soil moisture hysteresis are those associated

with capillary theory. Since the size of void at the air-water interface determines the capillary head, in case of dropping water column, a small void may develop a meniscus which can support the water in larger voids below its surface, although it could not raise the water past these large voids (e.g. Lambe and Whitman (1969); Lal and Shukla (2004)). Soil freezing is a dehydration process analogous to the drying in soils above 0 °C (Koopmans and Miller, 1966; Farouki, 1981; Krzewinski and Tart Jr, 1985). It is therefore reasonable to assume that parallels exist in the mechanisms giving rise to water content hysteresis in soils undergoing phase change.

In timeseries of unfrozen water content (figure 13b), at the end of each thawing event (end of June at 0.3 m depth), the soil reaches a very high water content, up to approximately 70% (according to the soil moisture probe). This is likely due to melting of ice lenses: to begin with, the water has nowhere to drain, as the ground below is still frozen. The drainage will progress as more and more of the active layer thaws and the soil structure rearranges itself as the water drains away. Fissures that occur particularly in fine-grained soil following repeated cycles of freezing and thawing cause higher water permeability and facilitate more rapid moisture redistribution in thawing soil (Czeratzki and Frese, 1958; Tsytovich, 1964). Excess water starts to disappear shortly after the water content maximum, with part of it satisfying hydration needs of the clay minerals and the remainder being displaced by gravitational forces (Tsytovich, 1964).

Ground resistivity is frequently used as proxy for estimation of soil moisture content, ice content changes and vice-versa (Archie et al., 1942; Hauck, 2002; Glover, 2010; Pellet et al., 2016). While the bulk ground resistivity depends on soil mineralogic composition, porosity, fraction of unfrozen pore water, and geochemical composition of the pore water (Hoekstra et al., 1975; Friedman, 2005), the aqueous solution is, in most cases, the main conducting phase in the soil. The aqueous solution and the ice content are also the only phases that substantially change proportions over the course of a year. Comparison of indirect measurements from the ground surface (resistivity) with point observations at a specific depth (temperature and moisture content) inherently faces scale and resolution issues. Furthermore, assumption of homogeneous half-space during inversion does not hold in a setting in which top-down freezing and thawing cause a layered earth structure with large resistivity contrasts. Nevertheless, the comparison in the present study reveals clearly defined **relationships between ground temperature, soil moisture and ground resistivity** (figure 15). The unfrozen water content hysteresis can be appreciated in data from all three available freeze-thaw seasons 2012 - 2015 (figure 15a, d, g). The inverted resistivity shows repeated hysteretic behavior in relation to temperature (figure 15b, e, h). This is expected, considering the temperature-water content hysteresis and resistivity dependence on water content. However the relationship between resistivity and unfrozen water content exhibits hysteresis too (figure 15c, f, i), with inverted resistivities up to one order of magnitude higher during freezing than during thawing at the same unfrozen water content.

It has been recognized in laboratory conditions that because of hysteresis effects, soils may show markedly different properties at the same water content, depending on whether this content was reached by wetting or by drying. This has been demonstrated for the heat capacity by Williams (1963) and Carles M et al. (2011), for thermal conductivity by Farouki (1965) and for electrical resistivity by Longeron et al. (1989), Knight (1991), and recently by Ruggeri et al. (2015). In all the studies, the recorded thermal and electrical properties were higher during drying than during wetting. In field conditions, Overduin et al. (2006) observed pronounced hysteresis of ground thermal conductivity and unfrozen water content during three cycles of freezing and thawing. They also report a sharp transition from frozen to thawed thermal conductivities during thaw, as opposed to a three-month transition period during ground freezing. This is similar to the fast rate of thawing versus slower freezing observed in the present study (figure 11); some of the mentioned laboratory studies also confirmed faster wetting rates compared to slower drying rates.

Results of Knight (1991) on electrical hysteresis of partially-saturated sandstones in particular show striking similarities to our field experience with electrical hysteresis during freezing and thawing of clayey soil. Similarly, we identify three stages of the relationship between electrical resistivity and water content (figure 15c):

1. **Region 1 - Frozen soil:** Volumetric unfrozen water content ≈17 - 23%. Ground temperature up to ≈−3 °C. The resistivity changes rapidly even with small changes in liquid water content. No hysteresis is observed.

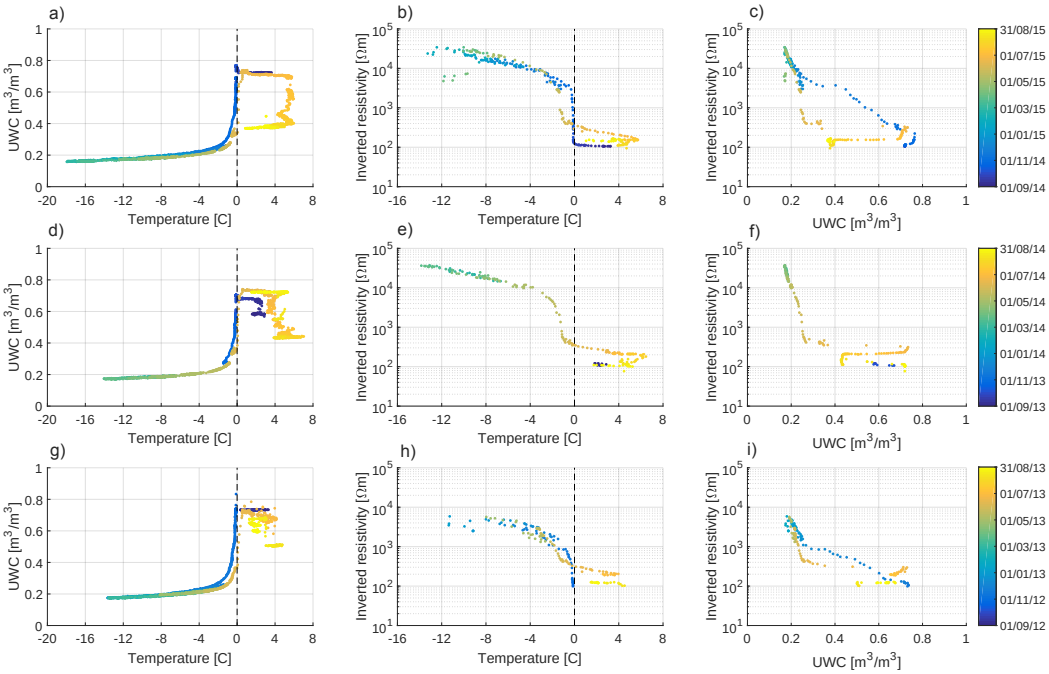

Figure 15: Scatter plots depicting hysteretic nature of dependence of ground temperature, inverted resistivity and unfrozen water content. Measurements of water content and temperature are from the HydraProbe at 0.3 m depth. The inverted resistivities are extracted from model layer between 0.15 - 0.32 m depth. Pictured are three freeze-thaw cycles (from-to 1stSeptember) 2012/2013 (a - c) 2013/2014 (d - f) and 2014/2015 (g - i); color gradient indicates the time scale.

2. **Region 2 - Freezing/thawing soil:** Volumetric unfrozen water content ≈23 - 70%. Hysteresis is pronounced in the freeze-thaw cycle, with resistivity during freezing consistently higher than resistivity during thawing at the same water content.

3. **Region 3 - Thawed soil:** Following the complete ground thawing in June/July and up until the beginning of the new freezing cycle at the beginning of October (i.e. when the ground temperatures are above the freezing point), changes in electrical resistivity are not directly controlled by ground temperature variation.

Suggested explanations for the electrical hysteresis in soil involve changes in pore-scale fluid distribution associated with saturation history (Knight et al., 1987; Knight, 1991), as well as surface conduction at the air/water interface resulting from charge density and zeta potential at the air/water interface (McShea and Callaghan, 1983; Laskowski et al., 1989; Knight, 1991).

We confirm, based on our field acquisitions, that resistivities differing by as much as one order of magnitude may be recorded at the same level of unfrozen water content due to freeze-thaw hysteresis. Furthermore, the magnitude of resistivity variation in the coldest portion of the year is larger than corresponding unfrozen water content variation. This implies that commonly used empirical resistivity mixing relations such as Archie et al. (1942), Somerton (1992); Guéguen and Palciauskas (1994) and Glover (2010) do not fully capture the complexity of the real-world processes. Large errors can be introduced into estimation of unfrozen water content from electrical resistivity if hysteresis effect is omitted from the consideration.

7 CONCLUSIONS

In this study, we describe what is presently the longest reported monitoring effort of high-latitude permafrost extending over three freeze-thaw cycles, and involving time-lapse acquisitions of ground electrical resistivity, soil moisture and temperature. The resistivity acquisition system is based on an array of 64 buried electrodes connected to a resistivity meter through a multiplexor. As the instruments were not designed for stand-alone, long-term acquisitions, the establishment of a remote control solution proved crucial for obtaining near-complete timeseries of resistivity data. Extended periods of station shutdown were eliminated, and the flexibility of the system was increased by gaining access to remote reconfiguration of acquisition protocols and automated data transmission.

Permanent installation - as opposed to varying sensor placement upon repeated one-off surveys - is expected to reduce measurements errors. Nevertheless, processes such as temperature-dependent grounding resistances and soil structural changes due to freeze-thaw cycles cause changes to the quality of sensor installation that cannot be entirely eliminated. Consequently, they should be considered during quantification of inter-annual changes in monitored variables.

We demonstrates under authentic field conditions the improvement that can be achieved in completeness of resistivity acquisitions by using optimized electrode shapes. The replacement of electrodes resulted in more complete resistivity timeseries over challenging winter months and overall reduced grounding resistances in both summer and winter seasons.

In spite of the high grounding resistances encountered at the site, percentage of discarded measurements was low. On the other hand, the interpretations of resistivity measurements were affected by serious equivalency issues that complicated correct resolution of resistivity dynamics below the active layer. This problem, inherent to mapping contrasting resistivity boundaries, highlights the necessity of careful interpretation of inverted resistivity models from permafrost settings.

We conclude that analogy of the water content hysteresis, known from studies on partially-saturated soils above 0 °C, exists in seasonally-frozen portion of the ground in permafrost areas. Magnitude of the hysteresis effect means that it should be considered in thermal modeling of permafrost, as water content is one of the key parameters influencing bulk soil thermal properties. The rate of phase change during thawing is markedly faster than during freezing. This is likely to translate into rather sudden unfrozen water content – and consequently ground stability – changes upon permafrost thawing in this area.

Inverted resistivity models correctly reflected changes in ground conditions throughout the seasons. The ground resistivity dependence on unfrozen water content exhibits hysteretic pattern, with resistivities during freezing up to one order of magnitude higher than during thawing at the same water content. This behavior, previously identified in laboratory studies for analogous processes of drying/wetting, is manifested in a seemingly identical manner in-situ, for seasonally-frozen soil. The existence of a resistivity hysteresis complicates the quantitative interpretation of unfrozen water contents from time-lapse resistivity monitoring surveys. Consequently, ground resistivity dependence on history of freeze-thaw cycles should be considered when using the geoelectrical data for quantitative interpretation of unfrozen water content changes in seasonally frozen portion of the ground.

REFERENCES

Agergaard, F. A., Ingeman-Nielsen, T., 2011. Modelling unfrozen water content in a silty clay permafrost deposit. In: Proceedings of 2011 Pan-am Cgs Geotechnical Conference.

Archie, G. E., et al., 1942. The electrical resistivity log as an aid in determining some reservoir characteristics. Transactions of the AIME 146 (01), 54–62.

Bennike, O., Björck, S., 2002. Chronology of the last recession of the greenland ice sheet. Journal of Quaternary Science 17 (3), 211–219.

Brown, J., Ferrians Jr, O., Heginbottom, J., Melnikov, E., 1998. revised february 2001. circum-arctic map of permafrost and ground-ice conditions. boulder, co: National snow and ice data center/world data center for glaciology. Digital media.

Cappelen, 2013. Technical report 14-08. weather observations from greenland 1958-2012. observation data with description. Tech. rep., Danish Meteorological Institute.

Carles M, R., Ramon, J., Francesc, F., 2011. Influence of the hysteretic behaviour on silt loam soil thermal properties. Open Journal of Soil Science 2011.

Czeratzki, W., Frese, H., 1958. Importance of water in formation of soil structure. Highway Research Board Special Report (40).

Dahl-Jensen, D., Mosegaard, K., Gundestrup, N., Clow, G. D., Johnsen, S. J., Hansen, A. W., Balling, N., 1998. Past temperatures directly from the greenland ice sheet. Science 282 (5387), 268–271.

Dahlin, T., Zhou, B., 2006. Multiple-gradient array measurements for multichannel 2d resistivity imaging. Near Surface Geophysics 4 (2), 113–123.

Doetsch, J., Ingeman-Nielsen, T., Christiansen, A. V., Fiandaca, G., Auken, E., Elberling, B., 2015. Direct current (dc) resistivity and induced polarization (ip) monitoring of active layer dynamics at high temporal resolution. Cold Regions Science and Technology 119, 16–28.

Farouki, O. T., 1965. Physical properties of granular materials. Soil Science 99 (5), 354.

Farouki, O. T., 1981. The thermal properties of soils in cold regions. Cold Regions Science and Technology 5 (1), 67–75.

Foged, N., 1979. Engineering geological investigations of quaternary marine clay deposits on west greenland. Ph.D. thesis, Ph. D. Thesis. The Institute for Applied Geology. Technical University of Denmark,.(In Danish with English Overview).

Foged, N., Ingeman-Nielsen, T., 2008. Permafrost in marine deposits at ilulissat airport in greenland, revisited. In: Ninth International Conference e on Permafrost (445-450).

Friedman, S. P., 2005. Soil properties influencing apparent electrical conductivity: a review. Computers and electronics in agriculture 46 (1), 45–70.

Glover, P. W., 2010. A generalized archie's law for n phases. Geophysics 75 (6), E247–E265.

Guéguen, Y., Palciauskas, V., 1994. Introduction to the physics of rocks. Princeton University Press.

Hammer, C. U., Johnsen, S. J., Clausen, H. B., Dahl-Jensen, D., Gundestrup, N. S., Steffensen, J. P., 2001. The paleoclimatic reocrd from a 345 m long ice core from the hans tausen iskappe. Meddelser Om Grønland, Geoscience.

Hauck, C., 2002. Frozen ground monitoring using dc resistivity tomography. Geophysical research letters 29 (21).

Hauck, C., Bach, M., Hilbich, C., 2008. A 4-phase model to quantify subsurface ice and water content in permafrost regions based on geophysical datasets. In: Proceedings Ninth International Conference on Permafrost, June. pp. 675–680.

Hilbich, C., Fuss, C., Hauck, C., 2011. Automated time-lapse ert for improved process analysis and monitoring of frozen ground. Permafrost and Periglacial Processes 22 (4), 306–319.

Hilbich, C., Hauck, C., Hoelzle, M., Scherler, M., Schudel, L., Völksch, I., Vonder Mühll, D., Mäusbacher, R., 2008. Monitoring mountain permafrost evolution using electrical resistivity tomography: A 7-year study of seasonal, annual, and long-term variations at schilthorn, swiss alps. Journal of Geophysical Research: Earth Surface 113 (F1).

Hoekstra, P., Sellmann, P. V., Delaney, A., 1975. Ground and airborne resistivity surveys of permafrost near fairbanks, alaska. Geophysics 40 (4), 641–656.

Ingeman-Nielsen, T., Foged, N., Romanovsky, V., Marchenko, S., Daanen, R., Svendsen, K., 2010. Geotechnical implications of a warming climate in greenland evaluated on the basis of permafrost temperature reanalysis and model projections. In: Poster presented at the European Permafrost Conference June.

Ingeman-Nielsen, T., Foged, N. N., Butzbach, R., Jørgensen, A. S., 2008. Geophysical investigations of saline permafrost at ilulissat, greenland. In: Ninth International Conference on Permafrost. Institute of Northern Engineering, University of Alaska Fairbanks.

Ingeman-Nielsen, T., Tomaškovičová, S., Dahlin, T., 2016. Effect of electrode shape on grounding resistances—part 1: The focus-one protocol. Geophysics 81 (1), WA159–WA167.

Knight, R., 1991. Hysteresis in the electrical resistivity of partially saturated sandstones. Geophysics 56 (12), 2139–2147.
Knight, R., Nur, A., et al., 1987. Geometrical effects in the dielectric response of partially saturated sandstones. The Log Analyst 28 (06).
Koopmans, R. W. R., Miller, R., 1966. Soil freezing and soil water characteristic curves. Soil Science Society of America Journal 30 (6), 680–685.
Krautblatter, M., Hauck, C., 2007. Electrical resistivity tomography monitoring of permafrost in solid rock walls. Journal of Geophysical Research: Earth Surface 112 (F2).
Krautblatter, M., Verleysdonk, S., Flores-Orozco, A., Kemna, A., 2010. Temperature-calibrated imaging of seasonal changes in permafrost rock walls by quantitative electrical resistivity tomography (zugspitze, german/austrian alps). Journal of Geophysical Research: Earth Surface 115 (F2).
Krzewinski, T. G., Tart Jr, R. G., 1985. Thermal design considerations in frozen ground engineering. ASCE Publications.
Lal, R., Shukla, M. K., 2004. Principles of soil physics. CRC Press.
Lambe, T., Whitman, R., 1969. Soil mechanics, 553 pp. Jhon Wiley & Sons, N. York.
Laskowski, J., Yordan, J., Yoon, R., 1989. Electrokinetic potential of microbubbles generated in aqueous solutions of weak electrolyte type surfactants. Langmuir 5 (2), 373–376.
Loke, M., 1999. Electrical imaging surveys for environmental and engineering studies. A practical guide to 2.
Longeron, D., Argaud, M., Feraud, J.-P., et al., 1989. Effect of overburden pressure and the nature and microscopic distribution of fluids on electrical properties of rock samples. SPE Formation Evaluation 4 (02), 194–202.
Lovell, C., 1957. Temperature effects on phase composition and strength of partially-frozen soil. Highway Research Board Bulletin (168).
Maillet, R., 1947. The fundamental equations of electrical prospecting. Geophysics 12 (4), 529–556.
McShea, J. A., Callaghan, I., 1983. Electrokinetic potentials at the gas-aqueous interface by spinning cylinder electrophoresis. Colloid & Polymer Science 261 (9), 757–766.
Nicolsky, D., Romanovsky, V., Tipenko, G., 2007. Using in-situ temperature measurements to estimate saturated soil thermal properties by solving a sequence of optimization problems. The Cryosphere 1 (1), 41–58.
Overduin, P. P., Kane, D. L., van Loon, W. K., 2006. Measuring thermal conductivity in freezing and thawing soil using the soil temperature response to heating. Cold Regions Science and Technology 45 (1), 8–22.
Parasnis, D. S., 2012. Principles of applied geophysics. Springer Science & Business Media.
Pellet, C., Hilbich, C., Marmy, A., Hauck, C., 2016. Soil moisture data for the validation of permafrost models using direct and indirect measurement approaches at three alpine sites. Frontiers in Earth Science 3, 91.
Rasch, M., 2000. Holocene relative sea level changes in disko bugt, west greenland. Journal of Coastal Research, 306–315.
Romanovsky, V., Osterkamp, T., et al., 2000. Effects of unfrozen water on heat and mass transport processes in the active layer and permafrost. Permafrost and Periglacial Processes 11 (3), 219–239.
Rosset, E., Hilbich, C., Schneider, S., Hauck, C., 2013. Automatic filtering of ert monitoring data in mountain permafrost. Near Surface Geophysics 11 (4), 423–433.
Ruggeri, P., Jougnot, D., Chavarriaga, R., Brandner, C., del Rocio Millán Ruiz, J., Linde, N., 2015. Studying the hysteretic behaviour of unconsolidated sediments using an electroencephalography apparatus: a laboratory study. In: EGU General Assembly Conference Abstracts. Vol. 17. p. 11381.
Somerton, W. H., 1992. Thermal properties and temperature-related behavior of rock/fluid systems. Vol. 37. Elsevier.
Telford, W. M., Telford, W., Geldart, L., Sheriff, R. E., 1990. Applied geophysics. Vol. 1. Cambridge university press.
Tomaskovicova, S., Ingeman-Nielsen, T., Christiansen, A. V., Brandt, I., Dahlin, T., Elberling, B., 2016. Effect of electrode shape on grounding resistances-part 2: Experimental results and cryospheric monitoring. Geophysics 81 (1).
Tomaskovicova, S., Paamand, E., Ingeman-Nielsen, T., Bauer-Gottwein, P., 2012. Coupled thermo-geophysical inversion for permafrost monitoring. In: 10th International Conference on Permafrost.
Tsytovich, N., 1964. Physical phenomena and processes in freezing, frozen and thawing soils.
Williams, P., 1963. Specific heats and unfrozen water content of frozen soils. In: Proc. First Can. Conference Permafrost. pp. 109–126.

APPENDIX D

Conference Abstract - TICOP 2012, Salekhard

Coupled Thermo-Geophysical Inversion for Permafrost Monitoring

S. Tomaškovičová, E. Paamand, T. Ingeman-Nielsen
Arctic Technology Centre, Department of Civil Engineering
P. Bauer-Gottwein
Department of Environmental Engineering, Technical University of Denmark, Kongens Lyngby, Denmark

Motivation

Significant permafrost degradation in the Arctic region has been predicted as a result of climate change, causing a risk of thaw settlements and mechanical failures of buildings and constructions in affected areas. Conventional approaches in permafrost monitoring, including thermal measurements, core analyses and borehole geophysical logs, have serious drawbacks because of their discrete character and high cost. In order to accurately simulate and forecast the thermal regime of the active layer and permafrost, this work aims at combining traditional thermal measurements with diverse geophysical data (mainly DC geoelectrical measurements) in a coupled inversion scheme using only air temperature data and time lapse geophysical measurements to set up and calibrate a heat transport model. The main benefits are reduced cost of geotechnical surveys, improved interpretation of soil properties, improved mapping of the vertical and horizontal extent of permafrost as well as enhanced model skill in predictions of future permafrost changes.

Approach

The generalized workflow is exemplified by use of geoelectrical data for heat model calibration (figure 1). A heat transport model (HTM) is developed calculating the temperature profile of the soil. The phase distribution between water and ice is found from the soil unfrozen water content and an equivalent 1D-multilayer geoelectrical profile is constructed using Archie´s law. The apparent resistivity is calculated based on the multilayer model and compared to measured electrical soundings. Finally, the parameters for the heat transport model are calibrated to fit the combined dataset of temperatures and apparent resistivities using a weighted iterative least squares approach. In practice, any kind of geophysical data can be used as long as a petrophysical relationship between any simulated state of the HTM and the relevant geophysical property of ground can be established.

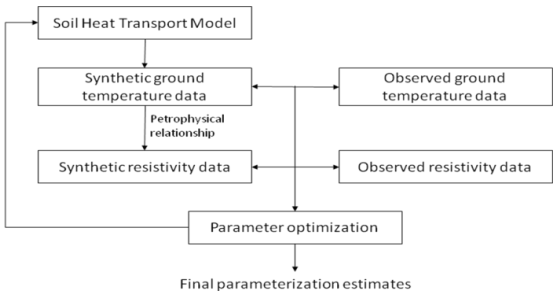

Fig. 1: Illustration of coupled inversion based on thermal measurements and electrical resistivity data.

Heat transport model

The HTM is used to describe the spatio-temporal evolution of subsurface temperature. The one-dimensional heat transport equation is [*Lunardini 1981*]:

$$c_e(x)\cdot\frac{\partial T}{\partial t}=-\frac{\partial}{\partial x}\left(-k_e(x)\cdot\frac{\partial T}{\partial x}\right)+S_s(x) \qquad (1)$$

where c_e is effective heat capacity (J/m^3/K ??), T is temperature (K), t is time (s), $k_e(x)$ is effective thermal conductivity ($W/m/K$) and S_s represents sources or sinks of heat (W/m^3). The phase change occurring at the transition between water and ice is regarded as an energy sink and is expressed as:

$$S_s(x)=-L\cdot\left(\frac{\rho_{ice}}{\rho_{water}}\right)\cdot\rho_{rock}\cdot\frac{\partial\theta_{ice}}{\partial t} \qquad (2)$$

where L is latent heat of fusion (J/kg_{ice}), ρ_{ice} is specific ice density (kg/m^3), ρ_{water} is specific water density (kg/m^3) and θ_{ice} is ice mass fraction based on dry weight of solids (kg/kg_{rock}).

Input parameters for the HTM are the specific heat capacities, specific thermal conductivities and specific densities of water, ice and rock, latent heat constant, water saturation, porosity and correlation coefficients a and b for unfrozen water content defined as [*Hoyer et al., 1975*]:

$$\theta_{water}(T)=a\cdot(273.15-T)^b \qquad (3)$$

for $T<T_{liq}$ (T_{liq} is temperature at which all the water is in the liquid form). The correlation coefficients are determined experimentally on the basis of dry weight of the material valid for saturated soils, relating them to the distinctive soil types. For the effective parameter estimation, the model domain is assumed to consist of a homogenous soil mixture of soil particles, water and ice and the effective parameters are derived as function of their respective volumetric fractions. Specific heat capacities of respective components are functions of temperature but vary a little in the range from 253.15 to 273.15 K [*Osterkamp 1987*] and are thus assumed constant. The resulting effective heat capacity is a product of volume fractional weighting of the specific heat capacities of the respective materials. Latent heat of fusion is incorporated in an apparent effective heat capacity and its temperature- and salinity-dependence is neglected. Density of water is set constant (1000 kg/ m^3) and density of ice is assumed to be equal to that of water. This assumption was proved satisfactory for both heat transport and apparent resistivity modeling.

The upper model boundary is prescribed by measured daily average soil surface temperatures from the investigation site (Ilulissat, West Greenland). The bottom boundary temperature is set to be constant in time. Consequently, to ensure stable conditions, the modeled domain needs to be deep enough (>20m). For each solving step taken by partial differential equation-solver (using MatLab built-in *pdepe*-function) the

phase distribution is found, the effective parameters are re-evaluated and used for calculating the temperature in time and space.

Geophysical resistivity model

The geophysical part of the modeling framework consists of a one-dimensional geoelectrical model with a large number of layers of equal thickness. For each layer-representative temperature, calculated based on eq. 1, the fractions of water, ice and rock are found. Input parameters for the resistivity model are specific densities and specific resistivities of water, ice and rock, water saturation, porosity, and correlation coefficients for the unfrozen water content. The effective bulk soil resistivity is established through rock-specific petrophysical relationships, based on a modified Archie´s law [*Hoyer et al., 1975*]

$$\rho_{pf} = \tau \cdot \Phi^{-m} \cdot \left(\frac{f_{water}}{\Phi} \right)^{1-n} \cdot \rho_{water} \cdot e^{-\left(\frac{T_\theta}{44.6} \right)} \qquad (4)$$

where ρ_{pf} is effective resistivity of the partially frozen soil, Φ is porosity (m^3/m^3), f_{water} is the volume fraction of liquid water in a sample (m^3/m^3), ρ_{water} is resistivity of the pore water (Ωm) and τ (tortuosity factor), n (saturation exponent of the soil related to pore geometry), m (porosity exponent, an intrinsic property of the soil related to the geometry of the electrically-conductive water network imposed by the pore walls or surfaces of solid insulating materials) are constants. T_θ is the temperature in degrees below 0°C, and the exponential term accounts for the resistivity of unfrozen water at lower temperatures.

Forward apparent resistivity response modeling is performed by the CR1Dmod program [*Ingeman-Nielsen & Baumgartner 2006*] and the result is compared to the geoelectrical measurements acquired on the investigation site.

Coupled thermo-geophysical inversion

The most significant changes in physical parameters occur during the phase change of water between the liquid and the solid form [*Scott et al., 1990*]. This phenomenon allows for finding a link between thermal and geophysical properties of the ground and enables the HTM-calibration.

Fixed parameters are used for the thermal properties of water and ice. The inversion is based on iterative least squares formulation. The cost function is the sum of squared deviations between measured and forward calculated apparent resistivities. This cost function is minimized by fitting the thermal properties of the HTM from which the resistivity profile was calculated rather than the input parameters for the resistivity model.

After single parameter calibration for each of the chosen calibration parameters, the most uncertain parameters with respect to the confidence intervals are re-calibrated in a paired calibration. Not more than two parameters can be fitted at the same time, otherwise the confidence limits get high. Thus fitting more parameters with thermo-geophysical inversion requires more time lapse data and possibly a better resistivity model to get more reliable results.

Parameters and sensitivity analysis

Sensitivity analysis of each of the input variables is conducted comparing its Composite Scaled Sensitivity (*css*) as a root mean square of the sensitivity among all depths and time steps. *css* is proportional to the absolute sensitivity in the dataset to the given input parameter. The sensitivity analysis is made for the HTM and the resistivity model separately to choose the focus for the calibration of the model. Both models showed the highest sensitivity to porosity and water saturation.

Preliminary results and further model development

In this initial study it was confirmed that time lapse geoelectrical signal contain information that may be used in the calibration of the soil HTM. Despite the number of simplifying assumptions it was found that a set of parameters existed for the HTM that reasonably described the heat transport between the atmosphere and the soil profile. If boundary temperatures and the specific electrical properties of the soil material are known, a reasonable calibration of the soil heat transport parameters may be obtained. A better calibration would be achieved from multi parameter calibration for which more time lapse series are needed. These are planned to be acquired by installation of semi-automatic geoelectrical acquisition system that would make possible to cover an entire active layer freezing/thawing period.

Further laboratory measurements are carried out in order to establish rock-specific petrophysical relationships linking thermal and physical properties. The empirical parameters will be used as constraints in the model optimization or as fixed parameters where necessary.

In the future, the model should be extended to 2 and possibly 3 spatial dimensions to give an overview of the permafrost table variations in larger context. Setting up the multilayer model for handling also electromagnetic measurements would allow for building a regional scale monitoring program for permafrost.

References

Hoyer, W.A., Simmons, S.O., Spann, M.M. & Watson, A.T. 1975. Evaluation of permafrost with logs. SPWLA 16th annual logging symposium.

Ingeman-Nielsen, T. & Baumgartner, F. 2006. CR1Dmod: A Matlab program to model 1D complex resistivity effects in electrical and electromagnetic surveys. Computers & Geosciences 32: 1411-1419.

Lunardini, V.J. 1981. Heat transfer in cold climates. Hanover, N.H., U.S. Army Cold Region Research and Engineering Laboratory.

Osterkamp, T.E. 1987. Freezing and thawing of soils and permafrost containing unfrozen water or brine. Water resources research 23: 2279-2285.

Scott, W.J., Sellmann, P.V., Hunters, J.A. 1990. Geophysics in the study of permafrost.

APPENDIX E

Conference Abstract - EGU 2013, Vienna

Geophysical Research Abstracts
Vol. 15, EGU2013-764, 2013
EGU General Assembly 2013

Coupled thermo-geophysical inversion for high-latitude permafrost monitoring – assessment of the method and practical considerations

Sonia Tomaskovicova (1), Eskild Paamand (2), Thomas Ingeman-Nielsen (1), and Peter Bauer-Gottwein (2)

(1) Technical University of Denmark, The Arctic Technology Centre, Department of Civil Engineering, Kgs. Lyngby, Denmark (soto@byg.dtu.dk), (2) Technical University of Denmark, Department of Environmental Engineering, Kgs. Lyngby, Denmark

The sedimentary settings of West Greenlandic towns with their fine-grained, often ice-rich marine deposits are of great concern in building and construction projects in Greenland, as they lose volume, strength and bearing capacity upon thaw. Since extensive permafrost thawing over large areas of inhabited Greenlandic coast has been predicted as a result of climate change, it is of great both technical and economical interest to assess the extent and thermal properties of such formations. Availability of methods able to determine the thermal parameters of permafrost and forecast its reaction to climate evolution is therefore crucial for sustainable infrastructure planning and development in the Arctic.

We are developing a model of heat transport for permafrost able to assess the thermal properties of the ground based on calibration by surface geoelectrical measurements and ground surface temperature measurements. The advantages of modeling approach and use of exclusively surface measurements (in comparison with direct measurements on core samples) are smaller environmental impact, cheaper logistics, assessment of permafrost conditions over larger areas and possibility of forecasting of the fate of permafrost by application of climate forcing.

In our approach, the heat model simulates temperature distribution in the ground based on ground surface temperature, specified proportions of the ground constituents and their estimated thermal parameters. The calculated temperatures in the specified model layers are governing the phase distribution between unfrozen water and ice. The changing proportion of unfrozen water content as function of temperature is the main parameter driving the evolution of electrical properties of the ground. We use a forward modeling scheme to calculate the apparent resistivity distribution of such a ground as if collected from a surface geoelectrical array. The calculated resistivity profile is compared to actual field measurements and a difference between the synthetic and the measured apparent resistivities is minimized in a least-squares inversion procedure by adjusting the thermal parameters of the heat model. A site-specific calibration is required since the relation between unfrozen water content and temperature is strongly dependent on the grain size of the soil.

We present details of an automated permanent field measurement setup that has been established to collect the calibration data in Ilulissat, West Greenland. Considering the station location in high latitude environment, this setup is unique of its kind since the installation of automated geophysical stations in the Arctic conditions is a challenging task. The main issues are related to availability of adapted equipment, high demand on robustness of the equipment and method due to the harsh environment, remoteness of the field sites and related powering issues of such systems.

By showing the results from the new-established geoelectrical station over the freezing period in autumn 2012, we prove the 2D time lapse resistivity tomography to be an effective method for permafrost monitoring in high latitudes. We demonstrate the effectivity of time lapse geoelectrical signal for petrophysical relationship calibration, which is enhanced comparing to sparse measurements.

APPENDIX F

Conference Abstract - GELMON 2013, Vienna

14

Comparison of alternative electrode types for improvement of electrode-ground coupling in highly-resistive environment. Experience from the time lapse geoelectrical station for high-latitude permafrost monitoring, Ilulissat, West Greenland

Tomaskovicova Sonia[1], Ingeman-Nielsen Thomas[1]
[1]*The Arctic Technology Centre - ARTEK, Department of Civil Engineering, Technical University of Denmark*

The contribution is concerning the experiments carried out in the spring 2013, having as purpose the improvement of grounding of the electrodes placed in fine-grained permafrost after we discovered that standard electrode types are surprisingly performing not well enough during the winter time (comparing to other, geologically less favorable sites in Greenland), when the ground resistance is extremely high.
The field experience revealed unexpected facts (unexpected based on previous experience) about problems with reliable ERT measurements that can be encountered in highly resistive environments (such as permafrost sites). We carried out a series of field test (and we still have ongoing laboratory test) in order to design the best electrode type for the challenging, highly resistive environments when reliable operation is required due to the remoteness of the sites.

Comparison of performance of different electrode types in extremely high ground resistivity conditions – case of automated high-latitude permafrost monitoring station (Ilulissat, West Greenland)

Sonia Tomaskovicova, Thomas Ingeman-Nielsen
The Arctic Technology Centre - ARTEK, Department of Civil Engineering, Technical University of Denmark

The extremely high contact resistances pose challenges to automated permafrost monitoring in remote areas, particularly in winter period. The electrode design is one of the important factors helping to maintain data quality when no electrode contact adjustment is possible prior to every single measurement sequence.
We have established a permanent high-latitude permafrost monitoring site in Ilulissat (West Greenland) in August 2012. Since then, the automated station has been collecting 1625 data points per day. The electrodes used on the profile were 10cm long steel rods inserted in the clayey material ca 10-20 cm below the ground surface. This electrode type was previously proved suitable at another permanent, though not automated station in Sisimiut (West Greenland) where the geology is even less favorable for good ground coupling then in Ilulissat. However, during the winter 2012/2013, major problems with the electrode contact resistances caused large gaps in the time lapse data series from the Ilulissat site.
Following series of field and laboratory experiments aimed to identify the optimal electrode type for the given setting, as well as to quantify the benefit of using a given electrode type. 3 compared electrode types include: 10 cm long steel rods, 10x5 cm steel plates and 10x10 cm metal mesh electrodes. In field conditions, both metal plates and mesh electrodes performed better then the originally used steel rods. The mesh electrodes reduced the contact resistance by as much as 61% (in average by 54%, measured 3 days after installation) and the plate electrodes reduced the contact resistance by 48% in average comparing to the steel rods with smaller surface area. The field results were confirmed in the laboratory, where different soil types and for different electrode types were used and contact resistance was measured at different temperature steps.

APPENDIX G

Conference Abstract - EUCOP 2014, Evora

Optimization of thermal parameters of frozen ground using surface geoelectrical data from permafrost monitoring and surface temperature measurements

Sonia Tomaskovicova, The Arctic Technology Centre, Technical University of Denmark, Denmark
Thomas Ingeman-Nielsen, The Arctic Technology Centre, Technical University of Denmark, Denmark
Peter Bauer-Gottwein, Department of Environmental Engineering, Technical University of Denmark, Denmark

Climate change is expected to significantly affect the Arctic regions. One of the effects of increase of mean annual air temperatures will be an increased soil warming. In the presence of permafrost, such a change of ground thermal regime will result in deepening of active layer, thawing of permafrost underneath and reduction of ground stability. In order to predict the extent of expected changes, it is desirable to have a modeling tool able to assess current and future thermal state of permafrost. Therefore we propose a method of calibrating ground thermal parameters based on non-invasive surface measurements, as opposite to direct borehole measurements and core sampling.

In our 1D inversion scheme, the observed apparent resistivities from a time-lapse ERT installation are used in combination with observed surface temperatures to optimize the parameters of a ground heat transport model. The surface temperature measurements are used to drive the heat transport model simulating a temperature distribution in the ground based on estimated ground thermal parameters. From the calculated temperature distribution, the effective resistivity distribution in the modeled domain is derived as geometric mean of specific resistivities of ground components (mineral grains, water and ice) weighted by their respective volumetric fractions in each model layer. An apparent resistivity response of such ground is calculated using CR1Dmod forward modeling tool. The simulated apparent resistivities are then compared to the field-measured apparent resistivities and the misfit between the measured and simulated apparent resistivity response is minimized by adjusting the parameters of the heat model. The coupling link between the thermal and electrical properties of ground is the temperature-dependent unfrozen water content. The advantage of the proposed optimization scheme is that the thermal model is coupled directly to the observed apparent resistivities, with no need for individual inversion of the resistivity profiles.

In a synthetic modeling study, the parameters used to describe the heat transport in frozen ground were recovered when synthetic apparent resistivity data with added noise were used for calibration. It was found that one full freezing season was sufficient to recover the uncertain parameters of the coupled thermo-geophysical model. One year´s worth of geoelectrical monitoring data from a field site in Ilulissat, Greenland, are used to validate the coupled inversion scheme.

It is consequently concluded that the surface geophysical measurements together with surface temperature measurements can be used to calibrate the heat model of the frozen ground without direct measurement of ground thermal parameters on soil samples. The model, when calibrated for specific site conditions, can be used for prediction of ground thermal stability changes under a chosen climate scenario when expected surface temperatures forcing is applied.

APPENDIX H

Conference Abstracts - ICOP 2016, Potsdam (1)

Optimizing electrode shapes for ERT monitoring in permafrost areas

Sonia Tomaskovicova[1], Thomas Ingeman-Nielsen[1], Anders V. Christiansen[2], Inooraq Brandt[3], Torleif Dahlin[4], & Bo Elberling[5]

[1] *Technical University of Denmark, Denmark*
[2] *Aarhus University, Denmark*
[3] *Orbicon, Greenland*
[4] *Lund University, Sweden*
[5] *University of Copenhagen, Denmark*

Very large and extreme variation in grounding resistances (GR) are some of the main challenges in the monitoring of permafrost and active layer processes with Electrical Resistivity Tomography in sedimentary deposits. The unfrozen, wet active layer typically results in low electrode grounding resistances in summer. In winter, however, when the active layer freezes, grounding resistances may increase many orders of magnitude, and hamper the acquisition of meaningfully long time series.

To investigate the factors conditioning the GR, we tested three stainless steel electrode types featuring increased size and surface area:

1. a rod electrode, with diameter 1 cm, length 8 cm and effective surface area: 27 cm^2
2. a square plate electrode, 10*10*0.1 cm (h*w*t), effective surface area: 204 cm^2
3. a wire mesh electrode, 10*10*0.6 cm (h*w*t), effective surface area: 985 cm^2

The electrodes were tested at three different localities in West Greenland: Qeqertarsuaq (69°15'N, 53°30'W, 30 m a.s.l.), Ilulissat (69°14'N, 51°3'W, 33 m a.s.l.) and Sisimiut site (66°56'N, 53°36'W, approx. 48 m a.s.l.). Each of these sites represents a different surface geology. The soil type at Ilulissat is a silty clay with little organic cover, at Sisimiut it is well drained fine sand likewise with very little organic cover, while at Qeqertarsuaq the surface deposits consists of a coarse sand with high organic content. Sisimiut and Qeqertarsuaq are located in the discontinuous permafrost zone, while Ilulissat has continuous permafrost.

At each site we installed three 10-electrode layouts (electrode separation 30 cm), each featuring a different electrode type. The grounding resistance of each individual electrode was measured using the focus-one protocol. The focus-one protocol, is essentially a two-electrode resistance measurement, where one electrode is connected to one terminal of the instrument, while all the other electrodes of the layout are connected in parallel to the other terminal, thereby effectively minimizing the contribution of their grounding resistances to the total measurement. Measurements were conducted at all three sites summer, fall and winter, to study also the effect of ground temperature.

The measured grounding resistances range from about 600 Ω to 1.2 MΩ (across seasons, electrode types and localities), and the effects of electrode type, locality (surficial geology) and ground temperature all tested statistically significant. Plate electrodes showed 28 to 69 % lower GR than rods during both thawed and frozen ground conditions at all sites. Mesh electrodes improved the GR by 29 to 37 % relative to plate electrodes in winter at the Ilulissat and Qeqertarssuaq sites. The increased effective surface area of the mesh electrodes seems to be an advantage when the electrodes are inserted or buried in fine grained mineral or organic soils with some cohesive properties, where the soil may fill the mesh openings. At the Sisimiut site, the coarser mineral soil results in no advantage of using mesh electrodes. Under thawed conditions, the plate and mesh electrodes did not test statistically different at any of the sites, indicating that the natural variation in soil and burial conditions is larger than the effect of the larger surface area.

An existing 64 electrode monitoring array installed at the Ilulissat site was used to further document the advantage of mesh electrodes over rod electrodes. Operating the monitoring setup, which was originally installed using rod electrodes, had been a challenge due to high grounding resistances in winter, effectively prohibiting the collection of measurements. Replacement of the rod electrodes with mesh electrodes

resulted in an immediate reduction of the average GR by 73 % from 1.5±0.9 to 0.4 ±0.1 kΩ (thawed conditions). Comparable winter grounding resistances were reduced from 64 ±32.1 to 25 ±11.4 kΩ, and following the replacement, measurements could be collected throughout the season.

We conclude that temperature, electrode shape and properties as well as lithology of the monitored site have significant impact on electrode grounding resistance and array performance, particularly in the cold/dry season. Thus, optimization of the electrode design should be a main consideration when planning a long-term monitoring project. Under the conditions we tested, the use of plate or mesh electrodes instead of rod electrodes were an advantage at all sites and all seasons. Mesh electrodes constitute an improvement only when the soil type allows to take advantage of the larger effective surface area (fine grained mineral or organic soils).

APPENDIX

Conference Abstracts - ICOP 2016, Potsdam (2)

Automated long-term time lapse ERT monitoring of high-latitude permafrost – results of 3 years of monitoring and modeling study

Sonia Tomaskovicova & Thomas Ingeman-Nielsen

Technical University of Denmark, Denmark

The importance of long-term, continuous and relatively dense ERT timeseries for improved process analysis in permafrost is well established. However, due to remoteness of sites, logistical constraints and harsh environment, high latitude permafrost presents a particular challenge for long-term ERT monitoring. Furthermore, extremely high grounding resistances hamper acquisition of series of complete freeze-thaw cycles that are needed for comparison with climate observations. In this contribution, we share how we resolved some of the logistical and technical challenges inevitably linked to the ERT monitoring in the Arctic. We also show results of a comprehensive permafrost monitoring project, currently running successfully for more than 3 years.

Since August 2012, we have been operating an automated monitoring station for measuring ground resistivity, water content and temperature at a site near the airport in Ilulissat, West Greenland (69°14' N, 51°3' W, 33 m a.s.l.). The site has a long observation history, starting with geotechnical investigations in late 1970's. The site is located in continuous permafrost zone, with mean annual air temperature -5.1 °C (2003-2012). The active layer thickness at the site is approximately 80 cm, below which ice-rich permafrost is found. The sediment cover consists of postglacial silt and clay marine deposits. These deposits are fully leached in the upper part, with residual salinity increasing with depth. Consequently, deeper parts of the soil profile are technically unfrozen due to freezing point depression. Gneiss bedrock is encountered at 7 m depth [Ingeman-Nielsen et al., 2008].

The monitoring station consist of one ERT profile, measurements of unfrozen water content at two depths in the active layer, measurement of ground temperature in 2 deep boreholes (4 and 6 m) and one temperature probe (length 1.5 m, with 16 sensors every 10 cm) for detailed monitoring of temperature dynamics of the active layer. Additional environmental observations include air temperature, approximate snow depth (using temperature sensors above ground) and ground thermal conductivity.

The ERT profile consists of 64 stainless steel, mesh-shaped electrodes, with spacing of 0.5 m. The mesh electrode shape is result of extensive field and laboratory testing study aiming to optimize the electrode design for long-term ERT monitoring. Automated ERT measurement system consists of a terrameter SAS1000 with electrode selector ES10-64 and an on-site mini computer. The computer controls daily acquisition of grounding resistances for each electrode of the array and a protocol of total 1625 datapoints of Schlumberger and Gradient array. The data are uploaded daily to a server at The Technical University of Denmark via GSM network.

The unfrozen water content is measured at 30 cm and 55 cm depth in the active layer by sensors using frequency domain reflectometry method. A soil-specific calibration equation is used to convert the measured permittivity into volumetric water content.

Comparison of results of joint resistivity, temperature and soil moisture monitoring evidences that changes of subsurface ground resistivity follow closely temperature and water dynamics in the ground. In the frozen period of the year (ca December to June), water content is consistently at its minimum, at 20 %. During this time, however, even relatively small temperature oscillations well below 0 °C produce noticeable changes in ground apparent resistivity. This suggests that notable phase change happens at temperatures as low as -5 to -10 °C and it points to high sensitivity of the ERT to track these changes. During the thawed season, the changes in resistivity are driven mainly by the changes of water content due to water movement in the active layer. After the initial ground thawing throughout the month of June, the ground reaches full saturation at up to 76 %. The thawing is reflected in sharp decrease of ground resistivity throughout the profile. Initial steep increase in soil moisture is followed by a period of drying out, or water runoff, during which the water content declines down to 40 % (while ground temperatures remain positive).

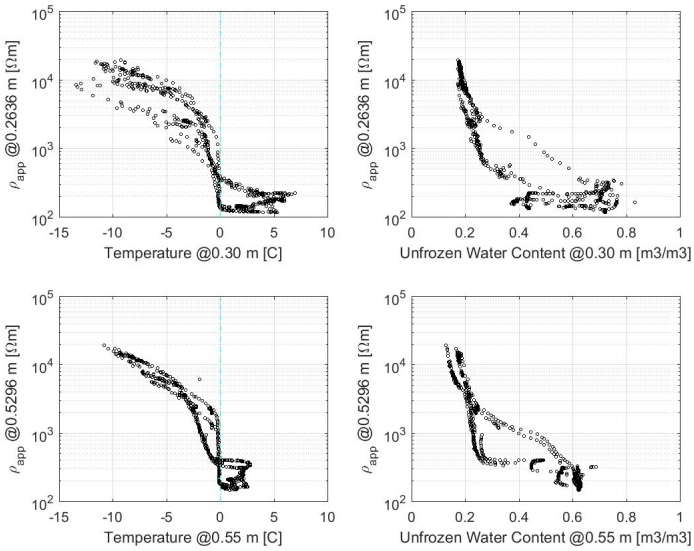

Figure 1: Scatter plots of the apparent resistivity against temperatureand water content at two depth levels in the active layer. Daily average values for 3 years.

This induces increase in resistivity at the top of the active layer, while the resistivity in the deeper portion of the profile steadily decreases as result of propagation of heat wave from ground thawing. The ground then reaches full saturation again during the relatively most humid months of August and September. It is only at this point that the ground resistivity reaches its yearly minimal values.

The ground surface temperature measurements have been successfully used in modeling of ground temperatures throughout the depth of the monitored profile. The 1D-heat model is able to reproduce the measured ground temperatures with mean deviation $\pm 0.2°$. While the full saturation condition at the site is valid (throughout the year except from July to mid-August), the unfrozen water content in the ground can be successfully modeled from ground temperatures (measured or modeled) using soil-specific freezing curve coefficients [Lovell, 1957]. As the changes in ground resistivity are intrinsically linked to the changes in the water content, this kind of integrated observation and modeling may pave the way for modeling of ground temperatures using exclusively surface observations (ground surface temperature and ground resistivity).

This ongoing monitoring project demonstrates feasibility and potential of long-term integrated high-latitude permafrost monitoring with focus on electrical and thermal properties of the ground. We present details of the permanent measurement setup and propose improvements to monitoring station design that mitigate the effects of extreme grounding resistances on acquisition of continuous resistivity timeseries. Results of 3 years of daily measurements of ground resistivity, temperature and water content provide insight into processes governing permafrost evolution and allow for modeling of important environmental parameters for which direct observations are difficult to acquire or missing.

References

Ingeman-Nielsen, T.; Foged, N.; Butzbach, R. and Stuhr Jørgensen, A. [2008]: Geophysical Investigation of Saline Permafrost at Ilulissat, Greenland. In: Kane, D.L. and Hinkel, K.M.(eds.), *Proceedings of the Ninth International Conference on Permafrost*, Institute of Northern Engineering, University of Alaska Fairbanks, Fairbanks, USA, 29 June–3 July 2008, volume 1, pages 773–778. ISBN 978-0-9800179-2-2. URL http://ipa.arcticportal.org/publications/conference-proceedings.

Lovell, C.W. Temperature effects on phase composition and strength of partially-frozen soil. *Highway Research Board Bulletin*, 168:74–95, 1957.

APPENDIX J

Conference Abstracts - ACOP 2017, Sapporo (1)

MODELING IN-SITU HYSTERETIC VARIATION OF UNFROZEN WATER CONTENT IN HIGH-LATITUDE FINE-GRAINED PERMAFROST

Sonia Tomaskovicova [1], Thomas Ingeman-Nielsen [1]

[1] *Department of Civil Engineering, Technical University of Denmark, Kongens Lyngby, Denmark*

Keywords: unfrozen water content, freeze-thaw hysteresis, thermal modeling, fine-grained permafrost

Unfrozen water content (UWC) is one of the key variables in modeling of thermal regime of permafrost as it influences calculation of bulk soil thermal parameters (e.g. Romanovsky & Osterkamp 2000). However, in-situ UWC measurements from periglacial environments are sparse and continuous timeseries over several complete freeze-thaw cycles are rarely available for validation of UWC parameterization schemes.

One of the models that describe variation of UWC with sub-freezing temperature T in fine-grained soil is a power function: $\theta(T) = a|T|^{-b}$ where $a, b > 0$ for $T < T^* < 0°C$ (Lovell, 1957). a and b are empirical parameters that require site-specific calibration. T^* is the lowest temperature at which all water in the soil sample is unfrozen; it depends on the soil grain size and freezing point of the pore water as a free substance.

With availability of 3 years of in-situ monitoring data from fine-grained high-latitude permafrost, we describe seasonal UWC dynamics in the active layer. We calibrate the parameters of the UWC model using one year of UWC and ground temperature records. We then use the calibrated model to predict UWC from ground temperatures in the following two years. The UWC was monitored at a site in Ilulissat, West Greenland (69° 14' N, 51° 3' W, 33 m above sea level), situated in continuous permafrost with mean annual air temperature -5.1°C (years 2003 - 2012). Core samples from the site contain up to 55% clay (grain size < 2μm) and 25% fine silt (grain size 2 - 6μm). Active layer thickness is 0.9 meters. The volumetric UWC and ground temperature are measured in 3-hourly intervals, 8 times per day, with two Steven's Hydra Probe II SD-12 sensors employing frequency domain reflectometry technology. The two sensors are placed at depths of 0.3 and 0.55 meters respectively.

The UWC dynamics are distinctly different between periods of soil freezing and thawing respectively. UWC during freezing is up to 50% higher than during thawing at the same ground temperature. Zero-curtain conditions during freezing lasts for ca. 3 weeks, during which UWC decreases steadily. On the contrary, the thawing of same volume of water happens abruptly over the course of ca. 2 days according to the sensor measurements. Microscopic processes of ice formation and melting likely contribute to different rates of freezing and thawing. Different freeze-thaw patterns can be observed even during events of partial thawing during frozen period. Nevertheless, we observe that the freezing and thawing patterns respectively remain the same every year. Between ca. 15th June – 31st August, the ground is unfrozen at the sensor depth and soil drying and possibly water runoff dominate the UWC variation despite low hydraulical conductivity of the soil.

Due to the observed freeze-thaw hysteresis, we split the UWC calibration into two seasons and calibrate two sets of a and b parameters on UWC measurements. Freezing season starts around the time when maximum depth of active layer is reached (1st September) and lasts until 28th February when the lowest ground temperatures are recorded. In the thawing season, only days between 1st March – 15th June (while the UWC variation is dominated by ground temperature as opposed to water circulation) are used for calibration. The model calibrated on freezing and thawing seasons 2012/2013 predicts UWC measurements in the following two years 2013/2014 and 2014/2015 within 5%.

In this work, we demonstrate that the calibrated model is able to predict the future UWC dynamics from measured or modeled ground temperatures with high accuracy. We also show that the freeze-thaw hysteresis is an important factor and its influence on heat transport in the ground should be considered when accounting for the UWC in permafrost models.

References:

Lovell, Jr. C. 1957. Temperature effects on phase composition and strength of partially-frozen soil. Highway Research Board Bulletin, 168.

Romanovsky, V. E. & Osterkamp, T. E. 2000. Effects of Unfrozen Water on Heat and Mass Transport Processes in the Active Layer and Permafrost. Permafrost and Periglacial Processes, 11: 219-239.

APPENDIX K

Conference Abstracts - ACOP 2017, Sapporo (2)

MODELING THE GROUND RESISTIVITY FROM UNFROZEN WATER CONTENT IN FINE-GRAINED HIGH-LATITUDE PERMAFROST

Sonia Tomaskovicova [1], Thomas Ingeman-Nielsen [1]

[1] *Department of Civil Engineering, Technical University of Denmark, Kongens Lyngby, Denmark*

Keywords: time lapse electrical resistivity tomography; unfrozen water content; coupled modeling; permafrost monitoring; fine-grained permafrost

Combination of time lapse electrical resistivity tomography (ERT) measurements, soil water content and borehole temperature measurements promises to hold better calibration for permafrost models (e.g. Pellet et al., 2016). The coupled modeling approaches rely on identification of valid petro-physical relationships, calibrated for the given geological setting. In this work, we use three years of monitoring data from a high-latitude permafrost site to model the relationships between ground temperature, unfrozen water content (UWC) and resistivity. 1D resistivity soundings were measured daily, and ground temperature and water content were monitored at three-hourly intervals at a site in continuous, fine-grained permafrost near Ilulissat, West Greenland (69° 14´ N, 51° 3´ W, 33 meters above sea level).

Between onset of freezing and ground temperature decrease down to -4°C at 0.3 meters depth, the volumetric UWC is reduced from 70% to 25%. This is accompanied by an increase in ground resistivity by two orders of magnitude, from $10^2\Omega$m to $10^4\Omega$m, within a period of three weeks. The minimum observed winter temperature at this depth is -17°C, and the corresponding minimum UWC is 18%. The resistivity at these temperatures could not be measured due to high electrode grounding resistances reaching up to 170 kΩ (Tomaskovicova et al., 2016). However, the maximum recorded resistivities are in the range of $4x10^4\ \Omega$m at a ground temperature of -10°C.

The UWC is the main parameter effectively controlling measured electric response of the ground at subfreezing temperatures. To test how the two are linked, we use the measured UWC to calculate a theoretical effective ground resistivity and compare it to the inverted resistivity measured at the field site. Knowing the UWC, volumetric fractions of ice and soil matrix can be calculated while assuming fully saturated soil and constant porosity throughout the simulation. The effective ground resistivity is estimated through geometric mean of specific resistivities of the respective soil constituents.

The model reproduces the observed increase in ground resistivity upon freezing very well. However, although there is good correlation between fluctuations in the observed and modelled ground resistivities in the frozen period, the amplitudes of the observed resistivity fluctuations are larger than those of the predicted. We speculate that variation in the electrode grounding resistances (correlated with surface temperature) contributes to larger amplitude excursions of the observed resistivities – a behavior that cannot be reproduced from UWC alone. During the thawing, the rate of decrease in ground resistivity is faster than increase of UWC. Consequently, for comparable UWC the observed resistivity during thawing is one order of magnitude lower than the resistivity during freezing. A plausible explanation is that even a slight increase in UWC during thawing creates current pathways sufficient for reduction of the ground resistivity. Microscopic processes of ice formation and melting likely contribute to different relationship patterns during freezing and thawing.

Our results indicate that timeseries of complete freeze-thaw cycles with sufficient sampling frequency (daily measurements for resistivity, up to 8 measurements per day for UWC) are necessary to accurately map fast temporal changes in UWC and ground resistivity during phase change, particularly if relationship between the two variables is to be used in calibration/validation of permafrost models.

References:

Pellet, C., Hilbich, C., Marmy, A., Hauck, C., 2016. Soil moisture data for the validation of permafrost models using direct and indirect measurement approaches at three alpine sites. Frontiers in Earth Science, 3:91.

Tomaskovicova, S., Ingeman-Nielsen, T., Christiansen, A. V. Brandt, I., Dahlin, T., Elberling, B. 2016. Effect of electrode shape on grounding resistances – Part 2: Experimental results and cryospheric monitoring. Geophysics, vol. 81, no. 1: 169-182.

APPENDIX L

Conference Abstracts - Plenary. ACOP 2017, Sapporo (3)

FIELD INVESTIGATIONS AND NUMERICAL MODELLING FOR INFRASTRUCTURE PLANNING IN GREENLAND

Sonia Tomaskovicova [1],
[1] *Technical University of Denmark,*

Keywords: Greenland, geotechnical investigations, permafrost monitoring, fine-grained permafrost, infrastructure development, coupled modelling

This talk aims to provide an introduction to challenges and approaches to site investigations for infrastructure planning and development in Greenland. Much of the existing infrastructure in Greenland - including residential buildings, roads and airport runways - is poorly adapted to existing conditions and is subject to deterioration or damage (Ingeman-Nielsen et al., in press). Built infrastructure affects permafrost conditions and may itself induce permafrost degradation. Climate change acts as an amplifying factor and with current predictions, it is expected to play an increasing role.

Meanwhile in Greenland, demands on infrastructure are rising due to increasing tourism and migration of population into larger towns. In the last two years, expansion or building of five airports, together with supporting infrastructure, have been decided by the Greenlandic Home Rule (The Government of Greenland). Structures such as airports and roads are distributed over broad areas, and therefore cross variety of environments. With permafrost in all of its forms affecting virtually the entire ice-free area in Greenland, there is a need for better permafrost knowledge and more reliable permafrost projections to support infrastructure design choices and justify the high cost associated with new engineering solutions and adaptation measures. Better projections require more engineering monitoring surveys and in-situ experimentation, as well as more spatially distributed and longer-term permafrost monitoring time series.

At numerous sites in Greenland, the geological history has resulted in a complex ground profile consisting of an upper ice-rich part and a lower zone with high residual salinity in pore water, high unfrozen water content, low or no ice content and low bearing capacity (Foged, 1979; Ingeman-Nielsen, 2008). In such settings, inadequate site investigation methods may fail to document these anomalies and thereby lead to poor choices of foundation design.

Two case studies of ongoing site investigations for large infrastructure projects in Greenland (a new airport in Ilulissat and a general geotechnical characterisation of permafrost conditions in Qaanaaq (Thule)) will illustrate the complex approaches for a more reliable assessment of ground geotechnical properties. We apply a range of methods, from studies of archive data, geophysical surveys, geotechnical drilling and borehole temperature monitoring for an integrated description of permafrost conditions. Aiming for a more spatially-distributed, longer-term predictions of ground thermal state, we develop and test alternative monitoring approaches, combining geophysical and thermal observations in a numerical modelling scheme. We share our practical experiences from these applications.

References:

Foged, N., 1979: Engineering Geological Investigations of Quaternary Marine Clay Deposits on West Greenland. Ph. D. Thesis. The Institute for Applied Geology. Technical University of Denmark.

Ingeman-Nielsen, T., N.N. Foged, R. Butzbach and A.S. Jørgensen, 2008: Geophysical investigations of saline permafrost at Ilulissat, Greenland. In: Kane, D.L. and K.M. Hinkel (Eds.). Proceedings of the Ninth International Conference on Permafrost, Fairbanks, Alaska, 2008. Volume 1, pp. 773-78. Institute of Northern Engineering, University of Alaska Fairbanks.

Ingeman-Nielsen, T., Lemay, M., Allard, M., Barrette, C., Bjella, K., Brooks, H., Carbonneau, A.-S., Doré, G., Ducharme, M.-A., Foged, N., L'Hérrault, E., Lading, T. & Mathon-Duffour, V. (2017): Chapter 10 - Built Infrastructure. In: AMAP: Adaptation Actions for a Changing Arctic - Perspectives from the Baffin Bay/Davis Strait Region. Arctic Monitoring and Assessment Programme (AMAP), Oslo, Norway. In press.

Bibliography

Anderson, Duwayne M and Allen R Tice (1972). "Predicting unfrozen water contents in frozen soils from surface area measurements". In: *Highway research record* 393.

Anderson, Duwayne M, Allen R Tice, and Harlan L McKim (1973). "The unfrozen water and the apparent specific heat capacity of frozen soils". In: *Proceedings of the second international conference on permafrost; North American contribution. Natl Acad Sci, Washington, DC*, pages 289–295.

Archie, Gustave E et al. (1942). "The electrical resistivity log as an aid in determining some reservoir characteristics". In: *Transactions of the AIME* 146.01, pages 54–62.

Auken, Esben et al. (2014). "An overview of a highly versatile forward and stable inverse algorithm for airborne, ground-based and borehole electromagnetic and electric data". In: *Exploration Geophysics* 46.3, pages 223–235.

Bennike, Ole and Svante Björck (2002). "Chronology of the last recession of the Greenland Ice Sheet". In: *Journal of Quaternary Science* 17.3, pages 211–219.

Brown, J et al. (1998). "revised February 2001. Circum-Arctic map of permafrost and ground-ice conditions. Boulder, CO: National Snow and Ice Data Center/World Data Center for Glaciology". In: *Digital media*.

Cappelen (2013). *Technical report 14-08. Weather observations from Greenland 1958-2012. Observation data with description.* Technical report. Danish Meteorological Institute.

Carslaw, HS and JC Jaeger (1959). *Heat in solids*. Volume 1. Clarendon Press, Oxford.

Coleman, Thomas F and Yuying Li (1996). "An interior trust region approach for nonlinear minimization subject to bounds". In: *SIAM Journal on optimization* 6.2, pages 418–445.

Daanen, RP et al. (2011). "Permafrost degradation risk zone assessment using simulation models". In: *The Cryosphere* 5.4, pages 1043–1056.

Dahl-Jensen, Dorthe et al. (1998). "Past temperatures directly from the Greenland ice sheet". In: *Science* 282.5387, pages 268–271.

Doetsch, Joseph et al. (2013). "Constraining CO 2 simulations by coupled modeling and inversion of electrical resistance and gas composition data". In: *International Journal of Greenhouse Gas Control* 18, pages 510–522.

Doetsch, Joseph et al. (2015). "Direct current (DC) resistivity and induced polarization (IP) monitoring of active layer dynamics at high temporal resolution". In: *Cold Regions Science and Technology* 119, pages 16–28.

Farouki, Omar T (1965). “Physical Properties of Granular Materials.” In: *Soil Science* 99.5, page 354.

— (1981). *Thermal properties of soils*. Technical report. DTIC Document.

Foged, N (1979). “Engineering Geological Investigations of Quaternary Marine Clay Deposits on West Greenland”. PhD thesis. Ph. D. Thesis. The Institute for Applied Geology. Technical University of Denmark,.(In Danish with English Overview).

Foged, Niels and Thomas Ingeman-Nielsen (2008). “Permafrost in Marine Deposits at Ilulissat Airport in Greenland, Revisited”. In: *Ninth International Conference e on Permafrost (445-450)*.

Fortier, Richard et al. (2008). “Internal structure and conditions of permafrost mounds at Umiujaq in Nunavik, Canada, inferred from field investigation and electrical resistivity tomography”. In: *Canadian Journal of Earth Sciences* 45.3, pages 367–387.

Friedman, Shmulik P (2005). “Soil properties influencing apparent electrical conductivity: a review”. In: *Computers and electronics in agriculture* 46.1, pages 45–70.

Gallardo, Luis A and Max A Meju (2011). “Structure-coupled multiphysics imaging in geophysical sciences”. In: *Reviews of Geophysics* 49.1.

Glover, Paul WJ (2010). “A generalized Archie’s law for n phases”. In: *Geophysics* 75.6, E247–E265.

Glover, Paul WJ, Malcolm J Hole, and Jaume Pous (2000). “A modified Archie’s law for two conducting phases”. In: *Earth and Planetary Science Letters* 180.3, pages 369–383.

Guéguen, Yves and Victor Palciauskas (1994). *Introduction to the physics of rocks*. Princeton University Press.

Hammer, Claus Uffe et al. (2001). “The Paleoclimatic Reocrd from a 345 m long Ice Core from the Hans Tausen Iskappe”. In: *Meddelser Om Grønland, Geoscience*.

Harris, Charles et al. (2009). “Permafrost and climate in Europe: Monitoring and modelling thermal, geomorphological and geotechnical responses”. In: *Earth-Science Reviews* 92.3, pages 117–171.

Hauck, C (2002). “Frozen ground monitoring using DC resistivity tomography”. In: *Geophysical research letters* 29.21.

Hauck, Christian, Mathias Bach, and Christin Hilbich (2008). “A 4-phase model to quantify subsurface ice and water content in permafrost regions based on geophysical datasets”. In: *Proceedings Ninth International Conference on Permafrost, June*, pages 675–680.

Herckenrath, Daan et al. (2013a). “Calibrating a Salt Water Intrusion Model with Time-Domain Electromagnetic Data”. In: *Groundwater* 51.3, pages 385–397.

Herckenrath, Daan et al. (2013b). “Sequential and joint hydrogeophysical inversion using a field-scale groundwater model with ERT and TDEM data”. In: *Hydrology and Earth System Sciences* 17.10, pages 4043–4060.

Hilbich, Christin, C Fuss, and Christian Hauck (2011). “Automated Time-lapse ERT for Improved Process Analysis and Monitoring of Frozen Ground”. In: *Permafrost and Periglacial Processes* 22.4, pages 306–319.

Hilbich, C et al. (2008). "Monitoring mountain permafrost evolution using electrical resistivity tomography: A 7-year study of seasonal, annual, and long-term variations at Schilthorn, Swiss Alps". In: *Journal of Geophysical Research: Earth Surface* 113.F1.

Hill, Mary C (1998). *Methods and guidelines for effective model calibration*. US Geological Survey Denver, CO, USA.

Hinnell, AC et al. (2010). "Improved extraction of hydrologic information from geophysical data through coupled hydrogeophysical inversion". In: *Water resources research* 46.4.

Hoekstra, Pieter, Paul V Sellmann, and A Delaney (1975). "Ground and airborne resistivity surveys of permafrost near Fairbanks, Alaska". In: *Geophysics* 40.4, pages 641–656.

Hördt, Andreas, Peter Weidelt, and Anita Przyklenk (2013). "Contact impedance of grounded and capacitive electrodes". In: *Geophysical Journal International* 193.1, pages 187–196.

Ingeman-Nielsen, Thomas and François Baumgartner (2006). "CR1Dmod: A matlab program to model 1D complex resistivity effects in electrical and electromagnetic surveys". In: *Computers & Geosciences* 32.9, pages 1411–1419.

Ingeman-Nielsen, Thomas, Soňa Tomaškovičová, and Torleif Dahlin (2016). "Effect of electrode shape on grounding resistances—Part 1: The focus-one protocol". In: *Geophysics* 81.1, WA159–WA167.

Ingeman-Nielsen, Thomas et al. (2017in press). *Chapter 10 - Built Infrastructure. In: AMAP: Adaptation Actions for a Changing Arctic - Perspectives from the Baffin Bay/Davis Strait Region*.

Ingeman-Nielsen, Thomas et al. (2008). "Geophysical Investigations of Saline Permafrost at Ilulissat, Greenland". In: *Ninth International Conference on Permafrost*. Institute of Northern Engineering, University of Alaska Fairbanks.

Ingeman-Nielsen, T et al. (2010). "Geotechnical implications of a warming climate in Greenland evaluated on the basis of permafrost temperature reanalysis and model projections". In: *Poster presented at the European Permafrost Conference June*.

Johansen, Oistein (1977). *Thermal conductivity of soils*. Technical report. Cold Regions Research and Engineering Lab Hanover NH.

Jørgensen, Anders Stuhr and Frank Andreasen (2007). "Mapping of permafrost surface using ground-penetrating radar at Kangerlussuaq Airport, western Greenland". In: *Cold regions science and technology* 48.1, pages 64–72.

Kneisel, Christof (2006). "Assessment of subsurface lithology in mountain environments using 2D resistivity imaging". In: *Geomorphology* 80.1, pages 32–44.

Knight, Rosemary (1991). "Hysteresis in the electrical resistivity of partially saturated sandstones". In: *Geophysics* 56.12, pages 2139–2147.

Koopmans, Ruurd Willem Rienk and RD Miller (1966). "Soil freezing and soil water characteristic curves". In: *Soil Science Society of America Journal* 30.6, pages 680–685.

Krautblatter, Michael and Christian Hauck (2007). “Electrical resistivity tomography monitoring of permafrost in solid rock walls”. In: *Journal of Geophysical Research: Earth Surface* 112.F2.

Krautblatter, Michael et al. (2010). “Temperature-calibrated imaging of seasonal changes in permafrost rock walls by quantitative electrical resistivity tomography (Zugspitze, German/Austrian Alps)”. In: *Journal of Geophysical Research: Earth Surface* 115.F2.

Krzewinski, Thomas G and Rupert G Tart Jr (1985). *Thermal design considerations in frozen ground engineering*. ASCE Publications.

LaBrecque, Douglas and William Daily (2008). “Assessment of measurement errors for galvanic-resistivity electrodes of different composition”. In: *Geophysics* 73.2, F55–F64.

Lal, Rattan and Manoj K Shukla (2004). *Principles of soil physics*. CRC Press.

Lochbühler, Tobias et al. (2013). “Structure-coupled joint inversion of geophysical and hydrological data”. In: *Geophysics* 78.3, pages ID1–ID14.

Lovell Jr, CW (1957). “Temperature effects on phase composition and strength of partially-frozen soil”. In: *Highway Research Board Bulletin* 168.

Lunardini, Virgil J (1981). *Heat transfer in cold climates*. Van Nostrand Reinhold Company.

Mankin, JB et al. (1975). “The importance of validation in ecosystem analysis”. In: *New directions in the analysis of ecological systems, part* 1, pages 309–317.

Mewes, Benjamin et al. (2016). “Resolution capacity of geophysical monitoring regarding permafrost degradation induced by hydrological processes”. In: *The Cryosphere Discussions*.

Nakano, Yoshisuke and Jerry Brown (1972). “Mathematical modeling and validation of the thermal regimes in tundra soils, Barrow, Alaska”. In: *Arctic and Alpine Research*, pages 19–38.

Nicolsky, DJ, VE Romanovsky, and GS Tipenko (2007). “Using in-situ temperature measurements to estimate saturated soil thermal properties by solving a sequence of optimization problems”. In: *The Cryosphere* 1.1, pages 41–58.

Osterkamp, TE (1987). “Freezing and thawing of soils and permafrost containing unfrozen water or brine”. In: *Water Resources Research* 23.12, pages 2279–2285.

Osterkamp, TE and VE Romanovsky (1997). “Freezing of the active layer on the coastal plain of the Alaskan Arctic”. In: *Permafrost and Periglacial Processes* 8.1, pages 23–44.

Overduin, Pier Paul, Douglas L Kane, and Wilko KP van Loon (2006). “Measuring thermal conductivity in freezing and thawing soil using the soil temperature response to heating”. In: *Cold Regions Science and Technology* 45.1, pages 8–22.

Parasnis, Dattetraya Shripad (2012). *Principles of applied geophysics*. Springer Science & Business Media.

Pedersen, Line Lindhardt (2013). “The mechanical properties of a saline fine-grained permafrost soil”. Bc. Thesis. Denmark: Technical University of Denmark.

Power, M (1993). “The predictive validation of ecological and environmental models”. In: *Ecological modelling* 68.1-2, pages 33–50.

Rasch, Morten (2000). "Holocene relative sea level changes in Disko Bugt, West Greenland". In: *Journal of Coastal Research*, pages 306–315.

Reynolds, John M (2011). *An introduction to applied and environmental geophysics*. John Wiley & Sons.

Riseborough, Daniel et al. (2008). "Recent advances in permafrost modelling". In: *Permafrost and Periglacial Processes* 19.2, pages 137–156.

Romanovsky, VE, TE Osterkamp, et al. (2000). "Effects of unfrozen water on heat and mass transport processes in the active layer and permafrost". In: *Permafrost and Periglacial Processes* 11.3, pages 219–239.

Romanovsky, VE et al. (2015). "Terrestrial permafrost [in 'state of the climate in 2014']". In: *Bull. Am. Meteorol. Soc.* 96.7, S139–S141.

Rykiel, Edward J (1996). "Testing ecological models: the meaning of validation". In: *Ecological modelling* 90.3, pages 229–244.

Smith, SL et al. (2010). "Thermal state of permafrost in North America: a contribution to the international polar year". In: *Permafrost and Periglacial Processes* 21.2, pages 117–135.

Stendel, Martin et al. (2008). "The fate of Greenland's permafrost; results from high-resolution transient climate simulations". In: *Ninth International Conference on Permafrost, Fairbanks*, pages 1705–1709.

Sunde, Erling Ditlef (1949). *Earth conduction effects in transmission systems*. Dover Publications Inc.

Telford, William Murray et al. (1990). *Applied geophysics*. Volume 1. Cambridge university press.

Tomaskovicova, Sonia and Thomas Ingeman-Nielsen (2016). "Automated long-term time lapse ERT monitoring of high-latitude permafrost–results of 3 years of monitoring and modeling study". In: *XI. International Conference on Permafrost*, pages 990–991.

Tomaskovicova, Sonia et al. (2016). "Effect of electrode shape on grounding resistances-Part 2: Experimental results and cryospheric monitoring". In: *Geophysics* 81.1.

Wait, James (2012). *Geo-electromagnetism*. Elsevier.

Williams, PJ (1963). "Specific heats and unfrozen water content of frozen soils". In: *Proc. First Can. Conference Permafrost*, pages 109–126.

Zhang, Yinsuo, Sean K Carey, and William L Quinton (2008). "Evaluation of the algorithms and parameterizations for ground thawing and freezing simulation in permafrost regions". In: *Journal of Geophysical Research: Atmospheres* 113.D17.

{2.7182818284}ϑφερτυθιοπσδφγηξκλ

This Ph.D. thesis summarizes results of field, laboratory and modeling studies of frost-susceptible, ice-rich permafrost in Ilulissat, West Greenland. We present a modeling tool for simulating the ground thermal regime driven by surface measurements only, using time lapse geoelectrical measurements and ground surface temperatures. These are results of the longest and most complete combined monitoring datasets of ground temperature, electrical resistivity and soil moisture from high-latitude permafrost to date.

DTU Civil Engineering
Technical University of Denmark

Brovej, Bygning 118
2800 Kongens Lyngby

www.byg.dtu.dk

ISBN 9788778774828
ISSN 1601-2917